Relativistic kinetic gas configurations surrounding black holes

TESIS

Que Presenta

Carlos Eduardo Gabarrete Fajardo

Para obtener el Grado de

Doctor en Ciencias en el Área de Física

Asesorado por

Dr. Olivier Charles Albert Sarbach

Universidad Michoacana de San Nicolás de Hidalgo
Instituto de Física y Matemáticas (IFM)
Morelia, Michoacán de Ocampo

Octubre, 2022.

To Darien & Lirio

The talent is formed in solitude and
the character in the storm of life.

-Johann Wolfgang von Goethe-

Acknowledgments

Agradezco a Dios por haberme permitido vivir este dia.

A mi Esposa Lirio por acompañarme en este proyecto de vida.

A mi hijo Darien por regalarme sus primeras sonrisas.

A nuestras Familias Gabarrete Fajardo y Castro Guillén por todo su apoyo a la distancia.

A mis amigos Susy, Leslie, Claudia, Wilmer, Cristian, Lucio, Alejandro, Addi; Karen, Melissa, Oliver, Fermin y Eduardo. A Felix, Rubén, Armando y Pankaj del IFM.

A mis profesores en el Doctorado: Dr. Cristian, Dr. Emilio, Dr. Ulises, Dr. Francisco, Dr. Thomas, Dra. Ana Laura. Al Dr. Dario y Aldo del ICN.

Y sobre todo a mi Asesor el Dr. Olivier Sarbach, de quien me llevo la mejor experiencia de vida, a quien le debo todo lo aprendido en este proyecto, siempre admiraré su talento, sabiduria e inteligencia infinita. Estoy muy orgulloso de haber sido su estudiante, amigo y colega.

¡ Muchas gracias por todo Dr!

Gracias al Consejo Nacional de Ciencia y Tecnología por el apoyo, No. CVU 940052.

Resumen

Esta tesis se enfoca en el estudio del comportamiento de un gas cinético relativista en un campo gravitacional fuerte. Para este propósito, adoptamos una perspectiva geométrica la cual ofrece la ventaja de incorporar la covarianza general de la teoría de forma natural. En particular, estamos interesados en nubes de gas cinético que se propagan en la vecindad de los agujeros negros, y en este proyecto de investigación exploramos diferentes escenarios que describen tales configuraciones.

Para simplificar el problema, consideramos el caso en el que las colisiones entre las partículas del gas, así como los efectos de la auto-gravedad del gas y el campo electromagnético pueden despreciarse. Esto lleva el problema a resolver la ecuación relativista de Boltzmann sin colisiones para la función de distribución de una partícula en un espacio-tiempo fijo de fondo que describe un agujero negro. Restringiéndonos a un agujero negro de Schwarzschild y eligiendo una función de distribución que depende únicamente de integrales de movimiento, la ecuación de Boltzmann sin colisiones se resuelve automáticamente y se pueden calcular los observables del espacio-tiempo, tales como la densidad de corriente de las partículas, el tensor de energía-momento-estrés y la densidad de flujo de entropía del gas.

En este trabajo estudiamos dos casos de interés. El primer caso describe una nube de gas cinética axisimétrica en estado estacionario atrapada en el potencial de un objeto central, tanto en el régimen relativista como en el no relativista. En particular, proporcionamos expresiones analíticas para las observables que describen configuraciones con masa total finita y momento angular, y proporcionamos un análisis detallado de las propiedades de estas observables, incluidas las densidades de partículas y energía, las presiones principales y la temperatura cinética. El segundo caso está dedicado a un problema de acreción en el que una nube de gas cinético esférica es acretada por el agujero negro. La novedad de este segundo escenario es que las propiedades del gas se especifican en una esfera de radio finito. Además, discutimos cómo los agujeros negros con baja luminosidad podrían explicarse parcialmente mediante una descripción cinética de la materia que cae.

Palabras Clave: *Agujeros Negros, Relatividad General, Teoría Cinética Relativista, Ecuación de Boltzmann Relativista, gas de Vlasov.*

Abstract

This thesis focuses on the study of the behavior of a relativistic kinetic gas in a strong gravitational field. To this purpose, we adopt a geometric perspective which offers the advantage of incorporating the general covariance of the theory in a natural way. In particular, we are interested in kinetic gas clouds which propagate in the vicinity of black holes, and in this research project we explore different scenarios describing such configurations.

To simplify the problem, we consider the case in which collisions between the gas particles, as well as effects of the self-gravity of the gas and the electromagnetic field can be neglected. This leads to the problem of solving the relativistic collisionless Boltzmann equation for the one-particle distribution function on a fixed spacetime background describing a black hole. Restricting ourselves to a Schwarzschild black hole and choosing a distribution function depending only on integrals of motion, the collisionless Boltzmann equation is solved automatically, and one can compute the spacetime observables such as the particle current density, the energy-momentum-stress tensor, and the entropy flux density of the gas.

In this work, we study two cases of interest. The first case describes a steady-state axisymmetric kinetic gas cloud trapped in the potential of a central object, both in the relativistic and non-relativistic regimes. In particular, we provide analytical expressions for the observables describing configurations with finite total mass and angular momentum, and we provide a detailed analysis of the properties of these observables, including the particle and energy densities, principal pressures, and kinetic temperature. The second case is devoted to an accretion problem in which a spherical kinetic gas cloud is accreted by the black hole. The novel feature in this second scenario is that the properties of the gas are specified at a sphere of finite radius. Furthermore, we discuss how black holes with low luminosity could be partially explained by a kinetic description of the infalling matter.

Key Words: *Black Holes, General Relativity, Relativistic Kinetic Theory, Relativistic Boltzmann equation, Vlasov gas.*

Notation

Some notation used in this work

$(\mathcal{M}, g, \nabla)$	Four-dimensional spacetime manifold with associated Levi-Civita connection
$T\mathcal{M}, T^*\mathcal{M}$	Tangent/cotangent bundle
$T_x\mathcal{M}, T_x^*\mathcal{M}$	Tangent/cotangent space at event $x \in \mathcal{M}$
$(-,+,+,+)$	Signature convention
$i, j, k, l, \ldots$	Latin indices run over $1, 2, 3$
$\alpha, \beta, \mu, \nu, \ldots$	Greek indices run over $0, 1, 2, 3$
$\hat{\alpha}, \hat{\beta}, \hat{\mu}, \hat{\nu}, \ldots$	Tetrad indices run over $0, 1, 2, 3$
$G_N = c = 1$	Geometrized units, in which distance, time and mass have the same units
C^∞	Infinitly differentiable
$\mathcal{F}(\mathcal{N})$	Class of C^∞-smooth functions on a differentiable manifold $\mathcal{N}$
$\mathcal{X}(\mathcal{N})$	Class of C^∞-smooth vector fields on a differentiable manifold $\mathcal{N}$
$\Lambda_p(\mathcal{N})$	Class of C^∞-smooth p-forms on a differentiable manifold $\mathcal{N}$
$\mathcal{T}(\mathcal{N})$	Class of C^∞-smooth tensor fields on a differentiable manifold $\mathcal{N}$
$d\omega$	Exterior derivative of p-form ω
$i_X\omega$	Interior derivative with respect to vector field $X \in \mathcal{X}(\mathcal{N})$
$\pounds_X\omega$	Lie derivative with respect to vector field $X \in \mathcal{X}(\mathcal{N})$
$\wedge$	Wedge product
$\otimes$	Tensor product
$:=$	Definition
$\simeq$	Isomorphism
$(\ )$	Symmetrization operation
$[\ ]$	Antisymmetrization operation

Index

Acknowledgments IV

Resumen V

Abstract VI

Notation VII

1 Introduction 1

1.1 Kinetic theory: motivation and applications . . . 1
1.2 Some details on the mathematical formulation of general relativity and kinetic theory . . . 2
1.2.1 A brief review of spacetime manifolds . . . 3
1.2.2 The geometric structures on the cotangent bundle . . . 9
1.2.3 Properties of the exterior Schwarzschild spacetime . . . 14
1.3 Summary of main results of this thesis . . . 18

2 Relativistic kinetic theory 21

2.1 The one-particle distribution function . . . 21
2.2 Derivation of the Liouville equation . . . 25
2.3 The spacetime observables . . . 26

3 The relativistic Boltzmann equation 29

3.1 Integro-differential form of the Boltzmann equation . . . 29
3.2 Global and local thermodynamical equilibrium . . . 33
3.2.1 Local thermodynamical equilibrium . . . 34
3.3 Limits of large and small Knudsen number . . . 36
3.3.1 The Vlasov limit . . . 37
3.3.2 The hydrodynamic limit . . . 38
3.4 Collisionless Boltzmann equation . . . 38

4 Axisymmetric, stationary collisionless gas clouds trapped in a Newtonian potential 40

4.1 Abstract . . . 40
4.2 Introduction . . . 40

4.3 Review of basic equations and polytropic model . . . 43
4.3.1 Basic equations describing a collisionless, stationary gas configuration in a central potential . . . 43
4.3.2 Spherical polytropes . . . 45
4.4 Stationary, axisymmetric models . . . 47
4.4.1 General bounds on the observables . . . 47
4.4.2 The (E, L_z)-models . . . 49
4.4.3 Total mass, energy and angular momentum . . . 53
4.5 Properties of the macroscopic observables . . . 56
4.5.1 Normalized particle density and morphology . . . 56
4.5.2 Mean particle velocity . . . 58
4.5.3 Kinetic temperature . . . 59
4.5.4 Pressure anisotropy . . . 61
4.5.5 Total mass, energy and angular momentum . . . 64
4.5.6 Comparison with fluid model . . . 65
4.6 Conclusions . . . 68
4.7 Appendix A: Integrals over angular momentum and energy . . . 71
4.8 Appendix B: Properties of the effective potential belonging to the isochrone model . . . 72
4.9 Appendix C: Total mass, energy and angular momentum . . . 73
4.10 Appendix D: Short review of circular hydrodynamic flows . . . 76

5 Axisymmetric, stationary collisionless gas configurations surrounding black holes 79
5.1 Abstract . . . 79
5.2 Introduction . . . 79
5.3 Collisionless gas configurations trapped in a Schwarzschild potential . . . 82
5.3.1 Free-particle Hamiltonian, integrals of motion and effective potential . . . 82
5.3.2 Collisionless Boltzmann equation and spacetime observables . . . 84
5.3.3 Explicit representation of the observables in terms of integrals over the conserved quantities . . . 85
5.4 Stationary, axisymmetric models . . . 89
5.4.1 The relativistic (E, L_z)-models . . . 89
5.4.2 Spacetime observables . . . 90
5.4.3 Total particle number, energy and angular momentum of the kinetic gas cloud . . . 94
5.5 Properties of the spacetime observables . . . 98
5.5.1 Normalized particle density and morphology of the gas cloud . . . 99
5.5.2 Kinetic temperature . . . 101

5.5.3 Pressure anisotropy 102
5.5.4 Comparison with fluid model 103
5.6 Conclusions 105
5.7 Appendix A: Parametrization of bound trajectories in terms of the variables (p, e) 109
5.8 Appendix B: Limits of integration for the fiber integrals defining the spacetime observables 110
5.9 Appendix C: Integrals over angular momentum 112
5.10 Appendix D: Properties of the integral kernels $\tilde{\mathrm{K}}_l(a, b)$ 114
5.11 Appendix E: Short review of polish doughnuts configurations 117

6 Accretion of a Vlasov gas onto a black hole from a sphere of finite radius and the role of angular momentum 121

6.1 Abstract 121
6.2 Introduction 122
6.3 Review of the general relativistic Vlasov equation 125
6.4 Purely radial infall from a finite radius 128
6.4.1 Non-relativistic limit 128
6.4.2 Relativistic case 131
6.5 Spherical accretion with angular momentum from a finite radius 133
6.5.1 Mono-energetic model 138
6.5.2 Maxwell-Jüttner-type distribution function 140
6.6 Summary of analytic models 145
6.7 Applications 146
6.7.1 Accretion onto Sgr A* from matter located near the Bondi radius 146
6.7.2 Accretion in the vicinity of Sgr A* and M87* 151
6.8 Summary and conclusions 152
6.9 Appendix: Fixed-L-models 154

7 Conclusions and future work 157

Figure List

1-1 Illustration of a tangent vector. 4
1-2 Parallel transport of a vector along a closed curve on a S^2-sphere. . . . 8
1-3 Projection map π and its inverse image π^{-1} on $T^*\mathcal{M}$. 10
1-4 Behavior of the effective potential. 16
1-5 Phase diagram in the (r, p_r)-plane. 18
1-6 Regime of bound, absorbed, and scattered trajectories. 19

2-1 Illustration of the current density vector field $\mathcal{J}$ through the surface Σ_0 with normal vector $\hat{\nu}$. 23
2-2 Illustration of the averaged number of occupied trajectories in the future mass shell and the averaged number of particles in the spacetime. . . 24

4-1 Normalized particle density on the equatorial plane for $l = 1$ and $k = 5, 6, 7$. 57
4-2 Normalized particle density on the equatorial plane for $k = 6$ and $l = 1, 2, 3$. 58
4-3 Contour plot for the normalized particle density. 59
4-4 Magnitude of the mean velocity. 60
4-5 Kinetic temperature of the rotating model. 61
4-6 Kinetic temperature of the non-rotating model. 61
4-7 Anisotropy parameter for a rotating model. 62
4-8 Anisotropy parameter for a non-rotating model. 63
4-9 Total mass. 64
4-10 Total energy per total mass. 65
4-11 Total angular momentum per total mass. 65
4-12 Comparison between the normalized densities and between the normalized temperatures. 68
4-13 Behavior of the dimensionless effective potential. 74
4-14 Contour plot for the enthalpy for Kepler case. 78
4-15 Contour plot for the enthalpy for isochrone case. 78

5-1 Behavior of effective potential. 87
5-2 Behavior of the critical minimum energy. 88

5-3 Comparison between the total mass in the Newtonian case with the Kepler and isochrone potentials and the total rest mass in the relativistic case. 98
5-4 Comparison between the absolute value of the internal energy. 98
5-5 Normalized particle density in the equatorial plane for $k = 5$, $l = 0, 1, 2$. 100
5-6 Normalized particle density in the equatorial plane for $l = 1$, $k = 5, 6, 7$. 100
5-7 Contour plot of the normalized particle density. 101
5-8 Comparison of the particle density between the even and rotating models. 101
5-9 Relative difference $n^{(\mathrm{even})}/n^{(\mathrm{rot})} - 1$ between the even and rotating models. 102
5-10 Equatorial kinetic temperature profiles. 102
5-11 Comparison between equatorial kinetic temperature profiles. 103
5-12 Behavior of the principal pressures. 103
5-13 Behavior of the principal pressures. 104
5-14 Normalized profiles between the kinetic and fluid descriptions. 106
5-15 Image of the (p, e) domain. 110
5-16 Illustration for the allowed region of integration in the (p, e)-plane. . . . 111
5-17 Integration domain corresponding to spacetime observable. 113
5-18 Behavior of the integrals $\tilde{\mathrm{K}}_l(a, b)$. 116
5-19 Contour plots for the effective potential. 120

6-1 Behavior of Schwarzschild' effective potential vs radius. 137
6-2 Dimensionless quantity Γ vs Lorentz factor γ for some fixed values of the injection sphere's radius R. 141
6-3 Dimensionless quantity Γ vs temperature z^{-1} for some fixed values of the injection sphere's radius R. 144

Table List

4-1 Effective adiabatic index. 68

4-2 Ratio between the radii corresponding to the maxima of the fluid and kinetic temperature profiles and ratio between the corresponding maxima of the temperature. 69

4-3 Ratio between the radii corresponding to the maxima of the fluid and kinetic temperature profiles and ratio between the corresponding maxima of the temperature. 69

5-1 Ratio between the radii corresponding to the maxima of the fluid and kinetic temperature profiles and ratio between the corresponding maxima of the temperature. 107

6-1 Mass accretion rate inferred for Sgr A* at $R = 0.06\,\mathrm{pc}$. 150

6-2 Mass accretion rate inferred for Sgr A* at $R = 5\,r_\mathrm{S}$. 152

6-3 Mass accretion rate inferred for M87* at $R = 5\,r_\mathrm{S}$. 152

1 Introduction

1.1. Kinetic theory: motivation and applications

The kinetic theory of dilute gases is a theory which allows one to understand macroscopic phenomena from the laws of micro-physics even if the system is off equilibrium. This theory can be treated through a suitable key concept, namely, the characterization of the state of the gas through the one-particle distribution function (DF). The DF is a time-dependent function defined on the one-particle phase space of the theory, whose time evolution is determined by Boltzmann's equation. For details in different contexts see [1, 2] for a classical gas, [3–6] for a relativistic gas and [7] for a quantum gas. For some recent works and reviews regarding the general relativistic description which use the modern differential geometry language, see references [8–12]. This geometric formulation point of view has the conceptual advantage of naturally incorporating the general covariance of the theory. We adopt this geometric perspective in this thesis work as much as possible; however, we also provide the coordinate representation for the relevant equations for readers who are unfamiliar with the differential geometry language.

The relativistic kinetic theory has been developed since the beginning of the twentieth century starting with F. Jüttner [13, 14] who generalized the equilibrium Maxwell-Boltzmann gas distribution and its equation of state to the relativistic case. Next, J.L. Synge [15] provided a covariant description of the theory by proposing the description of the gas based on the world lines of the gas particles. Later, many other prominent researchers such as W. Israel [16, 17], R. Lindquist [18], J. Ehlers [19], S.R. de Groot and W.A. van Leeuwen and Ch. G. van Weert [6], C. Cercignani and G.M. Kremer [3,4] to mention some relevant contributions, further developed the theory and its applications. As mentioned above, the relativistic kinetic theory formulation is based on the Boltzmann equation which is difficult to solve due to the fact that this equation is an integro-differential equation, as will see in chapter 3.

However, this theory can be applied in different physical scenarios which provide interesting predictions and applications as we will see through this thesis work and related references. Different systems can be treated jointly with the Boltzmann equation, for example, when including self-gravity effects between the massive particles or the charge for a gas consisting of two species (electrons and protons, for instance). When the gravitational self-interaction of the particles are important the system needs to be modeled using the Einstein-Boltzmann equation (c.f. [20]) or in the non-relativistic regime using the Boltzmann-Poisson system (c.f. [21]). When collisions between the particles in the kinetic gas are unimportant or negligible the Vlasov-Poisson or Einstein-Vlasov equations are the relevant systems in the non-relativistic and relativistic cases respectively. For applications of the first case we refer the reader to [22] and for the second case to [8, 23–30]. If we include the charge of the gas particles, the Einstein-Vlasov-Maxwell system [31–33] needs to be solved. We can add more and more features of microphysics which leads to additional coupled equations depending on the system of interest. For all those mentioned above the kinetic theory is subject to an active research activity, due to the richness of the model.

To mention some relevant examples, the kinetic theory is useful to describe the dynamics of a gas in a near-equilibrium state, or the relaxation process for a collisionless charged gas in plasma physics [34]. In galactic dynamics it is useful to describe a distribution of stars including their self-gravity in a self-consisting way [35]. Other applications can be treated in this way depending if the collisions between the particles are important or not. As an example of a collisionless kinetic gas, the accretion problem of baryonic (or dark) matter into black hole from an accretion disk (or the halo of the galaxy) has a lot of astrophysical interest, see [36–41] for baryonic matter and [42, 43] for dark matter falling into black holes. In the cosmological context, kinetic theory also plays an important role in studying the evolution of a spatially homogeneous and isotropic universe filled with a collisionless gas [44]. Including the collisions between the gas particles the works in [12, 45, 46] investigate the behavior of a massless or massive gas particles in a fully general relativistic expanding system.

As part of this thesis work we establish configurations of a collisionless kinetic gas cloud which is trapped in the potential of a central object in the Newtonian and relativistic regimes [47–49], and we also study accretion of a kinetic gas cloud into a black hole from a finite radius in [40]. A review of the relativistic kinetic theory on curved spacetimes in d-dimensions which is based on the geometric structure of the cotangent bundle was given in [12]; we base our thesis work on this formalism.

1.2. Some details on the mathematical formulation of general relativity and kinetic theory

This thesis work is about the description of the relativistic kinetic theory of gases on curved spacetimes. For this, we base our formulation of the relativistic space phase on a submanifold of the cotangent bundle $T^*\mathcal{M}$, which is naturally adapted to the Hamiltonian formulation. Although most previous work define this space phase as a submanifold of the tangent bundle $T\mathcal{M}$, the two formulations are equivalent since the metric tensor provides an isomorphism between the tangent and cotangent bundles. For further details on the tangent bundle formulation, see Refs. [9–11,50]. This section starts with a brief review of the spacetime manifold and its relevant results for this thesis work. In the following subsections we provide a summary of the principal structures of the cotangent bundle.

1.2.1. A brief review of spacetime manifolds

We start with the relevant structures of the four-dimensional spacetime manifold and its associated Levi-Civita connection ∇, which will be denoted for simplicity as $(\mathcal{M}, g)$. Here, $\mathcal{M}$ is a differentiable manifold and represents an adequate mathematical description in which the spacetime locally looks like $\mathbb{R}^4$. However, its global properties might be quite different from $\mathbb{R}^4$. See the standard book references on general relativity [51–55] and references [56,57] for a coordinate-invariant language as the one used in this work.

We introduce the first geometric concept: the tangent vectors. For this, consider a differentiable manifold $\mathcal{M}$, p a point on the manifold $p \in \mathcal{M}$, and $\epsilon > 0$ for which a C^∞-differential curve γ through p is given by

$$\gamma : (-\epsilon, \epsilon) \to \mathcal{M}, \quad \gamma(0) = p. \tag{1.2.1}$$

Next, let $f : U \to \mathbb{R}$ be a differential function defined in the vicinity of a local chart (U, ϕ) such that $p \in U$. The directional derivative of f in p along γ is defined by

$$X_p[f] := \left.\frac{d}{dt} f(\gamma(t))\right|_{t=0}. \tag{1.2.2}$$

X_p is called the tangent vector of γ at p. Figure **1-1** shows an illustration of a tangent vector at the point $p \in \mathcal{M}$. The set of tangent vectors at p form a four-dimensional vector space, called the tangent space $T_x\mathcal{M}$ at x. Its dual space is the cotangent space $T_x^*\mathcal{M}$ at x.

In general relativity the events are described by points x in the spacetime manifold $(\mathcal{M}, g)$. From the invariant definition of vectors (1.2.2) for all points in a local chart on the manifold $\mathcal{M}$ one can choose particular local coordinates x^μ to expand the vectors at each point. For example, one can expand a vector field $X \in \mathcal{X}(\mathcal{M})$ in terms of the

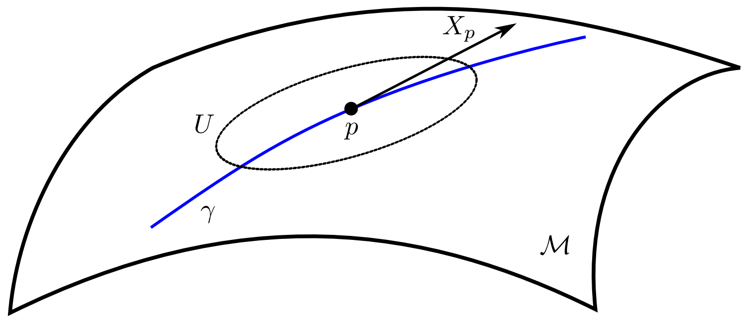

Figure 1-1: Illustration of a tangent vector X_p at the point $p \in \mathcal{M}$ in the vicinity of U. The blue curve represents the γ function which contains the point p.

basis $\left\{ \left.\frac{\partial}{\partial x^\mu}\right|_p \right\}$, and obtain

$$X = X_p^\mu \left.\frac{\partial}{\partial x^\mu}\right|_p, \tag{1.2.3}$$

where $X_p^\mu = X_p[x^\mu]$ are the components of the vector field at the point $p \in \mathcal{M}$. We can also expand this vector field X in terms of another basis $\left\{ \left.\frac{\partial}{\partial y^\nu}\right|_p \right\}$ with corresponding components Y_p^ν, and one obtains a transformation between the components and the basis of the vector field, such that

$$Y_p^\nu = \left.\frac{\partial y^\nu}{\partial x^\mu}\right|_p X_p^\mu, \quad \text{and} \quad \left.\frac{\partial}{\partial y^\nu}\right|_p = \left.\frac{\partial x^\mu}{\partial y^\nu}\right|_p \left.\frac{\partial}{\partial x^\mu}\right|_p. \tag{1.2.4}$$

In this way it is always possible to transform from a particular local coordinate system to another.

A tensor field $T \in \mathcal{T}^0{}_2(\mathcal{M})$ (here $(0,2)$ refers to the type of tensor field, i.e. twice covariant) can be defined as a map $T \;:\; T_x\mathcal{M} \times T_x\mathcal{M} \mapsto \mathbb{R}$ which takes two vectors $X_p, Y_p \in T_p(\mathcal{M})$ and returns a real value such that T is linear in each argument. In local coordinates one has

$$T = T_{\mu\nu} dx^\mu \otimes dx^\nu, \quad T_{\mu\nu} = T\left(\frac{\partial}{\partial x^\mu}, \frac{\partial}{\partial x^\mu}\right), \tag{1.2.5}$$

where $T_{\mu\nu}$ are the components of the tensor field. As for vector fields, the tensor fields transform according to

$$\widetilde{T}_{\alpha\beta} = \left.\frac{\partial x^\mu}{\partial y^\alpha}\right|_p \left.\frac{\partial x^\nu}{\partial y^\beta}\right|_p T_{\mu\nu}, \tag{1.2.6}$$

where $\left\{ \left.\frac{\partial}{\partial x^\mu}\right|_p, \left.\frac{\partial}{\partial y^\nu}\right|_p \right\}$ are two different basis at $p \in \mathcal{M}$ and $T = \widetilde{T}_{\alpha\beta} dy^\alpha \otimes dy^\beta$.

Similarly, tensor fields of the other types can be defined.

The next relevant concept is the affine connection ∇. This object permits one to introduce the concept of parallel transport of vectors along a curve γ (which depends on the election of the curve γ). This affine connection provides a map in which one can compare two tangent vectors defined at two different points on the manifold which are connected by a curve γ. It also permits to define a covariant derivative (i.e. a derivative of tensor fields) and the geodesics as preferred curves in $\mathcal{M}$, with the property that their tangent vector is parallel transported along themselves. Formally, the affine connection is a map

$$\begin{aligned} \nabla : \mathcal{X}(\mathcal{M}) \times \mathcal{X}(\mathcal{M}) &\rightarrow \mathcal{X}(\mathcal{M}) \\ (X, Y) &\mapsto \nabla_X Y, \end{aligned} \tag{1.2.7}$$

which satisfies the following properties: (i) $\nabla_X(Y+Z) = \nabla_X Y + \nabla_X Z$, (ii) $\nabla_{f\cdot X+g\cdot Y} Z = f \cdot \nabla_X Z + g \cdot \nabla_Y Z$, and (iii) $\nabla_X(f \cdot Y) = f \cdot \nabla_X Y + (Xf) \cdot Y$ for all $f, g \in \mathcal{F}(\mathcal{M})$, $X, Y, Z \in \mathcal{X}(\mathcal{M})$.

Let ∇ be an affine connection on $\mathcal{M}$, $X, Y \in \mathcal{X}(\mathcal{M})$ vector fields, and let $\omega \in \mathcal{X}^*(\mathcal{M})$ be a covector field. Using the previous properties of the affine connection, the covariant derivative $\nabla Y \in \mathcal{T}^1{}_1(\mathcal{M})$ is defined by

$$\nabla Y(\omega, X) := \omega(\nabla_X Y). \tag{1.2.8}$$

In terms of local coordinates x^μ and their corresponding basis $\left\{\dfrac{\partial}{\partial x^\mu}\right\}$ the well-known form of the components of the covariant derivative are

$$\nabla_\mu Y^\nu = \frac{\partial Y^\nu}{\partial x^\mu} + \Gamma^\nu_{\mu\alpha} Y^\alpha, \tag{1.2.9}$$

with

$$\Gamma^\alpha_{\mu\nu} := dx^\alpha \left(\nabla_{\frac{\partial}{\partial x^\mu}} \frac{\partial}{\partial x^\nu} \right) \tag{1.2.10}$$

the Christoffel symbols. This object is not a tensor field due to the fact that it does not transform according to the laws of tensor fields.

As mentioned above, there exist preferred curves γ called geodesics which have the property that their tangent vector is parallel transported along themselves. Mathematically, this geodesic motion is given as follows. Let a curve $\gamma \in \mathcal{M}$ with the corresponding tangent vector $\dot{\gamma} := \dfrac{d\gamma}{dt}$. The covariant derivative of $\dot{\gamma}$ along of the curve γ is required to vanish (for an affine parameter t)

$$\left.(\nabla_{\dot{\gamma}} \dot{\gamma})\right|_{\gamma(\tau)} = 0, \tag{1.2.11}$$

which implies, in terms of local coordinates,

$$\ddot{x}^{\alpha} + \Gamma^{\alpha}_{\mu\nu}\dot{x}^{\mu}\dot{x}^{\nu} = 0. \tag{1.2.12}$$

(1.2.12) is called the geodesic equation.

An important structure on the spacetime manifold is the metric tensor g from which we can define a notion of distance on the manifold $\mathcal{M}$, and which permits to identify timelike, spacelike, and null vectors depending on whether or not $g(X, X)$ is negative, positive or zero, respectively. The metric tensor is a tensor field $g \in \mathcal{T}^0{}_2(\mathcal{M})$ with two important properties:

(i) g is a symmetric tensor, and

(ii) is non-degenerated.

The first point means that $g(X, Y) = g(Y, X)$ for all $X, Y \in \mathcal{X}(\mathcal{M})$, and the second one implies that $g(X, \cdot\,) = 0$ only if $X = 0$. Taking local coordinates x^{μ} the metric tensor can be locally represented as

$$g := g_{\mu\nu} dx^{\mu} \otimes dx^{\nu}, \quad \text{where} \quad g_{\mu\nu} = g_{\nu\mu} = g\left(\frac{\partial}{\partial x^{\mu}}, \frac{\partial}{\partial x^{\nu}}\right). \tag{1.2.13}$$

A preferred affine connection associated with the spacetime manifold $(\mathcal{M}, g)$ is the Levi-Civita connection which is uniquely characterized by the following two properties:

$$\nabla g = 0, \quad \text{and} \quad \nabla \quad \text{is torsion free.} \tag{1.2.14}$$

The Christoffel symbols associated with the Levi-Civita connection are given by the components of the metric tensor (in local coordinates) as follows

$$\Gamma^{\alpha}_{\mu\nu} = \frac{1}{2} g^{\alpha\beta}\left(\frac{\partial g_{\nu\beta}}{\partial x^{\mu}} + \frac{\partial g_{\mu\beta}}{\partial x^{\nu}} - \frac{\partial g_{\mu\nu}}{\partial x^{\beta}}\right). \tag{1.2.15}$$

They are symmetric in the lower indices,

$$\Gamma^{\alpha}_{\mu\nu} = \Gamma^{\alpha}_{\nu\mu}, \tag{1.2.16}$$

which is a consequence of the torsion free property (1.2.14).

For timelike geodesics, equation (1.2.12) can be equivalently written as

$$u^{\mu}\nabla_{\mu}u^{\nu} = 0, \tag{1.2.17}$$

where $u^{\nu} = dx^{\nu}/dt$ is the four-velocity vector field along the geodesic curve and t is proper time. We define a Killing vector field k by the requirement

$$\pounds_k g = 0, \tag{1.2.18}$$

on the spacetime manifold $(\mathcal{M}, g)$; this means that the metric tensor is invariant along the flow generated by this vector field k. In terms of local coordinates this equation is equivalent to

$$\nabla_\mu k_\nu + \nabla_\nu k_\mu = 0, \tag{1.2.19}$$

and is called the Killing equation. One can show that the derivative along u of the product $g(u, k)$ vanishes:

$$\nabla_u g(u,k) = u^\mu \nabla_\mu \left(u^\nu k_\nu\right) = \left(u^\mu \nabla_\mu u^\nu\right) k_\nu + u^\mu u^\nu \nabla_\mu k_\nu = 0. \tag{1.2.20}$$

Here, we have used (1.2.17) and (1.2.19). This last result implies that the product $g(u, k)$ is constant along the geodesic trajectories.

From the concepts of parallel transport and the covariant derivative one defines the curvature of a differentiable manifold which is described by the Riemann curvature tensor. To this purpose, let $\omega \in \mathcal{X}^*(\mathcal{M})$ be a covector field. Applying two covariant derivatives on this object one finds that in general, they do not commute: $\nabla_\mu \nabla_\nu \neq \nabla_\nu \nabla_\mu$. However,

$$(\nabla_\mu \nabla_\nu - \nabla_\nu \nabla_\mu)(f\omega_\alpha) = f(\nabla_\mu \nabla_\nu - \nabla_\nu \nabla_\mu)\omega_\alpha + \underbrace{\left[(\nabla_\mu \nabla_\nu - \nabla_\nu \nabla_\mu) f\right]}_{=0} \omega_\alpha, \tag{1.2.21}$$

for all functions $f \in \mathcal{F}(\mathcal{M})$, which shows that $(\nabla_\mu \nabla_\nu - \nabla_\nu \nabla_\mu)\omega_\alpha$ only depends on the value of ω_α at p. The last term in Eq. (1.2.21) vanishes due to property (1.2.16). Therefore, there exists a tensor field $R \in \mathcal{T}^1{}_3(\mathcal{M})$, called the Riemann curvature tensor, such that

$$\left(\nabla_\mu \nabla_\nu - \nabla_\nu \nabla_\mu\right) \omega_\alpha = R_{\mu\nu\alpha}{}^\beta \omega_\beta. \tag{1.2.22}$$

It is related to the failure of a vector to return to its initial value when it is parallel transported along a closed curve. Figure **1-2** shows an illustration of a vector transported along of closed curve on the two-sphere.

For the Levi-Civita connection ∇, one can express the Riemann curvature tensor in the following form:

$$R^\alpha{}_{\beta\mu\nu} = \frac{\partial \Gamma^\alpha_{\nu\beta}}{\partial x^\mu} - \frac{\partial \Gamma^\alpha_{\mu\beta}}{\partial x^\nu} + \Gamma^\sigma_{\nu\beta}\Gamma^\alpha_{\mu\sigma} - \Gamma^\sigma_{\mu\beta}\Gamma^\alpha_{\nu\sigma}, \tag{1.2.23}$$

where the Christoffel symbols are give in equation (1.2.15). $R_{\alpha\beta\mu\nu}$ has the following key properties:

(i) $R_{\alpha\beta\mu\nu} = -R_{\alpha\beta\nu\mu}$,

(ii) $R_{\alpha\beta\mu\nu} = -R_{\beta\alpha\mu\nu}$,

(iii) $R_{\alpha\beta\mu\nu} = R_{\mu\nu\alpha\beta}$,

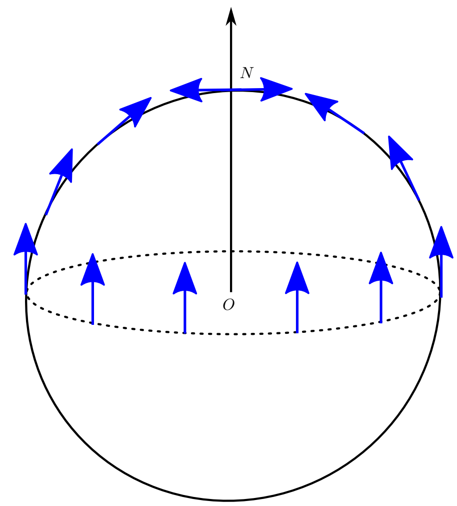

Figure 1-2: Illustration of parallel transport of a vector along a closed curve on a S^2-sphere. When the vector is transported along the equatorial curve the direction is always the same; however when it is transported along the two different meridians the vectors have completely opposite directions in the north pole. This is an effect of the curvature of S^2.

(iv) $\sum_{(\beta\mu\nu)} R_{\alpha\beta\mu\nu} = 0,$

(v) $\sum_{(\mu\nu\sigma)} \nabla_\sigma R_{\alpha\beta\mu\nu} = 0,$

where (iv) and (v) are the first and second Bianchi identities, respectively.

By contracting the first and third indices of the Riemann tensor one obtains a $(0, 2)$ symmetric tensor called the Ricci tensor which is defined by

$$R_{\mu\nu} = R_{\nu\mu} = R^{\alpha}{}_{\mu\alpha\nu}. \tag{1.2.24}$$

Further contracting μ with ν yields the Ricci scalar

$$R = R^{\mu}{}_{\mu}. \tag{1.2.25}$$

Having provided the essential geometric structures of the spacetime manifold we conclude this section with one of the prominent result of general relativity developed by A. Einstein in 1915 which is the Einstein equation. For this, one defines the Einstein tensor $G \in \mathcal{T}^0{}_2(\mathcal{M})$ which is a symmetric tensor given by

$$G_{\mu\nu} = R_{\mu\nu} - \frac{1}{2} R g_{\mu\nu} \tag{1.2.26}$$

in local coordinates. The Einstein tensor is divergence free

$$\nabla G = 0, \tag{1.2.27}$$

as a consequence of the twice-contracted second Bianchi identity.

The last ingredient to complete the formulation of general relativity is the energy-momentum-stress tensor $T \in \mathcal{T}^0{}_2(\mathcal{M})$ which is also symmetric and contains the information about the matter sources. The energy-momentum-stress tensor is also divergence free

$$\nabla T = 0, \tag{1.2.28}$$

as a consequence of the equations of motion for the matter fields, and hence it satisfies the same properties as the Einstein tensor (1.2.26). This allows one to couple the metric to the matter fields through Einstein's equations. In the presence of matter Einstein's equations are given by

$$G = \frac{8\pi G_N}{c^4} T, \tag{1.2.29}$$

in physical units. This system of equations can also be derived from a variation principle with a completely equivalent result [51–53]. Einstein's field equations constitute a system of ten coupled non-linear partial differential equations, and hence they are hard to solve exactly. Only a few exact solutions have been found. The most important ones are the solutions found by Karl Schwarzschild (1916) and Roy Kerr (1963), which describe non-rotating and spinning black holes, respectively. Despite their difficulty to solve for it has been shown that Einstein's equations predict incredible physical phenomena such as the existence of black holes, the expansion of the universe, gravitational waves, light deviation, all of which have been verify experimentally by now.

1.2.2. The geometric structures on the cotangent bundle

In this subsection we provide a brief review of the cotangent bundle $T^*\mathcal{M}$ associated with the spacetime manifold $(\mathcal{M}, g)$ (which is assumed connected and time-oriented) and its geometric structures and properties relevant for relativistic kinetic theory. The cotangent bundle is defined as

$$T^*\mathcal{M} := \{(x,p) : x \in \mathcal{M}, p \in T^*_x\mathcal{M}\}, \tag{1.2.30}$$

where p represent the dual of the momenta. The cotangent bundle has a natural projection map

$$\begin{array}{rccc} \pi: & T^*\mathcal{M} & \to & \mathcal{M}, \\ & (x,p) & \mapsto & x, \end{array} \tag{1.2.31}$$

which projects an element $(x,p) \in T^*\mathcal{M}$ onto $x \in \mathcal{M}$. It provided the fibre over x defined as the inverse image given by

$$\pi^{-1}(x) = (x, T^*_x\mathcal{M}) \simeq T^*_x\mathcal{M}. \tag{1.2.32}$$

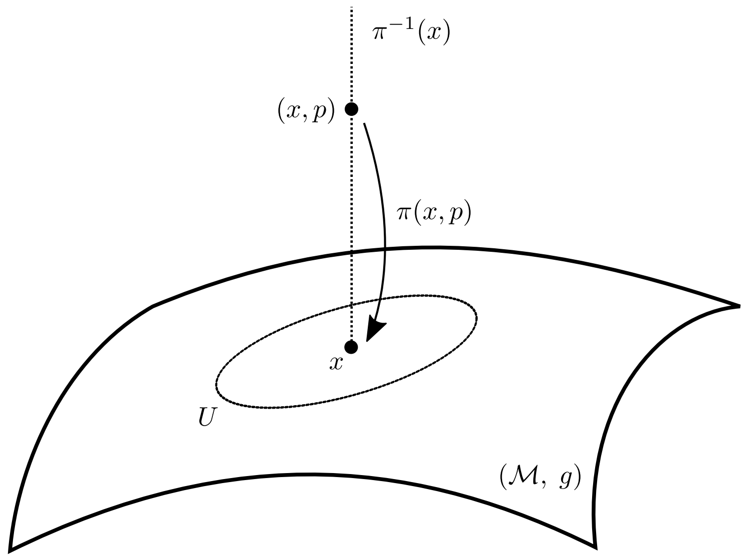

Figure 1-3: Illustration of the action of the projection map π and its inverse image $\pi^{-1}(x)$ on $T^*\mathcal{M}$. The projection map takes a point (x,p) and projects it onto the base point $x \in \mathcal{M}$.

Figure **1-3** shows the projection map π and the fibre $\pi^{-1}(x)$ in the cotangent bundle $T^*\mathcal{M}$. The spacetime metric induces a natural fibre metric on $\pi^{-1}(x)$ defined by

$$h_x((x,p),(x,q)) := g_x^{-1}(p,q), \tag{1.2.33}$$

where $(x,p),(x,q) \in \pi^{-1}(x)$.

For the following, it is usefully to take adapted local coordinates (x^μ, p_μ) on $T^*\mathcal{M}$ where x^μ are coordinates defined in a local chart U of $\mathcal{M}$ and p_μ are the components of p with respect to the basis of covectors $(dx^\mu|_x)$ of $T_x^*\mathcal{M}$ such that

$$p = p_\mu dx^\mu|_x \,. \tag{1.2.34}$$

These coordinates give us a basis of vector fields for all points $(x,p) \in T^*\mathcal{M}$. This basis and its associated dual basis of covector fields are given by

$$\left\{\frac{\partial}{\partial x^\mu}, \frac{\partial}{\partial p_\mu}\right\}\Bigg|_{(x,p)} \qquad \text{and} \qquad \{dx^\mu, dp_\mu\}|_{(x,p)}\,, \tag{1.2.35}$$

respectively.

Now, we introduce two important geometric objects on the cotangent bundle; the Poincaré one-form Θ and the bilinear symplectic form Ω_s, see [58] for further details of these structures. For the first one, let $X \in \mathcal{X}(T^*\mathcal{M})$, then the Poincaré one-form is defined by

$$\Theta_{(x,p)}\left(X_{(x,p)}\right) := p\left(d\pi_{(x,p)}\left(X_{(x,p)}\right)\right), \tag{1.2.36}$$

where $d\pi$ is the differential of the projection map π given by equation (1.2.31). In terms of adapted local coordinates (x^μ, p_μ) the Poincaré one-form is given by

$$\Theta = p_\mu dx^\mu. \tag{1.2.37}$$

For the second one, the symplectic form arises naturally as the exterior differential of the Poincaré one-form on the cotangent bundle as follows:

$$\Omega_s := d\Theta = dp_\mu \wedge dx^\mu, \tag{1.2.38}$$

where this symplectic form is an antisymmetric ($\Omega_s(X,Y) = -\Omega_s(Y,X)$), closed ($d\Omega_s = 0$), and non-degenerate ($\Omega_s(\,\cdot\,,X) = 0$ only if $X = 0$) two-form.

The symplectic form allows one to introduce a Hamiltonian vector field $X_{\mathcal{H}} \in \mathcal{X}(T^*\mathcal{M})$ associated with a given smooth function $\mathcal{H} \in \mathcal{F}(T^*\mathcal{M})$. It is defined as the unique vector field $X_{\mathcal{H}}$ such that

$$d\mathcal{H} := \Omega_s(\,\cdot\,, X_{\mathcal{H}}) = -i_{X_{\mathcal{H}}}\Omega_s, \tag{1.2.39}$$

where the operator i is the interior derivative. This Hamiltonian vector field in terms of adapted local coordinates is given by

$$X_{\mathcal{H}} = \frac{\partial \mathcal{H}}{\partial p_\mu}\frac{\partial}{\partial x^\mu} - \frac{\partial \mathcal{H}}{\partial x^\mu}\frac{\partial}{\partial p_\mu}, \tag{1.2.40}$$

and it plays an important role, in which the integral curves of (1.2.40) are determined by Hamilton's equations of motion

$$\frac{dx^\mu}{d\lambda} = \frac{\partial \mathcal{H}}{\partial p_\mu}, \quad \frac{dp_\mu}{d\lambda} = -\frac{\partial \mathcal{H}}{\partial x^\mu}, \tag{1.2.41}$$

where λ is a parameter along the curve. For the relativistic kinetic theory there exists an important Hamiltonian function which is called the free one-particle Hamiltonian, given by

$$\mathcal{H}(x,p) := \frac{1}{2}g^{-1}(p,p) = \frac{1}{2}g^{\mu\nu}(x)p_\mu p_\nu. \tag{1.2.42}$$

The associated Hamiltonian vector field $X_{\mathcal{H}}$ in equation (1.2.40) is called the Liouville vector field L, and it is given by

$$L := g^{\mu\nu}p_\nu\frac{\partial}{\partial x^\mu} - \frac{1}{2}\frac{\partial g^{\alpha\beta}}{\partial x^\mu}p_\alpha p_\beta\frac{\partial}{\partial p_\mu}. \tag{1.2.43}$$

The integral curves of the Liouville vector field L, when projected onto the spacetime manifold, are geodesics.

The symplectic form remains invariant with respect to the Hamiltonian flow $X_{\mathcal{F}}$ generated by any function $\mathcal{F} \in \mathcal{F}(\mathcal{M})$. This is a consequence of Cartan's formula and the fact that Ω_s is closed:

$$\pounds_{X_{\mathcal{F}}} \Omega_s = (d i_{X_{\mathcal{F}}} + i_{X_{\mathcal{F}}} d)\, \Omega_s = -d^2 \mathcal{F} = 0, \tag{1.2.44}$$

where $\pounds$ is the Lie derivative. Hence, the Hamiltonian vector field $X_{\mathcal{F}}$ generates canonical transformations.

For any $m > 0$, an important differential submanifold of $T^*\mathcal{M}$ is the mass shell Γ_m defined by

$$\Gamma_m := \left\{ (x,p) \in T^*\mathcal{M} : g^{-1}(p,p) = -m^2 \right\}, \tag{1.2.45}$$

which is seven-dimensional. The mass shell Γ_m (with $m > 0$) consists of two connected components. These components refer to the possible direction of the covectors p, the first one future-directed $(+)$ and the second one past-directed $(-)$. We denote these components according to these signs $\pm$,

$$\Gamma_m = \Gamma_m^+ \dot{\cup} \Gamma_m^-, \tag{1.2.46}$$

where the future mass shell Γ_m^+ is defined by

$$\Gamma_m^+ := \left\{ (x,p) \in T^*\mathcal{M} : g^{-1}(p,p) = -m^2,\ \ p \text{ is future directed} \right\}. \tag{1.2.47}$$

It is a fibre bundle over $\mathcal{M}$ whose fibres at each $x \in \mathcal{M}$ consist of the future mass hyperboloids defined as

$$P_x^+(m) := \left\{ p \in T_x^*\mathcal{M} : g^{-1}(p,p) = -m^2,\ \ p \text{ is future directed} \right\}. \tag{1.2.48}$$

At this point we mention an important result for the Liouville vector field L. It is tangent to the future mass shell Γ_m^+ at each point $(x,p) \in \Gamma_m$. This is a direct consequence of the fact that the Hamiltonian vector field $X_{\mathcal{H}}$ leaves the Hamiltonian function $\mathcal{H}$ invariant.

As we will see in subsection 3.4, the collisionless Boltzmann equation reads

$$L[f] = 0, \tag{1.2.49}$$

for a smooth function $f \in \mathcal{F}(\Gamma_m^+)$ on the future mass shell and L the Liouville vector field. The collisionless Boltzmann equation[1] is a key concept for the description of a collisionless kinetic gas as we will see later in this thesis work.

[1] This equation is also called the Liouville or Vlasov equation.

To conclude this subsection we introduce the invariant volume form $\eta_{T^*\mathcal{M}}$ on $T^*\mathcal{M}$. Explicitly, this volume form is given by

$$\begin{aligned}\eta_{T^*\mathcal{M}} &= -\frac{1}{24}\Omega_s \wedge \Omega_s \wedge \Omega_s \wedge \Omega_s \\ &= -dp_0 \wedge dp_1 \wedge dp_2 \wedge dp_3 \wedge dx^0 \wedge dx^1 \wedge dx^2 \wedge dx^3, \qquad (1.2.50)\end{aligned}$$

for the spacetime manifold. It is invariant with respect to the flow generated by the Liouville vector field L,

$$\pounds_L \eta_{T^*\mathcal{M}} = 0, \qquad (1.2.51)$$

as a consequence of (c.f. (1.2.44))

$$\pounds_L \Omega_s = 0. \qquad (1.2.52)$$

Hence, this flow is volume-preserving. This is the content of Liouville's theorem on $T^*\mathcal{M}$.

The eight-form $\eta_{T^*\mathcal{M}}$ induces a volume form $\eta_{\Gamma_m^+}$ on the future mass shell given by

$$\eta_{\Gamma_m^+} = \sqrt{-\det(g_{\mu\nu})}dx^0 \wedge dx^1 \wedge dx^2 \wedge dx^3 \wedge \frac{m}{|p_{\hat{0}}|}dp_{\hat{1}} \wedge dp_{\hat{2}} \wedge dp_{\hat{3}} \qquad (1.2.53)$$

in terms of an orthonormal basis of covector fields $\left\{\theta^{\hat{\alpha}}\right\}$ on $\mathcal{M}$. The volume form $\eta_{P_x^+(m)}$ on the future mass hyperboloid $P_x^+(m)$ is

$$\eta_{P_x^+(m)} = m\mathrm{dvol}_x(p), \qquad (1.2.54)$$

where

$$\mathrm{dvol}_x(p) := -\frac{dp_{\hat{1}} \wedge dp_{\hat{2}} \wedge dp_{\hat{3}}}{p_{\hat{0}}} = \frac{dp_{\hat{1}} \wedge dp_{\hat{2}} \wedge dp_{\hat{3}}}{\sqrt{m^2 + p_{\hat{1}}^2 + p_{\hat{2}}^2 + p_{\hat{3}}^2}} \qquad (1.2.55)$$

is the Lorentz-invariant volume element. In general (1.2.53) can be written as

$$\eta_{\Gamma_m^+} = \eta_{\mathcal{M}} \wedge \eta_{P_x^+(m)}, \qquad (1.2.56)$$

where $\eta_{\mathcal{M}}$ and $\eta_{P_x^+(m)}$ are the volume forms on $\mathcal{M}$ and $P_x^+(m)$ respectively. This provides the Fubini-type integration formula

$$\int_{\Gamma_m^+} f(x,p)\eta_{\Gamma_m^+} = m\int_{\mathcal{M}} \left(\int_{P_x^+(m)} f(x,p)\mathrm{dvol}_x(p) \right) \eta_{\mathcal{M}}, \qquad (1.2.57)$$

for any Lebesgue-integrable function f on the future mass shell Γ_m^+. Let $m > 0$, the volume form $\eta_{\Gamma_m^+}$ is invariant with respect to the flow generated by the Liouville vector field L on the future mass shell Γ_m^+, that is,

$$\pounds_L \eta_{\Gamma_m^+} = 0. \qquad (1.2.58)$$

1.2.3. Properties of the exterior Schwarzschild spacetime

A stationary solution of the Einstein vacuum equations representing a regular asymptotically flat black hole is described by the Kerr family of black holes (modulo technical assumptions, see the uniqueness theorems [59, 60]). If we neglect the rotation parameter of the Kerr black hole the exterior region is described by the Schwarzschild metric. According to Birkhoff's theorem the Schwarzschild spacetime is also the most general spherically-symmetric solution of the Einstein vacuum equations. In standard Schwarzschild coordinates $(t, r, \vartheta, \varphi)$ the metric is given by

$$g = -N(r)dt^2 + \frac{dr^2}{N(r)} + r^2\left(d\vartheta^2 + \sin^2\vartheta d\varphi^2\right), \quad N(r) := 1 - \frac{2M}{r}, \tag{1.2.59}$$

where N is a smooth function of the areal radius r and M is the mass of the black hole. This function N is positive for all $r > 2M$ and vanishes for $r = 2M$. The region $0 < r < 2M$ describes the interior of the black hole. Hence the spheres $r = 2M$ generate the event horizon of the black hole, and they are not physical singularities but coordinate ones. In contrast, the point $r = 0$ is a genuine singularity as can be understood from the Kretschmann curvature scalar

$$I := R^{\alpha\beta\mu\nu}R_{\alpha\beta\mu\nu} = \frac{48M^2}{r^6}, \tag{1.2.60}$$

which blows up as $r \to 0$. The result in this thesis work describe configurations of a kinetic gas (in a relativistic and non-relativistic regimes) surrounding a black hole, in which the strong gravitational field is dominant and is well described by the exterior Schwarzschild spacetime.

In the following we derive the principal properties of the radial effective potential and conserved quantities associated with the geodesic motion on the exterior Schwarzschild spacetime. The Schwarzschild effective potential is a function depending on the radius r, mass m, energy E, and total angular momentum L of the particle. As we will see later, the dependency on the conserved quantities (m, E, L) plays an important role in the behavior of the particles' trajectories in the kinetic gas. To this purpose, we analyze the behavior of the potential in terms of the parameter space with the goal of characterizing the trajectories of the kinetic gas according to whether they are trapped or not by the potential.

Let us start with the discussion of the conserved quantities in the Schwarzschild spacetime (1.2.59). To this purpose, we adopt the adapted local coordinates $(t, r, \vartheta, \varphi, p_t, p_r, p_\vartheta, p_\varphi)$ on $T^*\mathcal{M}$. In these coordinates the free one-particle Hamiltonian (1.2.42) of the system yields

$$\mathcal{H}(x, p) = \frac{1}{2}\left(-\frac{p_t^2}{N(r)} + N(r)p_r^2 + \frac{p_\vartheta^2}{r^2} + \frac{p_\varphi^2}{r^2\sin^2\vartheta}\right). \tag{1.2.61}$$

The Hamiltonian system described by (1.2.61) possesses five conserved quantities. Two conserved quantities related to the Killing vectors $k = \partial/\partial t$ and $\ell = \partial/\partial\varphi$ are the energy E and the azimuthal angular momentum L_z, see Eq. (1.2.20). As is visible from the Hamiltonian (1.2.61) it is explicitly independent of the coordinates (t, φ) and from the equations of motion (1.2.41)

$$\dot{x}^\mu = \frac{\partial \mathcal{H}}{\partial p_\mu}, \quad \dot{p}_\mu = -\frac{\partial \mathcal{H}}{\partial x^\mu}, \tag{1.2.62}$$

this immediately gives two conserved quantities (p_t, p_φ). Also, the rest-mass of the particles m and the angular momentum vector $\underline{L}$ are conserved. The conservation of m and L are given by the condition $2\mathcal{H} = g^{-1}(p,p) = -m^2$ and the spherical symmetry of the Schwarzschild spacetime. In summary, the relevant conserved quantities of the system, denoted by F_i, are given by

$$F_1 \;:\; m = \sqrt{-2\mathcal{H}}, \tag{1.2.63}$$

$$F_2 \;:\; E = -p_t, \tag{1.2.64}$$

$$F_3 \;:\; L_z = p_\varphi, \tag{1.2.65}$$

$$F_4 \;:\; L^2 = p_\vartheta^2 + \frac{L_z^2}{\sin^2\vartheta}. \tag{1.2.66}$$

It can be verify that F_i Poisson commute with each other, that is $\{F_i, F_j\} = 0$ for all $i \neq j$. Combining (1.2.63-1.2.66) with (1.2.61) one obtains an equation which describes the behavior of the radial motion in terms of the conserved quantities, such that

$$N(r)^2 p_r^2 = E^2 - N(r)\left(m^2 + \frac{L^2}{r^2}\right) = E^2 - V_{m,L}(r). \tag{1.2.67}$$

Here we have defined the radial effective potential of the Schwarzschild spacetime:

$$V_{m,L}(r) := N(r)\left(m^2 + \frac{L^2}{r^2}\right). \tag{1.2.68}$$

Next, we provide a discussion regarding the principal properties of the radial effective potential of the Schwarzschild spacetime (1.2.68) where we refer to [52, 53, 56] for more details. The qualitative behavior of the timelike geodesics of the particles in the effective potential $V_{m,L}$ depends on the angular momentum (for a given energy), see [36,61]. Figure **1-4** shows the behavior of the potential for some values of the angular momentum in a logarithmic scale. This effective potential $V_{m,L}$ possesses interesting properties; the most relevant ones for this thesis work are:

(i) For $L < \sqrt{12}Mm$ the potential does not have any critical points.

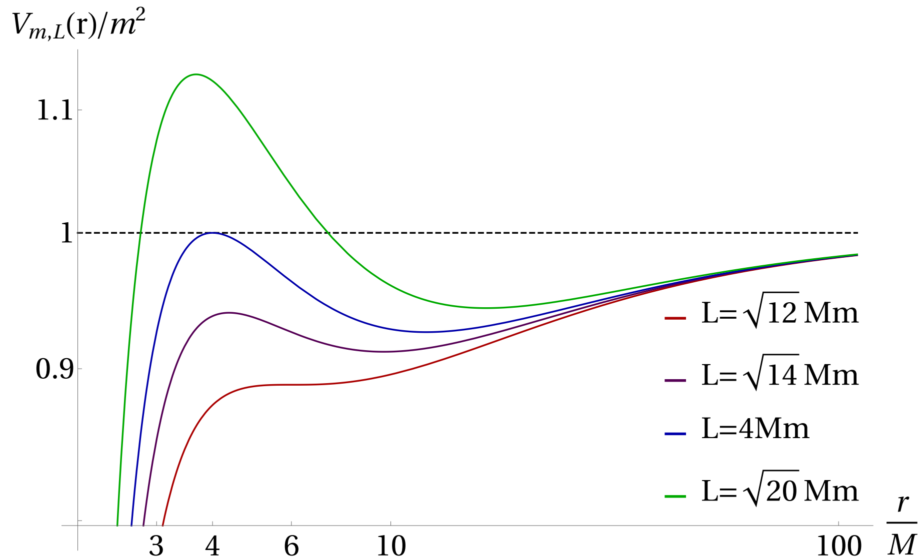

Figure 1-4: Behavior of the effective potential $V_{m,L}$ for $L = \sqrt{12}Mm, \sqrt{14}Mm, 4Mm, \sqrt{20}Mm$. In a kinetic gas, particles are interacting with this potential and their trajectories depend on it. As is visible in the figure, when the angular momentum increases only a fraction of all these particles are sufficiently energetic (larger than the maximum of the potential) such that they can reach the even horizon, while the remaining particles are scattered at the potential barrier.

(ii) In the limit $L = \sqrt{12}Mm$ the potential has an inflection point, at $r = 6M$.

(iii) If $L > \sqrt{12}Mm$ the potential have two critical points, located at

$$r_{\text{max}} = \frac{6M}{1 + \sqrt{1 - 12M^2m^2/L^2}}, \quad r_{\text{min}} = \frac{6M}{1 - \sqrt{1 - 12M^2m^2/L^2}}, \tag{1.2.69}$$

which represent the maximum and minimum of the effective potential given by

$$V_{m,L}(r_{\text{max}}) = \frac{8}{9}m^2 + \frac{L^2 - 12M^2m^2}{9Mr_{\text{max}}}, \tag{1.2.70}$$

$$V_{m,L}(r_{\text{min}}) = \frac{8}{9}m^2 + \frac{L^2 - 12M^2m^2}{9Mr_{\text{min}}}, \tag{1.2.71}$$

respectively.

Using these properties one can classify the trajectories of the massive particles in this effective potential as absorbed, scattered, and bound orbits. The absorbed trajectories are the incoming particles from infinity, which fall into the black hole. The scattered trajectories are the incoming particles that bounce at the barrier of the potential and become outgoing, returning to the asymptotic region. Finally, the bound trajectories are the particles which are trapped in the potential well. For an illustration, figure **1-5** shows the phase diagram in the (r, p_r)-plane for some different values of the energy and fixed angular momentum $L = \sqrt{14}Mm$.

To conclude this subsection we summarize the results that determine the three regions: absorbed, scattered, and bound in terms of the parameter space (E, L) [36, 61]. We leave the details to chapters 5 and 6. For a given energy level E, the range of angular momentum L and its corresponding characterization of the trajectories are

$$\sqrt{\frac{8}{9}}m < E < m : \begin{cases} L < L_{\text{c}}(E) & : \text{ absorbed,} \\ L_{\text{c}}(E) < L < L_{\text{ub}}(E) & : \text{ bound,} \end{cases}$$

and

$$E > m : \begin{cases} L < L_{\text{c}}(E) & : \text{ absorbed,} \\ L > L_{\text{c}}(E) & : \text{ scattered,} \end{cases}$$

where $L_{\text{c}}(E)$ ($L_{\text{ub}}(E)$) refers to the critical angular momentum corresponding to the case in which the effective potential's maximum (minimum) is equal to E^2. See chapter 5 and Ref. [36] for their explicit form. A graphical illustration of these three regions is shown in figure **1-6** for two different values of the angular momentum.

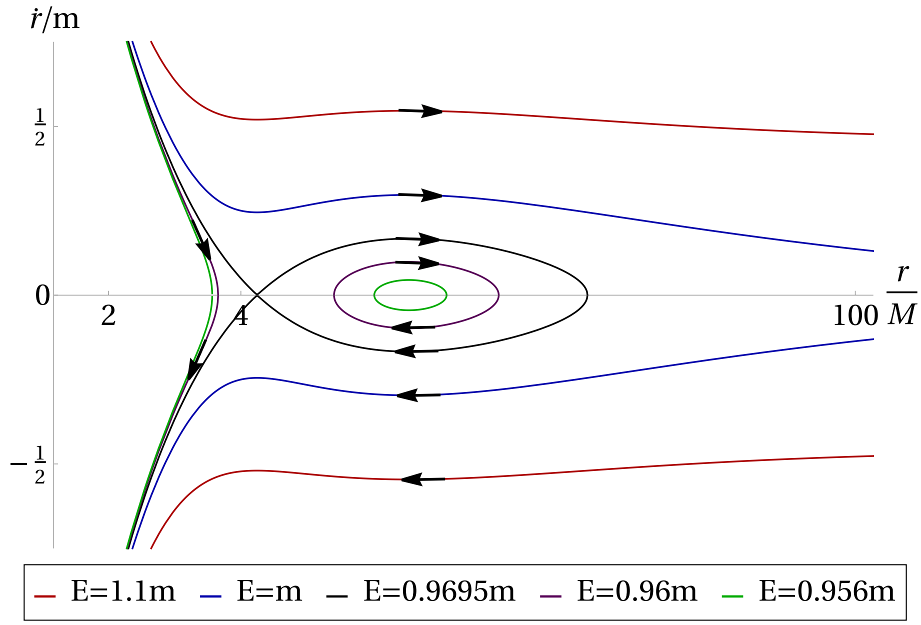

Figure 1-5: Phase diagram in the (r, p_r)-plane for some values of the energy of the particles. The red lines describe incoming particles from infinity which are absorbed by the black hole, the blue curve is the separatrix for the corresponding energy $E = m$. The black lines describe bound particles. The purple and green curves describe bound particles moving between the turning points, whereas the corresponding curves in the region $r < 4M$ are outgoing particles emitted from the white hole which bounce at the potential barrier and are finally absorbed by the black hole.

1.3. Summary of main results of this thesis

Part of the content included in chapters 1, 2, 3 is based on our review introduction to the relativistic kinetic theory of a dilute gas propagating on a curved spacetime manifold in arbitrary dimensions [12].[2] In chapter 2 we derive the main properties of the relativistic kinetic theory based on a modern geometric language. We start with the description of the one-particle DF and provide its physical meaning. Here, the Liouville equation is derived and we conclude this chapter with the construction of the spacetime observables from the one-particle DF. In chapter 3 we review the principal concepts of the Boltzmann equation and provide its integro-differential form. The H-theorem is established and the conditions for the existence of global and local equilibrium gas configurations are given. We also analyze the collisionless Boltzmann equation as one of the principal systems used in this thesis work.

[2] In [12] we also discuss an interesting application of this formalism for an expansion of a homogeneous and isotropic universe filled with a collisional simple gas, and we also analyze its corresponding behavior in the early and late epochs.

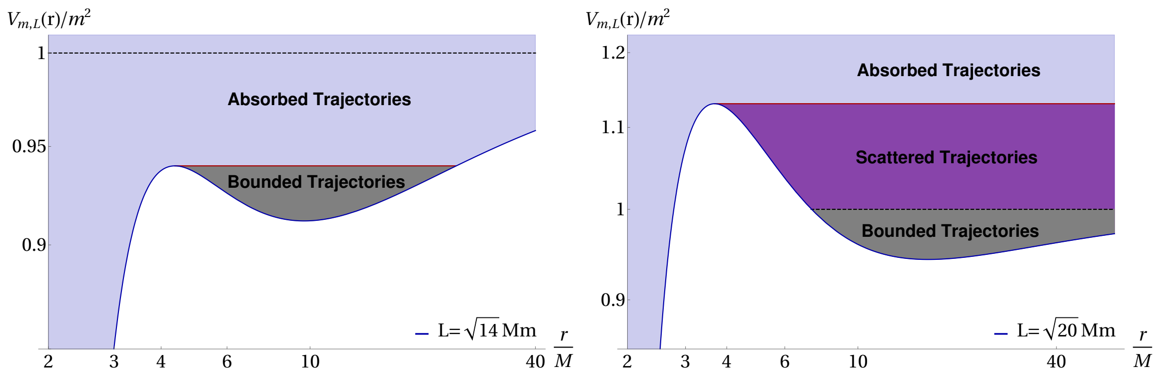

Figure 1-6: Effective potential (blue line) for $L = \sqrt{14}Mm$ (left panel) and $L = \sqrt{20}Mm$ (right panel). In the left panel the particle trajectories with energies higher than the maximum of the potential $V_{m,L}(r_{\text{max}})$ are absorbed by the black hole (light blue region); however the region between the maximum $V_{m,L}(r_{\text{max}})$ and minimum $V_{m,L}(r_{\text{min}})$ of the potential correspond to the particle trajectories that are bounded (gray region). In the example shown in the right panel the behavior of the absorbed particles is the same; however, there also exists a region in which a fraction of the incoming particles is scattered by the barrier of the potential (purple region). This region exists for trajectories of the particles whose energy lies between the maximum of the potential $V_{m,L}(r_{\text{max}})$ and the asymptotic limit $E = m$. Finally, the region corresponding to particles whose energy lies between the asymptotic limit $E = m$ and the minimum of the potential $V_{m,L}(r_{\text{min}})$ describes bound orbits.

Further results of this thesis are described in chapters 4, 5, and 6. First, in chapter 4 we discuss the properties of an axisymmetric, stationary gas cloud surrounding a massive central object. Here, we assume that the gravitational field is dominated by the central object and is modeled by a nonrelativistic rotationally-symmetric potential. We also assume a collisionless kinetic gas of identical massive particles following bound orbits. Several models for the one-particle DF are considered. We describe the behavior of the relevant macroscopical observables: particle and energy densities, pressure tensor, and the kinetic temperature and provide analytical solutions. Their properties are discussed and we specify configurations with finite total mass, energy and (zero or non-zero) angular momentum. Finally, our configurations are compared to their hydrodynamic analogs. This result serves (for example) as a first approach to describe bound configurations in a non-relativistic regime.

Next, in chapter 5 we generalize the results of chapter 4 to the general relativistic regime. Here, the properties of a stationary gas cloud surrounding a black hole are established. The assumption of a collisionless kinetic gas for identical massive particles following spatially bound geodesic orbits in the Schwarzschild spacetime is made. Several models for the one-particle DF are considered, and the essential formulae that describe the relevant macroscopic observables, like the current density four-vector and the stress-energy-momentum tensor, are derived. As in chapter 4, we provide configurations with finite total mass and angular momentum. To conclude, we analyze the differences between these configurations and their non-relativistic counterparts in a Newtonian potential. Furthermore, our configurations are compared to their hydrodynamic analogues, the "polish doughnuts". A related model, in which the DF is a product of a function of the energy and a function of the orbital inclination associated with the particle's trajectory is presented in [48].

Finally, the accretion problem of a spherically symmetric, collisionless kinetic gas cloud onto a Schwarzschild black hole is analyzed in chapter 6. The relevant idea here is to specify boundary conditions for the kinetic gas at a sphere of finite radius. The corresponding steady-state solutions are computed using different ansätze. The resulting mass accretion rates are analyzed and compared with previous models, including the standard Bondi model for a hydrodynamic flow. We also apply our models to the supermassive black holes Sgr A* and M87*. We discuss how their low luminosity could be partially explained by a kinetic description involving angular momentum. Furthermore, we get results consistent with previous model-dependent bounds for the accretion rate imposed by rotation measures of the polarized light coming from Sgr A* and with estimations of the accretion rate of M87* from the Event Horizon Telescope collaboration. Our methods and results could serve as a first approximation for more realistic black hole accretion models in various astrophysical scenarios in which the accreted material is expected to be nearly collisionless.

2 Relativistic kinetic theory

In this chapter we derive some details on the relativistic kinetic theory of dilute gases and its main properties which are relevant for this thesis. We start in section 2.1 with the description of the one-particle DF and its physical meaning through a flux integral on the relativistic phase space. Next, in section 2.2 we derive the Liouville equation which describes the dynamics of the system in absence of collisions. Finally, in section 2.3 we construct the most relevant (for this work) spacetime observables from the one-particle DF which contains information about the macroscopic observables.

2.1. The one-particle distribution function

The fact that the state of the gas can be described by a one-particle DF f is one of the key concepts in kinetic theory. In this work we focus our attention to a gas consisting of relativistic, massive, identical, electrically neutral, classical (not quantum), non-spinning, and free-falling test particles propagating in a curved spacetime manifold $(\mathcal{M}, g)$. More general descriptions of a gas involving different particles species, quantum or electrically charged particles are discussed for example in [4, 7, 10, 12] and references therein.

The one-particle DF is a smooth non-negative function $f \geq 0$ on the future mass shell Γ_m^+ describing gas configurations of massive particles $m > 0$ at the macroscopic level. In the next sections we discuss the covariant interpretation of the one-particle DF f, its physical meaning through a flux integral, and we provide a bridge with the usual Newtonian-type interpretation. Also, the spacetime observables are constructed by defining appropriate fibre integrals over f, and their most important properties are discussed in section 2.3.

We start with the definition of an interesting structure on the cotangent bundle, namely the Sasaki metric which was introduced in the context of the tangent bundle associated with a Riemannian manifold by Shigeo Sasaki in 1958, see [62, 63] and [12] for further details. The spacetime metric g with its associated Levi-Civita connection ∇ naturally induce a metric on $T^*\mathcal{M}$, called the Sasaki metric $\hat{g}$. For a coordinate-independent definition see [12]. In terms of adapted local coordinates (x^μ, p_μ) on $T^*\mathcal{M}$ the Sasaki metric is defined as

$$\hat{g} := g_{\mu\nu} dx^\mu \otimes dx^\nu + g^{\mu\nu} Dp_\mu \otimes Dp_\nu, \tag{2.1.1}$$

where Dp_μ is given by

$$Dp_\mu = dp_\mu - \Gamma^\alpha{}_{\beta\mu} p_\alpha dx^\beta. \tag{2.1.2}$$

One can demonstrate that the Liouville vector field L generates geodesics on the manifold $\left(T^*\mathcal{M}, \hat{g}, \hat{\nabla}\right)$, where $\hat{\nabla}$ is the Levi-Civita connection associated with the Sasaki metric $\hat{g}$. This statement implies that

$$\hat{\nabla}_L L = 0. \tag{2.1.3}$$

On the other hand, the induced metric $\hat{h}$ on the future mass shell Γ_m^+ and its associated Levi-Civita connection $\hat{D}$ for any $m > 0$ provide a Lorentzian manifold $\left(\Gamma_m^+, \hat{h}, \hat{D}\right)$ of signature $(-,+,+,+,+,+,+)$. This induced metric $\hat{h}$ is defined by

$$\hat{h}(X,Y) = \hat{g}(X,Y), \tag{2.1.4}$$

for all $X, Y \in \mathcal{X}(T^*\mathcal{M})$ tangent to Γ_m^+. Recalling that L is tangent to Γ_m^+ one can show that

$$\hat{D}_L L = 0, \tag{2.1.5}$$

hence L also generates geodesics on $(\Gamma_m^+, \hat{h}, \hat{D})$. Furthermore, the induced connection $\hat{D}$ on Γ_m^+ coincides with the induced connection $\hat{\nabla}$ on $T^*\mathcal{M}$, such that

$$\hat{h}\left(\hat{D}_X Y, Z\right) = \hat{g}\left(\hat{\nabla}_X Y, Z\right), \tag{2.1.6}$$

for all $X, Y, Z \in \mathcal{X}(T^*\mathcal{M})$ tangent to Γ_m^+.

The expressions above are relevant for the physical meaning of the one-particle DF through a flux integral interpretation. For this, we introduce a seven-velocity vector field $\mathcal{U}$ on the future mass shell Γ_m^+, defined as

$$\mathcal{U} := \frac{1}{m} L. \tag{2.1.7}$$

In view of the condition $\hat{h}(L,L) = -m^2$ the seven-velocity vector field $\mathcal{U}$ is a unit timelike vector field on $\left(\Gamma_m^+, \hat{h}, \hat{D}\right)$. Furthermore, the divergence of $\mathcal{U}$ is zero due to Liouville's theorem. We now introduce the one-particle DF f with its associated current density vector field $\mathcal{J}$ as follows:

$$\mathcal{J} := f\mathcal{U} = \frac{1}{m} f L. \tag{2.1.8}$$

This relation between the current density $\mathcal{J}$, the one-particle DF f, and the seven-velocity vector field $\mathcal{U}$ can be interpreted analogously to a fluid flow on the spacetime

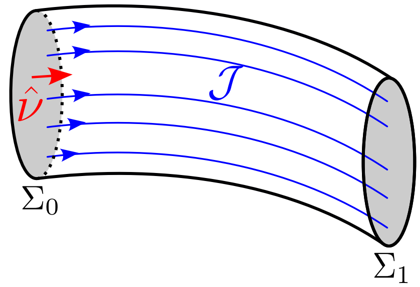

Figure 2-1: Illustration of the current density vector field $\mathcal{J}$ through the surface Σ_0 with normal vector $\hat{\nu}$. The surface Σ_1 is obtained by transporting Σ_0 along the flow of $\mathcal{J}$.

manifold $(\mathcal{M}, g)$. For this, let n denote the number of particles per unit volume (called the particle density) measured by a comoving observer. Let $S \in \mathcal{M}$ be a three-dimensional spacelike hypersurface, representing a volume at some given time, with future-directed unit normal $\hat{s}$. The total number of particles contained in S is given by

$$N[S] = -\int\limits_S g(J, \hat{s})\eta_S, \quad J := nu, \tag{2.1.9}$$

where η_S is the induced volume element on S. Here, the minus sign arises from the requirement that N should be positive if $n > 0$ and $\hat{s}$ and u are future-directed timelike. The total number of particles $N[S]$ in equation (2.1.9) is interpreted as the flux of the particle current density $J = nu$ through the surface S. The continuity equation

$$\nabla \cdot J = 0, \tag{2.1.10}$$

implies that, for a Cauchy surface S in a globally hyperbolic spacetime, the total particle number $N[S]$ is independent of S, i.e. it is conserved.

Motivated by this fluid analogy, we define the averaged number of occupied trajectories $\mathcal{N}[\Sigma]$ crossing a six-dimensional surface Σ in Γ_m^+ with unit normal vector field $\hat{\nu}$ by

$$\mathcal{N}[\Sigma] := -\int\limits_\Sigma \hat{h}(\mathcal{J}, \hat{\nu})\eta_\Sigma, \tag{2.1.11}$$

where η_Σ is the induced volume form on Σ and $\hat{h}$ the induced metric on the future mass shell Γ_m^+. The physical interpretation of the DF f is provided by the analogy between the flux integrals (2.1.9) for the fluid description and (2.1.11) for the kinetic description. Figure **2-1** shows an illustration of the current density $\mathcal{J}$ and its flow crossing the surface Σ_0 with normal vector $\hat{\nu}$.

In order to compare our definition (2.1.11) with the usual non-relativistic definition of the DF we introduce a spacelike hypersurface $S \in (\mathcal{M}, g)$ with future-directed normal

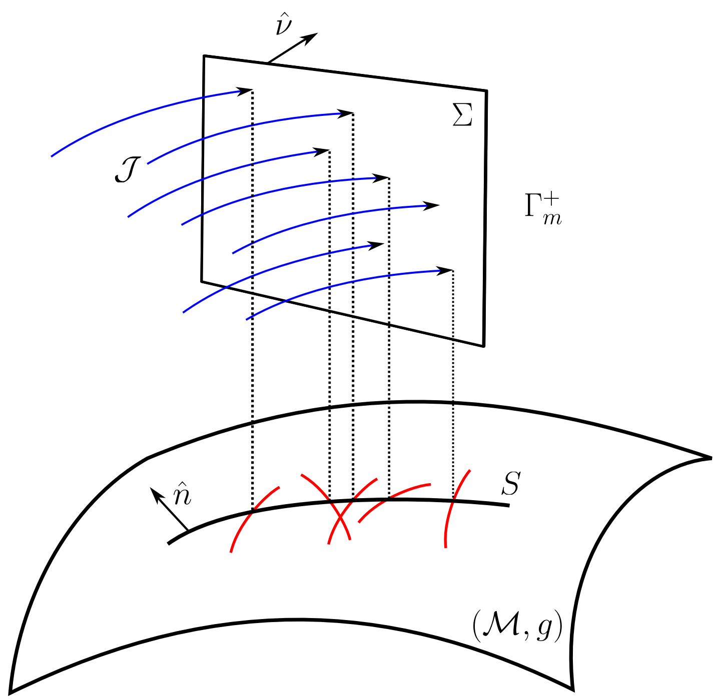

Figure 2-2: Illustration of the averaged number of occupied trajectories in the future mass shell and the averaged number of particles contained in the volume S in the spacetime $(\mathcal{M}, g)$. The current density flux $\mathcal{J}$ (blue arrows) crosses the surface Σ with associated normal vector $\hat{\nu}$ on Γ_m^+. These intersections are projected onto the spacetime $(\mathcal{M}, g)$ which are represented by red curves crossing the volume S with associated normal vector $\hat{n}$.

vector $\hat{s}$ and set

$$\Sigma := \left\{ (x, p) \ : \ x \in S, p \in P_x^+(m) \right\}, \tag{2.1.12}$$

which defines a six-dimensional surface in the future mass shell Γ_m^+. The induced metric in (2.1.4) satisfies

$$\hat{h}(\mathcal{J}, \hat{\nu}) = \frac{1}{m} f \hat{g}(L, \hat{\nu}) = \frac{1}{m} f p(\hat{s}). \tag{2.1.13}$$

Here, the last representation is due to the fact that the Liouville vector field L is horizontal. Hence, the resulting averaged number of occupied trajectories (2.1.11) is

$$\mathcal{N}[\Sigma] = - \int\limits_S \left(\int\limits_{P_x^+(m)} f(x, p) p_{\hat{\alpha}} \hat{s}^{\hat{\alpha}} \mathrm{dvol}_x(p) \right) \eta_S = N[S], \tag{2.1.14}$$

where we have used the results (1.2.55, 1.2.56, 1.2.57). The averaged number of occupied trajectories in the future mass shell represents the averaged number of particles contained in the volume S in the spacetime. For a representation of this averaged numbers see figure **2-2**.

Finally, assuming an orientation of the orthonormal basis $\{e_{\hat{\alpha}}\}$ such that $e_{\hat{0}} = \hat{s}$, one obtains $p_{\hat{0}} = p_{\hat{\alpha}} s^{\hat{\alpha}}$, and also assuming that the surface S is characterized by $x^0 = const$, the number of occupied trajectories (2.1.14) simplifies to

$$\mathcal{N}[\Sigma] = \int\limits_{\mathbb{R}^6} f(x,p) d^3x d^3p. \tag{2.1.15}$$

Here, x is the manifold point associated with the local coordinates x^μ, $p = p_\mu dx^\mu$ is the momentum covector on the future mass shell Γ_m^+ with spatial coordinates p_i, and the volume element in these coordinates is given by $d^3xd^3p = dx^1dx^2dx^3dp_1dp_2dp_3$. This provides the relation with the usual Newtonian interpretation of the DF.

2.2. Derivation of the Liouville equation

In this section we derive the Liouville equation which describes the dynamics of the system in absence of collisions. For this, let Σ_0 be a six-dimensional surface transversal to $\mathcal{J}$ with associated normal vector $\hat{\nu}$. As we saw in the previous section, the averaged number of occupied trajectories crossing Σ_0 is given by equation (2.1.11):

$$\mathcal{N}[\Sigma_0] = -\int\limits_{\Sigma_0} \mathcal{J}^\mu \hat{\nu}_\mu \eta_{\Sigma_0}. \tag{2.2.1}$$

Here we recall that the current density $\mathcal{J}$ is proportional to the seven velocity $\mathcal{U}$. Now, if we let Σ_0 flow along $\mathcal{U}$ to the surface Σ_1, as shown in figure **2-1**, one obtains

$$\mathcal{N}[\Sigma_1] - \mathcal{N}[\Sigma_0] \underbrace{=}_{\text{Gauss' theorem}} \int\limits_{\Omega} \nabla_\mu \mathcal{J}^\mu \eta_{\Gamma_m^+}, \tag{2.2.2}$$

where Ω is the enclosed volume between Σ_0 and Σ_1, and in the last step we have used Gauss' theorem. Both sides of this equation (2.2.2) vanish if

$$\mathcal{N}[\Sigma_1] = \mathcal{N}[\Sigma_0], \tag{2.2.3}$$

which implies that the continuity equation holds $\nabla_\mu \mathcal{J}^\mu = 0$. For a collisionless gas the number of occupied trajectories crossing a surface Σ_0 is the same as Σ_1, that is the number of occupied trajectories is conserved along the current density flow $\mathcal{J}$. Furthermore, by Eq. (2.1.8) one notes that

$$0 = \nabla_\mu \mathcal{J}^\mu = \nabla_\mu (f\mathcal{U}^\mu) = \mathcal{U}^\mu \nabla_\mu f + f \underbrace{\nabla_\mu \mathcal{U}^\mu}_{=0} = \mathcal{U}[f] = \frac{1}{m} L[f]. \tag{2.2.4}$$

Hence, for a collisionless kinetic gas, the DF f must be satisfy the Liouville equation, which implies that the DF is constant along each flow line of the Liouville vector field L.

2.3. The spacetime observables

From the one-particle DF f of a simple gas one can construct physical observables which are the most important C^{∞}-smooth tensor fields on the spacetime manifold $(\mathcal{M}, g)$. They are obtained by suitable fibre integrals over the momenta. These tensor fields are[1]: the particle current density vector field $J \in \mathcal{X}(\mathcal{M})$, the energy-momentum-stress tensor field $T \in \mathcal{T}^2{}_0(\mathcal{M})$, and the the entropy flux vector field $S \in \mathcal{X}(\mathcal{M})$.

These relevant quantities, through the momentum average of the DF, contain the information about the particle, energy, and entropy densities, mean particle four-velocity, heat flow, pressure tensor, and the kinetic temperature. Following the philosophy of this thesis work to formulate everything in a relativistic covariant way, we introduce the particle current density covector field $J \in \mathcal{X}^*(\mathcal{M})$, the energy-momentum-stress tensor field $T \in \mathcal{T}^0{}_2(\mathcal{M})$, and the the entropy flux covector field $S \in \mathcal{X}^*(\mathcal{M})$ defined as follows:

$$J_x(X) := \int\limits_{P_x^+(m)} f(x,p)p(X)\mathrm{dvol}_x(p), \tag{2.3.1}$$

$$T_x(X,Y) := \int\limits_{P_x^+(m)} f(x,p)p(X)p(Y)\mathrm{dvol}_x(p), \tag{2.3.2}$$

$$S_x(X) := -k_B \int\limits_{P_x^+(m)} f(x,p)\log(Af(x,p))p(X)\mathrm{dvol}_x(p), \tag{2.3.3}$$

where k_B denotes the Boltzmann constant, A is an arbitrary constant with inverse units of f, $P_x^+(m)$ is the future mass hyperboloid defined in (1.2.48), $\mathrm{dvol}_x(p)$ is the invariant Lorentz-invariant volume form given in (1.2.55), and $X, Y \in T_x(\mathcal{M})$. In terms of adapted local coordinates (x^{μ}, p_{μ}) these quantities read

$$J_{\mu}(x) = \int\limits_{P_x^+(m)} f(x,p)p_{\mu}\mathrm{dvol}_x(p), \tag{2.3.4}$$

$$T_{\mu\nu}(x) = \int\limits_{P_x^+(m)} f(x,p)p_{\mu}p_{\nu}\mathrm{dvol}_x(p), \tag{2.3.5}$$

$$S_{\mu}(x) = -k_B \int\limits_{P_x^+(m)} f(x,p)\log(Af(x,p))p_{\mu}\mathrm{dvol}_x(p). \tag{2.3.6}$$

The fields in (2.3.4) and (2.3.5) are also called the first and second moment of the DF respectively. The physical information at the macroscopic level is provided by the spacetime observables (2.3.4, 2.3.5, 2.3.6) which describe the gas configuration and its

[1] Other tensor fields of higher type can be constructed from the one-particle DF; however they will not be relevant for the purpose of this thesis work.

thermodynamics properties.

From (2.3.4) one can define the first two relevant quantities which are

$$n(x) := \sqrt{-J^\mu(x) J_\mu(x)} \qquad \text{(invariant particle density)}, \tag{2.3.7}$$

$$u_N^\mu(x) := \frac{1}{n(x)} J^\mu(x) \qquad \text{(mean particle velocity)}. \tag{2.3.8}$$

The invariant particle density n can be understood as the number of particles per unit volume measured by an observer which is comoving with the mean particle flow u_N. From (2.3.5) one can also derive the following quantities. Let u_E be the timelike eigenvector of the energy-momentum-stress tensor T i.e.,

$$T^\mu{}_\nu u_E^\nu = -\varepsilon u_E^\mu, \tag{2.3.9}$$

this tensor can be diagonalized [64] and admits the following decomposition

$$T^\mu{}_\nu(x) = \varepsilon(x)(e_{\hat{0}})^\mu \otimes (e_{\hat{0}})_\nu + P_i(x)(e_{\hat{i}})^\mu \otimes (e_{\hat{i}})_\nu, \tag{2.3.10}$$

where $e_{\hat{0}} = u_E$ and $e_{\hat{i}}$ are perpendicular to $e_{\hat{0}}$. From these observations one defines:

(i) the energy density ε defined as the negative of the eigenvalue corresponding to the timelike eigenvector of the energy-momentum-stress tensor $T^\mu{}_\nu$, and

(ii) the principal components of the pressure tensor P_i, defined as the eigenvalues belonging to the spacelike eigenvectors of $T^\mu{}_\nu$.

Finally, from the entropy current density covector field (2.3.6) one can define

$$S(x) := \sqrt{-S^\mu(x) S_\mu(x)} \qquad \text{(invariant entropy density)}, \tag{2.3.11}$$

$$u_S^\mu(x) := \frac{1}{S(x)} S^\mu(x) \qquad \text{(entropy velocity)}. \tag{2.3.12}$$

By contracting the entropy current density (2.3.6) with the entropy velocity u_S^μ one obtains

$$\mathcal{S}(x) := -S_\mu(x) u_S^\mu(x). \tag{2.3.13}$$

an entropy density $\mathcal{S}$ measured by a comoving observer with the entropy velocity u_S. This quantity is of special interest for thermodynamics considerations; we will return to this point later in section 3.2. We remark here that the three velocities (u_N, u_E, u_S) defined by the covectors (2.3.1, 2.3.3) and tensor (2.3.2) do not need to coincide in general. However, as we will see in chapter 3, if local thermodynamical equilibrium is reached, these velocities are equal to each other.

Another important result arises by comparing (2.1.14) with the definition (2.3.1) which yields

$$N[S] = \mathcal{N}[\Sigma] = -\int\limits_S J(\hat{s})\eta_S. \tag{2.3.14}$$

This result implies that the covector field J represents the averaged particle current density of the gas. Taking the divergence of (2.3.4) and (2.3.5) one can shows that [12]

$$\nabla^\mu J_\mu(x) = \int\limits_{P_x^+(m)} L[f](x,p)\mathrm{dvol}_x(p), \tag{2.3.15}$$

$$\nabla^\mu T_{\mu\nu}(x) = \int\limits_{P_x^+(m)} L[f](x,p)p_\nu\mathrm{dvol}_x(p), \tag{2.3.16}$$

where L is the Liouville vector field defined in (1.2.43). These divergences vanish if the Liouville equation is satisfied, see section (2.2), in this case

$$\nabla^\mu J_\mu = 0, \quad \nabla^\mu T_{\mu\nu} = 0, \tag{2.3.17}$$

are divergence free. On the other hand, the divergence of the covector field (2.3.6) is

$$\nabla^\mu S_\mu(x) = -k_B \int\limits_{P_x^+(m)} \left[1 + \log(Af(x,p))\right] L[f](x,p)\mathrm{dvol}_x(p), \tag{2.3.18}$$

which vanishes again if f satisfies the Liouville equation. As will see, when collisions are included, one has

$$\nabla^\mu S_\mu(x) \geq 0, \tag{2.3.19}$$

as a consequence of Boltzmann's H-theorem [16] (see also section 3.1).

In the next chapter we analyze the Boltzmann equation including the effects from collisions. In particular, this provides the correct description of a thermodynamic equilibrium state. Also, in the next chapter, we explain the main formulae for the collisionless kinetic gas and its applications through the integrable Hamiltonian system theory and the phase space mixing effect.

3 The relativistic Boltzmann equation

In this chapter we briefly review a gas configuration in which the individual gas particles are subject to binary collisions. This interaction can be modeled by the Boltzmann equation which is responsible for the dynamics and the evolution of the system. The Boltzmann equation is an integro-differential equation which contains a differential part represented by the Liouville operator (usually called the transport term) depending linearly on the distribution function. The integral part (called the collision term) is an integral over momentum space depending bilinearly on the distribution function and this term describes the collisions. Furthermore, we study here two relevant cases: the collisionless kinetic gas (the Vlasov limit) and the case of a kinetic gas dominated by the collisions (the hydrodynamic limit).

This chapter is organized as follows: in section 3.1 we provide a summary of the principal concepts of the Boltzmann equation and derive its integro-differential form. As a relevant consequence of the Boltzmann equation we study the H-theorem. Next, in section 3.2 the conditions for a global and local equilibrium gas configuration are analyzed. Section 3.3 is devoted to the study of the expansion of the DF and the Boltzmann equation in terms of the Knudsen number. Finally, in section 3.4 the details of the collisionless Boltzmann equation are analyzed, which is the principal system used in this thesis work.

3.1. Integro-differential form of the Boltzmann equation

In general the Boltzmann equation is difficult to solve; however, with some extra assumptions it can be solved providing interesting results which can be applied in many physical situations. For simplicity, we only discuss the case of a simple gas consisting of identical, spinless, massive, and neutral particles of mass $m > 0$, and we assume that the collisions are described by interactions which are short-ranged, such that each collision is regarded as pointlike, taking place at a fixed event $x \in \mathcal{M}$ in spacetime. Furthermore, we assume that the gas is sufficiently dilute, such that only binary collisions of the form

$$p_1 + p_2 \mapsto p_1^* + p_2^*, \tag{3.1.1}$$

need to be considered. Here and in the following, $p_1, p_2 \in P_x^+(m)$ refer to the physical momenta of the incoming particles and $p_1^*, p_2^* \in P_x^+(m)$ to those of the outgoing ones. Next, we assume that each such collision is elastic, preserving the total energy-momentum

$$p_1 + p_2 = p_1^* + p_2^*. \tag{3.1.2}$$

Finally, we assume that the gas is dilute enough such that the molecular chaos hypothesis is satisfied. This hypothesis is based on the supposition that just before of collisions the particles are uncorrelated, which allows one to specify a probabilistic description for the collisions and to derive a closed form equation for the one-particle DF.

As we will see, these assumptions lead to the relativistic Boltzmann equation, which has the form

$$L[f] = C_W[f, f], \tag{3.1.3}$$

where L is the Liouville vector field operator, which, recall, is given by

$$L[f](x,p) = g^{\mu\nu}(x) p_\nu \frac{\partial f(x,p)}{\partial x^\mu} - \frac{1}{2}\frac{\partial g^{\alpha\beta}(x)}{\partial x^\mu} p_\alpha p_\beta \frac{\partial f(x,p)}{\partial p_\mu}, \tag{3.1.4}$$

and C_W is the collision term. The latter depends (quadratically) on the one-particle DF f, and further it depends on the transition probability density $W_x \equiv W_x(p_1 + p_2 \mapsto p_1^* + p_2^*)$ for the binary collisions. To obtain an integral form of C_W we introduce the collision manifold C_x and the associated bundle T^*C. C_x represents the space of all collisions at $x \in \mathcal{M}$, which is defined by

$$C_x := \left\{(p_1, p_2, p_1^*, p_2^*) \in [P_x^+(m)]^4 \ : \ p_1 + p_2 = p_1^* + p_2^*, p_1 \neq p_2\right\}, \tag{3.1.5}$$

and its associated bundle T^*C is given by

$$T^*C := \{(x, p_1, p_2, p_1^*, p_2^*) \ : \ x \in \mathcal{M}, (p_1, p_2, p_1^*, p_2^*) \in C_x\}, \tag{3.1.6}$$

which has the space C_x as a fibre over each $x \in \mathcal{M}$. Here and the following we use the short notation $[P_x^+(m)]^4 = P_x^+(m) \times P_x^+(m) \times P_x^+(m) \times P_x^+(m)$. The collision manifold C_x possesses the following symmetries

$$(i) \qquad (p_1, p_2, p_1^*, p_2^*) \mapsto (p_2, p_1, p_1^*, p_2^*), \tag{3.1.7}$$

$$(ii) \qquad (p_1, p_2, p_1^*, p_2^*) \mapsto (p_1, p_2, p_2^*, p_1^*), \tag{3.1.8}$$

$$(iii) \qquad (p_1, p_2, p_1^*, p_2^*) \mapsto (p_1^*, p_2^*, p_1, p_2), \tag{3.1.9}$$

which have the following physical meaning:

(i) interchange of the incoming momenta,

(ii) interchange of the outgoing momenta,

(iii) interchange of incoming and outgoing particles,

for all $(x, p_1, p_2, p_1^*, p_2^*)$. $(i) - (ii)$ is due to the assumption that the incoming and outgoing particles are identical and indistinguishible. (iii) imposes the condition of microscopic reversibility which means that the transition probability density is invariant with respect to interchange of the incoming and outgoing momenta, and is a consequence of Lorentz invariance. Finally, as mentioned above, we base the Boltzmann equation on the molecular chaos hypothesis in which the gas is dilute enough, such that the particles are uncorrelated just before the collision. This property allows one to replace the two-particle DF by the product of the one-particle DF

$$f^{(2)}(x_1, p_1, x_2, p_2) = f(x, p_1)f(x, p_2) \equiv f_1 f_2, \tag{3.1.10}$$

at the point $x_1 = x_2 = x$. Here and the following, the short-hand notation f_j refers to the one-particle DF evaluated at (x, p_j).

The transition probability density W_x is a nonnegative real-valued smooth function

$$\begin{aligned} W \,:\, T^*C \;&\rightarrow\; \mathbb{R}, \\ (x, p_1, p_2, p_1^*, p_2^*) \;&\mapsto\; W_x(p_1, p_2, p_1^*, p_2^*) \end{aligned} \tag{3.1.11}$$

on the collision bundle T^*C which satisfies the symmetries (i), (ii) and (iii) in Eqs. (3.1.7-3.1.9), that is,

$$\begin{aligned} W_x(p_1 + p_2 \mapsto p_1^* + p_2^*) \;&=\; W_x(p_2 + p_1 \mapsto p_1^* + p_2^*) \\ &=\; W_x(p_1 + p_2 \mapsto p_2^* + p_1^*) \\ &=\; W_x(p_1^* + p_2^* \mapsto p_1 + p_2), \end{aligned}$$

for all $(x, p_1, p_2, p_1^*, p_2^*) \in T^*C$. Using the properties discussed above the integral form of the right-hand side C_W in the Boltzmann equation (3.1.3) is given by

$$\begin{aligned} C_W[f_1, f_2](x, p_1) := \iiint\limits_{[P_x^+(m)]^3} & W_x(p_1 + p_2 \mapsto p_1^* + p_2^*) \\ & \times (f_1^* f_2^* - f_1 f_2)\, \mathrm{dvol}_x(p_2)\mathrm{dvol}_x(p_1^*)\mathrm{dvol}_x(p_2^*), \end{aligned} \tag{3.1.12}$$

where it is understood that the integral is performed over the momenta p_2, p_1^*, p_2^* satisfying (3.1.2). Here, $f_1, f_2 \,:\, \Gamma_m^+ \rightarrow \mathbb{R}$ are smooth functions with compact support, $(x, p_1) \in \Gamma_m^+$ and $\mathrm{dvol}_x(p)$ is the Lorentz-invariant volume form defined in (1.2.55). Ref. [12, Section V] provides a detailed derivation of the collision term based on the collision manifold C_x using a suitable way to parametrize it, that is through the center of mass frame of the binary collisions. However, see for instance Refs. [4, 6, 16, 65] for other points of view on the derivation of the collision term. The integro-differential form of the relativistic Boltzmann equation is given by

$$\begin{aligned} g^{\mu\nu} p_\nu \frac{\partial f_1}{\partial x^\mu} \quad &- \quad \frac{1}{2} \frac{\partial g^{\alpha\beta}}{\partial x^\mu} p_\alpha p_\beta \frac{\partial f_1}{\partial p_\mu} \\ &= \iiint\limits_{[P_x^+(m)]^3} W_x \left(f_1^* f_2^* - f_1 f_2\right) \mathrm{dvol}_x(p_2) \mathrm{dvol}_x(p_1^*) \mathrm{dvol}_x(p_2^*). \end{aligned} \tag{3.1.13}$$

One of the most important consequences of the Boltzmann equation is the famous relativistic Boltzmann H-theorem which gives rise to a relativistic formulation of the second law of thermodynamics. For this, by multiplying both sides of the Boltzmann equation (3.1.3) with the function $-k_B[1 + \log(Af_1)]$ and integrating over the momentum p_1, one obtains,

$$\begin{aligned} &- \quad k_B \int\limits_{P_x^+(m)} [1 + \log(Af_1)] L[f_1] \mathrm{dvol}_x(p_1) \\ &= \iiiint\limits_{C_x} W_x \times \left(f_1 f_2 - f_1^* f_2^*\right) \left[\log(A^2 f_1 f_2) - \log(A^2 f_1^* f_2^*)\right] \eta_{C_x}, \end{aligned} \tag{3.1.14}$$

where C_x is a submanifold of $[P_x^+(m)]^4$ and η_{C_x} is the associated volume form of the collision manifold. The derivation and explicit expression for the volume form η_{C_x} is given in [12, Appendix E]. One recognize the left-hand side of (3.1.14) as the same expression as the divergence of the covector entropy flux $\nabla^\mu S_\mu$ in Eq. (2.3.18). Thus

$$\nabla^\mu S_\mu = \iiiint\limits_{C_x} W_x \times \left(f_1 f_2 - f_1^* f_2^*\right) \left[\log(A^2 f_1 f_2) - \log(A^2 f_1^* f_2^*)\right] \eta_{C_x}. \tag{3.1.15}$$

The right-hand side vanish either if $W_x = 0$ or $W_x > 0$ and $f_1 f_2 = f_1^* f_2^*$ at the point x. Furthermore, (3.1.15) implies that $\nabla^\mu S_\mu$ possesses a defined sign. This is obtained by analyzing the behavior of the function:

$$\mathcal{B} := \left(f_1 f_2 - f_1^* f_2^*\right) \left[\log(A^2 f_1 f_2) - \log(A^2 f_1^* f_2^*)\right], \quad f_1 f_2, f_1^* f_2^* > 0, \tag{3.1.16}$$

which is positive or zero since the logarithm function is a strictly increasing function. Therefore, $\mathcal{B} > 0$ for all $f_1 f_2 \neq f_1^* f_2^*$ and $\mathcal{B} = 0$ only if $f_1 f_2 = f_1^* f_2^*$.

By this analysis one obtains a formal justification of the H-theorem

$$\nabla^\mu S_\mu(x) \geq 0, \tag{3.1.17}$$

providing a description of the second law of thermodynamics, according to which the total entropy is a non-decreasing function of time. Here, we consider an asymptotically flat, globally hyperbolic spacetime (M, g) with two Cauchy surfaces C_2 and C_1 whose future-directed normal vector field is denoted by ν. Assuming that f decays sufficiently rapidly at infinity and that C_2 lies to the future of C_1, the inequality (3.1.17) and Gauss' theorem imply that

$$S[C_2] \geq S[C_1], \tag{3.1.18}$$

with

$$S[C_i] := -\int\limits_{C_i} S_\mu \nu^\mu \eta_{C_i}, \qquad i = 1, 2, \tag{3.1.19}$$

the entropy contained in the Cauchy surface C_i.

The following section 3.2 shows a local equilibrium DF as a result of the H-theorem in which the collision term vanishes for a particular form of the DF. In section 3.4 we analyze the case when the collisions between gas particles are unimportant and can be neglected.

3.2. Global and local thermodynamical equilibrium

The equilibrium configuration in which the divergence of the entropy flux is zero, assuming that W_x is strictly positive for all $x \in \mathcal{M}$, imply the condition $f_1 f_2 = f_1^* f_2^*$ for all binary elastic collisions. This condition is equivalent to the fact that $\log(Af)$ is a collision invariant. This requires that f must have the particular form [12, 66]

$$f(x, p) = \alpha(x) e^{p(\beta_x)} = \alpha(x) e^{\beta^\mu(x) p_\mu}. \tag{3.2.1}$$

Here $\alpha \in \mathcal{F}(\mathcal{M})$ is a positive function and $\beta \in \mathcal{X}(\mathcal{M})$ is a future-directed timelike vector field on $\mathcal{M}$. This last requirement is due to the requirement that f must decrease as $p \to \infty$ along of the future mass hyperboloid, such that the observables are well-defined. We discuss in subsection 3.2.1 an example using this form of the DF. Every DF of the form (3.2.1) cancels the collision term C_W in the Boltzmann equation. However, for f to be a solution of the Boltzmann equation, f must satisfy $L[f] = 0$, such that

$$0 = L[\log(Af)] = p_\mu p_\nu \nabla^\mu \beta^\nu + p_\mu \nabla^\mu \log(A\alpha), \tag{3.2.2}$$

which implies the following conditions for α and β:

$$\nabla^{(\mu} \beta^{\nu)} = 0, \quad \nabla^\mu \log(A\alpha) = 0. \tag{3.2.3}$$

The first condition means that

$$\pounds_\beta g = 0, \tag{3.2.4}$$

that is, the timelike vector field β must be a Killing vector field. The second condition means that α must be constant. Therefore, global equilibrium can only exist if the spacetime is stationary!

If the condition of stationarity on g is satisfied the timelike Killing vector field β is decomposed as follows

$$\beta^\mu = \frac{1}{k_B T} u^\mu, \tag{3.2.5}$$

where u satisfy the condition that $g(u,u) = -1$ and as will be understood later, T represent the temperature. As an interesting relativistic effect we note that the temperature $T(x)$ of a gas in thermodynamical equilibrium configuration is not necessarily constant on the stationary spacetime manifold $(\mathcal{M}, g)$. This effect is known as the Tolman-Ehrenfest theorem [67, 68] and its can be written as

$$\sqrt{-\beta^\mu(x)\beta_\mu(x)}\,T(x) = \text{const}, \tag{3.2.6}$$

for the Killing vector field β.

In summary, a global thermodynamical equilibrium configuration exists if and only if the field g is stationary and β^μ in (3.2.1) represents the (globally-defined) timelike Killing vector field. In the following subsection we analyze the properties of the observables associated with the DF (3.2.1) and explain their interpretation as describing local thermodynamic equilibrium states.

3.2.1. Local thermodynamical equilibrium

A local equilibrium state, implying the local non-production of entropy can be obtained from the conditions: $W_x > 0$ and $f_1 f_2 = f_1^* f_2^*$ derived in section 3.1. As we have discussed, this implies that the DF (3.2.1) must have the form

$$f(x,p) = \alpha(x) e^{\beta^\mu(x) p_\mu}, \tag{3.2.7}$$

where $\alpha \in \mathcal{F}(\mathcal{M})$ is a positive function and $\beta \in \mathcal{X}(\mathcal{M})$ is a future-directed timelike vector field. For the following we introduce the dimensionless parameter z defined as

$$z := m\sqrt{-\beta^\mu \beta_\mu}, \tag{3.2.8}$$

which, as we will see, is the ratio between the rest energy and the thermal energy of the particles[1]. By introducing (3.2.7) into (2.3.4) and (2.3.5) one finds [12, 16]

$$J^\mu = n(z) u^\mu, \quad \text{and} \quad T_{\mu\nu} = n(z)h(z)u_\mu u_\nu + P(z) g_{\mu\nu}, \tag{3.2.9}$$

[1] In natural units the dimensionless parameter z is given by

$$z := mc^2\sqrt{-\beta^\mu \beta_\mu},$$

with c the speed of light.

where h is the specific enthalpy and the resulting energy-momentum-stress tensor is described by a perfect fluid in which the pressure P is isotropic. By contracting

$$T^{\mu}{}_{\nu}u^{\nu} = (-nh + P)u^{\mu} = -\varepsilon u^{\mu}, \tag{3.2.10}$$

one obtains: $u = u_N = u_E$ and $\varepsilon = nh - P$. The resulting particle density n, energy density ε, specific enthalpy h, and the pressure P can be expressed in terms of the modified Bessel functions of the second kind [69]

$$\mathbf{K}_{\nu}(z) := \int_0^{\infty} e^{-z\cosh\chi}\cosh(\nu\chi)d\chi, \quad \nu > -\frac{1}{2}, \quad z > 0, \tag{3.2.11}$$

as follows

$$n(z) = 4\pi\alpha(x)m^3\frac{\mathbf{K}_2(z)}{z}, \tag{3.2.12}$$

$$P(z) = 4\pi\alpha(x)m^4\frac{\mathbf{K}_2(z)}{z^2}, \tag{3.2.13}$$

$$h(z) = m\frac{\mathbf{K}_3(z)}{\mathbf{K}_2(z)}, \tag{3.2.14}$$

$$\varepsilon(z) = 4\pi\alpha(x)m^4\left(\frac{\mathbf{K}_1(z)}{z} + 3\frac{\mathbf{K}_2(z)}{z^2}\right). \tag{3.2.15}$$

Here we have used the recurrence property

$$\frac{2\nu}{z}e^{i\pi\nu}\mathbf{K}_{\nu}(z) = e^{i\pi(\nu-1)}\mathbf{K}_{\nu-1}(z) - e^{i\pi(\nu+1)}\mathbf{K}_{\nu+1}(z). \tag{3.2.16}$$

Further, the resulting four-velocity vector field is given by

$$u^{\mu} = \frac{\beta^{\mu}}{\sqrt{-\beta^{\mu}\beta_{\mu}}}. \tag{3.2.17}$$

Finally, if we take the ratio

$$\frac{P}{n} = \frac{m}{z} = \frac{1}{\sqrt{-\beta^{\mu}\beta_{\mu}}}, \tag{3.2.18}$$

this relation has units of energy and provides a definition of kinetic temperature. By imposing the ideal gas equation

$$P = nk_BT. \tag{3.2.19}$$

the kinetic temperature is defined by

$$T(x) := \frac{1}{k_B}\frac{1}{\sqrt{-\beta^{\mu}(x)\beta_{\mu}(x)}}. \tag{3.2.20}$$

As we show now, the DF (3.2.7) describes a local equilibrium configuration of temperature T when the collisions are present. The resulting entropy flux for this DF is

$$S_\mu(x) = -k_B \left[\log(\alpha A) J_\mu(x) + \beta^\nu(x) T_{\mu\nu}(x)\right], \tag{3.2.21}$$

which provides an entropy density (2.3.13) given by

$$\mathcal{S}(x) = -k_B \log(\alpha(x) A) n(x) + \frac{1}{T(x)} \left[n(x)h(x) - P(x)\right]. \tag{3.2.22}$$

Also, $u_N = u_E = u_S$. Accordingly, the entropy per particle s is

$$s(x) := \frac{\mathcal{S}(x)}{n(x)} = -k_B \left[1 + \log(\alpha(x)A)\right] + \frac{h(x)}{T(x)}, \tag{3.2.23}$$

where we have used (3.2.19). Taking the differential on both sides of equation (3.2.23) in which we vary the functions (α, h, T), keeping A constant, yields

$$T ds = -k_B T \frac{d\alpha}{\alpha} + dh - h\frac{dT}{T}. \tag{3.2.24}$$

In order to eliminate the α-dependency in this last result one can take a differential of the pressure in equation (3.2.13) which yield

$$\frac{dP}{P} = \frac{d\alpha}{\alpha} + \frac{h}{k_B}\frac{dT}{T^2}, \tag{3.2.25}$$

where we have used the relation

$$\frac{d}{dz}\left[\frac{\mathbf{K}_\nu(z)}{z^\nu}\right] + \frac{\mathbf{K}_{\nu+1}(z)}{z^\nu} = 0. \tag{3.2.26}$$

Finally, by combining (3.2.24) and (3.2.25) one obtains the Gibbs relation

$$T ds = dh - \frac{dP}{n}, \tag{3.2.27}$$

using again the ideal gas equation (3.2.19). This last result justifies that T defined in equation (3.2.20) is the temperature of a thermal state. We remark here that, f is an exact solution of the Boltzmann equation only if β^μ is a Killing vector field and α is a constant. However, in the following section 3.3 we will discuss the hydrodynamical approximation in which the DF (3.2.7) describes local thermodynamical equilibrium to zeroth order in the Knudsen number.

3.3. Limits of large and small Knudsen number

When the spacetime is not globally stationary one can establish configurations in local equilibrium. For these solutions of the Boltzmann equation two length scales are introduced. First, a macroscopic characteristic length l_{ms} is defined as a typical length scale over which the spacetime observables vary. The second one is the length scale of microscopic nature which consists of the mean free path ℓ_{mfp}, that is the average distance traveled by a particle between successive collisions. Locally, it is defined through the relation

$$\sigma_T \ell_{\text{mfp}} n = 1, \tag{3.3.1}$$

with

$$\sigma_T := \int \frac{d\sigma}{d\Omega} d\Omega \tag{3.3.2}$$

the total cross section and n the particle density. The differential cross-section $d\sigma/d\Omega$ is related to the transition probability density W_x, see for example section V-F in [12] for details. Based on these two length scales l_{ms} and ℓ_{mfp}, we can rewrite the relativistic Boltzmann equation (3.1.3) in terms of dimensionless variables, such that

$$x^\mu = l_{\text{ms}} \overline{x}^\mu, \qquad p_\mu = m \overline{p}_\mu, \qquad f = \frac{1}{l_{\text{ms}}^4 m^4} \overline{f}, \qquad \frac{d\sigma}{d\Omega} = \frac{l_{\text{ms}}^4}{\ell_{\text{mfp}}} \frac{d\overline{\sigma}}{d\Omega}, \tag{3.3.3}$$

where all the quantities with a bar are dimensionless. In terms of these quantities one obtains

$$\overline{L}[\overline{f}] = \frac{1}{\text{Kn}} \overline{C}[\overline{f}, \overline{f}], \qquad \text{Kn} := \frac{\ell_{\text{mfp}}}{l_{\text{ms}}}. \tag{3.3.4}$$

The quantity Kn representing the ratio between the mean free path and the macroscopic scale and is known as the Knudsen number, see Refs. [70] and [71] for the original reference and a historical account.

3.3.1. The Vlasov limit

For large Knudsen numbers $\text{Kn} \gg 1$ as in plasma physics, the Boltzmann equation is dominated by the transport part. In this limit one can expand

$$\overline{f} = \overline{f}^{(0)} + \frac{1}{\text{Kn}} \overline{f}^{(1)} + \frac{1}{\text{Kn}^2} \overline{f}^{(2)} + \cdots, \tag{3.3.5}$$

with $\overline{f}^{(0)}$ satisfying the collisionless Boltzmann equation $\overline{L}[\overline{f}^{(0)}] = 0$ and the correction terms $\overline{f}^{(1)}$, $\overline{f}^{(2)}$ determined by the differential equations

$$\overline{L}[\overline{f}^{(1)}] = \overline{C}[\overline{f}^{(0)}, \overline{f}^{(0)}], \tag{3.3.6}$$

$$\overline{L}[\overline{f}^{(2)}] = 2\overline{C}[\overline{f}^{(0)}, \overline{f}^{(1)}]. \tag{3.3.7}$$

For a review on mathematical results regarding the nonrelativistic Boltzmann equation, see [72]. This limit is called the Vlasov limit. This approximation can be applied in rarefied gases (which are gases whose pressure is much smaller than the atmospheric pressure) or in plasma physics for instance.

3.3.2. The hydrodynamic limit

For small Knudsen numbers Kn $\ll 1$ the Boltzmann equation is dominated by the collision term which vanishes precisely for the DFs of the form (3.2.7) describing local thermodynamical equilibrium. In this limit one expands

$$\overline{f} = \overline{f}^{(0)} + \mathrm{Kn}\overline{f}^{(1)} + \mathrm{Kn}^2\overline{f}^{(2)} + \cdots , \tag{3.3.8}$$

with $\overline{f}^{(0)}$ of the form (3.2.7) and $\overline{f}^{(1)}$, $\overline{f}^{(2)}$ correction terms, which are determined by the integral equations

$$\begin{aligned} \overline{L}[\overline{f}^{(0)}] &= 2\overline{C}[\overline{f}^{(0)}, \overline{f}^{(1)}], && (3.3.9)\\ \overline{L}[\overline{f}^{(1)}] &= \overline{C}[\overline{f}^{(1)}, \overline{f}^{(1)}] + 2\overline{C}[\overline{f}^{(0)}, \overline{f}^{(2)}]. && (3.3.10) \end{aligned}$$

This approach lies at the base of the Hilbert expansion and Chapman-Enskog methods, see Refs. [4, 6, 16] for more details. It is called the hydrodynamics limit. An interesting application of this limit is the deduction of the Navier-Stokes equations.

3.4. Collisionless Boltzmann equation

As mention above, when the collisions between the gas particles can be neglected the collisionless Boltzmann equation is given by

$$g^{\mu\nu}(x)p_\nu \frac{\partial f(x,p)}{\partial x^\mu} - \frac{1}{2}\frac{\partial g^{\alpha\beta}(x)}{\partial x^\mu}p_\alpha p_\beta \frac{\partial f(x,p)}{\partial p_\mu} = 0, \tag{3.4.1}$$

and it describes the evolution of a collisionless DF. Assuming an integrable Hamiltonian system one can transform from the adapted local coordinates (x^μ, p_μ) to generalized action-angle variables $(\mathcal{Q}^\mu, \mathcal{J}_\mu)$ which allows one to provide a reduced expression for the collisionless Boltzmann equation and its solutions. Taking these symplectic coordinates $(\mathcal{Q}^\mu, \mathcal{J}_\mu)$, equation (3.4.1) simplifies to

$$\frac{\partial f}{\partial \mathcal{Q}^0} = 0, \tag{3.4.2}$$

and the most general solution of this equation is given by

$$f(x,p) = F\left(\mathcal{Q}^1, \mathcal{Q}^2, \mathcal{Q}^3, \mathcal{J}_0, \mathcal{J}_1, \mathcal{J}_2, \mathcal{J}_3\right). \tag{3.4.3}$$

For a Schwarzschild spacetime the integrals of motion are the mass m, energy E and the three components of the angular momentum (L_x, L_y, L_z) of the particles. Due to the phase space mixing phenomenon [36, 73] for an integrable Hamiltonian system [58], the macroscopic observables defined through the DF as solution of the collisionless Boltzmann equation converge at large times to those belonging to an average DF (average over the angle variables). Therefore, in all models studied in the following chapters we assume a DF depending only on integrals of motion.

In chapter 4 we study axisymmetric gas configurations which depend on energy E and the azimuthal component of the angular momentum L_z assuming a Newtonian potential as a central object. Here, collisions are completely neglected and the entropy production is zero. These configurations do not describe thermal equilibria since the Gibbs relation (3.2.27) does not hold. However, they describe steady-states. Next, in chapter 5 we generalize these gas configurations to the general relativistic case in which the central object is a black hole. In this context, a further result of this thesis work is based on a related model in which the DF depends on (E, L, L_z) by a suitable function of L_z/L, see [48]. Finally, the last result is presented in chapter 6 in which we analyze an accretion problem of a spherically symmetric, collisionless kinetic gas cloud falling into a Schwarzschild black hole. Whereas previous studies have treated this problem by specifying boundary conditions at infinity, here the properties of the gas are given at a sphere of finite radius. For that work we assume a DF depending on the energy and a uniform distribution in the total angular momentum L.

4 Axisymmetric, stationary collisionless gas clouds trapped in a Newtonian potential

This chapter is a loyal reproduction (with some minor changes due to the format) of the free arXiv:2209.05325 version [47]. However, the numbers of the equations and references could differ from the ones in the original version. The references are collected at the end of this thesis work.

4.1. Abstract

The properties of an axisymmetric, stationary gas cloud surrounding a massive central object are discussed. It is assumed that the gravitational field is dominated by the central object which is modeled by a nonrelativistic rotationally-symmetric potential. Further, we assume that the gas consists of collisionless, identical massive particles that follow bound orbits in this potential. Several models for the one-particle distribution function are considered and the essential formulae that describe the relevant macroscopical observables, such as the particle and energy densities, pressure tensor, and the kinetic temperature are derived. The asymptotic decay of the solutions at infinity is discussed and we specify configurations with finite total mass, energy and (zero or non-zero) angular momentum. Finally, our configurations are compared to their hydrodynamic analogs. In an accompanying paper, the equivalent general relativistic problem is discussed, where the central object consists of a Schwarzschild black hole.

4.2. Introduction

The main goal of this work is to initiate a systematic investigation for the description of steady-state kinetic gas configurations surrounding massive compact objects. From a theoretical point of view the motivation for this problem stems from the interest in understanding the behavior of a kinetic gas cloud which is trapped in a strong gravitational field background. This has many potential astrophysical applications, including the modeling of low-density hot accretion disks around compact stars or black holes, the description of distributions of stars around supermassive black holes or studying the behavior of dark matter surrounding a black hole. In particular, the recent breakthrough observations by the Event Horizon Telescope Collaboration (EHTC) [74–76] showing the first image of the shadows of the supermassive black holes M87* and Sgr A* provide a strong motivation for a thorough understanding of the behavior of a hot plasma in the vicinity of a strong gravitational field beyond the hydrodynamic approximation.

In this article, we start with a rather simple and idealized model which allows for a complete analytic description. However, despite its simplicity, it has many interesting features, as we will see. Furthermore, it serves as a starting point and benchmark for more complicated models. The models described in this article are based on the following assumptions. First, we assume that the gas is collisionless, that is, we completely neglect collisions between the individual gas particles. Second, we assume that the gas consists of identical, massive and uncharged particles. Third, we assume the gravitational field is dominated by the potential of the central massive object, such that the self-gravity of the gas can be neglected. Fourth, we assume that the central object is spherically symmetric, leading to a central gravitational potential. Fifth, in this article we further assume that the gravitational potential and the kinetic gas can be treated non-relativistically; the fully relativistic case will be treated in the accompanying paper [49]. Sixth, we focus on axisymmetric steady-states in which each gas particle follows a bound trajectory in the central gravitational potential generated by the central object.

The physical meaning of these assumptions are the following. The collisionless approximation is based on the assumption that the mean free path is large compared to the length scale over which the spatial gradients of the macroscopic quantities vary. This is most probably a reasonable assumption in all the aforementioned astrophysical scenarios. Our next assumption, namely that the gas consists of identical massive and uncharged particles makes sense for the modeling of distribution of stars and dark matter; however it is unrealistic for the description of low-density hot plasma disks since in this case the electromagnetic field is expected to play a prominent role. For this scenario, a model involving at least two species (protons and electrons) based on the Vlasov-Maxwell equations should be considered. The third assumption is justified as long as the central object is much more massive than the gas cloud. The fourth and fifth assumptions are well-founded if the gas configuration lies sufficiently far from the central object and the gas temperature is small compared to the particle's rest energy. The sixth assumption is partially based on the expectation that at sufficiently late times the gas is well-described by a distribution function (DF) depending only on integrals of motion (and hence describing a steady-state) and whose support lies in the region of phase space describing bound orbits. This is indeed expected to hold due to the fact that particles following unbound trajectories either disperse or fall into the central object in finite time [36] and due to the phase space mixing phenomena [42, 73, 77].

There has been much related work describing axisymmetric steady-state gas configurations without a massive central object, in which case the self-gravity cannot be neglected. In the non-relativistic limit, Shapiro and Teukolsky [78] numerically constructed axisymmetric static solutions of the Vlasov-Poisson system to model equilibrium stellar systems. Later, these solutions were generalized to the general relativistic case [79, 80]. More recently, Rein and Andréasson constructed axially symmetric disk solutions of the Vlasov-Poisson system [81] to model the rotation curves of disk galaxies without introducing dark matter. Further (analytic and numerical) models describing axisymmetric solutions of the Vlasov-Poisson system are discussed in section 4.4 of the book by Binney and Tremaine [35], see also [82]. For mathematical and numerical results regarding the stationary, axisymmetric Einstein-Vlasov system we refer the reader to the review article by Andréasson [8]. Recently, in [83, 84], axisymmetric and stationary solutions of the Vlasov-Poisson and Einstein-Vlasov systems were constructed numerically, based on a variety of ansätze for the DF leading to configurations with toroidal, disk-like, spindle-like and composite structures. Axially symmetric, stationary solutions of the Einstein-Vlasov and Einstein-Vlasov-Maxwell systems with and without rotation were constructed in [29, 85, 86] by deforming a spherically symmetric, static solution of the Vlasov-Poisson system and using the implicit function theorem. For related astrophysical work describing tori of axisymmetric collisionless plasmas around compact objects based on a quasi-stationary approximation, see [87, 88].

We mention in passing that a very similar model to the one considered in this work has been used to describe accretion phenomena of a collisionless gas into a central object, both in the non-relativistic [40, 89, 90] and the relativistic [36–40, 43] regimes. The main difference between the accretion model and the one considered in the present article resides in the fact that in the former case, unbounded trajectories are relevant, whereas here we focus on bound trajectories.

Returning to our model, we now describe its main features and properties. We use a four-parametric polytropic ansatz similar to Refs. [78, 83, 84] for which the one-particle DF depends only on the energy and the azimuthal angular momentum of the particles through a power law with certain cut-offs. Our ansatz allows for the description of both rotating and non-rotating stationary and axially symmetric configurations with finite total mass, energy and angular momentum. For the case of Hénon's isochrone potential (see, e.g. [35, 91]), which includes the Kepler potential as a special case, we compare configurations with the same total mass with each other. To this purpose we perform a detailed analytic derivation of the macroscopic observables corresponding to the DF, namely: the particle and the energy densities, the mean particle velocity, and the components of the pressure tensor. From these observables we define an anisotropy parameter and a kinetic temperature whose properties are analyzed. Finally, we compare our configuration's particle density and kinetic temperature with those of an analogous hydrodynamic model. We show that although the kinetic configurations are more compact than the fluid models, their normalized temperature profiles may be very similar to each other.

As mentioned before, relativistic generalizations of the models discussed in this article are provided in an accompanying paper [49]. See also Ref. [48] for a very similar disk model based on a DF depending on the energy and the inclination angle (instead of the energy and azimuthal component of the angular momentum).

This work is organized as follows: in section 4.3 we summarize the most relevant properties of a stationary, collisionless gas configuration trapped in a central potential and discuss the simple model of a spherical polytrope. In section 4.4 we present our stationary and axisymmetric models, and we derive explicit formulae for the macroscopic observables and the total mass, energy and angular momentum associated with our models. In section 4.5 we discuss the behavior of the macroscopic observables including the morphology of the resulting gas configurations. Further, in this section, we compare our kinetic models with the corresponding fluid models. Conclusions are drawn in section 4.6. Technical details including a list of relevant integrals, properties of Hénon's isochrone model, the derivation of the expressions for the total mass, energy and angular momentum and a short review of the circular fluid models can be found in appendices 4.7–4.10.

4.3. Review of basic equations and polytropic model

In this section, we first summarize the most relevant equations describing the properties of a stationary, collisionless gas configuration which is trapped in a central Newtonian potential $\Phi(r)$. Next, we consider the particular example of the polytropic model in which the one-particle DF depends only on the energy of the particles through a power law, thus yielding a spherically symmetric configuration. This model will be generalized to describe axisymmetric configurations in the subsequent section.

4.3.1. Basic equations describing a collisionless, stationary gas configuration in a central potential

In the following, we assume the potential $\Phi : (0,\infty) \to \mathbb{R}$ to be a smooth increasing function satisfying $\Phi(r) \to 0$ as $r \to \infty$ with the additional property that $r^3\Phi' : (0,\infty) \to \mathbb{R}$ is an increasing function from 0 to ∞. This implies that for each non-zero value of the total angular momentum $L \neq 0$ the effective potential

$$V_L(r) := m\Phi(r) + \frac{L^2}{2mr^2}, \qquad r > 0, \tag{4.3.1}$$

has a unique global minimum whose location $r = r_0$ is determined by the equation $r_0^3\Phi'(r_0) = L^2/m^2$ and corresponds to a stable circular trajectory with minimum energy $E_0(L) = V_L(r_0)$. For $L > 0$ any trajectory with energy $E_0(L) < E < 0$ is bounded and its radial motion is periodic with period $T_r(E,L) = \frac{\partial A(E,L)}{\partial E}$, where $A(E,L)$ denotes the area function (see for instance [58])

$$A(E,L) := \oint p_r dr = 2\int\limits_{r_1(E,L)}^{r_2(E,L)} \sqrt{2m(E - V_L(r))}dr \tag{4.3.2}$$

with $r_1(E,L) < r_2(E,L)$ referring to the turning points.

In this article, we consider collisionless gas configurations in which individual gas particles follow bound orbits. These are described by a one-particle DF f whose support lies in the region $E < 0$. As long as the potential $\Phi(r)$ satisfies the non-degeneracy condition $\det[D^2A(E,L)] \neq 0$ for almost all (E,L), it has been shown in [73] that an arbitrary initial configuration relaxes in time to a stationary configuration which can be described by a one-particle DF f depending only on the integrals of motion, that is, only on the energy and the angular momentum,

$$E = \mathcal{H}(\mathbf{x},\mathbf{p}) := \frac{|\mathbf{p}|^2}{2m} + m\Phi(r), \qquad \mathbf{L} = \mathbf{x}\wedge\mathbf{p}. \tag{4.3.3}$$

We shall be particularly interested in the properties of the resulting macroscopic observables describing the gas, namely (see, for instance [2]):

$$n(\mathbf{x}) := \int f(\mathbf{x},\mathbf{p})d^3p \qquad \text{(particle density)}, \tag{4.3.4}$$

$$\varepsilon(\mathbf{x}) := \int \mathcal{H}(\mathbf{x},\mathbf{p})f(\mathbf{x},\mathbf{p})d^3p \qquad \text{(energy density)}, \tag{4.3.5}$$

$$\mathbf{u}(\mathbf{x}) := \int \frac{\mathbf{p}}{mn(\mathbf{x})}f(\mathbf{x},\mathbf{p})d^3p \qquad \text{(mean particle velocity)}, \tag{4.3.6}$$

$$P_{ij}(\mathbf{x}) := \frac{1}{m}\int (p_i - mu_i)(p_j - mu_j)f(\mathbf{x},\mathbf{p})d^3p \qquad \text{(pressure tensor)}. \tag{4.3.7}$$

As a consequence of the collisionless Boltzmann equation and the assumption that f is time-independent, it follows that these quantities satisfy the conservation laws [2]

$$\nabla\cdot(n\mathbf{u}) = 0, \qquad (\mathbf{u}\cdot\nabla)u_i = -\partial^j P_{ij} - mn\partial_i\Phi. \tag{4.3.8}$$

If interested in thermodynamical considerations, one further considers the quantities

$$S(\mathbf{x}) := -k_B\int f(\mathbf{x},\mathbf{p})\log(Af(\mathbf{x},\mathbf{p}))d^3p \qquad \text{(entropy density)}, \tag{4.3.9}$$

$$\mathbf{S}(\mathbf{x}) := -k_B\int \frac{\mathbf{p}}{m}f(\mathbf{x},\mathbf{p})\log(Af(\mathbf{x},\mathbf{p}))d^3p \qquad \text{(entropy flux)}, \tag{4.3.10}$$

where k_B denotes Boltzmann's constant and A is an arbitrary positive constant which makes sure that Af is dimensionless.[1] Since there are no collisions, the entropy flux is divergence-free, i.e.

$$\nabla \cdot \mathbf{S} = 0, \tag{4.3.11}$$

and $S(\mathbf{x})$ is constant in time. Finally, we define the "kinetic temperature" T at position $\mathbf{x}$ through [35]

$$k_B T(\mathbf{x}) = \frac{\delta^{ij} P_{ij}(\mathbf{x})}{3n(\mathbf{x})} = \int \frac{|\mathbf{p} - m\mathbf{u}|^2}{3mn(\mathbf{x})} f(\mathbf{x}, \mathbf{p}) d^3p, \tag{4.3.12}$$

which is motivated by the ideal gas equation $P = nk_B T$ with $P = \delta^{ij} P_{ij}/3$ the isotropic pressure. Note, however, that the configurations analyzed in this article are not in thermodynamic equilibrium, since collisions are completely neglected. Therefore, $T(\mathbf{x})$ should be interpreted as a measure for the molecular mean square velocity rather than the property associated with a thermal state. An example illustrating this characteristic will be provided shortly.

Eqs. (4.3.3–4.3.7) and the definition of the temperature in Eq. (4.3.12) imply the general relation

$$\varepsilon = n \left[\frac{m}{2} |\mathbf{u}|^2 + \frac{3}{2} k_B T + m\Phi \right]. \tag{4.3.13}$$

4.3.2. Spherical polytropes

To provide a simple but useful example, we first discuss the polytropes (see, for instance, section 4.3.3 in Ref. [35]) for which

$$f(\mathbf{x}, \mathbf{p}) = F_{\text{poly}}(E) := \alpha \left(-\frac{E}{E_0} \right)_+^{k-\frac{3}{2}}, \tag{4.3.14}$$

with some positive constants E_0 (with units of energy) and α (with units of time^3 $\times$ mass^{-3} $\times$ length^{-6}) and the polytropic index $k > 1/2$. Here and in the following, the notation F_+ refers to the positive part of F, that is $F_+ = F$ if $F > 0$ and $F_+ = 0$ otherwise. The observables (4.3.4–4.3.7) and (4.3.9,4.3.10) can easily be computed by means of the "partition function"

$$Z(\alpha, k, \mathbf{x}) := \alpha \int \left(-\frac{E}{E_0} \right)_+^{k-\frac{3}{2}} d^3p, \tag{4.3.15}$$

according to the following relations:

$$\begin{aligned} n(\mathbf{x}) &= Z(\alpha, k, \mathbf{x}), \qquad \varepsilon(\mathbf{x}) = -E_0 Z(\alpha, k+1, \mathbf{x}), \\ S(\mathbf{x}) &= -k_B n(\mathbf{x}) \left[\log(\alpha A) + \left(k - \frac{3}{2} \right) \frac{\partial}{\partial k} \log Z(\alpha, k, \mathbf{x}) \right], \end{aligned} \tag{4.3.16}$$

[1] Note that a rescaling $A \mapsto \lambda A$ of A by a positive factor λ induces the transformations $S \mapsto S - (\log \lambda) k_B n$, $\mathbf{S} \mapsto \mathbf{S} - \log(\lambda) k_B n\mathbf{u}$, such that Eq. (4.3.11) remains invariant by this rescaling, due to the conservation law (4.3.8).

whereas $\mathbf{u} = \mathbf{S} = 0$ and $P_{ij} = P\delta_{ij}$ as a direct consequence of the fact that the DF only depends on the energy. Computing $Z(\alpha, k, \mathbf{x})$ explicitly and taking into account the relation (4.3.13) yields

$$\begin{aligned} n(\mathbf{x}) &= c_k\psi(r)^k, \qquad c_k := \alpha(2\pi m E_0)^{\frac{3}{2}}\frac{\Gamma\left(k-\frac{1}{2}\right)}{\Gamma(k+1)}, && (4.3.17)\\ k_B T(\mathbf{x}) &= \frac{P(\mathbf{x})}{n(\mathbf{x})} = \frac{E_0}{k+1}\psi(r), \qquad \varepsilon(\mathbf{x}) = -\left(k-\frac{1}{2}\right)P(\mathbf{x}), && (4.3.18)\\ \frac{S(\mathbf{x})}{n(\mathbf{x})} &= -k_B\left\{\log\left[\alpha A\psi(r)^{k-\frac{3}{2}}\right] + \left(k-\frac{3}{2}\right)\left[\Psi_{\text{di}}\left(k-\frac{1}{2}\right) - \Psi_{\text{di}}\left(k+1\right)\right]\right\}, && (4.3.19) \end{aligned}$$

where $\Psi_{\text{di}}(k) := \frac{\partial}{\partial k}\log\Gamma(k)$, $k > 0$, denotes the digamma function (see, e.g. [92, Eq. 5.2.2]) and for convenience we have introduced the dimensionless quantity

$$\psi(r) := -\frac{m\Phi(r)}{E_0}. \tag{4.3.20}$$

Note that the polytropic relation $P = Kn^\gamma$ holds, with adiabatic index $\gamma = 1 + 1/k$ and constant $K = E_0 c_k^{-1/k}/(k+1)$. Hence, the configuration described by the DF (4.3.14) gives rise to a static, isotropic perfect fluid configuration with polytropic equation of state. Remarkably, the radial profiles of the particle density, pressure and energy density are given by simple powers of the dimensionless potential $\psi(r)$; in particular they are monotonously decreasing for all $k > 1/2$ since $\psi(r)$ is, with their decay properties at $r \to \infty$ controlled by the ones of $\psi(r)$. A self-gravitating configuration can be obtained by requiring the fulfillment of Poisson's equation, which leads to the famous Lane-Emden equation (see [93] and references therein). However, we shall not go further into this direction since our work focuses on the case where the gravitational potential is dominated and shaped by a central object.

We conclude this section by remarking that the above configurations do not describe thermal equilibria. Indeed, by varying the DF (4.3.14) with respect to α and k, one obtains

$$\begin{aligned} d\left(\frac{\varepsilon}{n}\right) &- Td\left(\frac{S}{n}\right) + Pd\left(\frac{1}{n}\right)\\ &= \frac{P}{n}\left\{-\frac{3}{2}\frac{1}{k+1} + \left(k-\frac{3}{2}\right)\left[\Psi'_{\text{di}}\left(k-\frac{1}{2}\right) - \Psi'_{\text{di}}\left(k+1\right)\right]\right\}dk. \qquad (4.3.21) \end{aligned}$$

It can be verified that the right-hand side does not vanish for any $k > 1/2$, such that the Gibbs relation does not hold. Consequently, the gas configurations described by the DF (4.3.14) are not in local thermodynamical equilibrium, despite of the fact that they describe steady-states. Of course, there is not contradiction since collisions are completely neglected in our model, implying that there is no entropy production driving the gas towards thermal equilibrium.

4.4. Stationary, axisymmetric models

In this section, we consider steady-state configurations which are axisymmetric. Assuming that mixing has taken place[2] such that the DF only depends on the integrals of motion E and $\mathbf{L}$, and assuming without loss of generality that the axis of symmetry coincides with the z-axis, this implies that the one-particle DF only depends on E, $L := |\mathbf{L}|$ and L_z, such that

$$f(\mathbf{x}, \mathbf{p}) = F(E, L, L_z). \tag{4.4.1}$$

Here, F is a function which vanishes if its arguments (E, L, L_z) lie outside the admissible range describing bound trajectories, see Eq. (4.4.3) below. We start our investigation with some general bounds in section 4.4.1, which provide sufficient conditions for the ansatz (4.4.1) to describe a gas configuration with finite total mass and angular momentum. Next, in Section 4.4.2 we discuss the (E, L_z)-models in which the DF is a product between the polytropic function $F_{\text{poly}}(E)$ and some function $I(L_z)$ of the azimuthal angular momentum L_z. Finally, in Section 4.4.3 we derive general expressions for the total mass, energy and angular momentum for the (E, L_z)-models and compute them explicitly for the case of Hénon's gravitational potential which interpolates between the potential belonging to a point mass and the one belonging to a constant density sphere [35].

4.4.1. General bounds on the observables

Before specifying our models and deriving the corresponding expressions for the macroscopic observables, we derive some elementary bounds that can be inferred from the results in the previous subsection. For this, we assume that F satisfies the bound

$$0 \leq F(E, L, L_z) \leq F_{\text{poly}}(E), \tag{4.4.2}$$

for all admissible values (E, L, L_z) of the constants of motion leading to bound trajectories, where here $F_{\text{poly}}(E)$ is any function of the form given in Eq. (4.3.14) for *some fixed* positive constants α, E_0 and $k > 1/2$. In principle, one might think that the upper bound (4.4.2) on F which is uniform in (L, L_z) is rather restrictive. However, this is not the case as one can see by noticing that the admissible range of values for the constants of motion leading to bound trajectories is described by the inequalities

$$E_{\text{min}} := m\Phi(0) < E < 0, \qquad 0 \leq L \leq L_{\text{ub}}(E), \qquad |L_z| \leq L, \tag{4.4.3}$$

with $L_{\text{ub}}(E)$ denoting the critical angular momentum such that the minimum of the effective potential $V_L(r)$ is precisely E, i.e. such that $E_0(L_{\text{ub}}) = E$. Therefore, given

[2] As discussed in [73] mixing takes place in Hénon's isochrone potential used later in this work, as long as the parameter b characterizing this potential is positive.

$E \in (E_{\min}, 0)$, the admissible set of (L, L_z) satisfying Eq. (4.4.3) is compact, implying that Eq. (4.4.2) is really a bound on the energy-dependency of the DF.
Due to the monotony properties of the integral, Eq. (4.4.2) implies that the particle density associated with F is bounded according to

$$0 \leq n(\mathbf{x}) \leq c_k \psi(r)^k, \qquad \mathbf{x} \in \mathbb{R}^3, \tag{4.4.4}$$

with c_k as in Eq. (4.3.17). In particular, the decay of $n(\mathbf{x})$ for $r \to \infty$ is controlled by the decay of the dimensionless gravitational potential $\psi(r)$. For the typical $1/r$-decay of the potential, it follows that the particle density decays at least as fast as $1/r^k$ which leads to a finite mass configuration provided that $k > 3$.
From the bound (4.4.4) and the fact that $|\mathcal{H}| = -m\Phi - |\mathbf{p}|^2/(2m) \leq E_0\psi$, one also obtains

$$|\varepsilon(\mathbf{x})| \leq E_0 c_k \psi(r)^{k+1}, \qquad \mathbf{x} \in \mathbb{R}^3, \tag{4.4.5}$$

showing that the energy density's magnitue decays at least as fast as $\psi(r)^{k+1}$.
Similarly, we can estimate the magnitude of the mean velocity $|\mathbf{u}|$ according to

$$|\mathbf{u}(\mathbf{x})| \leq \frac{1}{mn(\mathbf{x})} \int |\mathbf{p}| F_{\text{poly}}(E) d^3p = \frac{32\pi m\alpha}{n(\mathbf{x})} \frac{E_0^2}{4k^2 - 1} \psi(r)^{k+\frac{1}{2}}, \qquad \mathbf{x} \in \mathbb{R}^3, \tag{4.4.6}$$

which shows that $|n(\mathbf{x})\mathbf{u}(\mathbf{x})|$ decays at least as fast as $1/r^{k+1/2}$ if $\psi(r)$ decays like $1/r$.
Next, the kinetic energy density can be bounded according to

$$0 \leq \int \frac{|\mathbf{p}|^2}{2m} f(\mathbf{x}, \mathbf{p}) d^3p \leq \int \frac{|\mathbf{p}|^2}{2m} F_{\text{poly}}(E) d^3p = \frac{3E_0 c_k}{2(k+1)} \psi(r)^{k+1}, \tag{4.4.7}$$

which implies that the individual components of the pressure tensor can be estimated according to

$$\begin{aligned} |P_{ij}(\mathbf{x})| &\leq \frac{1}{m} \int |\mathbf{p} - m\mathbf{u}|^2 f(\mathbf{x}, \mathbf{p}) d^3p \\ &= \frac{1}{m} \int |\mathbf{p}|^2 f(\mathbf{x}, \mathbf{p}) d^3p - mn(\mathbf{x})|\mathbf{u}(\mathbf{x})|^2 \leq \frac{3E_0 c_k}{k+1} \psi(r)^{k+1}, \end{aligned} \tag{4.4.8}$$

where we have used the bound (4.4.7) in the last step.
Summarizing, any stationary, axisymmetric DF satisfying the estimates (4.4.2) has the property that the quantities $n(\mathbf{x})$, $|\varepsilon(\mathbf{x})|$, $|P_{ij}(\mathbf{x})|$ and $n(\mathbf{x})|\mathbf{u}(\mathbf{x})|$ are bounded by powers of the dimensionless gravitational potential $\psi(r)$. In particular, any such configuration for which $k > 3$ and $\psi(r)$ is regular at $r = 0$ and decays as $1/r$ for $r \to \infty$ has finite total mass and energy, as follows from the bounds (4.4.4,4.4.5). Furthermore, taking into account the bound (4.4.6) one can also conclude that the slightly stronger bound $k > 7/2$ leads to configurations with finite total angular momentum. The results obtained in this subsection will be useful to describe the range of validity of the free parameters in the models introduced in the next subsection.

4.4.2. The (E, L_z)-models

For the following, we restrict our attention to DFs of the form (4.4.1) which are independent of L and which factorize, such that

$$F(E, L, L_z) = F_0(E)I(L_z), \tag{4.4.9}$$

with two functions $F_0(E)$ and $I(L_z)$. The independence of L can be motivated by the observation that if the self-gravity of the gas configuration was taken into account, then the gravitational potential would in general no longer be spherically symmetric, and thus L would cease to be an integral of motion, whereas an ansatz in which the DF depends on (E, L_z) is fully compatible with a self-gravitating axisymmetric configuration. Ansätze of the form (4.4.9) have been presented in the context of Newtonian [78, 94] and relativistic [79, 80] self-gravitating, stationary and axisymmetric stellar systems. See also Refs. [83,84] for more recent work on the numerical construction of self-gravitating disk, spindle and torus configurations in the relativistic case. For the following, we consider an ansatz of the form (4.4.9) with $F_0(E) = F_{\text{poly}}(E)$ as in Eq. (4.3.14) and $I(L_z) = I_{\text{poly}}^{(\text{even,rot})}(L_z)$ given by one of the following two models:

$$I_{\text{poly}}^{(\text{even})}(L_z) := \left(\frac{|L_z|}{L_0} - 1\right)_+^l, \tag{4.4.10}$$

or

$$I_{\text{poly}}^{(\text{rot})}(L_z) := 2\left(\frac{L_z}{L_0} - 1\right)_+^l, \tag{4.4.11}$$

with parameters $L_0 > 0$ and $l = 0, 1, 2, \ldots$. The parameter $L_0 > 0$ describes a lower-bound for the (magnitude of the) azimuthal angular momentum. In particular, since $|L_z| \leq L$, it implies that radial and almost radial trajectories are not populated, meaning that the gas configuration must vanish close to the center. On the other hand, since $|L_z| \leq L \leq L_{\text{ub}}(E)$ for bound orbits, one can show that $|I(L_z)|$ can be bounded by a power of $1/|E|$ for small $|E|$. For example, for typical $1/r$-decay at infinity, such that $\Phi(r) \approx -GM/r$ for large values of r, one finds the Keplerian expressions $r_0 \approx L^2/(GMm^2)$ and $L_{\text{ub}}(E) \approx GMm^2/\sqrt{-2mE}$, which means that for both ansätze (4.4.10) and (4.4.11), $|I(Lz)|$ can be bounded from above by a constant times $(-E/E_0)^{-l/2}$, and all the bounds obtained in the previous subsection hold provided k is replaced with $k - l/2$. In particular, one obtains finite mass configurations if $k > 3 + l/2$. Finally, we note that the main difference between the two ansätze (4.4.10) and (4.4.11) lies in the absolute value of L_z, which implies that $I_{\text{poly}}^{(\text{even})}$ is an even function of the azimuthal angular momentum, such that for every orbit with $L_z > L_0$ there is a corresponding orbit rotating in the opposite direction with reversed sign $-L_z$ of the azimuthal angular momentum, whereas $I_{\text{poly}}^{(\text{rot})}$ only considers orbits rotating with positive L_z. The factor 2 in Eq. (4.4.11) is introduced such that both configurations described by Eqs. (4.4.10,4.4.11) have the same density profile and total mass (see below).

After having specified our particular ansätze for the DF $F(E, L, L_z)$, we compute the associated observables (4.3.4,4.3.5,4.3.6,4.3.7). To this purpose, we transform the Cartesian components of the momentum **p** to its spherical components $(p_r, p_\vartheta, p_\varphi)$ and next to the constants of motion (E, L, L_z), which can be written as

$$E = \frac{p_r^2}{2m} + V_L(r), \qquad L^2 = p_\vartheta^2 + \frac{p_\varphi^2}{\sin^2\vartheta}, \qquad L_z = p_\varphi. \tag{4.4.12}$$

Consequently, the volume form transforms according to

$$d^3p = \frac{dp_r dp_\vartheta dp_\varphi}{r^2\sin\vartheta} = \frac{mL}{|p_\vartheta||p_r|}\frac{dEdLdL_z}{r^2\sin\vartheta}. \tag{4.4.13}$$

At this point, it is important to realize that the variable substitution $(p_r, p_\vartheta, p_\varphi) \mapsto (E, L, L_z)$ is not one-to-one but four-to-one, which is due to the possible sign choices for

$$p_r = \pm\sqrt{2m(E - V_L(r))}, \qquad p_\vartheta = \pm\sqrt{L^2 - L_z^2\sin^{-2}\vartheta}, \tag{4.4.14}$$

when the spherical components of **p** are reconstructed from the integrals of motion. These sign choices imply that there are four corresponding contributions when rewriting Eqs. (4.3.4,4.3.5,4.3.6,4.3.7) as integrals over (E, L, L_z). The domain of integration is restricted by the requirement that (for given values of r and ϑ) one must have $V_L(r) \leq E$ and $L_z^2\sin^{-2}\vartheta \leq L^2$, which gives[3]

$$E_{\text{min}}(r) < E < 0, \qquad 0 \leq L < L_{\text{max}}(E, r), \qquad |L_z| \leq L\sin\vartheta, \tag{4.4.15}$$

with $E_{\text{min}}(r) := m\Phi(r)$ and $L_{\text{max}}(E, r) := r\sqrt{2m(E - m\Phi(r))}$.

For an arbitrary DF of the form (4.4.1) this yields the following expression for the particle density

$$n(\mathbf{x}) = \frac{4m}{r^2\sin\vartheta}\int\limits_{E_{\text{min}}(r)}^{0} dE \int\limits_{0}^{L_{\text{max}}(E,r)} dLL \int\limits_{-L\sin\vartheta}^{+L\sin\vartheta} dL_z \frac{F(E, L, L_z)}{\sqrt{L^2 - L_z^2\sin^{-2}\vartheta}\sqrt{2m(E - V_L(r))}}, \tag{4.4.16}$$

and similar expressions for $\varepsilon(\mathbf{x})$, $\mathbf{u}(\mathbf{x})$ and $P_{ij}(\mathbf{x})$ (taking into account the correct signs of p_r and p_ϑ in each of the four contributions). For the particular product ansatz (4.4.9) considered in this subsection, one can interchange the order of the integrals over L and L_z and explicitly compute the resulting integral over L (see Appendix 4.7 for details), which gives

$$n(\mathbf{x}) = \frac{2\pi m}{r\sin\vartheta}\int\limits_{E_{\text{min}}(r)}^{0} dEF_0(E) \int\limits_{-L_{\text{max}}(E,r)\sin\vartheta}^{+L_{\text{max}}(E,r)\sin\vartheta} dL_z I(L_z), \tag{4.4.17}$$

[3] Note that the conditions in Eq. (4.4.15) automatically imply that (E, L, L_z) lies in the admissible range described by the inequalities (4.4.3) since $L\sin\vartheta \leq L$ and since, by definition, $L_{\text{max}}(E, r) \leq L_{\text{ub}}(E)$.

and similarly for the other observables. Specializing to the specific functions (4.3.14) for F_0 and Eqs. (4.4.10,4.4.11) for $I(L_z)$ these integrals can be computed explicitly. Introducing the cylindrical radius $R := r\sin\vartheta$ and the dimensionless variable (depending on r and ϑ)

$$\eta := \frac{R}{L_0}\sqrt{2mE_0\psi}, \tag{4.4.18}$$

(with the dimensionless potential ψ depending on r defined as in Eq. (4.3.20)) one obtains[4]

$$\begin{aligned} n^{(\mathrm{rot})} &= 4\pi\alpha(2mE_0)^{\frac{3}{2}}\frac{\eta^l}{l+1}\psi^k J_{k-\frac{3}{2},l}(\eta), &(4.4.19)\\ \varepsilon^{(\mathrm{rot})} &= -4\pi\alpha(2mE_0)^{\frac{3}{2}}E_0\frac{\eta^l}{l+1}\psi^{k+1}J_{k-\frac{1}{2},l}(\eta), &(4.4.20)\\ \mathbf{u}^{(\mathrm{rot})} &= \sqrt{\frac{2E_0}{m}\psi}\left[\frac{l+1}{l+2}\frac{J_{k-\frac{3}{2},l+1}(\eta)}{J_{k-\frac{3}{2},l}(\eta)}+\frac{1}{\eta}\right]\mathbf{e}_\varphi, &(4.4.21)\end{aligned}$$

with $\mathbf{e}_\varphi := (-\sin\varphi,\cos\varphi,0)$. Herein, $J_{s,l}$ refer to the integrals (defined for $s,l\geq 0$)

$$J_{s,l}(\eta) = \frac{1}{\eta^{2s+l+3}}\int_1^\eta(\eta^2-\xi^2)^s(\xi-1)_+^{l+1}\xi d\xi, \qquad \eta>0, \tag{4.4.22}$$

which vanish if $\eta\leq 1$. Using integration by parts, the variable substitution $\xi = 1+x$ and [95, Eq. 3.197.8] these integrals can be written as

$$\begin{aligned} J_{s,l}(\eta) &= \frac{1}{2}B(s+1,l+2){}_2F_1\left(-(s+1),l+1;s+l+3;-\frac{\eta-1}{\eta+1}\right)\\ &\quad\times\left(1+\frac{1}{\eta}\right)^{s+1}\left(1-\frac{1}{\eta}\right)_+^{s+l+2}, &(4.4.23)\end{aligned}$$

where $B(a,b)$ denotes the Beta function and ${}_2F_1(a,b;c;z)$ Gauss' hypergeometric function (see [92]). Taking into account the behavior of the integrand under the transformation $L_z\mapsto -L_z$, the observables belonging to the even ansatz (4.4.10) are given by

$$n^{(\mathrm{even})}(\mathbf{x}) = n^{(\mathrm{rot})}(\mathbf{x}), \qquad \varepsilon^{(\mathrm{even})}(\mathbf{x}) = \varepsilon^{(\mathrm{rot})}(\mathbf{x}), \qquad \mathbf{u}^{(\mathrm{even})}(\mathbf{x}) = \mathbf{0}. \tag{4.4.24}$$

[4] In the limit $\eta\to\infty$ one finds $J_{s,l}(\eta)\to\frac{1}{2}B\left(s+1,\frac{l+3}{2}\right)$. In particular, taking $l=0$ and $L_0\to 0$ yields

$$n^{(\mathrm{rot})} = 2\pi\alpha(2mE_0)^{\frac{3}{2}}B\left(k-\frac{1}{2},\frac{3}{2}\right)\psi^k, \qquad \varepsilon^{(\mathrm{rot})} = -2\pi\alpha(2mE_0)^{\frac{3}{2}}B\left(k+\frac{1}{2},\frac{3}{2}\right)E_0\psi^{k+1},$$

which coincides with the expression in Eqs. (4.3.17,4.3.18), as expected.

The pressure tensor can be computed from Eq. (4.3.7) and results to be diagonal:

$$\mathbf{P} = P_{\hat{r}}\mathbf{e}_r \otimes \mathbf{e}_r + P_{\hat{\vartheta}}\mathbf{e}_\vartheta \otimes \mathbf{e}_\vartheta + P_{\hat{\varphi}}\mathbf{e}_\varphi \otimes \mathbf{e}_\varphi, \tag{4.4.25}$$

with $\mathbf{e}_r := (\cos\varphi\sin\vartheta, \sin\varphi\sin\vartheta, \cos\vartheta)$ and $\mathbf{e}_\vartheta := \partial\mathbf{e}_r/\partial\vartheta$. Due to the identity (4.7.2) in Appendix 4.7 the principle pressures $P_{\hat{r}}$ and $P_{\hat{\vartheta}}$ turn out to be equal, and for the ansatz (4.4.11) one finds

$$P_{\hat{r}}^{(\mathrm{rot})} = 8\pi\alpha(2mE_0)^{\frac{3}{2}}E_0\frac{\eta^l\psi^{k+1}}{l+1}\left[\frac{1}{\eta}\frac{J_{k-\frac{3}{2},l+1}(\eta)}{l+2} + \frac{J_{k-\frac{3}{2},l+2}(\eta)}{l+3}\right], \tag{4.4.26}$$

$$\begin{aligned} P_{\hat{\varphi}}^{(\mathrm{rot})} &= 8\pi\alpha(2mE_0)^{\frac{3}{2}}E_0\frac{\eta^l\psi^{k+1}}{l+1} \\ &\quad\times\left[\frac{1}{\eta^2}J_{k-\frac{3}{2},l}(\eta) + \frac{2}{\eta}\frac{l+1}{l+2}J_{k-\frac{3}{2},l+1}(\eta) + \frac{l+1}{l+3}J_{k-\frac{3}{2},l+2}(\eta)\right] \\ &\quad -mn^{(\mathrm{rot})}\left|\mathbf{u}^{(\mathrm{rot})}\right|^2. \end{aligned} \tag{4.4.27}$$

For the interpretation of our results in the next section, it is convenient to introduce the isotropic pressure, defined by $P := (P_{\hat{r}} + P_{\hat{\vartheta}} + P_{\hat{\varphi}})/3$, and the corresponding kinetic temperature T, such that $P = nk_BT$. Using the identity

$$\left(\frac{1}{\eta^2} - 1\right)J_{s,l}(\eta) + \frac{2}{\eta}J_{s,l+1}(\eta) + J_{s,l+2}(\eta) = -J_{s+1,l}(\eta), \qquad s, l \geq 0. \tag{4.4.28}$$

one finds

$$P^{(\mathrm{rot})} = \frac{8\pi\alpha}{3}(2mE_0)^{\frac{3}{2}}E_0\frac{\eta^l\psi^{k+1}}{l+1}\left[J_{k-\frac{3}{2},l}(\eta) - J_{k-\frac{1}{2},l}(\eta)\right] - \frac{1}{3}mn^{(\mathrm{rot})}\left|\mathbf{u}^{(\mathrm{rot})}\right|^2, \tag{4.4.29}$$

and it can be checked that the relation (4.3.13) holds. The pressure variables belonging to the even ansatz (4.4.10) are given by the same expressions as in Eqs. (4.4.26,4.4.27, 4.4.29) where one replaces $\mathbf{u}^{(\mathrm{rot})}$ with zero. In the next subsection, we derive explicit expressions for the total mass, energy and angular momentum associated with the configurations described by the models (4.4.9,4.4.10,4.4.11).

We conclude this subsection by noting that the support of the particle and energy densities, as well as the pressure components is delimited by the condition $\eta \geq 1$, or

$$r\sqrt{\psi(r)}\sin\vartheta \geq \frac{L_0}{\sqrt{2mE_0}}. \tag{4.4.30}$$

This boundary is generated by parabolic-type orbits of maximal energy ($E = 0$) whose orbital plane has an inclination angle $\pi/2 - \vartheta$ with respect to the equatorial plane and whose total angular momentum $L = L_0/\sin\vartheta$ is minimal. Examples of the resulting surface will be presented in the next section. For the moment, we note that for the Kepler potential, for which ψ is proportional to $1/r$, this surface has the form

$$z^2 \leq R^2\left(\frac{R^2}{R_0^2} - 1\right) \tag{4.4.31}$$

for some constant $R_0 > 0$ corresponding to the radius of the inner edge of the disk.

4.4.3. Total mass, energy and angular momentum

In this subsection we derive useful formulae that allow one to compute the total mass M_{gas} as well as the total energy E_{gas} and angular momentum $\mathbf{J}_{\text{gas}}$ of the stationary, axisymmetric gas configurations described by DFs of the form (4.4.1) and the ansätze (4.4.9,4.4.10,4.4.11) in particular. In the latter case, we also compute explicit expressions for Hénon's isochrone potential. Recall that for the polytropes discussed in subsection 4.3.2 and their axisymmetric generalizations discussed in the previous subsection, these quantities are finite provided the gravitational potential $\Phi(\mathbf{x})$ decays to zero as fast as $1/r$ for $r \to \infty$ and $k > 7/2 + l/2$.

The computation of the total mass for a DF depending only on integrals of motion as in Eq. (4.4.1) is greatly simplified by introducing action-angle variables $(\mathbf{Q}, \mathbf{J})$ (see for instance Refs. [35,58]) on the region of phase space corresponding to bound orbits (that is, those orbits lying in the admissible range defined by Eq. (4.4.3)). Using the fact that the transformation $(\mathbf{x}, \mathbf{p}) \mapsto (\mathbf{Q}, \mathbf{J})$ is symplectic and hence volume-preserving, one obtains

$$M_{\text{gas}} = m \int n(\mathbf{x}) d^3x = m \int f(\mathbf{x}, \mathbf{p}) d^3x d^3p = m \int\limits_{\Omega_J} \int\limits_{\mathbb{T}^3} f(\mathbf{x}, \mathbf{p}) d^3Q d^3J, \qquad (4.4.32)$$

where $\Omega_J \subset \mathbb{R}^3$ denotes the domain over which the action variables $\mathbf{J}$ vary and $\mathbb{T}^3$ the three-torus parametrized by the angles $\mathbf{Q}$. A DF of the form given in Eq. (4.4.1) is independent of the angle variables, and hence in this case the integral over $\mathbb{T}^3$ is trivial and yields the factor $(2\pi)^3$. In order to perform the integral over the action variables, one uses the relation [35, 73] $\mathbf{J} = (J_1, J_2, J_3) = (A(E, L)/(2\pi), L, L_z)$, with $A(E, L)$ the area function defined in Eq. (4.3.2), and rewrites it as an integral over the constants of motion (E, L, L_z). Taking into account Eq. (4.4.3) to formulate the appropriate integration limits yields

$$\begin{aligned} M_{\text{gas}} &= 4\pi^2 m \int\limits_{E_{\text{min}}}^{0} dE \int\limits_{0}^{L_{\text{ub}}(E)} dL \int\limits_{-L}^{L} dL_z T_r(E, L) F(E, L, L_z), \\ T_r(E, L) &= \frac{\partial A(E, L)}{\partial E}, \end{aligned} \qquad (4.4.33)$$

which allows one to compute M_{gas} if the period of the radial motion T_r and the function F are known. The expression for E_{gas} is obtained from Eq. (4.4.33) by inserting the factor E/m inside the integral. Similarly, the total angular momentum of the gas configuration is given by

$$\mathbf{J}_{\text{gas}} = \int \int \mathbf{x} \wedge \mathbf{p} f(\mathbf{x}, \mathbf{p}) d^3x d^3p = \int\limits_{\Omega_J} \int\limits_{\mathbb{T}^3} \mathbf{x} \wedge \mathbf{p} f(\mathbf{x}, \mathbf{p}) d^3Q d^3J, \qquad (4.4.34)$$

which, for the stationary and axisymmetric configuration of the form (4.4.1) yields

$$\mathbf{J}_{\text{gas}} = 4\pi^2 \int\limits_{E_{\min}}^{0} dE \int\limits_{0}^{L_{\text{ub}}(E)} dL \int\limits_{-L}^{L} dL_z L_z T_r(E,L) F(E,L,L_z) \mathbf{e}_z \tag{4.4.35}$$

with $\mathbf{e}_z = (0,0,1)$. Without specifying the function F in more details, this is how far we can get.[5] For the following, we compute M_{gas}, E_{gas} and $\mathbf{J}_{\text{gas}}$ for the particular ansätze (4.4.9,4.4.10,4.4.11) of the previous subsection, assuming that the gravitational potential is given by Hénon's isochrone model (see [91] and [35]),

$$\Phi(r) = \Phi_b^{\text{iso}}(r) := -\frac{GM}{b + \sqrt{b^2 + r^2}}, \qquad r > 0, \tag{4.4.36}$$

which is parametrized in terms of the parameter $b > 0$ which has units of length. Note that in the limit $b \to 0$ this potential reduces to Kepler's potential; however for $b > 0$ the potential Φ_b^{iso} is finite and regular at the center. One of the interesting properties of this potential is that the period of the radial motion is independent of L and given by the same expression as Kepler's potential, i.e.

$$T_r(E,L) = 2\pi GM \left(\frac{m}{-2E}\right)^{\frac{3}{2}}. \tag{4.4.37}$$

The relevant limits of integration in this case are given by (see Appendix 4.8 for details)

$$E_{\min} = m\Phi(0) = -\frac{GMm}{2b}, \qquad L_{\text{ub}}(E) = \sqrt{\frac{m}{2}} \left(\frac{GMm}{\sqrt{-E}} - 2b\sqrt{-E}\right). \tag{4.4.38}$$

Introducing these expressions into Eqs. (4.4.33,4.4.35) yields, after some calculations

[5] Note that if $F(E,L,L_z) = F_0(E)$ is independent of L and L_z one can carry out the integrals over L and L_z explicitly. Using Eq. (4.3.2) one obtains

$$M_{\text{gas}} = 16\pi^2 m^2 \int_{E_{\min}}^{0} dE F_0(E) \int_0^{r_2(E,0)} dr r^2 \sqrt{2m(E - m\Phi(r))}.$$

Another interesting case is the one described by a DF of the form $F(E,L,L_z) = F_0(E)G(\beta)$ with $\beta = L_z/L$, for which

$$M_{\text{gas}} = \frac{1}{2}\int_{-1}^{1} G(\beta) d\beta \times M_{\text{gas}}|_{G=1}.$$

which are carried out in Appendix 4.9,

$$\begin{aligned}
M_{\text{gas}}^{(\text{rot})} &= 16\pi^3\alpha L_0^3 m \left(\frac{G^2M^2m^3}{2E_0L_0^2}\right)^{k-\frac{3}{2}} \frac{\Gamma(l+1)\Gamma(2k-l-6)}{\Gamma(2k-3)} \\
&\quad\times \frac{{}_2F_1\left(-(l+2), 2k-l-6, 2k-3, -\tanh^2\chi\right)}{(\cosh\chi)^{4k-2l-12}}, \qquad (4.4.39)\\
E_{\text{gas}}^{(\text{rot})} &= -16\pi^3\alpha L_0^3 E_0 \left(\frac{G^2M^2m^3}{2E_0L_0^2}\right)^{k-\frac{1}{2}} \frac{\Gamma(l+1)\Gamma(2k-l-4)}{\Gamma(2k-1)} \\
&\quad\times \frac{{}_2F_1\left(-(l+2), 2k-l-4, 2k-1, -\tanh^2\chi\right)}{(\cosh\chi)^{4k-2l-8}}, \qquad (4.4.40)\\
\mathbf{J}_{\text{gas}}^{(\text{rot})} &= L_0\frac{M_{\text{gas}}^{(\text{rot})}}{m}\left[1+\frac{l+1}{2k-l-7}\cosh^2\chi\right. \\
&\quad\left.\times\frac{{}_2F_1\left(-(l+3), 2k-l-7, 2k-3, -\tanh^2\chi\right)}{{}_2F_1\left(-(l+2), 2k-l-6, 2k-3, -\tanh^2\chi\right)}\right]\mathbf{e}_z, \qquad (4.4.41)
\end{aligned}$$

where the hyperbolic angle χ is defined by

$$\chi = \frac{1}{2}\sinh^{-1}\left(2\frac{\sqrt{GMm^2b}}{L_0}\right). \qquad (4.4.42)$$

Using the symmetries of the DF with respect to L_z, the corresponding quantities for the even ansatz (4.4.10) yield

$$M_{\text{gas}}^{(\text{even})} = M_{\text{gas}}^{(\text{rot})}, \qquad E_{\text{gas}}^{(\text{even})} = E_{\text{gas}}^{(\text{rot})}, \qquad \mathbf{J}_{\text{gas}}^{(\text{even})} = 0. \qquad (4.4.43)$$

Note that in the Kepler limit $b \to 0$ one has $\chi \to 0$ and the last factors on the right-hand sides of Eqs. (4.4.39) and (4.4.40) converge to one, while $\mathbf{J}_{\text{gas}}^{(\text{rot})}/M_{\text{gas}}^{(\text{rot})} \to (L_0/m)(2k-6)/(2k-l-7)$. Another interesting limit consists in taking $L_0 \to 0$ and $l = 0$, in which case one obtains[6]

$$\begin{aligned}
\lim_{L_0\to 0} M_{\text{gas}}^{(\text{rot})}\Big|_{l=0} &= \frac{8\pi^3\alpha m(2mb^2E_0)^{\frac{3}{2}}}{(k-1)(k-2)(k-3)}\left(\frac{GMm}{2bE_0}\right)^k, \qquad (4.4.44)\\
\lim_{L_0\to 0} E_{\text{gas}}^{(\text{rot})}\Big|_{l=0} &= -\frac{8\pi^3\alpha E_0(2mb^2E_0)^{\frac{3}{2}}}{k(k-1)(k-2)}\left(\frac{GMm}{2bE_0}\right)^{k+1}, \qquad (4.4.45)\\
\lim_{L_0\to 0} \mathbf{J}_{\text{gas}}^{(\text{rot})}\Big|_{l=0} &= \frac{128\pi^3\alpha(2mb^2E_0)^2}{(2k-1)(2k-3)(2k-5)(2k-7)}\left(\frac{GMm}{2bE_0}\right)^{k+\frac{1}{2}}\mathbf{e}_z, \qquad (4.4.46)
\end{aligned}$$

where the corresponding expressions for the even ansatz can be obtained from the general relations in Eq. (4.4.43). In the even case, one can check that these expressions

[6]For this, the identities [92, Eq. 15.4.26] ${}_2F_1(a,b;c;-1) = {}_2F_1(b,a;c;-1) = \Gamma(1+a-b)\Gamma(1+a/2)/(\Gamma(1+a)\Gamma(1-b+a/2))$ are useful.

give the total mass and energy of the spherical polytropes discussed in subsection 4.3.2. Note that the Kepler limit $b \to 0$ of the expressions in Eqs. (4.4.44,4.4.45,4.4.46) are ill-defined. This is due to the fact that the Kepler potential diverges at the center, implying that particles with low angular momentum can have arbitrarily low energy.
The qualitative behavior of M_{gas}, E_{gas} and $\mathbf{J}_{\text{gas}}$ as functions of the parameters λ_0, κ, k, l will be analyzed in more detail in the next section.

4.5. Properties of the macroscopic observables

In this section we analyze the behavior of the macroscopic observables derived in the previous section. For definiteness, we focus on the particle density, the mean velocity, the kinetic temperature, and the anisotropy parameter (defined below), assuming that the central gravitational potential is given by Hénon's isochrone potential, see Eq. (4.4.36). In general, these quantities depend on the parameters $\alpha > 0$, $E_0 > 0$, $L_0 > 0$, $l \geq 0$, $k > 7/2 + l/2$ and $M > 0$, $b \geq 0$ appearing in the DF and Hénon's potential. In the following, we compare configurations of equal total mass, which fixes the parameter α (see Eq. (4.4.39)), and we introduce the length scale

$$\Lambda := \frac{GMm}{E_0}, \tag{4.5.1}$$

in order to express our results in terms of the dimensionless quantities:

$$\xi := \frac{r}{\Lambda}, \qquad \kappa := \frac{b}{\Lambda}, \qquad \lambda := \frac{L}{\sqrt{m\Lambda^2 E_0}}, \qquad \lambda_0 := \frac{L_0}{\sqrt{m\Lambda^2 E_0}}, \tag{4.5.2}$$

which leaves the following dimensionless parameters: k, l, λ_0 and κ.

4.5.1. Normalized particle density and morphology

We start with the analysis of the dimensionless particle density per unit total mass, given by the function (see Eqs. (4.4.19, 4.4.39))

$$\begin{aligned}\bar{n}(\xi,\vartheta) &:= \Lambda^3 n^{(\text{rot})} \frac{m}{M_{\text{gas}}^{(\text{rot})}} \\ &= \frac{2^{k-2}}{\pi^2} \frac{\Gamma(2k-3)}{\Gamma(l+2)\Gamma(2k-l-6)} \\ &\quad \times \frac{\eta^l \psi^k J_{k-\frac{3}{2},l}(\eta) \lambda_0^{2k-6} (\cosh^2\chi)^{2k-l-6}}{{}_2F_1\left(-(l+2), 2k-l-6, 2k-3, -\tanh^2\chi\right)},\end{aligned} \tag{4.5.3}$$

where in terms of the dimensionless quantities defined in Eq. (4.5.2),

$$\chi = \frac{1}{2}\sinh^{-1}\left(\frac{2\sqrt{\kappa}}{\lambda_0}\right), \qquad \eta = \frac{\xi \sin\vartheta}{\lambda_0}\sqrt{2\psi}, \qquad \psi = \frac{1}{\kappa + \sqrt{\kappa^2 + \xi^2}}. \tag{4.5.4}$$

Note that ψ is a function of the dimensionless radius ξ, η a function of (ξ, ϑ), while χ is constant. We show in figures **4-1** and **4-2** the behavior of the normalized particle density (4.5.3) in the equatorial plane ($\vartheta = \pi/2$) for different values of k and l and fixed values of $\lambda_0 = \kappa = 1$. First, we observe from figure **4-1** that, for fixed $l = 1$, the configurations become more concentrated near their inner edge (determined by $\eta = 1$ corresponding to $\xi = \sqrt{5}/2$ when $\vartheta = \pi/2$) and exhibit a faster asymptotic decay as k increases. In this sense, they become more compact with growing k. Next, from the plots in figure **4-2**, we observe that, for fixed $k = 6$, the bulk of the particles moves away from the central region as l increases. This is, of course, expected, since l controls the exponent of the L_z-dependency of the DF, implying that the higher the value of l, the more populated are the configurations with high angular momentum.

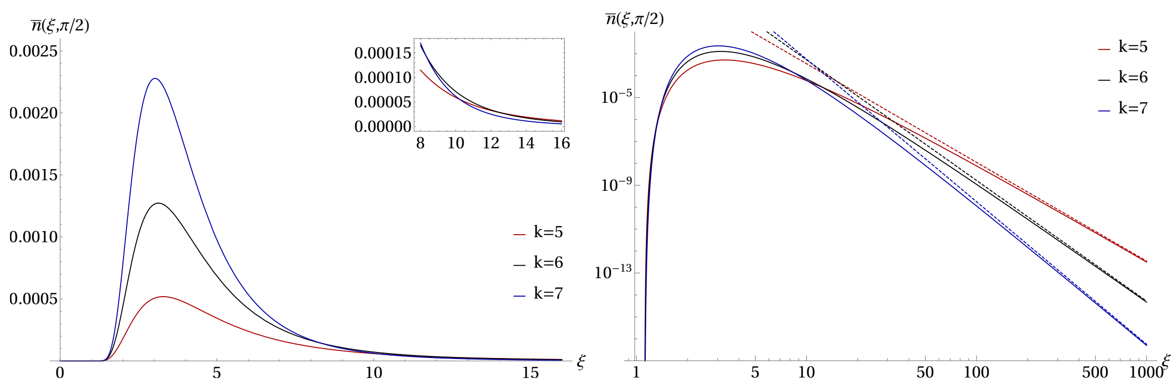

Figure 4-1: Normalized particle density $\bar{n}$ vs radius on the equatorial plane for $l = 1$ and $k = 5, 6, 7$. The remaining parameters have been chosen to be $\kappa = 1$ and $\lambda_0 = 1$. The left panel is a linear plot showing the range $0 \leq \xi \leq 16$, with the inset zooming into the region $8 \leq \xi \leq 16$ which makes visible the intersection between the different curves. This intersection is expected, since the higher concentration of particles near the central object has to be compensated by a faster decay in the density due to the fact that we compare configurations with equal masses. The right panel shows the same quantity in a log-log plot, making visible the different inverse power law decay behavior at large ξ. The dashed lines correspond to the inverse power law behavior found in Eq. (4.5.5).

As is visible from the plots in the right panels of figures **4-1** and **4-2**, the normalized density $\bar{n}$ exhibits an inverse power-law behavior for large values of ξ. Using Eqs. (4.5.3,4.5.4) one finds, for large values of ξ:

$$\bar{n} \sim \sigma \frac{\sin^l \vartheta}{\xi^{k-\frac{l}{2}}}, \tag{4.5.5}$$

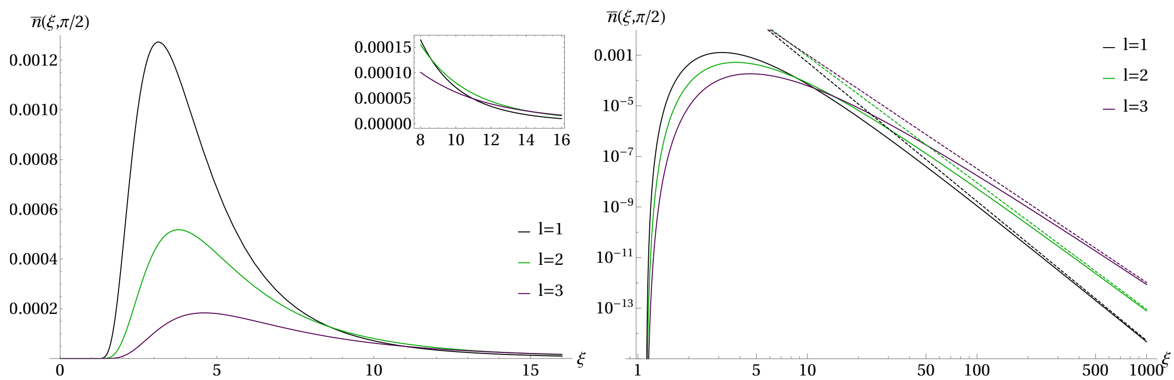

Figure 4-2: Same as in previous plot, except that here $k = 6$ and $l = 1, 2, 3$. Note that the maximum of $\bar{n}$ moves to the right as l increases.

where the constant σ is given by

$$\begin{aligned}\sigma &= \frac{(\sqrt{2})^{2k+l-6}}{\pi^2}\frac{\Gamma(2k-3)\Gamma(k-1/2)}{\Gamma(2k-l-6)\Gamma(k+l+3/2)} \\ &\times\frac{{}_2F_1\left(-(k-1/2), l+1, k+l+3/2, -1\right)}{{}_2F_1\left(-(l+2), 2k-l-6, 2k-3, -\tanh^2\chi\right)}\left(\lambda_0\cosh^2\chi\right)^{2k-l-6} \end{aligned} \tag{4.5.6}$$

For comparison, the asymptotic behavior (4.5.5) is also shown in the right panels of figures **4-1** and **4-2**.

In order to analyze the dependency of the particle density with respect to the polar angle, we show in figure **4-3** contour plots of $\bar{n}$ in the xz-plane for the parameter values $k = 5$, $l = 1, 2, 3$, and $\lambda_0 = \kappa = 1$. As is visible from these plots, the particle density is everywhere regular and the configurations become slimmer as l increases, which is compatible with the polar dependency of the asymptotic behavior (4.5.5).

4.5.2. Mean particle velocity

Next, we analyze the behavior of the mean particle velocity for rotating configurations, see Eq. (4.4.21) (recall that this velocity vanishes for the even ansatz). For definiteness, we restrict ourselves to the equatorial plane. In figure **4-4** we show the magnitude of the velocity as a function of the dimensionless radius ξ for different values of k and l and fixed $\kappa = \lambda_0 = 1$. We observe that this magnitude has a maximum at the inner edge ($\xi = \sqrt{5}/2$) and decays monotonically as ξ increases. At the inner edge one finds

$$\lim_{\eta\to 1^+}\sqrt{\frac{m}{E_0}}|\mathbf{u}^{(\mathrm{rot})}(\mathbf{x})| = \left.\sqrt{2\psi}\right|_{\xi=\sqrt{5}/2}, \tag{4.5.7}$$

which is independent of k and l. For large ξ one finds the following behavior:

$$\sqrt{\frac{m}{E_0}}|\mathbf{u}^{(\mathrm{rot})}| \sim \frac{\tau}{\sqrt{\xi}}, \qquad \tau = \sqrt{2}\frac{\Gamma\left(\frac{l}{2}+1\right)\Gamma\left(k+\frac{l}{2}+1\right)}{\Gamma\left(\frac{l}{2}+\frac{1}{2}\right)\Gamma\left(k+\frac{l}{2}+\frac{3}{2}\right)}, \tag{4.5.8}$$

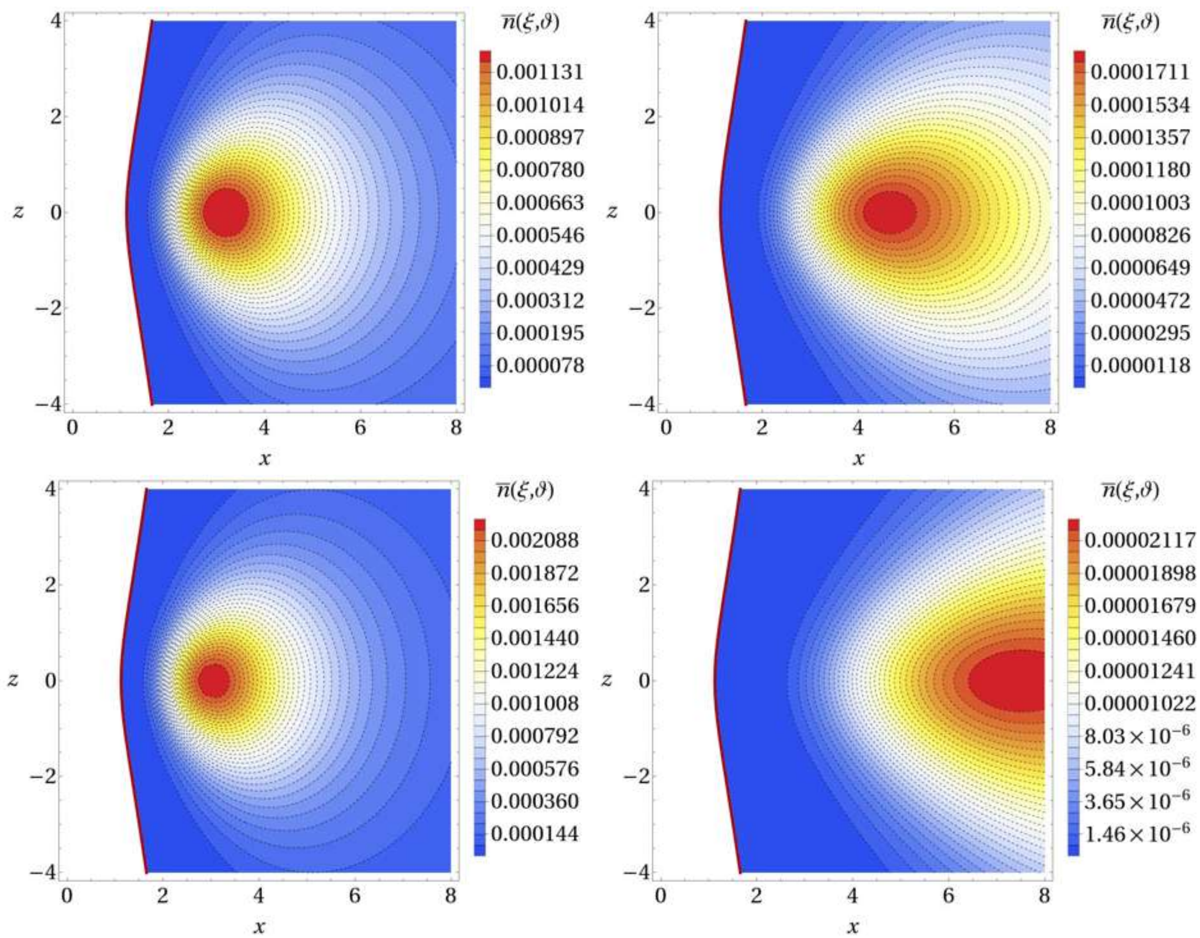

Figure 4-3: Contour plot for the normalized particle density $\bar{n}$ in the xz-plane for $\lambda_0 = \kappa = 1$ and different values of k and l. Top left panel: $(k, l) = (6, 1)$. Top right panel: $(k, l) = (6, 3)$. Bottom left panel: $(k, l) = (7, 1)$. Bottom right panel: $(k, l) = (7, 6)$. Note that as the value of l increases the disk becomes slimmer and the maximum of the density moves away from the central object, as expected. The thick red line indicates the location of the inner boundary of the configuration which is determined by $\eta \geq 1$.

which is (up to the factor τ which is of order unity) the expression for the tangential velocity for circular orbits in the Kepler potential. Note that τ is independent of the polar angle ϑ and the parameters λ_0 and κ.

4.5.3. Kinetic temperature

Next, we analyze the behavior of the kinetic temperature, which is given by the ratio between the pressure (4.4.29) and the particle density (4.4.19). For the ansätze (4.4.11,4.4.10)

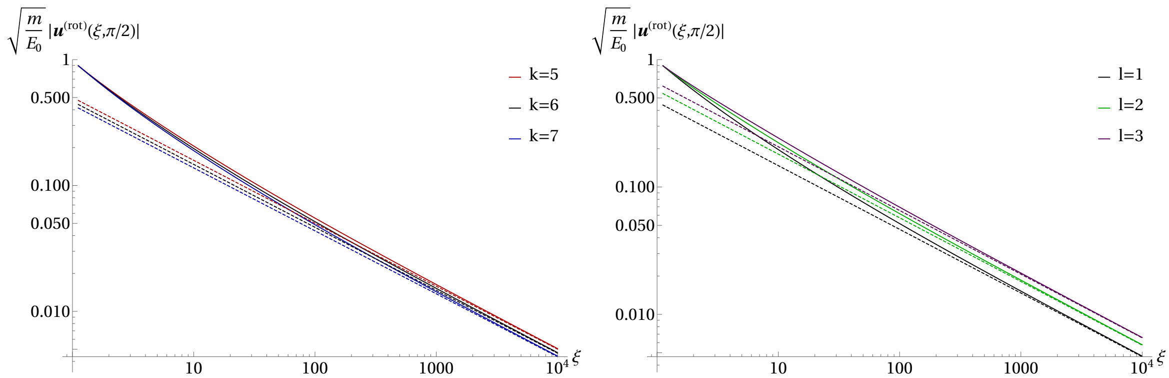

Figure 4-4: Log-log plot for the magnitude of the mean velocity vs radius for some values of l and k and fixed parameter values $\lambda_0 = \kappa = 1$. From the left panel we see that for $l = 1$ this magnitude decreases as k increases, while the right panel shows that, as expected, this magnitude increases as l increases. The dashed lines show the asymptotic behavior predicted by Eq. (4.5.8).

this yields

$$T^{(\mathrm{rot})}(\mathbf{x}) = \frac{2}{3}\frac{E_0\psi}{k_B}\left[1 - \frac{J_{k-\frac{1}{2},l}(\eta)}{J_{k-\frac{3}{2},l}(\eta)} - \left(\frac{l+1}{l+2}\frac{J_{k-\frac{3}{2},l+1}(\eta)}{J_{k-\frac{3}{2},l}(\eta)} + \frac{1}{\eta}\right)^2\right], \quad (4.5.9)$$

$$T^{(\mathrm{even})}(\mathbf{x}) = \frac{2}{3}\frac{E_0\psi}{k_B}\left[1 - \frac{J_{k-\frac{1}{2},l}(\eta)}{J_{k-\frac{3}{2},l}(\eta)}\right]. \quad (4.5.10)$$

In figures **4-5** and **4-6** we show the temperature profiles on the equatorial plane for these two models. As before, we fix $\lambda_0 = \kappa = 1$ and vary the parameters k and l. The asymptotic values in the limits $\eta \to 1$ and $\eta \to \infty$ for the kinetic temperature in both models are given by

$$\lim_{\eta\to 1^+} T^{(\mathrm{rot})} = 0,$$

$$\lim_{\eta\to\infty} T^{(\mathrm{rot})} = \frac{2}{3}\frac{E_0\psi}{k_B}\left\{\frac{l+3}{2k+l+2} - \left[\frac{\Gamma\left(\frac{l}{2}+1\right)\Gamma\left(k+\frac{l}{2}+1\right)}{\Gamma\left(\frac{l}{2}+\frac{1}{2}\right)\Gamma\left(k+\frac{l}{2}+\frac{3}{2}\right)}\right]^2\right\}, \quad (4.5.11)$$

$$\lim_{\eta\to 1^+} T^{(\mathrm{even})} = \frac{2}{3}\frac{E_0\psi}{k_B}, \qquad \lim_{\eta\to\infty} T^{(\mathrm{even})} = \frac{2}{3}\frac{E_0\psi}{k_B}\frac{l+3}{2k+l+2}. \quad (4.5.12)$$

From the plots and these expressions, we observe that the temperature profile for the rotating model is continuous, $T^{(\mathrm{rot})}$ being zero at the inner boundary of the disk. The temperature has a maximum inside the disk configuration, as is visible from figure **4-5**, and decays as $1/\xi$ for large radii. In contrast to this, the temperature profile for the even model in the equatorial plane is monotonously decaying for all values of ξ, the maximum temperature being located at the inner edge of the disk. As is also visible from the plots, the temperature decreases as k increases, which can be understood by remarking that the lower energy levels are more populated when k is high.

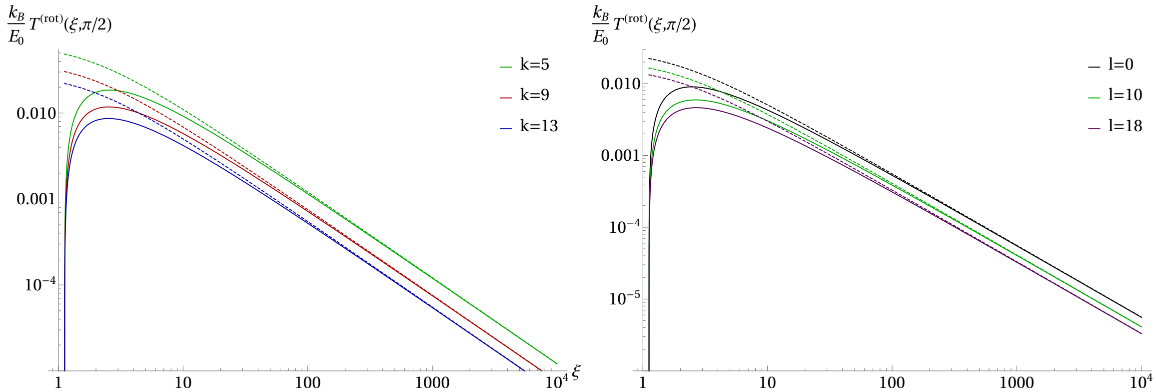

Figure 4-5: Log-log plot for the kinetic temperature of the rotating model (see Eq. (4.5.9)) vs radius in the equatorial plane for $l = 1$, $k = 5, 9, 13$ (left panel) and $k = 13$ and $l = 0, 10, 18$ (right panel) and $\lambda_0 = \kappa = 1$. The corresponding asymptotic limits from Eq. (4.5.11) are shown in dashed lines.

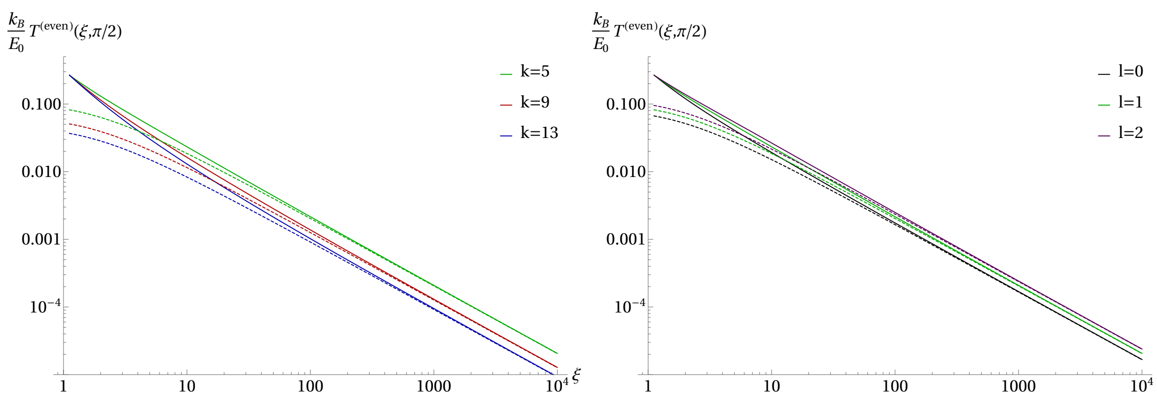

Figure 4-6: Same as previous plot for the even model (see Eq. (4.5.10))

4.5.4. Pressure anisotropy

In this section we analyze the pressure anisotropy of our configurations. To this purpose, recall that the principle pressures $P_{\hat{r}}$, $P_{\hat{\vartheta}}$ and $P_{\hat{\varphi}}$ defined in Eqs. (4.4.25,4.4.26,4.4.27) satisfy $P_{\hat{r}} = P_{\hat{\vartheta}}$. Therefore, in analogy to what is being defined in galactic dynamics [35, 96] we introduce the anisotropy parameter

$$\beta := 1 - \frac{P_{\hat{\varphi}}}{P_{\hat{r}}}, \tag{4.5.13}$$

which is positive for a configuration in which the radial pressure dominates the azimuthal one and negative otherwise, while $\beta = 0$ for an isotropic configuration. For the rotating configurations (4.4.11) one obtains

$$\beta^{(\mathrm{rot})}(\mathbf{x}) = 1 - \left[\frac{l+1}{l+3}J_{k-\frac{3}{2},l+2}(\eta) - \left(\frac{l+1}{l+2}\right)^2 \frac{J_{k-\frac{3}{2},l+1}(\eta)^2}{J_{k-\frac{3}{2},l}(\eta)}\right] \times \left[\frac{1}{\eta}\frac{J_{k-\frac{3}{2},l+1}(\eta)}{l+2} + \frac{J_{k-\frac{3}{2},l+2}(\eta)}{l+3}\right]^{-1}, \tag{4.5.14}$$

while for the even model (4.4.10) the anisotropy parameter yields

$$\beta^{(\mathrm{even})}(\mathbf{x}) = 1 - \left[\frac{1}{\eta^2}J_{k-\frac{3}{2},l}(\eta) + \frac{2}{\eta}\frac{l+1}{l+2}J_{k-\frac{3}{2},l+1}(\eta) + \frac{l+1}{l+3}J_{k-\frac{3}{2},l+2}(\eta)\right] \times \left[\frac{1}{\eta}\frac{J_{k-\frac{3}{2},l+1}(\eta)}{l+2} + \frac{J_{k-\frac{3}{2},l+2}(\eta)}{l+3}\right]^{-1}. \tag{4.5.15}$$

Note that these expressions only depend on (ξ, ϑ) through the parameter η. The behavior of β on the equatorial plane is shown in figures **4-7** and **4-8** for both models for different values of k and l and fixed $\lambda_0 = \kappa = 1$.

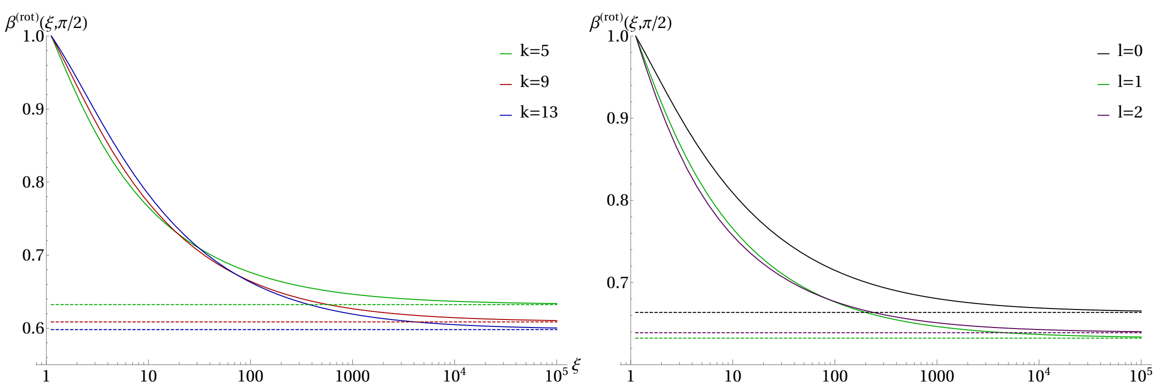

Figure 4-7: Anisotropy parameter β vs ξ for different values of k and l and fixed $\lambda_0 = \kappa = 1$. Note that we use a logarithmic scale in ξ. The dashed lines refer to the asymptotic limits computed in Eq. (4.5.16). In the left panel $l = 1$ and $k = 5, 9, 13$ while in the right panel $k = 5$ is fixed and l varies over $0, 1, 2$. In all cases, we observe that $\beta \to 1$ when ξ approaches the inner edge's radius, while for large ξ, β decreases and approaches a constant positive value, indicating that the radial pressure always dominates the azimuthal one.

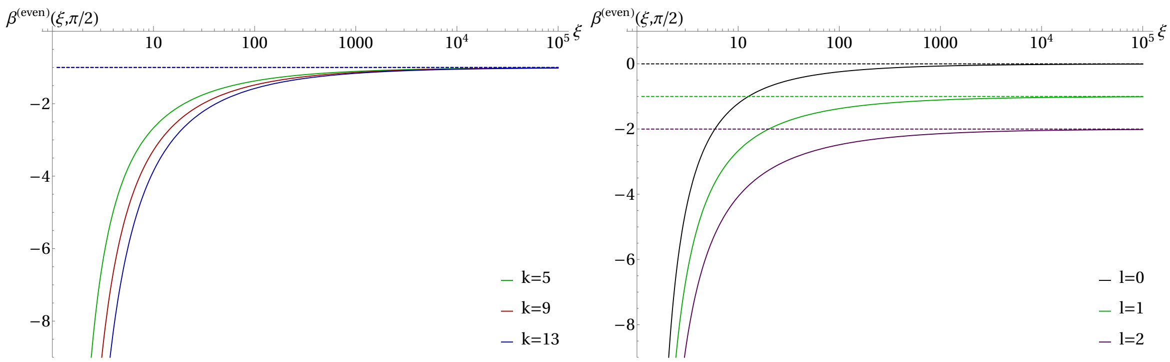

Figure 4-8: Same as previous plot for the even model. In this case, the anisotropy parameter β diverges to $-\infty$ as ξ approaches the inner edge's radius, while in the limit $\xi \to \infty$, β approaches a negative value, indicating that the azimuthal pressure dominates in this case.

The asymptotic limits of β when $\eta \to 1$ and $\eta \to \infty$ are given by

$$\begin{aligned} \lim_{\eta\to 1^+} \beta^{(\mathrm{rot})} &= 1, \\ \lim_{\eta\to\infty} \beta^{(\mathrm{rot})} &= -l + \frac{2\Gamma\left(k+\frac{l}{2}+1\right)\Gamma\left(k+\frac{l}{2}+2\right)\Gamma\left(\frac{l}{2}+1\right)^2}{\Gamma\left(k+\frac{l}{2}+\frac{3}{2}\right)^2\Gamma\left(\frac{l}{2}+\frac{1}{2}\right)^2}, \end{aligned} \tag{4.5.16}$$

and

$$\lim_{\eta\to 1^+} \beta^{(\mathrm{even})} = -\infty, \qquad \lim_{\eta\to\infty} \beta^{(\mathrm{even})} = -l. \tag{4.5.17}$$

From these plots and expressions, we see that in the rotating case, the anisotropy parameter is always positive, showing that the azimuthal pressure is always less than the radial pressure, the difference being largest at the inner edge of the disk. This fact can be partially understood by noticing that in this case, all particles orbit in the same direction, leading to a small azimuthal velocity dispersion. However, the dependency of $\beta^{(\mathrm{rot})}$ on k and l seems to be intricate.

In contrast to this, the anisotropy parameter for the even configurations is always negative, meaning that the azimuthal pressure dominates in this case (which is expected since each particle has a pair rotating in the opposite direction). As one approaches the boundary of the disk ($\eta \to 1$), this difference becomes larger and larger such that $\beta^{(\mathrm{even})} \to -\infty$. This is expected, since the boundary of the disk is generated by the turning points of parabolic-type orbits (see the discussion following Eq. (4.4.30)), such that $P_{\hat{r}}^{(\mathrm{even})} \to 0$ as $\eta \to 1$; however $P_{\hat{\varphi}}^{(\mathrm{even})}$ remains positive since these orbits are populated by pairs of particles rotating in the opposite direction. Notice also that as k and l increase, the anisotropy of the even configurations becomes more pronounced.

4.5.5. Total mass, energy and angular momentum

Next, we discuss some qualitative properties of the total mass, energy and angular momentum given by the expressions found in Eqs. (4.4.39,4.4.40,4.4.41). Recall that the total mass and energy of the even model coincide with those of the rotating one, whereas $\mathbf{J}_{\mathrm{gas}}^{(\mathrm{even})} = 0$. Therefore, it is sufficient to focus our attention on the rotating case.
First, we analyze the behavior of the total mass as a function of the cut-off value λ_0 for the angular momentum and the parameter κ in Hénon's potential, fixing the values of k and l. Figure **4-9** shows this behavior for the values $k = 5$ and $l = 0$. As expected,

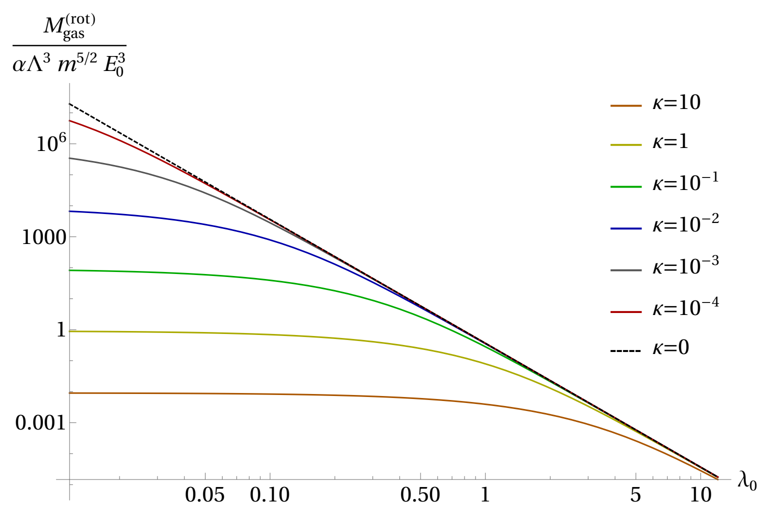

Figure 4-9: Log-log plot for the total mass vs the cut-off value of the azimuthal angular momentum λ_0 for $k = 5$, $l = 0$ and different values of κ.

when κ approaches zero or λ_0 becomes very large, the total mass converges to the Kepler expression with the power-law dependency λ_0^{-4}, see Eq. (4.4.39) with $\chi = 0$ and $k = 5$. When $\lambda_0 \to 0$, one recovers the limit computed in Eq. (4.4.44) corresponding to the spherical polytropes.
Next, in figure **4-10** we show the ratio between the total energy and mass as a function of k and l for fixed values $\kappa = \lambda_0 = 1$. As is visible from this plot, for fixed l this ratio decreases for increasing k. This is expected since the lower energy levels become more populated as k increases. In contrast, the ratio increases when l becomes larger, which is also expected due to the fact that the orbits with larger angular momentum (which have larger energies) become more populated as l increases.
Finally, in figure **4-11** we show the ratio between the total angular momentum and mass as a function of k and l for fixed values $\kappa = \lambda_0 = 1$. As can be seen, this ratio decreases for increasing k and fixed value of l, which is again expected since configurations with high k have most of their particles lying on low-energy orbits for which the maximum angular momentum is low. In contrast, for fixed value of k and increasing l, the ratio increases. Also, note that $|\mathbf{J}_{\mathrm{gas}}^{(\mathrm{rot})}|/M_{\mathrm{gas}}^{(\mathrm{rot})}$ diverges as $k \to (7 + l)/2$ which means that

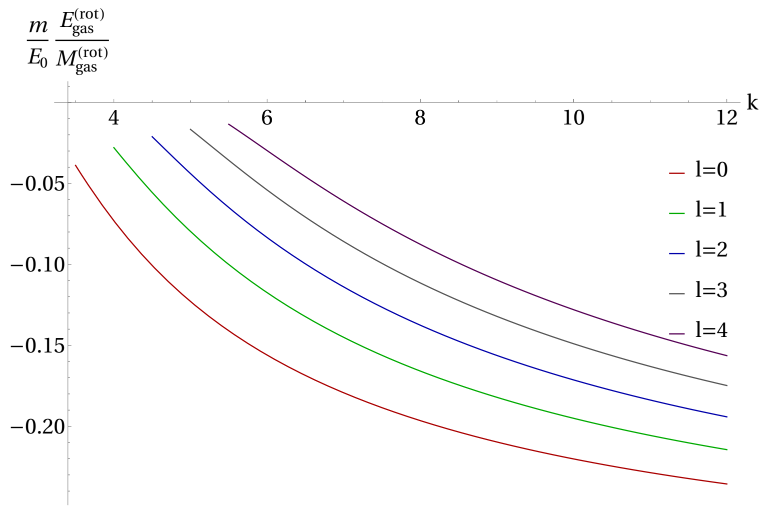

Figure 4-10: Total energy per total mass vs k for $l = 0, 1, 2, 3, 4$ and $\kappa = \lambda_0 = 1$.

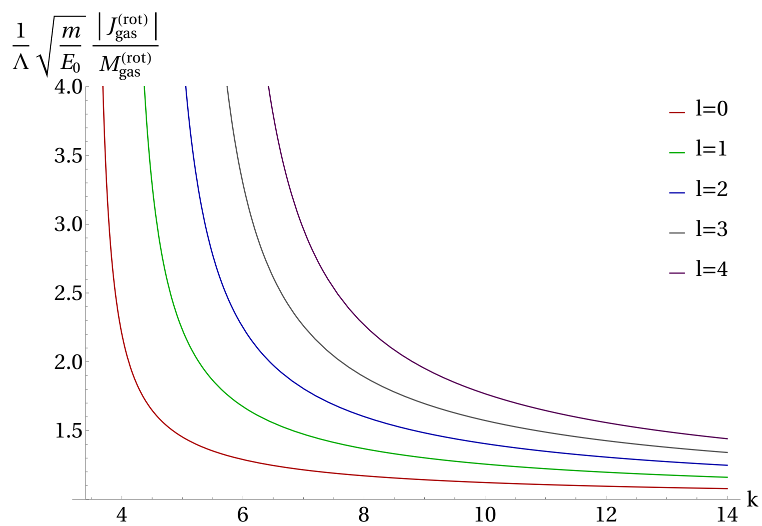

Figure 4-11: Total angular momentum per total mass vs k for different values of $l = 0, 1, 2, 3, 4$ and fixed $\kappa = \lambda_0 = 1$.

the configurations can have arbitrary high angular momentum. This divergence is due to the fact that when $k = (7 + l)/2$, the decay of the solution is not fast enough for the total angular momentum integral (4.4.34) to converge, while $M_{\mathrm{gas}}^{(\mathrm{rot})}$ is still finite.

4.5.6. Comparison with fluid model

We end this section with a comparison between the kinetic configurations based on the (E, L_z)-models and their hydrodynamic analogues whose properties are summarized in Appendix 4.10.

First, we compare the boundary surface of the configurations. As follows from Eq. (4.10.12), in the fluid case the gas is supported in the domain

$$\bar{h}_\infty + \psi(\xi) - \frac{\lambda_0^2}{2\xi^2 \sin^2\vartheta} \geq 0, \tag{4.5.18}$$

where $\bar{h}_\infty$ refers to the asymptotic value of the specific enthalpy (up to a constant factor), ψ to the dimensionless isochrone potential defined in Eq. (4.5.4) and ξ and λ_0 to the dimensionless radius and constant azimuthal angular momentum per unit mass, see Eq. (4.10.9). Interestingly, in the collisionless kinetic case, the condition $\eta \geq 1$ yields precisely the same domain if one sets $\bar{h}_\infty = 0$ and identifies ξ and λ_0 with the corresponding quantities defined in Eq. (4.5.2). This coincidence is due to the fact that as one approaches the boundary surface, the fluid elements' pressure gradient decreases to zero such that in this limit they move as point particles with zero energy and azimuthal angular momentum parameter equal to λ_0, as in the kinetic case. Therefore, taking $\bar{h}_\infty = 0$ for the following,[7] in both cases the minimum dimensionless radius at given ϑ is

$$\xi_{\text{min}}(\vartheta) = \frac{\lambda_0^2}{2\sin^2\vartheta}\sqrt{1 + \frac{4\kappa \sin^2\vartheta}{\lambda_0^2}}. \tag{4.5.19}$$

Whereas the boundary surface does not depend on whether one considers the fluid or the collisionless kinetic case, one clearly expects differences to occur in the interior region since the two matter models are rather different in nature. In the fluid description, the pressure is enforced to be isotropic and it is assumed that the specific azimuthal angular momentum is constant throughout the gas configuration. In contrast, in the kinetic model the gas is collisionless, anisotropic and the azimuthal angular momentum is not constant; rather it is distributed according to the functions given in Eqs. (4.4.10) or (4.4.11). For the following, we focus on the latter distribution for which all particles rotate in the same direction with minimal azimuthal angular momentum λ_0 when performing the comparison with the fluid case, since in the former case the total angular momentum is zero.

To perform the comparison, for definiteness we restrict our attention to the profiles of the mass density and the temperature in the equatorial plane. In the kinetic case these profiles can be read off from the expressions (4.4.19) and (4.5.9) with $\vartheta = \pi/2$. In the fluid case the mass density ρ and temperature can be determined by using Eq. (4.10.12) again and assuming a polytropic equation of state $P = K\rho^\gamma$ with K a constant and $\gamma > 1$ the adiabatic index. Integrating the first law of thermodynamics (with constant entropy) $dh = dP/\rho$ and taking into account the ideal gas equation $P = \rho k_B T/\bar{m}$ with $\bar{m}$ the averaged rest mass per particle, one obtains

$$h = \frac{\gamma}{\gamma-1}K\rho^{\gamma-1} = \frac{\gamma}{\gamma-1}\frac{P}{\rho} = \frac{\gamma}{\gamma-1}\frac{k_B T}{\bar{m}}, \tag{4.5.20}$$

[7] For the behavior of the boundary surface for solutions with $\bar{h}_\infty \neq 0$, see Appendix 4.10.

which allows one to express ρ and T in terms of the specific enthalpy h. Note that taking $\bar{h}_\infty = 0$ as before, it follows from Eqs. (4.5.20,4.10.12) that the enthalpy and temperature decay as ψ for large ξ. To proceed, we need a relation between the adiabatic index γ and the parameters k and l characterizing the kinetic configuration. To this purpose, we note that in the fluid case,

$$\lim_{\xi\to\infty} \frac{k_B T^{(\text{fluid})}(\xi,\vartheta)}{-\bar{m}\Phi(r)} = 1 - \frac{1}{\gamma}, \tag{4.5.21}$$

whereas in the kinetic case one finds from Eq. (4.5.11) that

$$\lim_{\xi\to\infty} \frac{k_B T^{(\text{kinetic})}(\xi,\vartheta)}{-m\Phi(r)} = \frac{2}{3}\left\{\frac{l+3}{2k+l+2} - \left[\frac{\Gamma\left(\frac{l}{2}+1\right)\Gamma\left(k+\frac{l}{2}+1\right)}{\Gamma\left(\frac{l}{2}+\frac{1}{2}\right)\Gamma\left(k+\frac{l}{2}+\frac{3}{2}\right)}\right]^2\right\}. \tag{4.5.22}$$

This motivates the introduction of an effective adiabatic index $\gamma^{(\text{kinetic})}$ depending on (k, l) (but not on κ nor λ_0), which is defined in such a way that the right-hand side of Eq. (4.5.22) is equal to $1 - 1/\gamma^{(\text{kinetic})}$. It follows from this definition that

$$1 < \gamma^{(\text{kinetic})} < \frac{6k+3l+6}{6k+l}. \tag{4.5.23}$$

Some specific values for $\gamma^{(\text{kinetic})}$ are shown in table **4-1**. Note that $\gamma^{(\text{kinetic})} \to 1$ as k tends to infinity and l remains finite, corresponding to the isothermal limit. Furthermore, the condition $k > (7+l)/2$ implies that $\gamma^{(\text{kinetic})} < 3/2$, although the maximum effective adiabatic index found from the table is for $l = 0$ and $k = 4$, for which

$$\gamma^{(\text{kinetic})} = \frac{297675\pi^2}{131072 + 238140\pi^2} \approx 1.1840. \tag{4.5.24}$$

Therefore, for what follows we compare our kinetic gas configurations with a fluid model with adiabatic index $\gamma = \gamma^{(\text{kinetic})} \leq 1.1840$ (note that our prescription excludes the typical values of $4/3$ and $5/3$ describing a monoatomic gas in the ultra and non-relativistic limits, respectively).

In figure **4-12** we show the comparison between the normalized mass densities and temperature profiles for $(k,l) = (4,0)$ and fixed $\lambda_0 = \kappa = 1$. Here, the normalization is performed in such a way that the maxima of the profiles is one. As is visible from these plots, the density distribution is different, the fluid configuration being more compact than the kinetic one (a similar behavior is found for other values of k and l). In contrast, the temperature profiles look very similar to each other. In order to partially quantify this assertion, we show in tables **4-2** and **4-3** the ratios between the radii and the values of the maxima of the temperature profiles for different values of (k,l) and λ_0. We see from these results that the locations of these maxima are very similar in both matter models (within $5\,\%$ relative error), at least for $l = 0$, which is consistent with the right plot in figure **4-12**. For higher values of l, the radius of the temperature maximum in the

Table 4-1: Effective adiabatic index $\gamma^{(\text{kinetic})}$ for different values of k and l (five significant figures are shown).

	$k=4$	$k=5$	$k=6$	$k=7$	$k=10$
$l=0$	1.1840	1.1492	1.1254	1.1082	1.0766
$l=1$		1.1382	1.1181	1.1031	1.0746
$l=2$		1.1267	1.1097	1.0968	1.0714
$l=3$			1.1020	1.0908	1.0682
$l=4$			1.0951	1.0853	1.0651
$l=5$				1.0804	1.0623
$l=6$				1.0760	1.0596
$l=7$					1.0572
$l=8$					1.0549

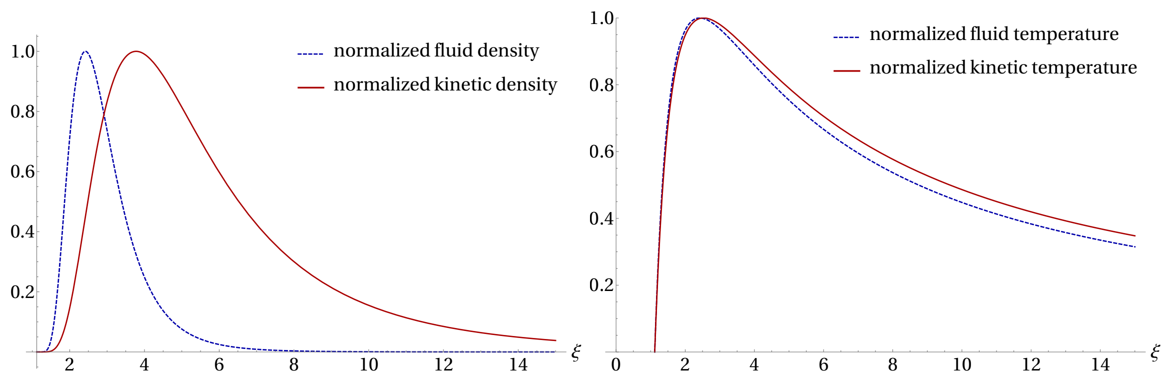

Figure 4-12: Comparison between the normalized densities (left panel) and between the normalized temperatures (right panel) in the equatorial plane for $\kappa = \lambda_0 = 1$ and $(k,l) = (4,0)$ and the corresponding value $\gamma = 1.18397$ for the adiabatic index. In both cases the normalization is chosen such that the maximum is one.

kinetic model tends to increase with respect to the fluid case, while the example shown in table **4-3** indicates that both ratios become independent of λ_0 for large values of λ_0. Finally, we see from these tables that the temperature in the fluid case is somehow larger than in the kinetic description.

4.6. Conclusions

We have provided a complete analytic description for stationary axisymmetric and collisionless kinetic gas clouds consisting of identical massive and neutral particles surrounding a massive central object. Our models are based on the assumptions that the

Table 4-2: Top row: Ratio between the radii corresponding to the maxima of the fluid and kinetic temperature profiles. Bottom row: Ratio between the corresponding maxima of the temperature. Here we choose $\kappa = \lambda_0 = 1$ and different values for k and l and set $\gamma = \gamma^{(\text{kinetic})}$ in the fluid case.

	$l=0$				$l=1$				$l=2$			
	$k=4$	$k=5$	$k=6$	$k=10$	$k=5$	$k=6$	$k=7$	$k=10$	$k=5$	$k=6$	$k=7$	$k=10$
$\frac{mh_0}{E_0}\frac{r_{\max}^{(\text{fluid})}}{r_{\max}^{(\text{kinetic})}}$	0.956	0.960	0.963	0.971	0.941	0.945	0.948	0.955	0.929	0.933	0.937	0.945
$\frac{E_0}{mh_0}\frac{T_{\max}^{(\text{fluid})}}{T_{\max}^{(\text{kinetic})}}$	1.206	1.199	1.195	1.186	1.253	1.245	1.239	1.228	1.286	1.275	1.267	1.251

Table 4-3: Same as in previous table fixing the parameter values $(\kappa, k, l) = (1, 5, 1)$ and varying λ_0. As in the previous table, we set $\gamma = \gamma^{(\text{kinetic})}$ in the fluid case.

	$\lambda_0 = 1$	$\lambda_0 = 4$	$\lambda_0 = 7$	$\lambda_0 = 10$
$\frac{mh_0}{E_0}\frac{r_{\max}^{(\text{fluid})}}{r_{\max}^{(\text{kinetic})}}$	0.941	0.960	0.962	0.962
$\frac{E_0}{mh_0}\frac{T_{\max}^{(\text{fluid})}}{T_{\max}^{(\text{kinetic})}}$	1.253	1.29	1.30	1.30

gravitational field is dominated by the central object, giving rise to a central Newtonian potential, and that the gas particles follow bound orbits in this potential. Although our nonrelativistic description restricts the validity of our configurations to radii much larger than the central object's gravitational radius, it serves as a basis for the corresponding general relativistic model in our accompanying article [49] and will allow us to better understand the effects from the relativistic corrections on the properties of the gas clouds. The one-particle DF in our models is a function depending only on the energy E and the azimuthal angular momentum L_z of the particles through the polytropic ansätze (4.4.9,4.3.14,4.4.10,4.4.11) describing both rotating and nonrotating stationary and axisymmetric configurations. In the former case, all particles have positive values of L_z larger than a cut-off value L_0, giving rise to a net angular momentum while in the latter case the DF is an even function of L_z. By choosing the polytropic index k sufficiently large, the resulting configurations have finite total mass, energy and angular momentum, although they have infinite extend. (Finite volume configurations could easily be considered as well by introducing a cut-off in the energy.)

We have computed the most relevant macroscopic observables associated with the DF, including the particle and energy densities, mean particle velocity, pressure tensor, and the kinetic temperature. Interestingly, these quantities can be expressed explicitly in terms of the Gamma function and Gauss' hypergeometric function for any central potential. Using action-angle variables we have been able to reduce the expressions for the total mass, energy and angular momentum to a triple integral which involves the period function $T_r(E, L)$ describing the period of the radial motion for an orbit with energy E and total angular momentum L. For the particular class of Hénon's isochrone potential (which is characterized by a parameter b whose limits $b \to 0$ and $b \to \infty$ correspond to Kepler's and the spherical harmonic potential, respectively) this period function is independent of L and given by exactly the same expression as in the Kepler case, and for this class the total quantities can be computed analytically.

Based on our analytic expressions, we have provided a detailed analysis for the behavior of the macroscopic quantities, including their dependence on the parameters k, l, L_0, b of the model and their asymptotic decay for large radii r. In particular, we have analyzed the morphology of our configurations and shown that both slim and thick toroidal-type configurations can be constructed. Further, we have analyzed the temperature profile in the equatorial plane and shown that it decays as $1/r$ for large values of r. For the rotating model, the temperature at the inner edge is zero, has a maximum at some radius and then decays while for the even models the temperature at the inner edge is positive and decays monotonically. Next, we have analyzed the pressure anisotropy. In all our models, the principal pressures in the radial and polar directions are always equal to each other (a property that does not necessarily hold in the relativistic case [49]), while the principal pressure in the azimuthal direction can be quite different from the radial and polar ones, as we have shown.

Finally, we have compared our kinetic configurations to analogous fluid configurations with fixed specific angular momentum ℓ_0 which we briefly reviewed in Appendix 4.10. This comparison has led to the following discoveries: (i) By suitably identifying the parameters L_0/m and ℓ_0 we obtain configurations with exactly the same boundary surface in both models. (ii) With this identification, the fluid configurations are slightly more compact. More precisely, the radius at which both the density and temperature have their maximum value in the fluid configurations is smaller than the corresponding radii of the kinetic configurations,[8] see table **4-2** for a few representative examples. (iii) By matching the asymptotic behavior of the temperature profile, one can introduce an effective adiabatic index $\gamma^{(\text{kinetic})}$ in the kinetic case, which, in our models has a maximum value of about 1.1840. This allows one to compare the density and temperature profiles of the fluid configurations (which depend on the adiabatic index γ) to those of the kinetic configurations by setting $\gamma = \gamma^{(\text{kinetic})}$. This comparison reveals that while the fluid configurations are more compact, the normalized temperature profile is very similar in both cases, see figure **4-12**. Nevertheless, the fluid configurations are slightly hotter than the kinetic ones, as can be seen from tables **4-2** and **4-3**. The fact that the behavior of the temperature is at least qualitatively similar in both models is surprising, since in the fluid case one assumes local thermodynamic equilibrium, while in our kinetic model the gas is collisionless and the temperature cannot be associated with a thermal state, as has been exemplified towards the end of section 4.3.2.

The fully relativistic generalization of our models, for which the central object is a black hole, is under investigation. In a first step towards this goal we have restricted this generalization to a non-rotating (Schwarzschild) black hole, see [49] and [48] for a related model based on a slightly different ansatz for the DF. Another interesting generalization of the models discussed in the present article is to study the effects of binary collisions between the gas particles or to include a magnetic field and study its effect on a gas of charged particles.

4.7. Appendix A: Integrals over angular momentum and energy

In this appendix we list a few integrals which are useful when computing the observables in our models. They arise in subsection 4.4.2 when performing the explicit integrals over the total and azimuthal angular momenta and over the energy. For notational simplicity we use the short-hand notations $L_1 := |L_z|\sin^{-1}\vartheta$ and $L_2 := L_{\text{max}}(E, r)$ and $L_3 := L_2 \sin\vartheta$. Note that in our integrals, $L_1 \leq L_2$.

[8] Unlike the fluid configurations, the radii of maximum density and temperature do not coincide in the kinetic configurations. This is probably due to the pressure anisotropy.

First, by means of the variable substitution $u = \sqrt{L^2 - L_1^2}$ one easily finds

$$\int_{L_1}^{L_2} \frac{LdL}{\sqrt{L^2 - L_1^2}\sqrt{L_2^2 - L^2}} = \frac{\pi}{2}, \tag{4.7.1}$$

$$\int_{L_1}^{L_2} \frac{\sqrt{L_2^2 - L^2}}{\sqrt{L^2 - L_1^2}} LdL = \int_{L_1}^{L_2} \frac{\sqrt{L^2 - L_1^2}}{\sqrt{L_2^2 - L^2}} LdL = \frac{\pi}{4}\left(L_2^2 - L_1^2\right). \tag{4.7.2}$$

Next, the integrals over the azimuthal angular momentum encountered in subsection 4.4.2 have the form

$$\int_0^{L_3} \left(\frac{L_z}{L_0} - 1\right)_+^l dL_z = \frac{L_0}{l+1}\left(\frac{L_3}{L_0} - 1\right)_+^{l+1}, \tag{4.7.3}$$

$$\int_0^{L_3} \left(\frac{L_z}{L_0} - 1\right)_+^l L_z dL_z = \frac{L_0^2}{l+1}\left(\frac{L_3}{L_0} - 1\right)_+^{l+1} + \frac{L_0^2}{l+2}\left(\frac{L_3}{L_0} - 1\right)_+^{l+2}, \tag{4.7.4}$$

$$\begin{aligned}\int_0^{L_3} \left(\frac{L_z}{L_0} - 1\right)_+^l L_z^2 dL_z &= \frac{L_0^3}{l+1}\left(\frac{L_3}{L_0} - 1\right)_+^{l+1} + \frac{2L_0^3}{l+2}\left(\frac{L_3}{L_0} - 1\right)_+^{l+2} \\ &\quad + \frac{L_0^3}{l+3}\left(\frac{L_3}{L_0} - 1\right)_+^{l+3}.\end{aligned} \tag{4.7.5}$$

Finally, the energy integrals found in subsection 4.4.2 have the form

$$\begin{aligned}&\int_{m\Phi(r)}^{0} \left(-\frac{E}{E_0}\right)^s \left(\frac{R}{L_0}\sqrt{2m[E - m\Phi(r)]} - 1\right)_+^{l+1} dE \\ &= \frac{L_0^2}{mR^2}\left[\frac{L_0^2}{2mR^2E_0}\right]^s \int_1^{\eta} \left(\eta^2 - \xi^2\right)^{\alpha} (\xi - 1)_+^{l+1} \xi d\xi \\ &= 2E_0 \eta^{l+1} \psi(r)^{s+1} J_{s,l}(\eta),\end{aligned} \tag{4.7.6}$$

where we have used the variable substitution $\xi := R\sqrt{2m[E - m\Phi(r)]}/L_0$ and recalled the definitions of the functions $\eta = R\sqrt{-2m^2\Phi(r)}/L_0$, $\psi(r) = -m\Phi(r)/E_0$ and $J_{s,l}(\eta)$ defined in Eqs. (4.4.18,4.3.20,4.4.22), respectively.

4.8. Appendix B: Properties of the effective potential belonging to the isochrone model

The effective potential (4.3.1) associated with Hénon's isochrone model in Eq. (4.4.36) is

$$V_L(r) = -\frac{GMm}{b + \sqrt{b^2 + r^2}} + \frac{L^2}{2mr^2}, \qquad r > 0, \tag{4.8.1}$$

with the parameter $b \geq 0$ having units of length. The equilibrium points are obtained by analyzing the critical points of V_L which are determined by the equation

$$0 = -\frac{d}{dr} V_L(r) = -\frac{GMmr}{\sqrt{b^2+r^2}\left(b+\sqrt{b^2+r^2}\right)^2} + \frac{L^2}{mr^3}. \tag{4.8.2}$$

There is a unique critical point describing a global minimum of V_L which is located at $r = r_0(L)$ with

$$\begin{aligned} r_0^2(L) &= \left(\frac{L^2}{4GMm^2}\right)^2 \left(1+\sqrt{1+\frac{4bGMm^2}{L^2}}\right)^4 - b^2 \\ &= \left(\frac{L^2}{2GMm^2}\right)^2 \sqrt{1+\frac{4bGMm^2}{L^2}} \left(1+\sqrt{1+\frac{4bGMm^2}{L^2}}\right)^2. \end{aligned} \tag{4.8.3}$$

The corresponding minimal energy is

$$E_0(L) = V_L(r_0) = -\frac{2(GM)^2 m^3}{L^2\left(1+\sqrt{1+\frac{4bGMm^2}{L^2}}\right)^2}. \tag{4.8.4}$$

The condition for the upper bound of the total angular momentum $L_{\text{ub}}(E)$ is obtained from this by setting $E = E_0(L)$, which yields

$$L_{\text{ub}}(E) = \sqrt{\frac{m}{2}}\left(\frac{GMm}{\sqrt{-E}} - 2b\sqrt{-E}\right). \tag{4.8.5}$$

Using the dimensionless quantities defined in Eqs. (4.5.1, 4.5.2), the dimensionless effective potential $U_\lambda(\xi) = V_L(r)/E_0$ reads

$$U_\lambda(\xi) = -\frac{1}{\kappa+\sqrt{\kappa^2+\xi^2}} + \frac{\lambda^2}{2\xi^2}, \qquad \xi > 0, \tag{4.8.6}$$

and for illustrative purposes its behavior is shown in figure **4-13**.

4.9. Appendix C: Total mass, energy and angular momentum

In this appendix we provide details for the computation of the integrals determining the total mass, energy and angular momentum of the gas. These integrals have the following form (cf. Eqs. (4.4.33,4.4.35)):

$$I_{M,E,J_z} := (2\pi)^2 \int\limits_{E_{\min}(0)}^{0} dE \int\limits_{0}^{L_{\text{ub}}(E)} dL \int\limits_{-L}^{+L} dL_z T_r(E,L) F(E,L,L_z) W_{M,E,J_z}, \tag{4.9.1}$$

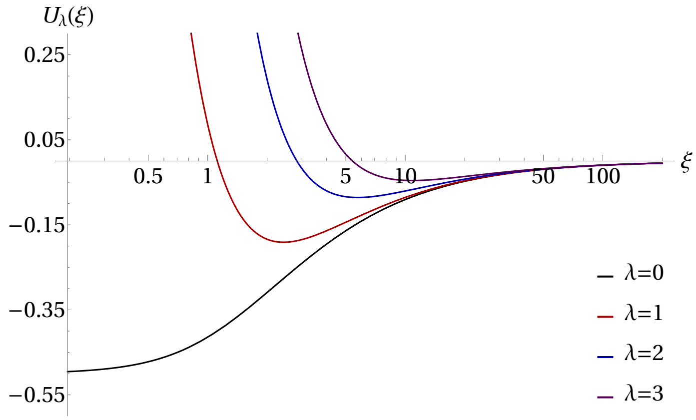

Figure 4-13: Behavior of the dimensionless effective potential $U_\lambda(\xi)$ for the isochrone model for different values of the parameter λ and setting $\kappa = 1$. The black line corresponding to $\lambda = 0$ shows the profile of the isochrone potential itself.

where the indices M, E, J_z refer, respectively, to the total mass M_{gas}, energy E_{gas} and the z-component of the angular momentum $\mathbf{J}_{\text{gas}} \cdot \mathbf{e}_z$ and correspondingly, $W_M = m$, $W_E = E$ and $W_{J_z} = L_z$. For the example discussed in section 4.4.3 the period T_r and the DF are independent of L. Using the explicit expressions for T_r, E_{min} and L_{ub} in Eqs. (4.4.37,4.4.38) , the length scale defined in (4.5.1), the dimensionless quantities (4.5.2) and the corresponding definitions for the particular (E, L_z)-models (4.3.14, 4.4.9, 4.4.11), one obtains from Eq. (4.9.1):

$$\begin{aligned}
\frac{M_{\text{gas}}^{(\text{rot})}}{\alpha\Lambda^3\sqrt{m^5 E_0}} &= 4\sqrt{2}\pi^3 \int\limits_{-E_0/2\kappa}^{0} dE \left(-\frac{E}{E_0}\right)_+^{k-3} \int\limits_0^{\lambda_{\text{ub}}(E)} d\lambda \int\limits_{-\lambda}^{+\lambda} d\lambda_z \left(\frac{\lambda_z}{\lambda_0} - 1\right)_+^l, \\
\lambda_{\text{ub}}(E) &= \sqrt{-\frac{E_0}{2E}} - \kappa\sqrt{-\frac{2E}{E_0}}.
\end{aligned} \tag{4.9.2}$$

The integrals over λ_z and λ can be carried out immediately. In order to perform the integral over E we use the variable substitution

$$E := -\frac{E_0}{2\kappa}\sigma^2, \tag{4.9.3}$$

where σ is dimensionless, and obtain

$$\frac{M_{\text{gas}}^{(\text{rot})}}{\alpha\Lambda^3\sqrt{m^5 E_0^3}} = \frac{\pi^3}{2^{k-\frac{11}{2}}} \frac{1}{(l+1)(l+2)\lambda_0^l \kappa^{k-3-\frac{l}{2}}} \int\limits_0^1 d\sigma \sigma^{2k-l-7} \left(1 - \frac{\lambda_0}{\sqrt{\kappa}}\sigma - \sigma^2\right)_+^{l+2}. \tag{4.9.4}$$

The second-order polynomial in σ can be expressed as $(\sigma_+ - \sigma)_+(\sigma - \sigma_-)_+$ where the roots are given by

$$\sigma_\pm = -\frac{\lambda_0}{2\sqrt{\kappa}} \pm \sqrt{1 + \frac{\lambda_0^2}{4\kappa}}, \tag{4.9.5}$$

and satisfy $\sigma_- < -1$ and $0 < \sigma_+ < 1$. Since the integrand only contributes when $\sigma_- < \sigma < \sigma_+$ and the integration limits vary from 0 to 1 one can replace the upper limit with σ_+ and remove the index $+$ in the integrand. Using [95, Eq. 3.197.8] yields

$$\begin{aligned} \frac{M_{\text{gas}}^{(\text{rot})}}{\alpha\Lambda^3\sqrt{m^5E_0^3}} &= \frac{\pi^3}{2^{k-\frac{11}{2}}}\frac{(-\sigma_-)^{l+2}(\sigma_+)^{2k-4}}{(l+1)(l+2)\lambda_0^l\kappa^{k-3-\frac{l}{2}}}B(l+3,2k-l-6) \\ &\quad \times {}_2F_1\left(-l-2,2k-l-6,2k-3,\frac{\sigma_+}{\sigma_-}\right). \end{aligned} \tag{4.9.6}$$

To make further progress we introduce the variable χ, defined by $\dfrac{2\sqrt{\kappa}}{\lambda_0} := \sinh(2\chi)$, in terms of which the roots can be expressed as $\sigma_+ = \tanh\chi$ and $\sigma_- = -\coth\chi$. After some algebra one finally obtains

$$\begin{aligned} \frac{M_{\text{gas}}^{(\text{rot})}}{\alpha\Lambda^3\sqrt{m^5E_0^3}} &= \frac{\pi^3}{2^{k-\frac{11}{2}}}\frac{\Gamma(l+1)\Gamma(2k-l-6)}{\Gamma(2k-3)} \\ &\quad \times\frac{{}_2F_1\left(-(l+2),2k-l-6,2k-3,-\tanh^2\chi\right)}{\lambda_0^{2k-6}(\cosh\chi)^{4k-2l-12}}. \end{aligned} \tag{4.9.7}$$

In a similar way, choosing $W_E = E$ in Eq. (4.9.1) yields

$$\begin{aligned} \frac{E_{\text{gas}}^{(\text{rot})}}{\alpha\Lambda^3\sqrt{m^3E_0^5}} &= -\frac{\pi^3}{2^{k-\frac{9}{2}}}\frac{1}{(l+1)(l+2)\lambda_0^l\kappa^{k-2-\frac{l}{2}}}\int_0^{\sigma_+} d\sigma\sigma^{2k-l-5}\left(\sigma_+-\sigma\right)_+^{l+2}\left(\sigma-\sigma_-\right)_+^{l+2} \\ &= -\frac{\pi^3}{2^{k-\frac{9}{2}}}\frac{\Gamma(l+1)\Gamma(2k-l-4)}{\Gamma(2k-1)} \\ &\quad \times\frac{{}_2F_1\left(-(l+2),2k-l-4,2k-1,-\tanh^2\chi\right)}{\lambda_0^{2k-4}(\cosh\chi)^{4k-2l-8}}. \end{aligned} \tag{4.9.8}$$

For the z-component of the total angular momentum one obtains

$$\begin{aligned} \frac{|\mathbf{J}_{\text{gas}}^{(\text{rot})}|}{\alpha\Lambda^4m^2E_0^2} &= \frac{\pi^3}{2^{k-\frac{11}{2}}}\frac{\Gamma(l+1)\Gamma(2k-l-6)}{\Gamma(2k-3)} \\ &\quad \times\frac{{}_2F_1\left(-(l+2),2k-l-6,2k-3,-\tanh^2\chi\right)}{\lambda_0^{2k-7}(\cosh\chi)^{4k-2l-12}} \\ &\quad \times\left[1+\frac{l+1}{2k-l-7}\cosh^2\chi\right. \\ &\quad \left.\times\frac{{}_2F_1\left(-(l+3),2k-l-7,2k-3,-\tanh^2\chi\right)}{{}_2F_1\left(-(l+2),2k-l-6,2k-3,-\tanh^2\chi\right)}\right] \end{aligned} \tag{4.9.9}$$

4.10. Appendix D: Short review of circular hydrodynamic flows

For comparison with the kinetic, collisionless configurations analyzed in this article, in this appendix we discuss their hydrodynamical equivalent, namely the circular flows describing steady-state, axisymmetric rotating perfect fluid configurations around a compact object (see [97] for a recent reference which generalize these configurations to include a magnetic field). These flows can be obtained by integrating the continuity and Euler equations for an external axisymmetric potential $\Phi(\mathbf{x})$,

$$\frac{\partial\rho}{\partial t} + \nabla\cdot(\rho\mathbf{v}) = 0, \qquad \frac{\partial\mathbf{v}}{\partial t} + (\mathbf{v}\cdot\nabla)\,\mathbf{v} + \frac{1}{\rho}\nabla P + \nabla\Phi = 0, \tag{4.10.1}$$

where the state of the fluid is specified by its mass density $\rho(t,\mathbf{x})$, pressure $P(t,\mathbf{x})$, velocity field $\mathbf{v}(t,\mathbf{x})$, temperature $T(t,\mathbf{x})$, and the enthalpy per unit of mass (or specific enthalpy) $h(t,\mathbf{x})$. For a steady-state axisymmetric configuration, the scalar quantities only depend on the radius r and the polar angle ϑ, and the velocity field has the form $\mathbf{v} = r\sin\vartheta\Omega(r,\vartheta)\mathbf{e}_\varphi$, with $\Omega(r,\vartheta)$ the angular velocity. It follows that the continuity equation is automatically satisfied. Furthermore, using the fact that $\mathbf{v}\cdot\nabla = \Omega\frac{\partial}{\partial\varphi}$, the nontrivial components of the Euler equations yield

$$\begin{aligned} -r\sin^2\vartheta\Omega^2 + \frac{1}{\rho}\frac{\partial P}{\partial r} + \frac{\partial\Phi}{\partial r} &= 0, && (4.10.2)\\ -r^2\sin\vartheta\cos\vartheta\Omega^2 + \frac{1}{\rho}\frac{\partial P}{\partial\vartheta} + \frac{\partial\Phi}{\partial\vartheta} &= 0. && (4.10.3) \end{aligned}$$

Considering a baritropic fluid for which the pressure is a function of the mass density only, it follows from the first law of thermodynamics (with constant entropy) that $\frac{dP}{\rho} = dh$. Substituting this relation into Eqs. (4.10.2) and (4.10.3) one obtains

$$d\left[h+\Phi\right] = \Omega^2\left[r\sin^2\vartheta dr + r^2\sin\vartheta\cos\vartheta d\vartheta\right] = \frac{1}{2}\Omega^2 d(R^2), \tag{4.10.4}$$

where $R := r\sin\vartheta$ is the cylindrical radius. On the other hand, introducing the specific azimuthal angular momentum $\ell := R^2\Omega$, one can rewrite Eq. (4.10.4) as

$$d\left[h+\Phi\right] = \frac{1}{2}\Omega^2 d\left(\frac{\ell}{\Omega}\right) = \frac{1}{2}\left[\Omega d\ell - \ell d\Omega\right]. \tag{4.10.5}$$

Taking the exterior derivative on both sides and recalling $d^2 = 0$ yields

$$d\Omega\wedge d\ell = 0, \tag{4.10.6}$$

which implies that $d\Omega$ is proportional to $d\ell$ and hence that Ω is a function of ℓ only.

Therefore, given any function $\Omega_0(\ell)$ of ℓ, one obtains a fluid configuration by setting $\Omega = \Omega_0$ which yields the implicit relation $\ell = R^2\Omega_0(\ell)$ for ℓ. This allows one to express Ω and ℓ as functions of the cylindrical coordinate R. Subsequently, Eq. (4.10.5) is integrated,

$$h = h_\infty - \Phi - \frac{1}{2}\ell\Omega_0(\ell) + \int_0^\ell \Omega_0(\bar{\ell})d\bar{\ell}, \tag{4.10.7}$$

with a free constant h_∞. In particular, the quantities Ω, ℓ, $h + \Phi$ are constant on the "von Zeipelçylinders $R = const$ [98].

As a simple example, consider the case for which $\ell = \ell_0$ is constant which implies that $\Omega = \ell_0/R^2$ and hence

$$h = h_\infty - \left(\Phi + \frac{\ell_0^2}{2R^2}\right), \tag{4.10.8}$$

with a constant h_∞ describing the asymptotic value of the specific enthalpy. The boundary of the configuration is determined by the equation $h = 0$ which corresponds to a level set of the "effective potential"$\Phi + \ell_0^2/(2R^2)$.

For the case of the Kepler potential, Eq. (4.10.8) can be rewritten in terms of the following dimensionless quantities

$$r = \frac{GM}{h_0}\xi, \quad \ell_0 = \frac{GM}{\sqrt{h_0}}\lambda_0, \quad h_\infty = h_0\bar{h}_\infty, \quad \text{and} \quad h = h_0\bar{h}, \tag{4.10.9}$$

with a positive constant h_0, such that

$$\bar{h}(\xi,\vartheta) = \bar{h}_\infty + \frac{1}{\xi} - \frac{\lambda_0^2}{2\xi^2\sin^2\vartheta}. \tag{4.10.10}$$

The condition $\bar{h} > 0$ implies that $\xi > \xi^{\min}(\vartheta)$ with

$$\xi^{\min}(\vartheta) = \begin{cases} \dfrac{\lambda_0^2}{2\sin^2\vartheta}, & \bar{h}_\infty = 0, \\ \dfrac{1}{2\bar{h}_\infty}\left(-1 + \sqrt{1 + \dfrac{2\bar{h}_\infty\lambda_0^2}{\sin^2\vartheta}}\right), & \bar{h}_\infty > 0. \end{cases} \tag{4.10.11}$$

The boundary surface and the contours of the enthalpy function $\bar{h}$ in the xz-plane are shown in figure **4-14** for different values of $\bar{h}_\infty$ and λ_0.

For the more general case of the isochrone potential defined in Eq. (4.4.36), the dimensionless enthalpy is given by

$$\bar{h}(\xi,\vartheta) = \bar{h}_\infty + \frac{1}{\kappa + \sqrt{\kappa^2 + \xi^2}} - \frac{\lambda_0^2}{2\xi^2\sin^2\vartheta}, \tag{4.10.12}$$

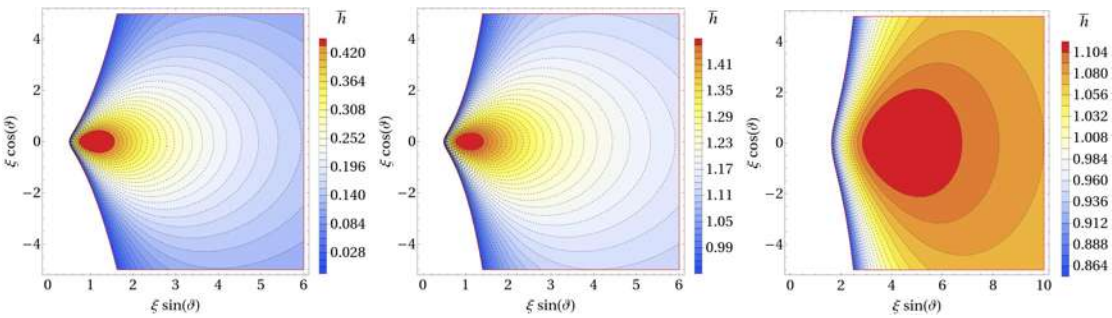

Figure 4-14: Contour plot for the enthalpy $\bar{h}$ in the xz-plane for different values of $\bar{h}_\infty$ and λ_0, assuming the Kepler potential. Left $\bar{h}_\infty = 0, \lambda_0 = 1$, center $\bar{h}_\infty = 1, \lambda_0 = 1$, right $\bar{h}_\infty = 1, \lambda_0 = 2$.

where $\kappa := \frac{h_0 b}{GM}$. In this case, the boundary condition for the minimum radius of the configuration generally leads to a cubic equation for ξ^2 which yields

$$\xi^{\min}(\vartheta) = \begin{cases} \dfrac{\lambda_0^2}{2\sin^2\vartheta}\sqrt{1+\dfrac{4\kappa\sin^2\vartheta}{\lambda_0^2}}, & \bar{h}_\infty = 0, \\ \dfrac{1}{\sqrt{2}\bar{h}_\infty}\sqrt{1+\bar{h}_\infty\left(2\kappa+\dfrac{\lambda_0^2}{\sin^2\vartheta}\right)-\sqrt{\left(1+2\bar{h}_\infty\kappa\right)^2+\dfrac{2\bar{h}_\infty\lambda_0^2}{\sin^2\vartheta}}}, & \bar{h}_\infty > 0. \end{cases} \tag{4.10.13}$$

The boundary surfaces and the contours of $\bar{h}$ in the xz-plane for different values of $\bar{h}$ and $\lambda_0 = \kappa = 1$ are shown in figure **4-15**.

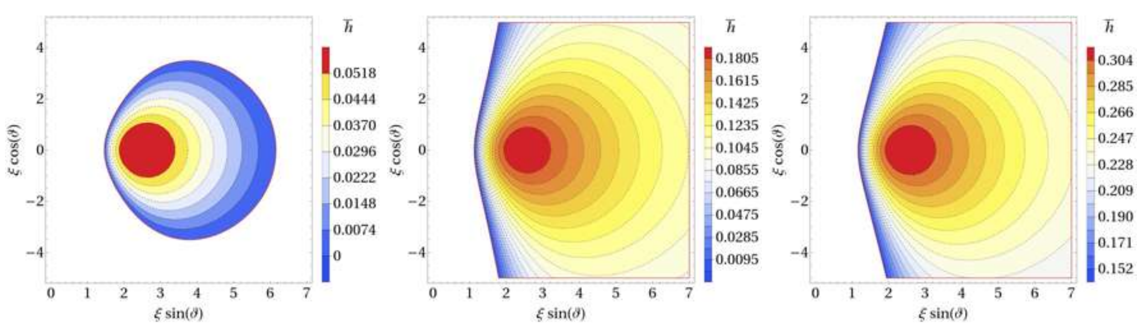

Figure 4-15: Contour plot for the enthalpy $\bar{h}$ in the xz-plane for different values of $\bar{h}_\infty$ and $\lambda_0 = \kappa = 1$. Left panel ($\bar{h}_\infty = -1/8$): Here a negative value of $\bar{h}_\infty$ is chosen, which leads to a configuration with finite extend. Center panel ($\bar{h}_\infty = 0$): the marginal case $\bar{h}_\infty = 0$. Right panel ($\bar{h}_\infty = 1/8$): a case with $\bar{h}_\infty > 0$.

5 Axisymmetric, stationary collisionless gas configurations surrounding black holes

This chapter is a loyal reproduction (with some minor changes due to the format) of the free arXiv:2209.05327 version [49]. However, the numbers of the equations and references could differ from the ones in the original version. The references are collected at the end of this thesis work.

5.1. Abstract

The properties of a stationary gas cloud surrounding a black hole are discussed, assuming that the gas consists of collisionless, identical massive particles that follow spatially bound geodesic orbits in the Schwarzschild spacetime. Several models for the one-particle distribution function are considered, and the essential formulae that describe the relevant macroscopic observables, like the current density four-vector and the stress-energy-momentum tensor are derived. This is achieved by rewriting these observables as integrals over the constants of motion and by a careful analysis of the range of integration. In particular, we provide configurations with finite total mass and angular momentum. Differences between these configurations and their nonrelativistic counterparts in a Newtonian potential are analyzed. Finally, our configurations are compared to their hydrodynamic analogues, the "polish doughnuts".

5.2. Introduction

The goal of this work is to extend the non-relativistic steady-state collisionless kinetic gas tori around compact objects discussed in our accompanying article [47] (referred to as paper I in the following) to the relativistic case, assuming that the central object is a black hole. Such tori have many potential astrophysical applications, including the modeling of low-density hot accretion disks and studying the behavior of dark matter or a distribution of stars surrounding supermassive black holes. In particular, the recent observations by the Event Horizon Telescope Collaboration (EHTC) [74–76] revealing the shadows of the supermassive black holes M87* and Sgr A* call for a profound understanding for the behavior of a hot plasma in the vicinity of a strong gravitational field beyond the hydrodynamic approximation.

The configurations discussed in this work are based on the same assumptions as the nonrelativistic model in paper I, except that the kinetic gas is treated in a fully relativistic description and the central object is assumed to be a black hole. For the sake of completeness and clarity, in the following we list all the assumptions made in this article. First, we assume the gas to be collisionless,[1] neglecting the effects of collisions between the gas particles. Second, we consider a gas consisting of identical, massive and uncharged particles, and hence we do not take into account electromagnetic effects (which is justified for dark matter or star distributions but nor for plasmas). Third, we assume that the self-gravity of the gas can be neglected, the gravitational field being dominated by the one generated by the central black hole. This implies that we may regard the black hole as being described by an asymptotically flat, stationary solution of the Einstein vacuum equations with an event horizon. Modulo technical assumptions, the uniqueness theorems (see, for instance Refs. [59, 60]) imply that the central black hole belongs to the Kerr family. Fourth, in this article we further neglect the rotation of the black hole, implying that the exterior region is described by the Schwarzschild metric. Finally, similar to paper I and motivated by phase space mixing [73, 77] and dispersion [36] on a fixed Schwarzschild background, we restrict ourselves to steady-states in which each gas particle follows a spatially bound geodesic trajectory in the Schwarzschild geometry. Moreover, for simplicity, we restrict our analysis to axisymmetric configurations in which the one-particle distribution function (DF) only depends on the energy and azimuthal component of the angular momentum of the gas particles.

Our models are based on the ansätze for the DF that have been used in previous works to construct self-gravitating axisymmetric configurations in the absence of a central black hole, see for example [29, 79, 80, 85, 100, 101]. In particular, we consider the generalized polytropic ansatz used more recently in Refs. [83, 84] to numerically construct configurations with toroidal, disk-like, spindle-like and composite structures. In these ansätze, the one-particle DF is the product of a function of the energy times a function of the azimuthal component of the angular momentum. Contrary to the works in [79, 80, 83, 84, 100, 101], the gravitational field in our configurations is dominated by the central black hole, such that the self-gravity can be neglected. One of the main achievements of this work is to derive explicit expressions for the spacetime observables (namely, the current density and energy-momentum-stress tensor) which have the form of a single integral of an analytic (albeit complicated) function of the energy. In the Newtonian limit these integrals simplify and reduce to the corresponding expres-

[1] Note that for hot and diffuse plasmas accreting into black holes the mean free path is expected to be comparable or even larger than the macroscopic length scale, which justifies a kinetic description [99].

sions in paper I. By analyzing the properties of these spacetime observables, we show that our configurations have the morphology of a thick torus extending all the way to spatial infinity, having a sharp inner boundary surface. Next, we show that although they have infinite extend, for suitable values of the free parameters our configurations have finite total particle number, energy and angular momentum. Finally, we provide a detailed analysis for the radial profile of the spacetime observables, including the particle density, the kinetic temperature and the principle pressures and compare them with an analogous fluid model.

Relevant to the self-consistency of our models is the recent work by Jabiri [102, 103] who proves the mathematical existence of solutions to the stationary, axisymmetric Einstein-Vlasov system of equations describing self-gravitating tori of Vlasov matter which, in the limit of vanishing amplitude, reduce to configurations which are similar[2] to the ones analyzed in the present article. In this sense, the work in [102] suggests that (for small enough amplitude) our configurations can likely be generalized to include their self-gravity. We also mention related recent work on the accretion of a Vlasov gas by a central black hole [36–43, 104] in which unbounded (instead of bounded) timelike geodesics are relevant.

This work is organized as follows. In section 5.3 we provide a brief review of the collisionless Boltzmann equation on a Schwarzschild spacetime. We focus our attention on the subset of phase space which corresponds to spatially bound future-directed timelike geodesics. Assuming that the one-particle DF is supported on this set, we establish general expressions for the current density vector and energy-momentum-stress tensor which allow one to compute these spacetime observables when the one-particle DF is a function only of the integrals of motion. Next, in section 5.4 we consider an ansatz in which the one-particle DF depends only on the energy and azimuthal component of the angular momentum of the gas particles. We concentrate on two models; the first one (rotating) describes a gas configuration that has nonvanishing total angular momentum while in the second one (even) the DF is an even function of the angular momentum such that the total angular momentum vanishes although the individual gas particles rotate. For these models, we reduce the expressions for the spacetime observables to single integrals over the energy variable. Furthermore, we compute the total particle number, energy and angular momentum of our configurations and compare them with the analogous Newtonian models in paper I. The properties of some spacetime observables are analyzed in section 5.5 where we also compare our kinetic configurations with the corresponding fluid models. Conclusions are drawn in section 5.6 and technical –yet important– aspects of our calculations are described in appendices 5.7–5.11.

Throughout this work, we use the signature convention $(-,+,+,+)$ for the spacetime

[2]The self-gravitating configurations constructed [102] have finite support, whereas in our case the support is infinite, although we could also easily obtain finite support configurations with our ansatz as discussed further below.

metric and work in geometrized units, such that $G_N = c = 1$. For recent reviews on mathematical results regarding the Einstein-Vlasov system and the geometric structure in the relativistic kinetic theory on curved spacetimes we refer the reader to Refs. [8, 9, 11, 12].

5.3. Collisionless gas configurations trapped in a Schwarzschild potential

In this section we review the basic formalism necessary to describe a collisionless kinetic gas propagating in the exterior of a non-rotating black hole spacetime. Since the self-gravity of the gas is neglected, we may assume that the spacetime is described by the Schwarzschild metric with fixed mass parameter $M > 0$, as explained in the introduction. We focus our attention on the case in which the individual gas particles follow future-directed spatially bound timelike geodesic. In the next subsection we provide a brief recapitulation of the Hamiltonian description of such geodesics, its integrals of motion and the properties of the effective potential describing the radial motion. In subsection 5.3.2 we summarize a few well-known results concerning the formulation of general relativistic kinetic theory which are essential to this work, and in subsection 5.3.3 we express the particle current density vector and the energy-momentum-stress tensor in terms of an integral over the conserved quantities.

The case of unbound trajectories has been analyzed in detail in [36] and applied to accretion problems [36, 37, 39–41, 43], see also Ref. [38] for the analogous problem on the Reissner-Nordström background and Ref. [104] for a thin accretion disk confined to the equatorial plane of a Kerr black hole.

5.3.1. Free-particle Hamiltonian, integrals of motion and effective potential

Since we are only interested in the exterior region, it is sufficient to work in standard Schwarzschild coordinates $(x^\mu) = (t, r, \vartheta, \varphi)$, for which the spacetime metric is

$$g := -N(r)dt^2 + \frac{dr^2}{N(r)} + r^2 d\vartheta^2 + r^2 \sin^2\vartheta d\varphi^2, \qquad N(r) := 1 - \frac{2M}{r} > 0. \quad (5.3.1)$$

As this spacetime is static and spherically symmetric, the geodesic motion possesses several integrals of motion. First, we have the conserved energy E, which is associated with the timelike Killing vector field ∂_t. Next, we have the three components of the angular momentum (L_x, L_y, L_z) which correspond to the generators of the rotations. Finally, the particles' rest mass m is conserved. The integral of motion corresponding to $-m^2/2$ is the free-particle Hamiltonian of the theory, given by

$$\mathcal{H}(x,p) := \frac{1}{2} g_x^{-1}(p,p) = \frac{1}{2}\left(-\frac{p_t^2}{N(r)} + N(r)p_r^2 + \frac{p_\vartheta^2}{r^2} + \frac{p_\varphi^2}{r^2\sin^2\vartheta}\right), \tag{5.3.2}$$

in adapted local coordinates $(x^\mu, p_\mu) = (t, r, \vartheta, \varphi, p_t, p_r, p_\vartheta, p_\varphi)$ on the cotangent bundle $T^*\mathcal{M}$ associated with the spacetime manifold $(\mathcal{M}, g)$. In this article, we focus our attention on the conserved quantities

$$m = \sqrt{-2\mathcal{H}}, \quad E = -p_t, \quad L_z = p_\varphi, \quad \text{and} \quad L^2 := L_x^2 + L_y^2 + L_z^2 = p_\vartheta^2 + \frac{L_z^2}{\sin^2\vartheta}, \tag{5.3.3}$$

which Poisson commute with each other.[3] For the following, it is useful to introduce the orthonormal basis of vector fields

$$e_{\hat{0}} := \frac{1}{\sqrt{N(r)}}\frac{\partial}{\partial t}, \quad e_{\hat{1}} := \sqrt{N(r)}\frac{\partial}{\partial r}, \quad e_{\hat{2}} := \frac{1}{r}\frac{\partial}{\partial\vartheta}, \quad e_{\hat{3}} := \frac{1}{r\sin\vartheta}\frac{\partial}{\partial\varphi}. \tag{5.3.4}$$

In terms of the conserved quantities, the orthonormal components of p have the form

$$(p_{\hat{\mu}})(\epsilon_r, \epsilon_\vartheta) = \left(-\frac{E}{\sqrt{N(r)}}, \frac{\epsilon_r}{\sqrt{N(r)}}\sqrt{E^2 - V_{m,L}(r)}, \frac{\epsilon_\vartheta}{r}\sqrt{L^2 - \frac{L_z^2}{\sin^2\vartheta}}, \frac{L_z}{r\sin\vartheta}\right), \tag{5.3.5}$$

where the signs $\epsilon_r = \pm 1$ and $\epsilon_\vartheta = \pm 1$ determine the corresponding signs of p_r and p_ϑ, and $V_{m,L}(r)$ is the effective potential for radial geodesic motion in the Schwarzschild spacetime, which is given by

$$V_{m,L}(r) := N(r)\left(m^2 + \frac{L^2}{r^2}\right). \tag{5.3.6}$$

The properties of this potential are well-know, see for example Appendix A in [36] for a summary. The most relevant features for the purpose of the present article are the following: (i) there exists a potential well with associated stable bound orbits only if $L > L_{\text{ms}} := \sqrt{12}Mm$. In the limit $L = L_{\text{ms}}$ the potential has an inflection point at $r = r_{\text{ms}} = 6M$ describing the marginally stable circular orbits which have energy $E_{\text{ms}} = \sqrt{8/9}m$. (ii) Bound orbits exist only when $E \in (E_{\text{ms}}, m)$ and the total angular momentum is confined to the interval $L \in (L_{\text{c}}(E), L_{\text{ub}}(E))$, with $L_{\text{c}}(E)$ ($L_{\text{ub}}(E)$) the critical angular momentum corresponding to the case in which the effective potential's maximum (minimum) is equal to E^2. These extrema of $V_{m,L}$ are located at

$$r_{\text{max}} = \frac{6M}{1 + \sqrt{1 - 12M^2m^2/L^2}}, \qquad r_{\text{min}} = \frac{6M}{1 - \sqrt{1 - 12M^2m^2/L^2}}, \tag{5.3.7}$$

[3] In terms of adapted local coordinates the Poisson bracket $\{\mathcal{F}, \mathcal{G}\}$ between two functions F and G on $T^*\mathcal{M}$ is defined as

$$\{\mathcal{F}, \mathcal{G}\} = \frac{\partial\mathcal{F}}{\partial p_\mu}\frac{\partial\mathcal{G}}{\partial x^\mu} - \frac{\partial\mathcal{G}}{\partial p_\mu}\frac{\partial\mathcal{F}}{\partial x^\mu},$$

see [12] and references therein for more details and a coordinate-free definition.

with r_{max} decreasing monotonously from $6M$ to $3M$ and r_{min} increasing monotonously from $6M$ to ∞ as L increases from L_{ms} to ∞. The unstable circular orbit at $r = r_{\text{max}}$ separate those orbits that are reflected at the potential from those that plunge into the black hole, and they have energies smaller than m as long as $L_{\text{ms}} < L < 4Mm$. Therefore, for fixed values of L in this interval, the bound orbits with minimum radius are those whose energies and left turning points approach $E_{\text{max}} = \sqrt{V_{m,L}(r_{\text{max}})}$ and r_{max}, respectively. For these reasons, the limiting orbits with $E = E_{\text{max}}$ are called innermost stable orbits (ISO). In the limit $L = L_{\text{mb}} = 4Mm$ the ISOs are marginally bound, and they have energy $E = m$ and minimum radius $r = r_{\text{mb}} = 4M$.

5.3.2. Collisionless Boltzmann equation and spacetime observables

The collisionless Boltzmann (or Vlasov) equation on the curved spacetime manifold $(\mathcal{M}, g)$ can be written in a compact way as

$$\{\mathcal{H}, f\} = 0, \tag{5.3.8}$$

where $f : T^*\mathcal{M} \to \mathbb{R}$ is the one-particle DF, and it expresses the fact that f is constant along the Liouville flow. When restricted to the subset Γ_{bound} of $T^*\mathcal{M}$ corresponding to bound orbits, one can transform (x^μ, p_μ) to generalized action-angle variables $(\mathcal{Q}^\mu, \mathcal{J}_\mu)$ which allows one to provide an explicit solution representation for the DF [73]. The explicit form of these variables will not be used in this article, although the existence of the symplectic transformation $(x^\mu, p_\mu) \mapsto (\mathcal{Q}^\mu, \mathcal{J}_\mu)$ will turn out to be useful when computing the total particle number, energy and angular momentum in the next section. For the following, we restrict ourselves to gas configurations consisting of identical particles of positive rest mass $m > 0$. In this case, the momentum is confined to the future mass hyperboloid,

$$P_x^+(m) := \left\{ p \in T_x^*\mathcal{M} \ : \ g_x^{-1}(p,p) = -m^2, \text{ the vector dual to } p \text{ is future directed} \right\} \tag{5.3.9}$$

and f is a function on the future mass shell

$$\Gamma_m^+ := \{(x,p) : x \in \mathcal{M}, p \in P_x^+(m)\}. \tag{5.3.10}$$

Due to phase space mixing (see [73, 77] and references therein), it is expected that a gas configuration consisting of purely bound particles (such that it is described by a DF supported in Γ_{bound}) relaxes in time to a stationary configuration which can be described by a one-particle DF f depending only on the integrals of motion, that is, only on (E, L_x, L_y, L_z). Notice that such a function f automatically satisfies the collisionless Boltzmann equation (5.3.8) since E, L_x, L_y, L_z Poisson commute with $\mathcal{H}$. In this article, we will assume, in addition, that f depends only on E and *one* components of the angular momentum, say L_z, such that

$$f(x,p) = F(E, L_z), \tag{5.3.11}$$

for some suitable function F that we specify further below. In particular, the ansatz (5.3.11) implies that the gas configuration is stationary and axisymmetric. Provided that f vanishes outside Γ_{bound} and other suitable hypotheses hold, it has been shown recently [102, 103] that such configurations can be made self-gravitating, provided their amplitude is sufficiently small.

To extract the physical content of our gas configurations, we compute the most relevant spacetime observables, that is, the particle current density J and the energy-momentum-stress tensor T. In particular, these quantities contain the information about the particle density n, mean particle four-velocity, the energy density ε, heat flow, pressure tensor P_{ij} and kinetic temperature. They are defined as follows (see, for instance, Refs. [4, 12])

$$J_\mu(x) := \int\limits_{P_x^+(m)} f(x,p) p_\mu \mathrm{dvol}_x(p), \qquad T_{\mu\nu}(x) := \int\limits_{P_x^+(m)} f(x,p) p_\mu p_\nu \mathrm{dvol}_x(p), \tag{5.3.12}$$

where $\mathrm{dvol}_x(p)$ is the Lorentz-invariant volume form, which, in terms of the orthonormal basis (5.3.4) is defined as

$$\mathrm{dvol}_x(p) := \frac{dp_{\hat{1}} \wedge dp_{\hat{2}} \wedge dp_{\hat{3}}}{\sqrt{m^2 + p_{\hat{1}}^2 + p_{\hat{2}}^2 + p_{\hat{3}}^2}} = \frac{dp_{\hat{1}} \wedge dp_{\hat{2}} \wedge dp_{\hat{3}}}{|p_{\hat{0}}|}. \tag{5.3.13}$$

Any DF f that satisfies the collisionless Boltzmann equation (5.3.8) and is positive implies that J is future-directed timelike, that T satisfies the standard energy conditions (strong, dominated, weak, null) and that J and T are divergence-free:

$$\nabla^\mu J_\mu = 0, \qquad \nabla^\mu T_{\mu\nu} = 0. \tag{5.3.14}$$

In the next subsection, we rewrite J_μ and $T_{\mu\nu}$ in terms of integrals over the conserved quantities E, L and L_z, such that these quantities can be evaluated more easily for any DF of the form (5.3.11).

5.3.3. Explicit representation of the observables in terms of integrals over the conserved quantities

Re-expressing the fibre integrals in terms of the conserved quantities E, L and L_z involves two steps. The first one is to rewrite the volume form (5.3.13) in terms of these quantities. The second is to determine the correct integration limits for them.

The first step is straightforward. Using Eqs. (5.3.3,5.3.5) one obtains, fixing m, r and ϑ,

$$\mathrm{dvol}_x(p) = \frac{1}{r^2 \sin\vartheta} \frac{dE\ L dL\ dL_z}{\sqrt{E^2 - V_{m,L}(r)}\sqrt{L^2 - L_z^2/\sin^2\vartheta}}. \tag{5.3.15}$$

The second step is more involved and has to be analyzed carefully. In order to determine the correct intervals over which E, L and L_z need to be integrated over, we make the following observations:

(i) As mentioned above, we restrict ourselves to DFs whose support lies in Γ_{bound}, that is the subset of relativistic phase space corresponding to bound orbits, which implies that $E_{\text{ms}} < E < m$ and $L_{\text{c}}(E) < L < L_{\text{ub}}(E)$.

(ii) Given the position $r = r_{\text{obs}}$ of the observer, one needs that $V_{m,L}(r) \leq E^2$ for r to lie in the classically allowed region. This implies that the total angular momentum must satisfy the additional bound

$$L \leq L_{\text{max}}(E, r) := r\sqrt{\frac{E^2}{N(r)} - m^2}. \tag{5.3.16}$$

(iii) A further restriction comes from the requirement that the radius of the observer $r = r_{\text{obs}}$ must lie between the turning points $r_1 < r_2$ of the bound orbit with given E and L, that is, $r_1 \leq r_{\text{obs}} \leq r_2$.

(iv) When $r_{\text{obs}} > r_{\text{ms}} = 6M$ the minimum possible value for the energy E, such that a bound trajectory satisfying $r_1 < r_{\text{obs}} < r_2$ exists, occurs when r_{obs} coincides with the right turning point r_2 of the ISO, see figure **5-1**. As shown in Appendix 5.8 (cf. Eq. 5.8.10 and the right panel of figure **5-16**) this implies that

$$E > E_{\text{c}}(r) := m\frac{r + 2M}{\sqrt{r\,(r + 6M)}}, \qquad r > 6M. \tag{5.3.17}$$

For $E \in (E_{\text{c}}(r), m)$ the lower bound $L = L_{\text{c}}(E)$ for the total angular momentum corresponds to the situation for which orbits with the same value of E but slightly smaller value for L plunge into the black hole.

(v) When $4M < r_{\text{obs}} < r_{\text{ms}}$ the minimum value for E such that a bound trajectory satisfying $r_1 < r_{\text{obs}} < r_2$ exists occurs when r_{obs} coincides with the position of the local maximum of the effective potential (see figure **5-1**), such that

$$E > E_{\text{c}}(r) := m\frac{r - 2M}{\sqrt{r\,(r - 3M)}}, \qquad 4M < r < 6M. \tag{5.3.18}$$

For $E \in (E_{\text{c}}(r), m)$ the lower bound for L is again given by $L = L_{\text{c}}(E)$.

(vi) For $r = r_{\text{obs}} < r_{\text{mb}} = 4M$ there are not bound orbits.

(vii) Note that in both cases (iv) and (v), one has $L_{\text{max}}(E, r_{\text{obs}}) \leq L_{\text{ub}}(E)$. To prove this, consider a trajectory with $L = L_{\text{max}}(E, r_{obs})$, such that r_{obs} is a turning

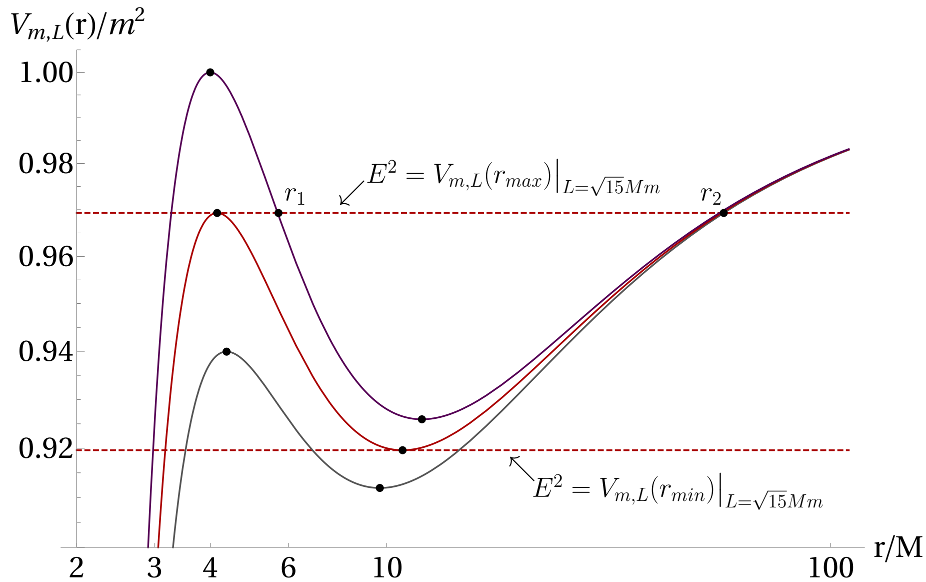

Figure 5-1: Behavior of effective potential vs radius for $L = \sqrt{14}Mm$ (gray), $L = \sqrt{15}Mm$ (red), and $L = 4Mm$ (purple). (r_1, r_2) are the turning points and the dashed (red) lines represent the energy level corresponding to the maximum and minimum values of the potential with $L = \sqrt{15}Mm$.

point, and consider the effective potential $V_{m,L'}$ with $L' = L_{\text{ub}}(E)$, such that its local minimum is equal to E^2. Then, clearly, $V_{m,L'}(r_{\text{obs}}) > E^2$ which implies $L' > L_{\max}(E, r_{\text{obs}})$. The limit $L' = L_{\max}(E, r_{\text{obs}})$ occurs when r_{obs} coincides with the position of the minimum of $V_{m,L'}$.

(viii) Finally, the range of L_z is restricted by the requirement that $L^2 \geq 0$, which yields $|L_z| \leq L \sin\vartheta$.

Based on these observations, we conclude that the relevant range of integration for the conserved quantities (E, L, L_z) is given by

$$E_{\text{c}}(r) < E < m, \quad L_{\text{c}}(E) < L < L_{\max}(E, r), \quad \text{and} \quad |L_z| < L \sin\vartheta, \tag{5.3.19}$$

where

$$E_{\text{c}}(r) = \begin{cases} m\dfrac{r - 2M}{\sqrt{r(r-3M)}}, & 4M \leq r \leq 6M, \\[2ex] m\dfrac{r + 2M}{\sqrt{r\,(r+6M)}}, & r \geq 6M. \end{cases} \tag{5.3.20}$$

and

$$L_{\rm c}(E) = \frac{4\sqrt{2}Mm^3}{\sqrt{36m^2E^2 - 8m^4 - 27E^4 + E\left(9E^2 - 8m^2\right)^{3/2}}}. \quad (5.3.21)$$

$$L_{\max}(E,r) = r\sqrt{\frac{E^2}{N(r)} - m^2}. \quad (5.3.22)$$

For an alternative derivation of these limits and further details, see Appendix 5.8. The behavior of the critical minimum energy $E_c(r)$ and the critical angular momentum $L_{\rm c}(E)$ are shown in figure **5-2**. Note that E_c decreases from m to E_{ms} in the interval $[4M, 6M]$ and increases from E_{ms} to m in the interval $[6M, \infty)$. Furthermore, this function is continuously differentiable at $r = 6M$. The function $L_{\rm c}(E)$ increases monotonously from $L_{\rm ms}$ to $L_{\rm mb}$.

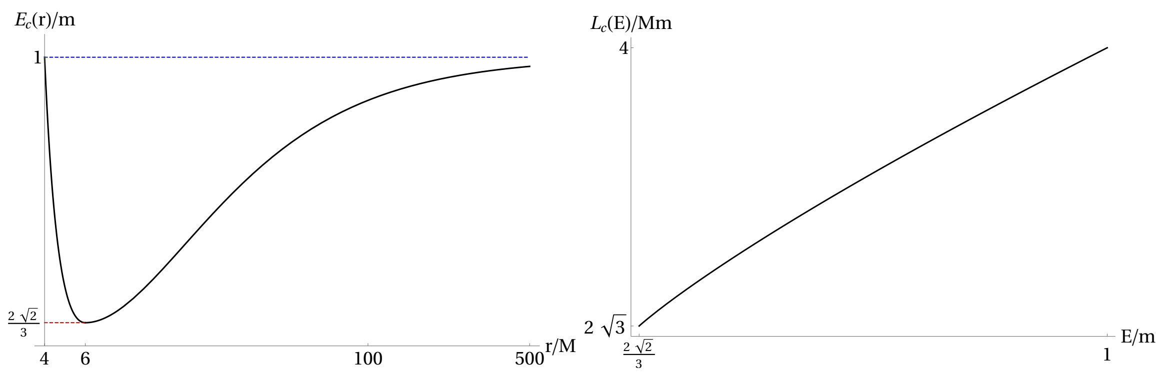

Figure 5-2: Behavior of the critical minimum energy $E_{\rm c}$ vs radius (left) and the critical angular momentum $L_{\rm c}$ vs energy (right).

Now that the integration limits are understood, the explicit form for the particle current density and the energy-momentum-stress tensor in terms of conserved quantities can be given:

$$J_{\hat\mu}(x) = \sum_{\epsilon_r,\epsilon_\vartheta=\pm1} \int\limits_{E_{\rm c}(r)}^{m} \int\limits_{L_{\rm c}(E)}^{L_{\max}(E,r)} \int\limits_{-L\sin\vartheta}^{+L\sin\vartheta} \frac{1}{r^2\sin\vartheta} \frac{f(x,p)p_{\hat\mu}(\epsilon_r,\epsilon_\vartheta)dL_z\ LdL\ dE}{\sqrt{E^2 - V_{m,L}(r)}\sqrt{L^2 - L_z^2/\sin^2\vartheta}}, \quad (5.3.23)$$

$$T_{\hat\mu\hat\nu}(x) = \sum_{\epsilon_r,\epsilon_\vartheta=\pm1} \int\limits_{E_{\rm c}(r)}^{m} \int\limits_{L_{\rm c}(E)}^{L_{\max}(E,r)} \int\limits_{-L\sin\vartheta}^{+L\sin\vartheta} \frac{f(x,p)p_{\hat\mu}(\epsilon_r,\epsilon_\vartheta)p_{\hat\nu}(\epsilon_r,\epsilon_\vartheta)dL_zLdLdE}{r^2\sin\vartheta\sqrt{E^2 - V_{m,L}(r)}\sqrt{L^2 - L_z^2/\sin^2\vartheta}}, \quad (5.3.24)$$

where the functions $p_{\hat\mu}(\epsilon_r, \epsilon_\vartheta)$ are given by Eq. (5.3.5) and the effective potential $V_{m,L}$ is defined in Eq. (5.3.6). The expressions (5.3.23,5.3.24) are valid for any DF f which decays sufficiently fast in the momentum space such that these integrals converge. In the following section, we further reduce these integrals under the assumption that $f(x,p)$ has the form (5.3.11).

5.4. Stationary, axisymmetric models

In this section, we further reduce the expressions (5.3.23,5.3.24) for the current density and energy-momentum-stress tensor for the case that the DF has the form (5.3.11), where we assume that $F(E, L_z)$ is given by a generalized polytropic ansatz as in Refs. [83, 84]. Furthermore, we compute the total particle number, energy and angular momentum for these configurations and compare them with the analogous Newtonian models in paper I. For a related model in which the DF depends only on E and L_z/L, see Ref. [48].

5.4.1. The relativistic (E, L_z)-models

For the following, we assume that the function F in Eq. (5.3.11) has the product form

$$F(E, L_z) := F_0(E) \times I(L_z), \tag{5.4.1}$$

with F_0 given by the polytropic ansatz

$$F_0(E) := \alpha \left(1 - \frac{E}{E_0}\right)_+^{k-\frac{3}{2}}. \tag{5.4.2}$$

Here, α, E_0 are positive parameters, $k > 1/2$, and the notation F_+ refers to the positive part of the quantity F, that is $F_+ = F$ if $F > 0$ and $F_+ = 0$ otherwise. The cut-off parameter E_0 provides an upper bound for the energy. For $E_0 < m$, the resulting configurations have finite extend. However, in the results shown below we shall choose the limiting case $E_0 = m$ in which the configurations extend to infinity, similar to the Newtonian configurations constructed in paper I. In turn, the function $I(L_z) = I_{\text{poly}}^{(\text{even,rot})}(L_z)$ is given by one of the following two functions:

$$I^{(\text{even})}(L_z) := \left(\frac{|L_z|}{L_0} - 1\right)_+^l \tag{5.4.3}$$

or

$$I^{(\text{rot})}(L_z) := 2\left(\frac{L_z}{L_0} - 1\right)_+^l, \tag{5.4.4}$$

with parameters L_0 and $l = 0, 1, 2, \ldots$. Here, the superscript “evenrefers to the fact that $I(L_z)$ is an even function of L_z, meaning that for any particle orbiting in the positive sense around the black hole, there is a corresponding particle moving in the opposite direction with the same absolute value of L_z. As a consequence, the corresponding configurations are static and have vanishing total angular momentum. In contrast, the configurations denoted by the superscript “rotçonsist of particles with positive values of L_z, and hence they rotate. The cut-off parameter L_0 provides a lower bound for the absolute value of the azimuthal angular momentum; hence when $L_0 > 0$ the gas configuration vanishes in the vicinity of the z-axis. As follows from the analysis in paper I, the total particle number, energy and angular momentum for the infinitely extended configurations $E_0 = m$ are finite provided $2k > l + 7$.

5.4.2. Spacetime observables

Since the DF is independent of L, it is convenient to interchange the order of integration of L and L_z in Eq. (5.3.23), which yields

$$\begin{aligned} J_{\hat{\mu}}(x) &= \sum_{\epsilon_r,\epsilon_\vartheta=\pm 1} \int\limits_{E_c(r)}^{m} dE F_0(E) \int\limits_{-L_{\max}(E,r)\sin\vartheta}^{L_{\max}(E,r)\sin\vartheta} dL_z I(L_z) \\ &\quad \times \int\limits_{\text{máx}\{L_c(E),\frac{|L_z|}{\sin\vartheta}\}}^{L_{\max}(E,r)} \frac{dLL}{\sqrt{E^2 - V_{m,L}(r)}\sqrt{L^2 - L_z^2/\sin^2\vartheta}} \frac{p_{\hat{\mu}}(\epsilon_r,\epsilon_\vartheta)}{r^2\sin\vartheta}. \end{aligned} \quad (5.4.5)$$

Using the identity $E^2 - V_{m,L}(r) = N(r)[L_{\max}(E,r)^2 - L^2]/r^2$, Eq. (5.3.5) and the formulae in Appendix 5.9, the integral over L can be performed analytically, obtaining

$$\begin{aligned} \begin{pmatrix} J_{\hat{0}} \\ \\ J_{\hat{3}} \end{pmatrix}(x) &= \frac{2\pi}{\sqrt{N} r\sin\vartheta} \int\limits_{E_c(r)}^{m} dE F_0(E) \int\limits_{-L_{\max}(E,r)\sin\vartheta}^{+L_{\max}(E,r)\sin\vartheta} dL_z I(L_z) \begin{pmatrix} -\frac{E}{\sqrt{N}} \\ \\ \frac{L_z}{r\sin\vartheta} \end{pmatrix} \\ &\quad - \frac{4}{\sqrt{N} r\sin\vartheta} \int\limits_{E_c(r)}^{m} dE F_0(E) \\ &\quad \times \int\limits_{-L_c(E)\sin\vartheta}^{+L_c(E)\sin\vartheta} dL_z I(L_z) \arctan\sqrt{\frac{L_c(E)^2 - L_z^2/\sin^2\vartheta}{L_{\max}(E,r)^2 - L_c(E)^2}} \begin{pmatrix} -\frac{E}{\sqrt{N}} \\ \\ \frac{L_z}{r\sin\vartheta} \end{pmatrix}, \end{aligned} \quad (5.4.6)$$

while the remaining components are zero: $J_{\hat{1}} = J_{\hat{2}} = 0$. Note that the contribution to $J_{\hat{0}}$ and $J_{\hat{3}}$ corresponding to the integrals in the first line are independent of $L_c(E)$ and very similar to the corresponding expression for the particle density n in the Newtonian case (see Eq. (38) in paper I). In contrast, the integrals on the second line depend on the critical angular momentum $L_c(E)$ which is related to the maximum of the potential, and thus they are due to relativistic effects. Similar expressions for $T_{\hat{\mu}\hat{\nu}}(x)$ are obtained following the same steps, starting from Eq. (5.3.24).

The next step consists in computing the integrals over L_z for the specific models (5.4.3, 5.4.4). The integrals on the right-hand side of the first line of Eq. (5.4.6) are easily evaluated. For the corresponding integrals on the second line, it is convenient to introduce the shorthand notation

$$a = a(E,\vartheta) := \frac{L_c(E)\sin\vartheta}{L_0}, \qquad b = b(E,r) := \frac{L_c(E)}{L_{\max}(E,r)}, \qquad L_z := aL_0\lambda_z. \quad (5.4.7)$$

Using integration by parts one finds, for instance,

$$\int\limits_{-L_c(E)\sin\vartheta}^{+L_c(E)\sin\vartheta} dL_z I(L_z) \arctan\sqrt{\frac{L_c(E)^2 - L_z^2/\sin^2\vartheta}{L_{\max}(E,r)^2 - L_c(E)^2}}$$

$$= \frac{2L_0}{l+1} b\sqrt{1-b^2} \int\limits_{1/a}^{1} \frac{d\lambda_z \lambda_z}{\sqrt{1-\lambda_z^2}} \frac{(a\lambda_z - 1)_+^{l+1}}{1 - b^2\lambda_z^2}, \tag{5.4.8}$$

for both models (5.4.3,5.4.4). To write down the final result, it is convenient to introduce the functions

$$\tilde{\mathrm{K}}_l(a,b) := \frac{2}{\pi}\sqrt{1-b^2} \int\limits_{1/a}^{1} \frac{d\lambda_z \lambda_z}{\sqrt{1-\lambda_z^2}} \frac{(a\lambda_z - 1)_+^{l+1}}{1 - b^2\lambda_z^2}, \qquad a > 0, \quad 0 < b < 1, \tag{5.4.9}$$

and

$$\mathrm{K}_l(a,b) := \frac{1}{l+1}\left[\left(\frac{a}{b} - 1\right)_+^{l+1} - b\tilde{\mathrm{K}}_l(a,b)\right], \qquad a > 0, \quad 0 < b < 1. \tag{5.4.10}$$

As shown in Appendix 5.10, these functions are continuous in (a,b) with $\tilde{\mathrm{K}}_l(a,b)$ satisfying the bound $0 \leq \tilde{\mathrm{K}}_l(a,b) \leq (a-1)_+^{l+1}$ for all $a > 0$ and $0 < b < 1$, which implies $\mathrm{K}_l(a,b) \geq 0$. In particular, $\tilde{\mathrm{K}}_l(a,b)$ vanishes if $0 < a \leq 1$, that is, if $L_c(E)\sin\vartheta \leq L_0$, which is always the case if $L_0 \geq L_{\text{mb}} = 4Mm$, see figure **5-2**. Consequently, $\mathrm{K}_l(a,b) = 0$ if $a \leq b \leq 1$, that is, if $L_{\max}(E,r)\sin\vartheta \leq L_0$. Although we have not found a closed-form expression for the functions $\mathrm{K}_l(a,b)$ for generic values of l, it is possible to obtain explicit expressions at least for $l = 0, 1, 2$ using a symbolic integration package such as MAPLE or Wolfram Mathematica, see Appendix 5.10 for more details.

Gathering the results, one obtains

$$J_{\hat{0}}^{(\text{even})}(x) = J_{\hat{0}}^{(\text{rot})}(x) = -\frac{4\pi L_0}{N(r)R} \int\limits_{E_c(r)}^{m} dE E F_0(E) \mathrm{K}_l(a,b), \tag{5.4.11}$$

$$J_{\hat{3}}^{(\text{rot})}(x) = \frac{4\pi L_0^2}{\sqrt{N(r)}R^2} \int\limits_{E_c(r)}^{m} dE F_0(E) \left[\mathrm{K}_{l+1}(a,b) + \mathrm{K}_l(a,b)\right], \tag{5.4.12}$$

while $J_{\hat{3}}^{(\text{even})}(x) = 0$, and the remaining orthonormal components of $J_{\hat{\mu}}$ are identically zero. Here, and in the following, $R := r\sin\vartheta$ refers to the cylindrical radius, and we recall the definitions of the quantities a and b in Eq. (5.4.7). The orthonormal components of the particle current density in Eqs. (5.4.11,5.4.12) determine the invariant particle density and four-velocity of the gas:

$$n := \sqrt{-J^{\hat{\mu}} J_{\hat{\mu}}} = \sqrt{J_{\hat{0}}^2 - J_{\hat{3}}^2}, \qquad u^{\hat{\mu}} = \frac{1}{n} J^{\hat{\mu}}. \tag{5.4.13}$$

Repeating the calculations for the energy-momentum-stress tensor (see Appendix 5.9 for further details) one obtains

$$\begin{pmatrix} T_{\hat{0}\hat{0}} \\ \\ T_{\hat{0}\hat{3}} \\ \\ T_{\hat{3}\hat{3}} \end{pmatrix}(x) = \frac{4}{\sqrt{N(r)}R}\left[\frac{\pi}{2}\int\limits_{E_{\mathrm{c}}(r)}^{m} dEF_0(E)\int\limits_{-L_{\max}(E,r)\sin\vartheta}^{+L_{\max}(E,r)\sin\vartheta} dL_z I(L_z)\begin{pmatrix} \frac{E^2}{N(r)} \\ \\ \frac{-EL_z}{\sqrt{N(r)}R} \\ \\ \frac{L_z^2}{R^2} \end{pmatrix}\right.$$
$$- \int\limits_{E_{\mathrm{c}}(r)}^{m} dEF_0(E)\int\limits_{-L_{\mathrm{c}}(E)\sin\vartheta}^{+L_{\mathrm{c}}(E)\sin\vartheta} dL_z I(L_z)$$
$$\left.\times \arctan\sqrt{\frac{L_{\mathrm{c}}(E)^2 - L_z^2/\sin^2\vartheta}{L_{\max}(E,r)^2 - L_{\mathrm{c}}(E)^2}}\begin{pmatrix} \frac{E^2}{N(r)} \\ \\ \frac{-EL_z}{\sqrt{N(r)}R} \\ \\ \frac{L_z^2}{R^2} \end{pmatrix}\right], \tag{5.4.14}$$

and $T_{\hat{1}\hat{1}} = A - B$, $T_{\hat{2}\hat{2}} = A + B$ with

$$\begin{aligned} A &= \frac{2}{\sqrt{N}r^2R}\left\{\frac{\pi}{2}\int\limits_{E_{\mathrm{c}}(r)}^{m} dEF_0(E)\int\limits_{-L_{\max}(E,r)\sin\vartheta}^{+L_{\max}(E,r)\sin\vartheta} dL_z I(L_z)\left[L_{\max}(E,r)^2 - \frac{L_z^2}{\sin^2\vartheta}\right]\right. \\ &\quad - \int\limits_{E_{\mathrm{c}}(r)}^{m} dEF_0(E)\int\limits_{-L_{\mathrm{c}}(E)\sin\vartheta}^{+L_{\mathrm{c}}(E)\sin\vartheta} dL_z I(L_z)\left[L_{\max}(E,r)^2 - \frac{L_z^2}{\sin^2\vartheta}\right] \\ &\quad \left.\times \arctan\sqrt{\frac{L_{\mathrm{c}}(E)^2 - L_z^2/\sin^2\vartheta}{L_{\max}(E,r)^2 - L_{\mathrm{c}}(E)^2}}\right\}, && (5.4.15) \\ B &= \frac{2}{\sqrt{N}r^2R}\int\limits_{E_{\mathrm{c}}(r)}^{m} dEF_0(E)\int\limits_{-L_{\mathrm{c}}(E)\sin\vartheta}^{+L_{\mathrm{c}}(E)\sin\vartheta} dL_z I(L_z) \\ &\quad \times\sqrt{L_{\max}(E,r)^2 - L_{\mathrm{c}}(E)^2}\sqrt{L_{\mathrm{c}}(E)^2 - \frac{L_z^2}{\sin^2\vartheta}}. && (5.4.16) \end{aligned}$$

For the specific model (5.4.4) one obtains, recalling the definitions of a, b, $\mathrm{K}_l(a,b)$ and

$\tilde{\mathrm{K}}_l(a,b)$ in Eqs. (5.4.7,5.4.9,5.4.10):

$$T^{(\mathrm{rot})}_{\hat{0}\hat{0}}(x) = \frac{4\pi L_0}{\sqrt{N(r)^3}R} \int_{E_{\mathrm{c}}(r)}^{m} dE F_0(E) E^2 \mathrm{K}_l(a,b), \tag{5.4.17}$$

$$T^{(\mathrm{rot})}_{\hat{0}\hat{3}}(x) = -\frac{4\pi L_0^2}{N(r)R^2} \int_{E_{\mathrm{c}}(r)}^{m} dE F_0(E) E \left[\mathrm{K}_l(a,b) + \mathrm{K}_{l+1}(a,b)\right], \tag{5.4.18}$$

$$T^{(\mathrm{rot})}_{\hat{3}\hat{3}}(x) = \frac{4\pi L_0^3}{\sqrt{N(r)}R^3} \int_{E_{\mathrm{c}}(r)}^{m} dE F_0(E) \left[\mathrm{K}_l(a,b) + 2\mathrm{K}_{l+1}(a,b) + \mathrm{K}_{l+2}(a,b)\right], \tag{5.4.19}$$

$$\begin{aligned} T^{(\mathrm{rot})}_{\hat{1}\hat{1}}(x) = \frac{2\pi L_0^3}{\sqrt{N(r)}R^3} \int_{E_{\mathrm{c}}(r)}^{m} dE F_0(E) \Bigg[&\left(\frac{a^2}{b^2} - 1\right) \mathrm{K}_l(a,b) - 2\mathrm{K}_{l+1}(a,b) \\ &- \mathrm{K}_{l+2}(a,b) - \frac{a^2}{b}\frac{\sqrt{1-b^2}}{l+1}\tilde{\mathrm{K}}_l(a,0)\Bigg], \end{aligned} \tag{5.4.20}$$

$$\begin{aligned} T^{(\mathrm{rot})}_{\hat{2}\hat{2}}(x) = \frac{2\pi L_0^3}{\sqrt{N(r)}R^3} \int_{E_{\mathrm{c}}(r)}^{m} dE F_0(E) \Bigg[&\left(\frac{a^2}{b^2} - 1\right) \mathrm{K}_l(a,b) - 2\mathrm{K}_{l+1}(a,b) \\ &- \mathrm{K}_{l+2}(a,b) + \frac{a^2}{b}\frac{\sqrt{1-b^2}}{l+1}\tilde{\mathrm{K}}_l(a,0)\Bigg]. \end{aligned} \tag{5.4.21}$$

Here, the function $\tilde{\mathrm{K}}_l(a,0)$ can be expressed in terms of hypergeometric functions ${}_2F_1(a,b;c;z)$, see Appendix 5.10 for the explicit form. For the even model (5.4.3) one finds $T^{(\mathrm{even})}_{\hat{\mu}\hat{\nu}} = T^{(\mathrm{rot})}_{\hat{\mu}\hat{\nu}}$ for the diagonal elements $(\hat{\mu}\hat{\nu}) = (\hat{0}\hat{0},\hat{1}\hat{1},\hat{2}\hat{2},\hat{3}\hat{3})$, whereas all non-diagonal components (including $(\hat{\mu}\hat{\nu}) = (03)$) are zero. The orthonormal components of the energy-momentum-stress tensor allow one to construct the energy density ε and principal pressures $P_{\hat{r}}$, $P_{\hat{\vartheta}}$, $P_{\hat{\varphi}}$, which can be determined by diagonalizing $T^{\hat{\mu}}{}_{\hat{\nu}}$ [9, 64]. More specifically, $-\varepsilon$ is the eigenvalue of $T^{\hat{\mu}}{}_{\hat{\nu}}$ corresponding to the timelike eigenvector, and $P_{\hat{r}}$, $P_{\hat{\vartheta}}$, $P_{\hat{\varphi}}$ are the eigenvalues belonging to the spacelike ones. Explicitly, this yields

$$\begin{aligned} \varepsilon &= \frac{1}{2}\left[T_{\hat{0}\hat{0}} - T_{\hat{3}\hat{3}} + \sqrt{\left(T_{\hat{3}\hat{3}} + T_{\hat{0}\hat{0}}\right)^2 - 4T^2_{\hat{0}\hat{3}}}\right], && (5.4.22)\\ P_{\hat{r}} &= T_{\hat{1}\hat{1}}, && (5.4.23)\\ P_{\hat{\vartheta}} &= T_{\hat{2}\hat{2}}, && (5.4.24)\\ P_{\hat{\varphi}} &= \frac{1}{2}\left[-T_{\hat{0}\hat{0}} + T_{\hat{3}\hat{3}} + \sqrt{\left(T_{\hat{3}\hat{3}} + T_{\hat{0}\hat{0}}\right)^2 - 4T^2_{\hat{0}\hat{3}}}\right]. && (5.4.25) \end{aligned}$$

For the even model (5.4.3) one has $T^{(\mathrm{even})}_{\hat{0}\hat{3}} = 0$ and the expressions above simplify to $\varepsilon = T_{\hat{0}\hat{0}}$ and $P_{\hat{\varphi}} = T_{\hat{3}\hat{3}}$, as expected since in this case the energy-momentum-stress tensor is diagonal.

We end this subsection by observing that the support of the configuration is determined by those values of (r,ϑ) for which $L_{\mathrm{max}}(E,r)\sin\vartheta \geq L_0$ for some $E \in [E_{\mathrm{c}}(r), m]$ in the allowed range (see the comments below Eq. (5.4.10)). Since for fixed r, $L_{\text{max}}(E, r)$ is an increasing function of E, we conclude that the support of the configuration is delimited by

$$L_{\text{max}}(m, r) \sin\vartheta \geq L_0, \qquad r \geq 4M, \tag{5.4.26}$$

or

$$\frac{1}{N(r)} - 1 - \frac{L_0^2}{m^2 r^2 \sin^2\vartheta} \geq 0, \qquad r \geq 4M, \tag{5.4.27}$$

which, in the Newtonian limit, reduces to the expression in Eq. (51) of paper I with the dimensionless Kepler potential $\psi(r) = Mm/(E_0 r)$. However, in stark contrast to the nonrelativistic case, the inner boundary of the configuration cannot lie arbitrarily close to the central object even if L_0 is small. The minimal value $r = 4M$ is due to the presence of the ISOs which are absent in the Newtonian case.

5.4.3. Total particle number, energy and angular momentum of the kinetic gas cloud

In this subsection we derive expressions for the total particle number, energy and angular momentum of the gas configuration. These are the conserved quantities associated with the divergence-free currents J^μ, $J_E^\mu := -T^\mu{}_\nu k^\nu$ and $J_L^\mu := T^\mu{}_\nu v^\nu$, respectively, with $k = \partial_t$ and $v = \partial_\varphi$ the timelike and azimuthal Killing vector fields of the Schwarzschild metric. Denoting by S a spacelike Cauchy surface and by $\hat{n}$ the associated future-directed unit normal, the corresponding conserved quantities are

$$N_{\text{gas}} = -\int\limits_S J^\mu \hat{n}_\mu \eta_S, \qquad E_{\text{gas}} = -\int\limits_S J_E^\mu \hat{n}_\mu \eta_S, \qquad J_{\text{gas}} = -\int\limits_S J_L^\mu \hat{n}_\mu \eta_S, \tag{5.4.28}$$

with η_S the induced volume form on S. Choosing without loss of generality S to be a hypersurface of constant (Schwarzschild) time t with spatial coordinates (x^1, x^2, x^3), the first integral can be rewritten as [12]

$$N_{\text{gas}} = \int\limits_{\mathbb{R}^6} f(x, p_\mu dx^\mu) dx^1 dx^2 dx^3 dp_1 dp_2 dp_3, \tag{5.4.29}$$

where x is the manifold point with local coordinates (t, x^1, x^2, x^3) and $p_\mu dx^\mu \in P_x^+(m)$ is the momentum covector on the future mass shell with spatial coordinates (p_1, p_2, p_3). To make further progress, it is very useful to transform the spatial phase space coordinates (x^i, p_i) to action-angle variables $(\mathcal{Q}^i, \mathcal{J}_i)$, see for example [73]. Since the the transformation $(x^i, p_i) \mapsto (\mathcal{Q}^i, \mathcal{J}_i)$ is symplectic, the volume form transforms trivially, and one obtains

$$N_{\text{gas}} = \int\limits_{\Omega_J} \int\limits_{\mathbb{T}^3} f(x, p) d\mathcal{Q}^1 d\mathcal{Q}^2 d\mathcal{Q}^3 d\mathcal{J}_1 d\mathcal{J}_2 d\mathcal{J}_3, \tag{5.4.30}$$

with $\Omega_J \subset \mathbb{R}^3$ the range of the action variables $\mathcal{J}_i$. In the models considered in this article the DF f only depends on the integrals of motion and hence only on $\mathcal{J}_i$. Therefore, the integral over the angle variables $\mathcal{Q}^i$ is trivial and yields the simple factor $(2\pi)^3$ corresponding to the volume of the three-torus $\mathbb{T}^3$. On the other hand, the action variables can be expressed in terms of the conserved quantities (E, L, L_z), and one can show that

$$d\mathcal{J}_1 d\mathcal{J}_2 d\mathcal{J}_3 = \frac{1}{2\pi} T_r(E, L) dE dL dL_z, \tag{5.4.31}$$

where $T_r(E, L)$ denotes the period function for the radial motion (see [73] for details). This yields

$$N_{\text{gas}} = 4\pi^2 \int\limits_{\Omega} F(E, L_z) T_r(E, L) dE dL dL_z, \tag{5.4.32}$$

where Ω is the range for (E, L, L_z) corresponding to Ω_J. Similarly, one obtains the following expressions for the total energy and angular momentum:

$$\begin{aligned} E_{\text{gas}} &= 4\pi^2 \int\limits_{\Omega} E F(E, L_z) T_r(E, L) dE dL dL_z, \\ J_{\text{gas}} &= 4\pi^2 \int\limits_{\Omega} L_z F(E, L_z) T_r(E, L) dE dL dL_z. \end{aligned} \tag{5.4.33}$$

The period function can be expressed analytically in terms of Legendre's elliptic integrals and the roots $r_0 < r_1 < r_2$ of the cubic equation $r^3(E^2 - V_{m,L}(r)) = 0$, with r_1 and r_2 the turning points (see Appendix 5.7 for more details). In terms of the dimensionless quantities

$$\varepsilon := \frac{E}{m}, \quad \varepsilon_0 := \frac{E_0}{m}, \quad \lambda := \frac{L}{Mm}, \quad \lambda_0 := \frac{L_0}{Mm}, \quad \xi := \frac{r}{M}, \tag{5.4.34}$$

the period function has the form (cf. Appendix in [77])

$$T_r(\varepsilon, \lambda) = 2M\varepsilon \left[\mathbb{H}_2 - \mathbb{H}_0\right], \tag{5.4.35}$$

where

$$\begin{aligned} \mathbb{H}_0 :=& -\sqrt{\frac{\xi_{012}}{2\xi_1(\xi_2 - \xi_0)}} \\ &\times \left[(\xi_0\xi_{012} - \xi_1\xi_2)\mathbb{F}(\kappa) + \xi_1(\xi_2 - \xi_0)\mathbb{E}(\kappa) + \xi_{012}(\xi_1 - \xi_0)\Pi\left(b^2, \kappa\right)\right], \quad (5.4.36) \\ \mathbb{H}_2 :=& \sqrt{\frac{8\xi_{012}}{\xi_1(\xi_2 - \xi_0)}} \\ &\times \left[\frac{\xi_0^2}{\xi_0 - 2}\mathbb{F}(\kappa) + (\xi_1 - \xi_0)\Pi\left(b^2, \kappa\right) - \frac{4(\xi_1 - \xi_0)}{(\xi_1 - 2)(\xi_0 - 2)}\Pi\left(\beta^2, \kappa\right)\right]. \quad (5.4.37) \end{aligned}$$

Here, $\mathbb{F}(\kappa)$, $\mathbb{E}(\kappa)$, and $\Pi(b^2, \kappa)$ are Legendre's complete elliptic integrals of the first, second and third kind, respectively, as defined in [92]. Further, we have abbreviated

$\xi_{012} := \xi_0 + \xi_1 + \xi_2$ and have defined

$$b := \sqrt{\frac{\xi_2 - \xi_1}{\xi_2 - \xi_0}}, \quad \kappa := \sqrt{\frac{\xi_0}{\xi_1}}b, \quad \beta := \sqrt{\frac{\xi_0 - 2}{\xi_1 - 2}}b. \tag{5.4.38}$$

Using the DF (5.4.1) for the models (5.4.2-5.4.4) and taking into account that $T_r(E, L)$ is independent of L_z, the integral over L_z in Eq. (5.4.32) can be computed explicitly, and one obtains for both the (rot) and (even) models

$$\frac{N_{\text{gas}}}{M^3 m^3 \alpha} = 4(2\pi)^2 \frac{\lambda_0}{l+1} \int\limits_{\varepsilon_{\min}}^{1} d\varepsilon\, \varepsilon \left(1 - \frac{\varepsilon}{\varepsilon_0}\right)_+^{k-\frac{3}{2}} \int\limits_{\lambda_c(\varepsilon)}^{\lambda_{\text{ub}}(\varepsilon)} d\lambda\, (\mathbb{H}_2 - \mathbb{H}_0) \left(\frac{\lambda}{\lambda_0} - 1\right)_+^{l+1}. \tag{5.4.39}$$

The remaining two integrals on the right-hand side of Eq. (5.4.39) are computed numerically. For this, it is very useful to perform a further change of variables from (ε, λ) to (p, e) which generalize the ”semi-latus rectum.ªnd eccentricity to the Schwarzschild case (see [105, 106]). These new variables are related to the turning points through

$$\xi_1 = \frac{p}{1+e}, \quad \xi_2 = \frac{p}{1-e}. \tag{5.4.40}$$

The main advantage of this transformation is the fact that it maps the region of integration to the simpler region $0 < e < 1$ and $p > 6 + 2e$. Furthermore, the third root ξ_0 and the dimensionless energy and angular momentum can be expressed explicitly in terms of (p, e) as

$$\xi_0 = \frac{2p}{p-4}, \quad \varepsilon = \sqrt{\frac{(p-2)^2 - 4e^2}{p\,(p - e^2 - 3)}}, \quad \lambda = \frac{p}{\sqrt{p - e^2 - 3}}, \qquad p > 6 + 2e, \tag{5.4.41}$$

see Eqs. (5.7.3,5.7.4) in Appendix 5.7. Further, using Eqs. (5.7.4,5.7.5) one obtains

$$\varepsilon d\varepsilon d\lambda = \frac{e\left[(p-6)^2 - 4e^2\right]}{2p\sqrt{(p - e^2 - 3)^5}} de dp. \tag{5.4.42}$$

Gathering these results yields the final expression for the total particle number:

$$\frac{N_{\text{gas}}}{M^3 m^3 \alpha} = \frac{8\pi^2 \lambda_0}{l+1} \int\limits_0^1 dee \int\limits_{6+2e}^{\infty} dp \frac{(p-6)^2 - 4e^2}{p\sqrt{(p - e^2 - 3)^5}} \left(1 - \frac{\varepsilon}{\varepsilon_0}\right)_+^{k-\frac{3}{2}} \left(\frac{\lambda}{\lambda_0} - 1\right)_+^{l+1} (\mathbb{H}_2 - \mathbb{H}_0). \tag{5.4.43}$$

The corresponding expression for the total energy E_{gas} is obtained from this by adding the factor $E = m\varepsilon$ in the integrand on the right-hand side of Eq. (5.4.43). The total angular momentum is obtained from a similar calculation, starting from Eq. (5.4.33), and yields

$$\begin{aligned} \frac{J_{\text{gas}}^{(\text{rot})}}{M^4 m^4 \alpha} &= \frac{8\pi^2 \lambda_0^2}{l+1} \int\limits_0^1 dee \int\limits_{6+2e}^{\infty} dp \frac{(p-6)^2 - 4e^2}{p\sqrt{(p - e^2 - 3)^5}} \left(1 - \frac{\varepsilon}{\varepsilon_0}\right)_+^{k-\frac{3}{2}} \\ &\times \left[\left(\frac{\lambda}{\lambda_0} - 1\right)_+^{l+1} + \frac{l+1}{l+2}\left(\frac{\lambda}{\lambda_0} - 1\right)_+^{l+2}\right] (\mathbb{H}_2 - \mathbb{H}_0), \end{aligned} \tag{5.4.44}$$

whereas $J_{\text{gas}}^{(\text{even})} = 0$.
These expressions simplify considerably in the Newtonian limit, in which $\lambda_0 \gg 1$. Since $\lambda \sim \sqrt{p}$ for large values of λ, this implies that $p \gg 1$, and using the asymptotic expressions

$$\xi_0 = 2 + \frac{8}{p} + \mathcal{O}(p^{-2}), \tag{5.4.45}$$

$$b = \sqrt{\frac{2e}{1+e}}\left[1 + \mathcal{O}(p^{-1})\right], \quad \kappa = 2\sqrt{\frac{e}{p}}\left[1 + \mathcal{O}(p^{-1})\right],$$

$$\beta = \frac{4\sqrt{e}}{p}\left[1 + \mathcal{O}(p^{-1})\right], \tag{5.4.46}$$

$$\varepsilon = 1 - \frac{1-e^2}{2p} + \mathcal{O}(p^{-2}), \quad \mathbb{H}_2 - \mathbb{H}_0 = \pi\left(\frac{p}{1-e^2}\right)^{3/2}\left[1 + \mathcal{O}(p^{-1})\right], \tag{5.4.47}$$

one finds, choosing $\varepsilon_0 = E_0/m = 1$,

$$\begin{aligned}
\frac{N_{\text{gas}}}{M^3 m^3 \alpha} &\simeq \frac{\pi^3}{2^{k-\frac{9}{2}}} \frac{1}{(l+1)\lambda_0^l} \int_0^1 de\, e(1-e^2)^{k-3} \int_{\lambda_0^2}^{\infty} \frac{dp}{p^{k-\frac{3}{2}}} \left(\sqrt{p} - \lambda_0\right)_+^{l+1} \\
&= \frac{\pi^3}{2^{k-\frac{11}{2}}} \frac{\Gamma(l+1)\Gamma(2k-l-6)}{\Gamma(2k-3)} \frac{1}{\lambda_0^{2k-6}}.
\end{aligned} \tag{5.4.48}$$

This agrees with the corresponding expression for the total rest mass of the Newtonian model, see Eq. (C7) in paper I with $\chi = 0$, $E_0 = mc^2$ and taking into account that in natural units M should be replaced with the gravitational radius $r_g := GM/c^2$ and m with mc in the left-hand side of Eq. (5.4.48). Likewise, the internal energy, $E_{\text{gas}} - mN_{\text{gas}}$, reduces to the corresponding expression in the Newtonian limit for large values of λ_0,

$$\frac{E_{\text{gas}} - mN_{\text{gas}}}{M^3 m^4 \alpha} \simeq -\frac{\pi^3}{2^{k-\frac{9}{2}}} \frac{\Gamma(l+1)\Gamma(2k-l-4)}{\Gamma(2k-1)} \frac{1}{\lambda_0^{2k-4}}, \tag{5.4.49}$$

see Eq. (C8) in paper I.
In order to analyze the differences between the relativistic and non-relativistic cases, we evaluate numerically the expression in Eq. (5.4.43) for the total particle number and compare it with the analogous expression from Eq. (C7) in paper I with $E_0 = mc^2$ for the Newtonian model in the Kepler and isochrone potentials (the latter being regular at the center). This comparison is shown in figure **5-3** for different values of the parameters (k, l) and the parameter values $\kappa = 0$ (corresponding to the Kepler potential) and $\kappa = 1$ characterizing the isochrone potential. For large values of λ_0, the three descriptions show the same behavior, as expected. However, the relativistic configurations have a smaller total rest mass than their non-relativistic counterparts for $\lambda_0 \lesssim 1$ while their mass is slightly larger for some intermediate values of λ_0 lying in a small interval between 1 and 10. Similarly, in figure **5-4** we provide a comparison

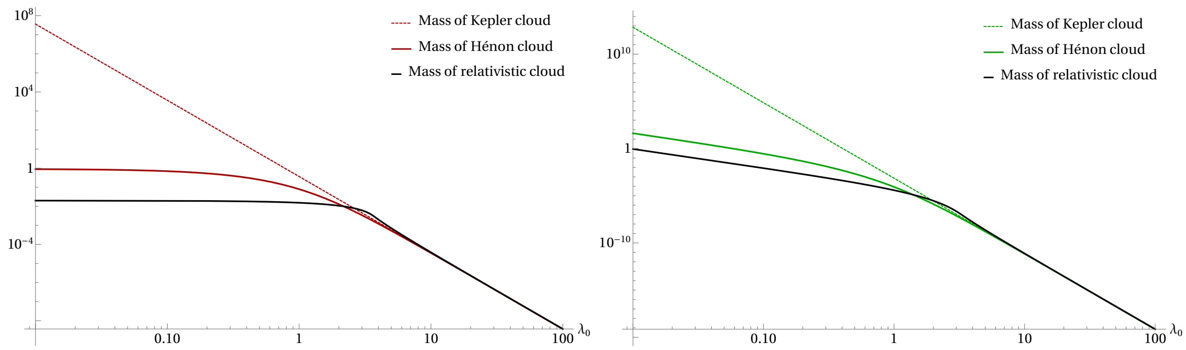

Figure 5-3: Comparison between the total mass in the Newtonian case with the Kepler ($\kappa = 0$) and isochrone ($\kappa = 1$) potentials and the total rest mass mN_{gas} in the relativistic case as a function of λ_0 for different values of (k, l). In all cases, the total mass is normalized by the factor $\alpha r_g^3 m^4 c^3$. Left panel: $(k, l) = (5, 0)$. Right panel: $(k, l) = (7, 2)$.

between the internal energy $E_{\text{gas}} - mN_{\text{gas}}$ in the relativistic and Newtonian cases. As in the total mass case, we note that the three descriptions agree with each other when λ_0 is large, while for small values of λ_0 the relativistic internal energy has the smallest absolute value.

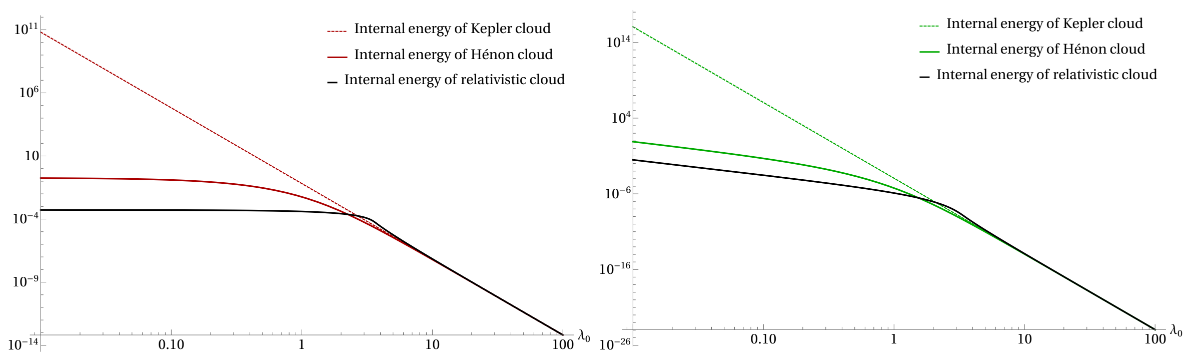

Figure 5-4: Comparison between the (absolute value of the) internal energy for the same configurations as in the previous figure. In all cases, the energy is normalized by the factor $\alpha r_g^3 m^4 c^5$.

In the next section we discuss the properties of the spacetime observables associated with the relativistic gas configurations, keeping fixed the total particle number computed from Eq. (5.4.43).

5.5. Properties of the spacetime observables

In this section we discuss the properties of the spacetime observables derived from the particle current density vector and the energy-momentum-stress tensor. For definiteness, we focus our attention on the particle density, the kinetic temperature, the pressure anisotropy, and we compare their properties with those of the corresponding Newtonian model in paper I. Recall that these quantities depend on the amplitude α of the DF and the dimensionless parameters ε_0, λ_0 (see Eq. (5.4.34)), k and l. As explained previously, we choose the maximum value $\varepsilon_0 = 1$ in all the results shown, which leads to an infinitely extended cloud. The cut-off value λ_0 for the azimuthal angular momentum is an arbitrary positive parameter, while $l \geq 0$ and $k > 7/2 + l/2$ is necessary in order to guarantee a finite total particle number, energy and angular momentum. In the following, we compare configurations of equal total particle number N_{gas}, which fixes the amplitude α. At the end of this section we also compare our kinetic configurations with the well-known ”polish doughnuts”based on a perfect fluid model.

5.5.1. Normalized particle density and morphology of the gas cloud

In this subsection we discuss the properties of the normalized particle density

$$\bar{n}(\xi, \vartheta) := M^3 \frac{n(\xi, \vartheta)}{N_{\text{gas}}}, \tag{5.5.1}$$

which can be computed from Eqs. (5.4.13) and (5.4.43) for both the even and rotating models. Although both models have the same total particle number N_{gas}, their particle densities differ from each other, $n^{(\text{even})} \neq n^{(\text{rot})}$, which is due to the fact that n depends on the $\hat{3}$-component of J. After fixing $\varepsilon_0 = 1$ the quantity $\bar{n}(\xi, \vartheta)$ depends only on λ_0, k and l, as discussed above. In figures **5-5** and **5-6** we show the profiles of $\bar{n}$ and $\bar{n}\xi^2$ on the equatorial plane ($\vartheta = \pi/2$) for different values of the free parameters for the rotating model. As is visible from these plots, the configurations become more compact as l decreases or k increases. This is the same qualitative behavior as in the Newtonian case, see paper I.

The morphology of the particle density for configurations with $(k, l) = (5, 1)$ and $\lambda_0 = 4$ and $\lambda_0 = 1$ is shown in figure **5-7** for the rotating case and reveals the toroidal-like structure of the configuration. As can also be seen from this plot, the particle density is everywhere regular, has a maximum at some circle lying in the equatorial plane, and decays for large radii. Note also the difference in the shape of the disk near the black hole in the two cases. For $\lambda_0 = 1$ the inner boundary has a spherical part (with radius equal to $4M$, i.e. the radius of the marginally bound orbits) delimited by two cusps, whereas for $\lambda_0 = 4$ the inner part of the disk is wedge-like. This is related to the fact that when $\lambda_0 \leq 4$, the ISOs become occupied, which yields a change of behavior in the minimum radius.

The differences in the profiles of the particle density between the even and rotating cases is small in all cases we have examined. As an example, we show in figure **5-9**

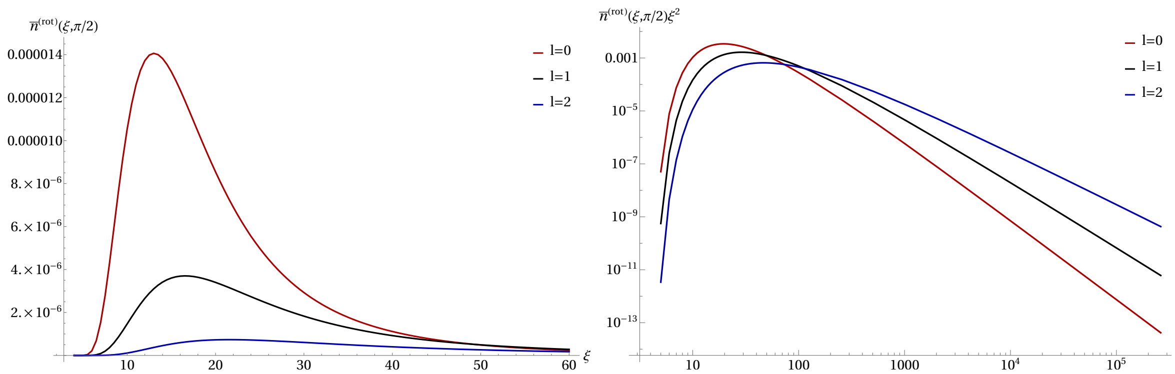

Figure 5-5: Normalized particle density $\bar{n}^{(\mathrm{rot})}$ (left panel) and $\bar{n}^{(\mathrm{rot})}$ times the square radius (right panel) as a function of the dimensionless radius ξ in the equatorial plane for $k = 5$, $l = 0, 1, 2$, $\lambda_0 = 4$. As l increases, the location of the maximum moves outwards, as expected. Although configurations with smaller values of l have a higher maximum of $\bar{n}^{(\mathrm{rot})}$, we see that they eventually intersect the curves belonging to higher values of l and they decay faster for large ξ, as is visible from the plot in the right panel.

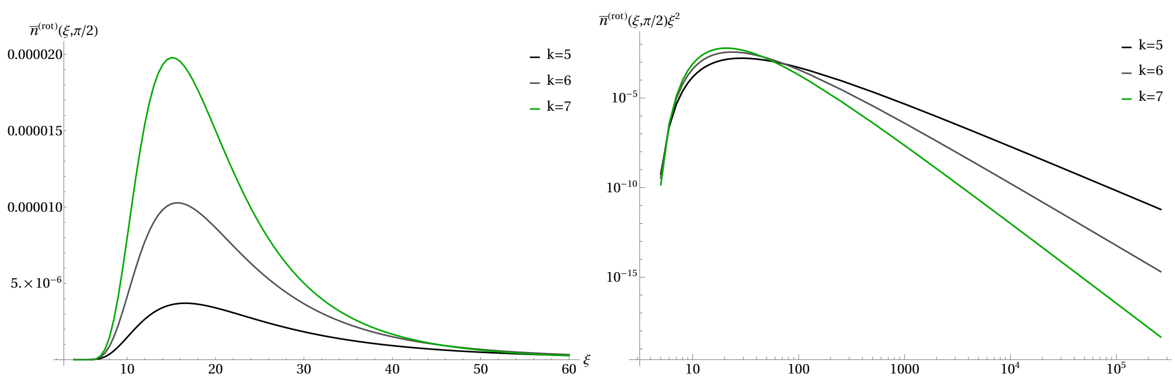

Figure 5-6: Same as previous plot for the parameter values $l = 1$, $k = 5, 6, 7$ and $\lambda_0 = 4$.

the relative difference $n^{(\mathrm{even})}/n^{(\mathrm{rot})} - 1$ between the two models for different values of (k, l) and $\lambda_0 = 4$. The maximum relative difference is about 0.414 and occurs at the inner radius of the disk.

Finally, in figure **5-8** we compare the particle density profiles and compare them with the corresponding profiles of the nonrelativistic models with the Kepler ($\kappa = 0$) and isochrone potentials ($\kappa = 1$). As expected, these profiles agree with each other for large values of ξ. However, the nonrelativistic configurations have an inner radius that is larger than their relativistic counterparts, and hence the relativistic and nonrelativistic profiles are considerably different from each other for smaller values of ξ.

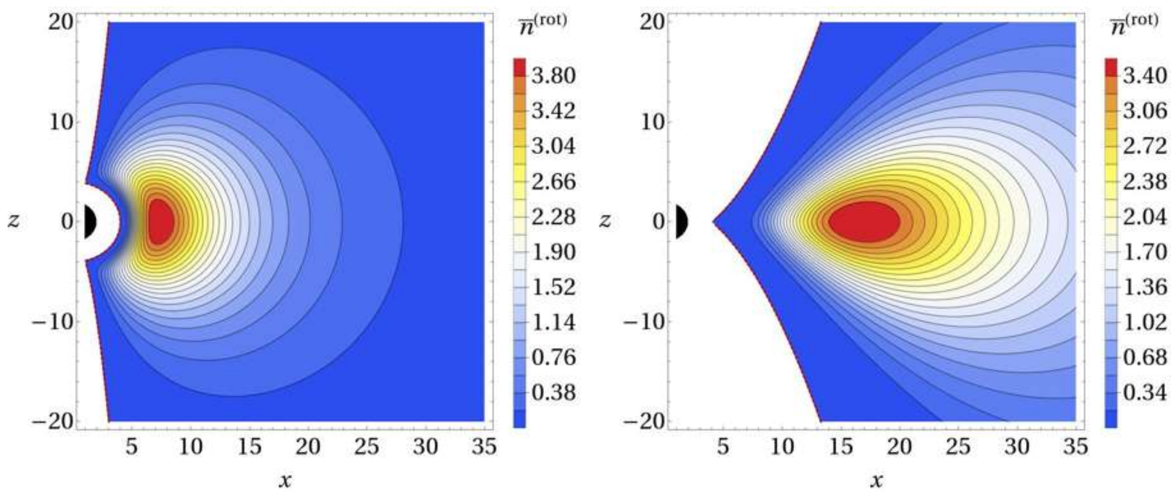

Figure 5-7: Contour plot of the normalized particle density $\bar{n}^{(\mathrm{rot})}$ in the xz-plane for $(k, l) = (5, 1)$. In the left panel $\lambda_0 = 1$ and the scale is 1×10^{-5} while in the right panel $\lambda_0 = 4$ and the scale is 1×10^{-6}. The dashed red line, computed using Eq. (5.4.27), denotes the boundary of the corresponding kinetic gas cloud, while the black region represents the black hole.

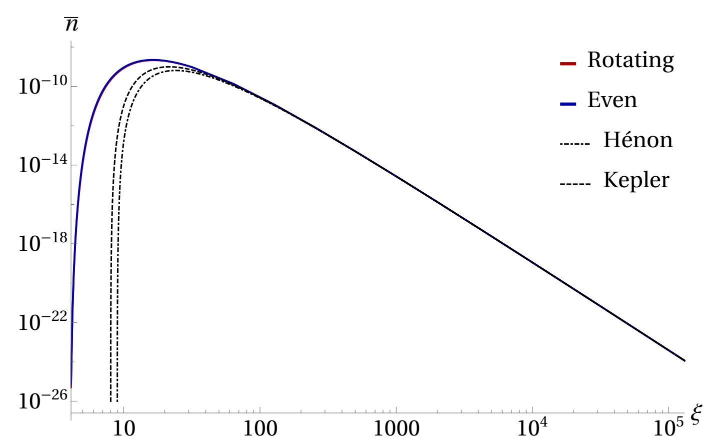

Figure 5-8: Comparison of the particle density between the even (blue) and rotating (red) models and the corresponding nonrelativistic models for $(k, l) = (5, 1)$ and $\lambda_0 = 4$. The difference between the first two models is not visible in this plot. The relative difference is shown in the next plot.

5.5.2. Kinetic temperature

As in paper I, we define the kinetic temperature T through the ideal gas equation $nk_BT = \overline{P}$ with the average pressure $\overline{P} := (P_{\hat{r}} + P_{\hat{\vartheta}} + P_{\hat{\varphi}})/3$ and the particle density n. We show the equatorial temperature profile in figure **5-10** for the cases $\lambda_0 = 4$ and $(k, l) = (4, 0)$ and $(k, l) = (5, 1)$ and the rotating model, along with the corresponding results in the Newtonian cases. The behavior is qualitatively similar to the profile of the

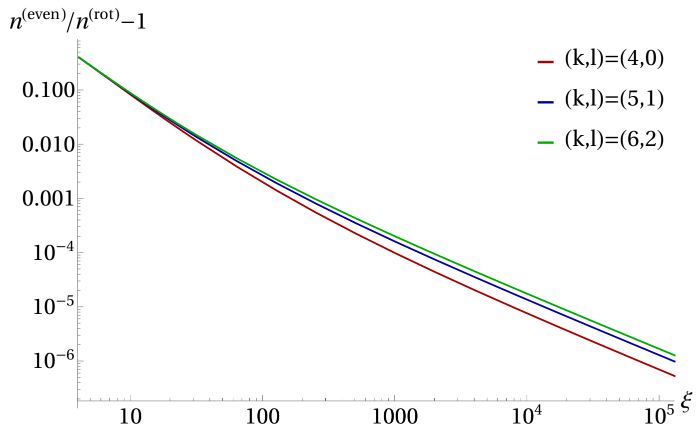

Figure 5-9: Relative difference $n^{(\text{even})}/n^{(\text{rot})} - 1$ between the even and rotating models for $(k,l) = (4,0)$ (red), $(k,l) = (5,1)$ (blue), $(k,l) = (6,2)$ (green), and $\lambda_0 = 4$.

particle number density.

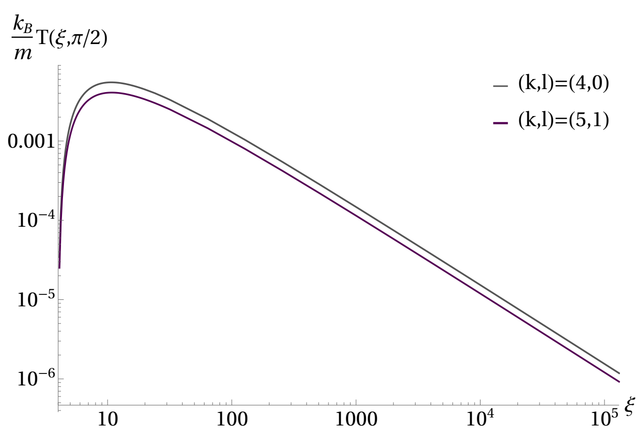

Figure 5-10: Equatorial kinetic temperature profiles for the model with parameter values $(k,l) = (4,0)$ and $(5,1)$ and $\lambda_0 = 4$.

5.5.3. Pressure anisotropy

Figures **5-12** and **5-13** show the principal pressures as a function of the dimensionless areal coordinate $\xi = r/M$ on the equatorial plane for the rotating model. Note that for $\lambda_0 = 1$ these pressures are different from each other, while for $\lambda_0 \geq 4$ the principle pressures $P_{\hat{r}}$ and $P_{\hat{\vartheta}}$ corresponding to the radial and polar directions are always equal to each other. This can be understood by realizing that the expressions (5.4.20,5.4.21) differ from each other only in the sign of the last term in the integrand. However, this term is proportional to $\tilde{\mathbf{K}}_l(a,0)$ which vanishes if $\lambda_0 \geq 4$. As expected, for large values

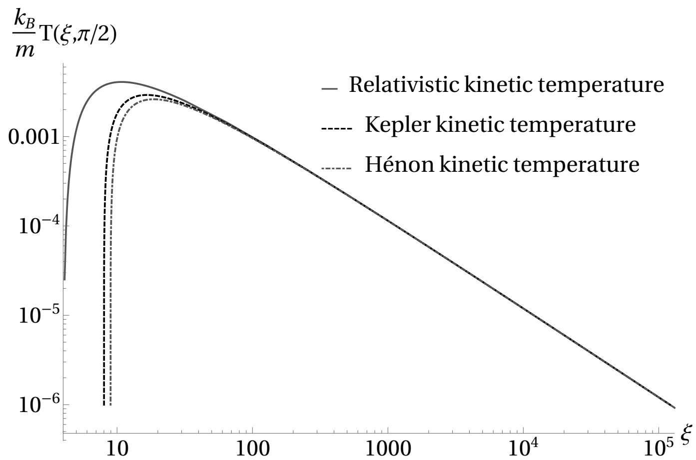

Figure 5-11: Equatorial kinetic temperature profile for the model with parameter values $k = 5$, $l = 1$ and $\lambda_0 = 4$ in the relativistic and Newtonian cases.

of ξ, the results agree with the corresponding results from the Newtonian models discussed in paper I. As seen from the plots in figure **5-13**, as r increases from its value at the inner edge of the configuration to large values, the radial pressure decays while the azimuthal pressure increases monotonically.

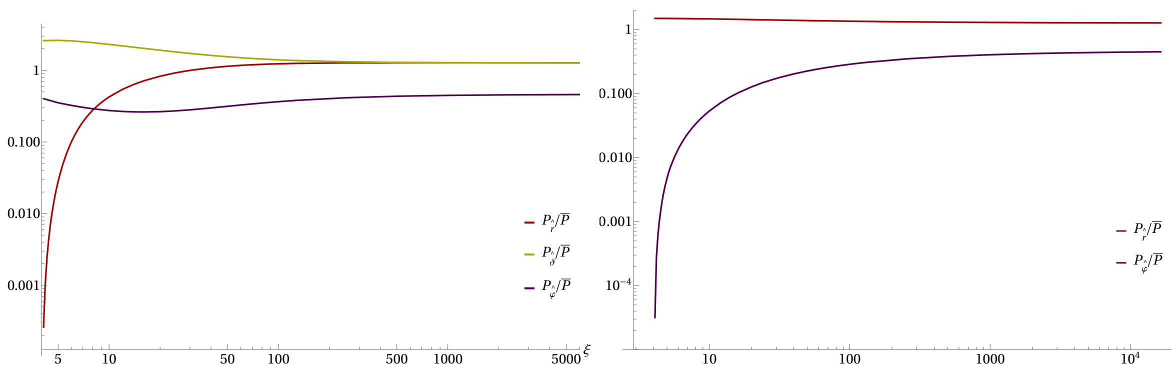

Figure 5-12: Log-log plot showing the behavior of the principal pressures (normalized by the average pressure $\overline{P}$) as a function of the areal radius r in the equatorial plane for the parameter values $k = 5$, $l = 1$, $\varepsilon_0 = 1$ and the rotating model. Left panel: $\lambda_0 = 1$. Note that in this case the three pressures are different from each other, with $P_{\hat{r}}$ converging to $P_{\hat{\vartheta}}$ for large r. Right panel: $\lambda_0 = 4$. In this case, $P_{\hat{r}} = P_{\hat{\vartheta}}$ everywhere.

5.5.4. Comparison with fluid model

We end this section by comparing our kinetic configurations to the well-known ”polish doughnuts”hydrodynamics configurations whose construction is briefly reviewed

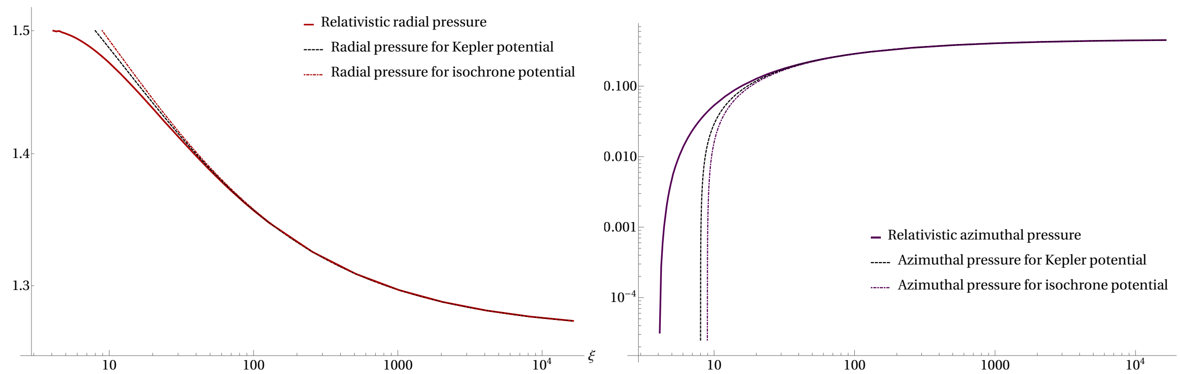

Figure 5-13: Behavior of the principal pressures $P_{\hat{r}}$ and $P_{\hat{\varphi}}$ (normalized by the average pressure $\overline{P}$) as a function of the areal radius r in the equatorial plane (note that we use a logarithmic scale in r) for the parameter values $k = 5, l = 1$, $\varepsilon_0 = 1$, $\lambda_0 = 4$ and the rotating model. For comparison, we also show the corresponding results from the Newtonian case with the Kepler ($\kappa = 0$) and the isochrone ($\kappa = 1$) potentials. Left panel: The principal pressure $P_{\hat{r}}$ corresponding to the radial direction. Right panel: Principal pressure $P_{\hat{\varphi}}$ corresponding to the azimuthal direction. Note that the inner radius of the Newtonian configurations is located at $\xi = 8$ (for the Kepler case) and $\xi = 4\sqrt{5} \simeq 8.94$ (for the isochrone potential with $\kappa = 1$) while the relativistic configurations have their inner edge located at $\xi = 4$. As this inner radius is approached, $P_{\hat{\varphi}}/\overline{P}$ converges to zero in all cases. As expected, for large values of r, the relativistic and Newtonian profiles agree with each other.

in Appendix 5.11. We start with the comparison of the boundary surface delimiting the support of the gas. In the kinetic case, this boundary is determined by Eq. (5.4.27). Written in terms of the dimensionless quantities introduced in Eq. (5.4.34) this gives

$$\frac{2}{\xi - 2} - \frac{\lambda_0^2}{\xi^2 \sin^2 \vartheta} \geq 0, \qquad \xi \geq 4, \tag{5.5.2}$$

which is equivalent to the condition $\xi \geq \xi_{\text{min}}(\vartheta)$ with

$$\xi_{\text{min}}(\vartheta) := \begin{cases} \dfrac{\lambda_0^2}{4 \sin^2 \vartheta} \left[1 + \sqrt{1 - \dfrac{16 \sin^2 \vartheta}{\lambda_0^2}} \right] & \text{if} \quad 4 \sin \vartheta \leq \lambda_0, \\ 4 & \text{if} \quad 4 \sin \vartheta > \lambda_0. \end{cases} \tag{5.5.3}$$

In the fluid case, restricting ourselves to the region $r > 4M$, the boundary surface is determined by the level one set of the enthalpy function h. According to Eq. (5.11.15), this yields precisely the same condition $\xi \geq \xi_{\text{min}}(\vartheta)$ where now λ_0 stands for the (constant) azimuthal angular momentum per energy of the fluid elements divided by M.

As explained in paper I, this coincidence is due to the fact that as one approaches the boundary surface from the inside of the fluid configuration, the pressure's gradient converges to zero implying that the fluid elements follow timelike geodesics with specific azimuthal angular momentum $M\lambda_0$, as in the kinetic case.
Although the boundary surface in the kinetic and fluid models coincide exactly with each other, the structure of the interior cloud cannot be identical in both models. Indeed, in the fluid model, the pressure is enforced to be isotropic and each fluid element has constant azimuthal angular momentum per energy along the stream lines, whereas in the kinetic model, the pressure is anisotropic and the gas particles' azimuthal angular momenta obey the distributions $I^{(\text{even})}$ or $I^{(\text{rot})}$, see Eqs. (5.4.3,5.4.4).
In order to compare both model's morphology with each other, for the following we use the particle density n and the temperature T. In the fluid case, we assume a polytropic equation of state $P = Kn^\gamma$ with K a constant and γ the adiabatic index subject to $1 < \gamma \leq 2$, and obeying the ideal gas equation $P = nk_BT$. Integrating the first law one obtains the following relation between the specific enthalpy h, n and T (see Appendix 5.11 for details):

$$h - 1 = \frac{\gamma}{\gamma - 1}\frac{K}{\bar{m}}n^{\gamma-1} = \frac{\gamma}{\gamma - 1}\frac{k_B}{\bar{m}}T, \tag{5.5.4}$$

with $\bar{m}$ the averaged rest mass per particle. Figure **5-14** shows the normalized (with respect to its maximum value) density and temperature profiles for the fluid and the kinetic models with different values of (k, l) and $\lambda_0 = 4$. As in the Newtonian case, the fluid configurations are more compact and slightly hotter than the kinetic ones. Nevertheless, remarkably, the equatorial temperature profile of the fluid configuration (which is independent of the adiabatic index γ) agrees very well with the corresponding profile of the kinetic model with $(k, l) = (4, 0)$ or $(k, l) = (5, 1)$. A quantitative comparison between the locations and values of the maximum temperature in both models are given in table **5-1**. These values should be compared with the corresponding values reported in Table III of paper I.

5.6. Conclusions

In this work we derived analytic solutions describing relativistic stationary and axisymmetric collisionless kinetic gas clouds consisting of identical massive neutral particles surrounding a non-rotating black hole. Based on the assumption that the gravitational field is dominated by the black hole, the self-gravity of the gas is neglected, such that the gas particles follow bound geodesic orbits in the Schwarzschild exterior spacetime. As we have shown, our gas configurations agree with their non-relativistic counterparts constructed in paper I [47] in the limit in which the angular momentum cut-off parameter L_0 tends to infinity. The one-particle DF in our models depends on the energy

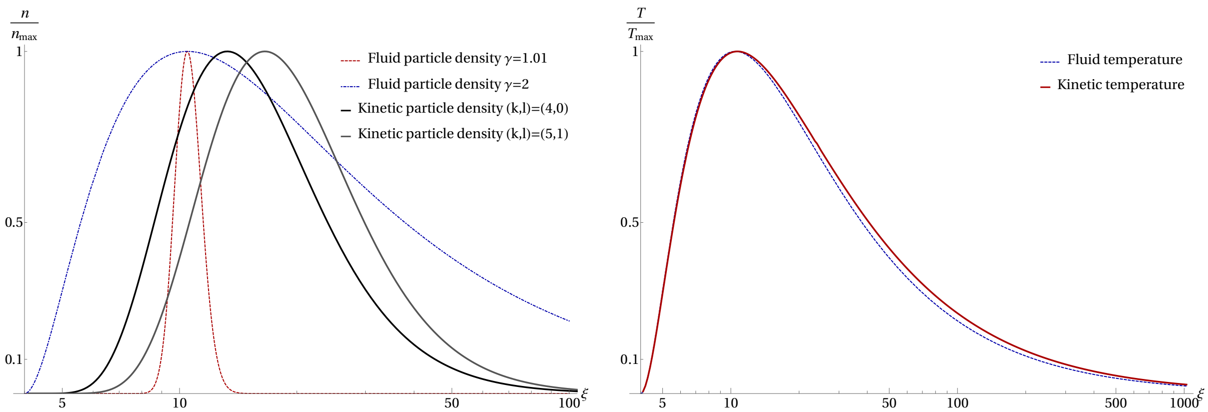

Figure 5-14: Normalized profiles between the kinetic and fluid descriptions. The left panel shows the profile of the particle density for the fluid model in the extreme cases with adiabatic indices $\gamma = 1.01$ (dashed red) and $\gamma = 2$ (dotted dashed blue) and the corresponding particle density for the rotating kinetic models with $(k, l) = (4, 0)$ (black) and $(k, l) = (5, 1)$ (gray). The right panel shows the normalized profile for the fluid (dashed blue) and kinetic temperature with $(k, l) = (4, 0)$ (red). The temperature profile for the kinetic model with $(k, l) = (5, 1)$ lies almost on the top of the profile for the $(k, l) = (4, 0)$ model, and thus it is not plotted. In both panels the normalization is chosen such that the maximum is one.

E and the azimuthal component of the angular momentum L_z of the particles through the generalized polytropic ansätze (5.4.1,5.4.2,5.4.3,5.4.4) describing both rotating and nonrotating stationary and axisymmetric configurations. In the rotating case all particles have positive values of L_z larger than some cut-off value L_0, giving rise to a net angular momentum while in the nonrotating case the DF is an even function of L_z. We have derived explicit expressions for the spacetime observables in terms of a single integral over a function depending solely on the energy. This has been achieved by rewriting the fibre integrals over the particles' momenta as integrals over the constants of motion E, L and L_z. A challenging problem in this change of variables is the determination of the correct range of integration over which E, L and L_z vary, as this range depends on the observer's radius r. The result which was derived in section 5.3.3 and Appendix 5.8 is summarized in Eqs. (5.3.19, 5.3.20,5.3.21,5.3.22), and it should have applications extending beyond the ones given in the current work.

By choosing the polytropic index k sufficiently large, it follows from the asymptotic analysis in paper I that our configurations have finite total particle number, energy and angular momentum. By introducing action-angle variables we have been able to reduce the expressions for these total quantities to a triple integrals which involve the period function $T_r(E, L)$ describing the period of the radial motion for an orbit with energy E and total angular momentum L. For our models, the integral over L_z can be performed

Table 5-1: Top row: Ratio between the radii corresponding to the maxima of the fluid and kinetic temperature profiles. Bottom row: Ratio between the corresponding maxima of the temperature. Here we choose $(k, l) = (5, 1)$, and in the fluid case the adiabatic index is determined as in Paper I, i.e. $\gamma = \gamma^{(\text{kinetic})}$ which fits the asymptotic decay of the kinetic configuration. Three significant figures are shown.

	$\lambda_0 = 4$	$\lambda_0 = 7$	$\lambda_0 = 10$
$\frac{r_{\text{max}}^{(\text{fluid})}}{r_{\text{max}}^{(\text{kinetic})}}$	0.970	0.970	0.968
$\frac{m}{\bar{m}} \frac{T_{\text{max}}^{(\text{fluid})}}{T_{\text{max}}^{(\text{kinetic})}}$	1.31	1.30	1.30

analytically, which leaves a double integral over E and L. To perform this integral, we used the fact that for the case of a Schwarzschild spacetime, $T_r(E, L)$ can be expressed in terms of Legendre's elliptic integrals whose arguments depend on the eccentricity and the "semi-latus rectum", and one ends up with a numerical integral over these new variables. The behavior of the total quantities was compared with those of the corresponding non-relativistic quantities, and we have verified that they agree with each other in the limit $L_0 \to \infty$, see figures **5-3** and **5-4**.

In addition to the aforementioned total quantities, we have computed and analyzed the behavior of the particle density, the principal pressures, and the kinetic temperature as a function of the free parameters k, l, E_0, L_0 in our models (the first two corresponding to the polytropic indices and the last two describing the cut-off parameters associated with the energy and angular momentum). We have shown that these quantities agree with their non-relativistic counterparts computed in paper I in the limit in which L_0 tends to infinity. However, when $L_0/(Mm)$ is of the order one or smaller, several relativistic effects become visible. The most important difference consists in the morphology of the inner part of the torus. In the Newtonian case the boundary surface is completely smooth and its minimum radius shrinks continuously to zero as $L_0 \to 0$. However, in the relativistic case, there are no bound orbits at all in the region $r < 4M$. This is due to the presence of the maximum of the effective potential $V_{m,L}$ which drops below the asymptotic value m^2 of $V_{m,L}$ when $L_0/(Mm) < 4$. Hence, in this case, the minimum inner radius is given by the location of the turning point of the orbit with maximum energy $E = m$ for orbits with $L > 4Mm$, while for $L < 4Mm$ this inner radius is determined by the ISOs. This transition leads to the two cusps which are visible in the left panel of figure **5-7**. Another relativistic effect that appears when L_0 drops below $4Mm$ can be seen from the pressure anisotropies: in this case the three principal pressures are different from each other (see figures **5-12**) while for $L_0 \geq 4Mm$ the radial and polar principal pressures are always equal to each other, like in the Newtonian case. As explained in the article, this is again related to the presence of the ISOs. Finally, though less dramatic, a further relativistic effect is related to the difference between the particle density in the even and rotating models. In the Newtonian case the density is exactly equal in both models. In contrast, in the relativistic case the, this density is slightly larger in the even model as shown in the figure **5-9**. This is due to the fact that the relativistic invariant particle density n depends on all components of the current density four-vector, see Eq. (5.4.13). Therefore, even though the orthonormal component $J_{\hat{0}}$ in the time direction coincides exactly in both models, the presence of the azimuthal component in the rotating case diminishes the invariant particle density n.

Finally, we have compared our kinetic configurations with their hydrodynamic analogues, namely the well-known "polish doughnutsçonfigurations. This comparison revealed the following properties: (i) by matching the value of the cut-off parameter $L_0/(Mm)$ with the (constant) fluid angular momentum ℓ, we have shown that both configurations are delimited by exactly the same boundary surface. (ii) The normalized equatorial radial profile of the particle density has its maximum lying closer to the black hole in the fluid case, meaning that the fluid configurations are generally more compact than the kinetic ones. (iii) Surprisingly however, the normalized equatorial radial profile of the temperature, which is independent of the adiabatic index in the fluid case and largely insensitive to the polytropic indices (k, l) in the kinetic case, is very similar in both cases (see the right panel of figure **5-14**). This correspondence was also found in the nonrelativistic configurations of paper I. Like in the Newtonian case, choosing the adiabatic index such that it fits the asymptotic temperature decay of the kinetic configuration, it was found that the fluid configurations are slightly hotter than the kinetic ones as can be inferred from table **5-1**.

We close this article by emphasizing that, although they have finite total rest mass, energy and angular momentum, the configurations we have considered in this article extend all the way to infinity. A related model in which the function $I(L_z)$ is replaced by a function of L_z/L in Eq. (5.4.1) was studied in [48]. Solutions with finite support could also have been considered by choosing $E_0 < m$ instead of $E_0 = m$ in the ansatz (5.4.2). The recent work by Jabiri [102, 103] suggests that the effects from the self-gravity can be included for such finite configurations, provided the amplitude of the DF is sufficiently small. It should also be interesting to generalize the models studied here to a rotating (Kerr) black hole or to include effects from binary collisions or an electromagnetic field. We leave these generalizations to future work.

5.7. Appendix A: Parametrization of bound trajectories in terms of the variables (p, e)

In this appendix we recollect some useful formulae that can be used to parametrize the spatially bound timelike geodesics in the Schwarzschild exterior. In the body of the article these orbits have mainly been parametrized in terms of the conserved quantities (E, L), corresponding to the energy and total angular momentum of the particle. Here we show that these orbits can also be parametrized in terms of their turning points (r_1, r_2) or the associated dimensionless "semi-latus rectum" p and eccentricity e defined by $r_1 = Mp/(1+e)$, $r_2 = Mp/(1-e)$. For more details and generalizations to the Kerr spacetime, see Refs. [77, 105, 106].
The turning points are determined by the equation $V_{m,L}(r) = E^2$, which, in terms of the dimensionless variables introduced in Eq. (5.4.34) yields the following quartic equation for $\xi = r/M$:

$$R(\xi) := \xi\left[\left(\varepsilon^2 - 1\right)\xi^3 + 2\xi^2 - \lambda^2\xi + 2\lambda^2\right] = 0. \tag{5.7.1}$$

For bound orbits, there are four real roots 0, ξ_0, ξ_1, and ξ_2 of $R(\xi)$ satisfying $0 < \xi_0 < \xi_1 < \xi_2$, the largest two ones corresponding to the turning points. Comparing Eq. (5.7.1) with $R(\xi) = (\varepsilon^2 - 1)\xi(\xi - \xi_0)(\xi - \xi_1)(\xi - \xi_2)$ one obtains the following relations between the conserved quantities (ε, λ) and the roots ξ_0, ξ_1 and ξ_2:

$$\varepsilon^2 = 1 - \frac{2}{\xi_0 + \xi_1 + \xi_2}, \qquad \lambda^2 = \frac{\xi_0\xi_1\xi_2}{\xi_0 + \xi_1 + \xi_2}, \qquad 2 = \frac{\xi_0\xi_1\xi_2}{\xi_0\xi_1 + \xi_0\xi_2 + \xi_1\xi_2}. \tag{5.7.2}$$

The last relation allows one to express the roots explicitly in terms of (p, e):

$$\xi_0 = \frac{2p}{p-4}, \qquad \xi_1 := \frac{p}{1+e}, \qquad \xi_2 := \frac{p}{1-e}, \tag{5.7.3}$$

where $0 < e < 1$ and the condition $\xi_1 > \xi_0$ leads to the restriction $p > p_{ISO}(e) := 6 + 2e$. Note that the limits $e = 0$ and $p = p_{ISO}(e)$ correspond to stable circular and ISOs, respectively. Inserting this into the first two relations in Eq. (5.7.2), one obtains

$$\varepsilon^2 = \frac{(p-2)^2 - 4e^2}{p\left(p - e^2 - 3\right)}, \qquad \lambda^2 = \frac{p^2}{p - e^2 - 3}. \tag{5.7.4}$$

This yields the following relation between the elements $\lambda d\lambda d\varepsilon$ and $dedp$ (cf. Eq. (14) in Ref. [77]):

$$\lambda d\lambda d\varepsilon = \frac{e\sqrt{p}\left[(p-6)^2 - 4e^2\right]}{2\sqrt{\left(p - e^2 - 3\right)^5\left[(p-2)^2 - 4e^2\right]}} dedp. \tag{5.7.5}$$

For illustrative purpose, we show in figure **5-15** the image of the domain $p > 6 + 2e$, $0 < e < 1$ under the transformation (5.7.4).

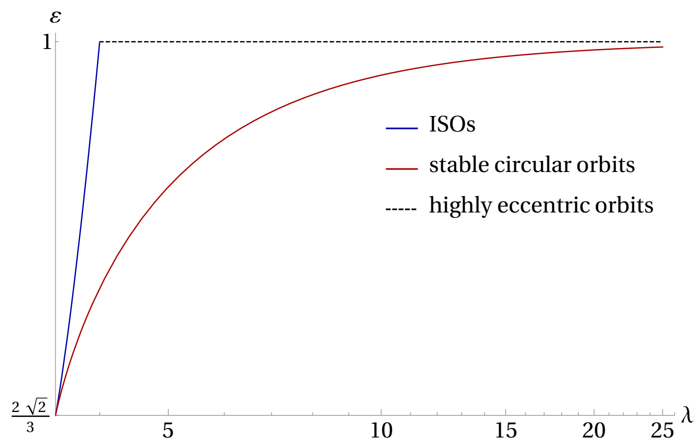

Figure 5-15: Image of the domain $p > 6 + 2e$, $0 < e < 1$ under the transformation (5.7.4). Its boundary consists of the dashed line, corresponding to highly eccentric orbits ($e = 1$), the blue line representing the ISOs and the purple line corresponding to the stable circular orbits.

5.8. Appendix B: Limits of integration for the fiber integrals defining the spacetime observables

In this appendix we provide an alternative derivation for the integration limits for E and L in Eq. (5.3.19), given an observer located at a certain radius r_{obs}. As in the previous appendix, for simplicity we work with the dimensionless variables introduced in Eq. (5.4.34).

The first key observation is that the observer must lie between the turning points of the orbits, in order to perceive it; that is one must have $\xi_1 < \xi_{\text{obs}} < \xi_2$. Using Eq. (5.7.3) and the restriction $p > 6 + 2e$ this yields the following restrictions for p:

$$p^{(1)}_{\text{min}}(\xi_{\text{obs}}, e), p^{(2)}_{\text{min}}(\xi_{\text{obs}}, e) < p < p_{\text{max}}(\xi_{\text{obs}}, e), \tag{5.8.1}$$

where

$$p_{\text{max}}(\xi_{\text{obs}}, e) \;:=\; (1 + e)\xi_{\text{obs}}, \tag{5.8.2}$$

$$p^{(1)}_{\text{min}}(\xi_{\text{obs}}, e) \;:=\; p_{ISO}(e) = 6 + 2e, \qquad p^{(2)}_{\text{min}}(\xi_{\text{obs}}, e) := (1 - e)\xi_{\text{obs}}. \tag{5.8.3}$$

To determine this range more explicitly, we first note that the equations $p^{(1)}_{\text{min}}(\xi_{\text{obs}}, e) = p_{\text{max}}(\xi_{\text{obs}}, e)$ and $p^{(1)}_{\text{min}}(\xi_{\text{obs}}, e) = p^{(2)}_{\text{min}}(\xi_{\text{obs}}, e)$ are satisfied if and only if $e = e^{(1)}_{\text{c}}(\xi_{\text{obs}})$ and $e = e^{(2)}_{\text{c}}(\xi_{\text{obs}})$, respectively, with

$$e^{(1)}_{\text{c}}(\xi_{\text{obs}}) = \frac{\xi_{\text{obs}} - 6}{2 - \xi_{\text{obs}}}, \qquad e^{(2)}_{\text{c}}(\xi_{\text{obs}}) = \frac{\xi_{\text{obs}} - 6}{2 + \xi_{\text{obs}}}, \tag{5.8.4}$$

where the first function lies in the required range $0 \leq e < 1$ if $4 < \xi_{\text{obs}} \leq 6$ and the second one if $\xi_{\text{obs}} \geq 6$. These observations allow one to conclude that the permitted values of (p, e) are given by:

$$4 < \xi_{\text{obs}} \leq 6 : p_{\text{min}}^{(1)}(\xi_{\text{obs}}, e) < p < p_{\text{max}}(\xi_{\text{obs}}, e) \quad \text{and} \quad e_{\text{c}}^{(1)}(\xi_{\text{obs}}) < e < 1. \quad (5.8.5)$$

$$\xi_{\text{obs}} > 6 : p_{\text{min}}^{(2)}(\xi_{\text{obs}}, e) < p < p_{\text{max}}(\xi_{\text{obs}}, e) \quad \text{for} \quad 0 < e < e_{\text{c}}^{(2)}(\xi_{\text{obs}}),$$

$$p_{\text{min}}^{(1)}(\xi_{\text{obs}}, e) < p < p_{\text{max}}(\xi_{\text{obs}}, e) \quad \text{for} \quad e_{\text{c}}^{(2)}(\xi_{\text{obs}}) < e < 1. (5.8.6)$$

We illustrate two representative examples of the resulting domain in the (p, e)-plane in figure **5-16**. Note that e cannot approach zero when $\xi_{\text{obs}} < 6$, which is compatible with the fact that there are no stable circular orbits in this region.

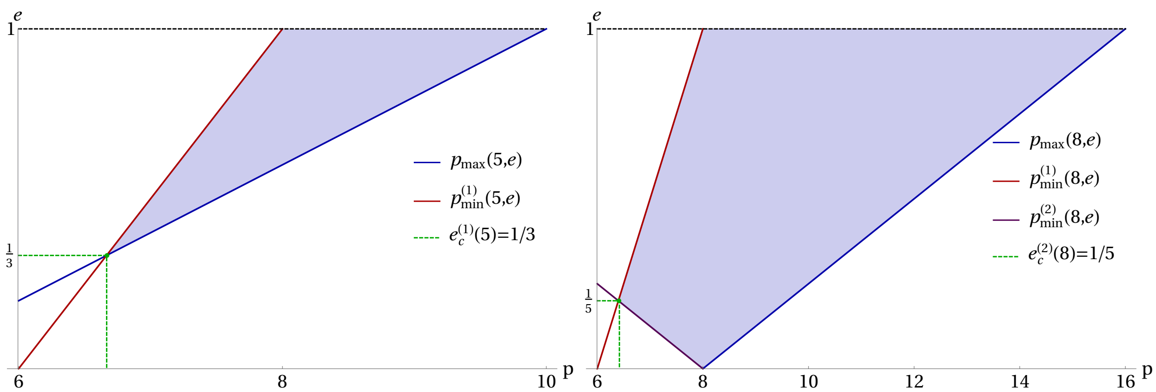

Figure 5-16: Illustration for the allowed region of integration in the (p, e)-plane. Left panel: the observer is located at $\xi_{\text{obs}} = 5$ and the domain is delimited by a triangle. Right panel: the observer is located at $\xi_{\text{obs}} = 8$. In this case the domain is delimited by a quadrilateral.

Now that we have determined the correct domain of integration in terms of the variables (p, e), we translate the results to the variables (E, L) by means of the transformation $(p, e) \mapsto (\varepsilon, \lambda)$ defined in Eq. (5.7.4). To understand the resulting region, it is sufficient to map the boundary of the allowed region in the (p, e) plane, which consists of straight line segments. First, note that the line segment with $e = 1$ is mapped to $\varepsilon = 1$. Next, consider the line $p = p_{\text{min}}^{(1)}(\xi_{\text{obs}}, e)$ corresponding to the ISOs. Its image under the the transformation $(p, e) \mapsto (\varepsilon, \lambda)$ yields

$$\varepsilon_{\text{ISO}}^2 = \frac{8}{9 - e^2}, \qquad \lambda_{\text{ISO}}^2 = \frac{4(3 + e)^2}{(1 + e)(3 - e)}, \qquad 0 < e < 1. \qquad (5.8.7)$$

Eliminating e from these expression one obtains $\lambda = \lambda_{\text{c}}(\varepsilon)$ with

$$\lambda_{\text{c}}(\varepsilon) := \frac{4\sqrt{2}}{\sqrt{36\varepsilon^2 - 8 - 27\varepsilon^4 + \varepsilon\sqrt{[9\varepsilon^2 - 8]^3}}}, \qquad \frac{8}{9} < \varepsilon^2 < 1, \qquad (5.8.8)$$

which is precisely the critical angular momentum $L_\mathrm{c}/(Mm)$ introduced below Eq. (5.3.6). Finally, by noticing that $p = p^{(2)}_\mathrm{min}(\xi_\mathrm{obs}, e)$ and $p = p_\mathrm{max}(\xi_\mathrm{obs}, e)$ correspond to the turning points, where the effective potential $V_{m,L}(r)$ is equal to E^2, one obtains $\lambda = \lambda_\mathrm{max}(\varepsilon, \xi)$ with

$$\lambda_\mathrm{max}(\varepsilon, \xi) := \xi\sqrt{\frac{\varepsilon^2}{1-\frac{2}{\xi}} - 1}. \tag{5.8.9}$$

In fact, this expression can also be obtained by substituting either $p = (1+e)\xi_\mathrm{obs}$ or $p = (1-e)\xi_\mathrm{obs}$ into Eq. (5.7.4) and eliminating e. At first sight, it seems curious that the wedge-like portion of the boundary consisting of the two line segments $p = (1 \pm e)\xi_\mathrm{obs}$ is transformed into the smooth curve $\lambda = \lambda_\mathrm{max}(\varepsilon, \xi)$. The reason for this relies in the factor e in Eq. (5.7.5), which implies that the transformation $(p, e) \mapsto (\varepsilon, \lambda)$ is singular at $e = 0$, which is the location where the two line segments cross each other. The point corresponding to the minimum value of p corresponds to the point of minimal energy ε. It can be obtained by substituting Eq. (5.8.4) into the expression for the energy in Eq. (5.8.7), which yields

$$\varepsilon_\mathrm{c}(\xi) := \begin{cases} \dfrac{\xi - 2}{\sqrt{\xi(\xi-3)}} & \text{for} \quad 4 \leq \xi \leq 6, \\[2ex] \dfrac{\xi + 2}{\sqrt{\xi\,(\xi+6)}} & \text{for} \quad \xi \geq 6. \end{cases} \tag{5.8.10}$$

We conclude that the allowed region for bound trajectories which intersect an observer located at $\xi = \xi_\mathrm{obs}$ is given by

$$\lambda_\mathrm{c}(\varepsilon) < \lambda < \lambda_\mathrm{max}(\varepsilon, \xi) \quad \text{and} \quad \varepsilon_\mathrm{c}(\xi) < \varepsilon < 1. \tag{5.8.11}$$

This coincides with the result in Eq. (5.3.19) which is derived in section 5.3.3 by different means. Figure **5-17** shows the behavior of the curves $\lambda = \lambda_\mathrm{c}(\varepsilon)$, $\lambda = \lambda_\mathrm{ub}(\varepsilon)$ and $\lambda = \lambda_\mathrm{max}(\varepsilon, \xi)$ for two representative values of ξ.

5.9. Appendix C: Integrals over angular momentum

In this appendix we list the relevant integrals that are used in subsection 5.4.2 in order to compute the spacetime observables. For the integrals over the total angular momentum L, we first introduce the notation $L_1 := |L_z|/\sin\vartheta$, $L_2 := L_\mathrm{max}(E, r)$, and $L_3 := \mathrm{máx}\{L_\mathrm{c}(E), |L_z|/\sin\vartheta\}$. By virtue of Eq. (5.3.19) these quantities satisfy the inequality $L_1 \leq L_3 \leq L_2$. By means of the variable substitution

$$\sin^2\phi = \frac{L^2 - L_1^2}{L_2^2 - L_1^2}, \qquad 0 \leq \phi \leq \frac{\pi}{2}, \tag{5.9.1}$$

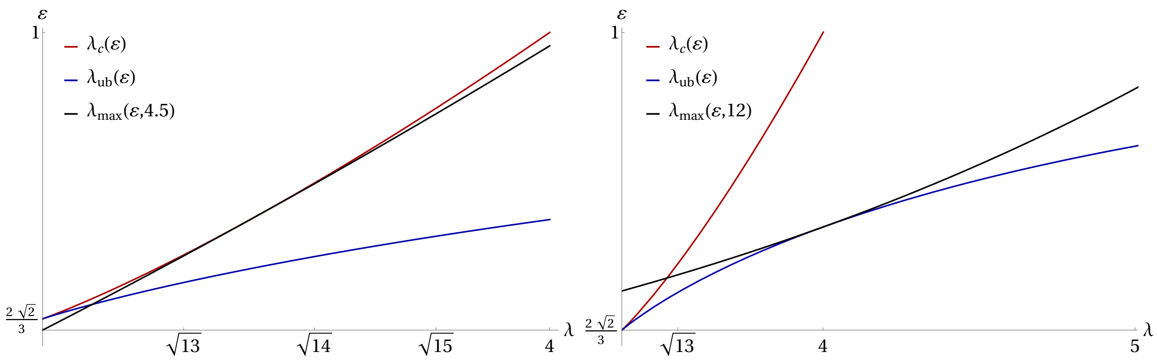

Figure 5-17: The curves $\lambda = \lambda_\mathrm{c}(\varepsilon)$, $\lambda = \lambda_\mathrm{up}(\varepsilon)$ and $\lambda = \lambda_\mathrm{max}(\varepsilon, \xi)$ which are relevant for computing the integration domain corresponding to a spacetime observable at ξ. Left panel: $\xi = 4.5$. Note that the curves $\lambda = \lambda_\mathrm{c}(\varepsilon)$ and $\lambda = \lambda_\mathrm{max}(\varepsilon, \xi)$ "touch each other" at $m\varepsilon = E_c(r)$. Right panel: $\xi = 12$. In this case, it is the curves $\lambda = \lambda_\mathrm{up}(\varepsilon)$ and $\lambda = \lambda_\mathrm{max}(\varepsilon, \xi)$ that touch each other. In both cases the relevant domain is delimited by the curves $\lambda = \lambda_\mathrm{c}(\varepsilon)$ and $\lambda = \lambda_\mathrm{max}(\varepsilon, \xi)$.

one finds

$$
\begin{aligned}
\int_{L_3}^{L_2} \frac{LdL}{\sqrt{L^2 - L_1^2}\sqrt{L_2^2 - L^2}} &= \frac{\pi}{2} - \arcsin\sqrt{\frac{L_3^2 - L_1^2}{L_2^2 - L_1^2}} \\
&= \frac{\pi}{2} - \arctan\sqrt{\frac{L_3^2 - L_1^2}{L_2^2 - L_3^2}}, \qquad (5.9.2) \\
\int_{L_3}^{L_2} \frac{\sqrt{L_2^2 - L^2}}{\sqrt{L^2 - L_1^2}} LdL &= \frac{1}{2}\left(L_2^2 - L_1^2\right)\left(\frac{\pi}{2} - \arctan\sqrt{\frac{L_3^2 - L_1^2}{L_2^2 - L_3^2}}\right) \\
&\quad - \frac{1}{2}\sqrt{L_3^2 - L_1^2}\sqrt{L_2^2 - L_3^2}, \qquad (5.9.3) \\
\int_{L_3}^{L_2} \frac{\sqrt{L^2 - L_1^2}}{\sqrt{L_2^2 - L^2}} LdL &= \frac{1}{2}\left(L_2^2 - L_1^2\right)\left(\frac{\pi}{2} - \arctan\sqrt{\frac{L_3^2 - L_1^2}{L_2^2 - L_3^2}}\right) \\
&\quad + \frac{1}{2}\sqrt{L_3^2 - L_1^2}\sqrt{L_2^2 - L_3^2}. \qquad (5.9.4)
\end{aligned}
$$

Note that the contributions from the $\arctan$ on the right-hand side of these equations vanish when $L_3 = L_1$, that is, when $|L_z|/\sin\vartheta \geq L_c(E)$.

In order to treat the integrals over the azimuthal angular momentum for the models (5.4.3,5.4.4) which appear in equations (5.4.6, 5.4.14, 5.4.15, 5.4.16) we use the following equations for $a > b > 0$ which can be obtained using integration by parts,

$$a \int_{1/a}^{1} d\lambda_z \sqrt{1-\lambda_z^2}\,(a\lambda_z - 1)_+^l = \frac{1}{l+1}\int_{1/a}^{1} \frac{d\lambda_z \lambda_z}{\sqrt{1-\lambda_z^2}}\,(a\lambda_z-1)_+^{l+1}, \tag{5.9.5}$$

$$\begin{aligned}
a \int_{1/a}^{1} d\lambda_z\,(a\lambda_z-1)_+^l \arctan\sqrt{\frac{1-\lambda_z^2}{(1/b^2)-1}} &= \frac{b\sqrt{1-b^2}}{l+1}\int_{1/a}^{1}\frac{\lambda_z d\lambda_z}{\sqrt{1-\lambda_z^2}}\frac{(a\lambda_z-1)_+^{l+1}}{(1-b^2\lambda_z^2)} \\
&= \frac{\pi}{2}\frac{b}{l+1}\tilde{\mathrm{K}}_l(a,b),
\end{aligned} \tag{5.9.6}$$

$$\begin{aligned}
a^2 \int_{1/a}^{1} d\lambda_z \lambda_z\,(a\lambda_z-1)_+^l \arctan\sqrt{\frac{1-\lambda_z^2}{(1/b^2)-1}} &= \int_{1/a}^{1}\frac{\lambda_z d\lambda_z}{\sqrt{1-\lambda_z^2}}\frac{b\sqrt{1-b^2}}{(1-b^2\lambda_z^2)} \\
&\quad\times\left[\frac{(a\lambda_z-1)_+^{l+1}}{l+1}+\frac{(a\lambda_z-1)_+^{l+2}}{l+2}\right] \\
&= \frac{\pi}{2}b\left[\frac{1}{l+1}\tilde{\mathrm{K}}_l(a,b)+\frac{1}{l+2}\tilde{\mathrm{K}}_{l+1}(a,b)\right],
\end{aligned} \tag{5.9.7}$$

$$\begin{aligned}
a^3 \int_{1/a}^{1} d\lambda_z \lambda_z^2\,(a\lambda_z-1)_+^l \arctan\sqrt{\frac{1-\lambda_z^2}{(1/b^2)-1}} &= \frac{\pi}{2}b\left[\frac{1}{l+1}\tilde{\mathrm{K}}_l(a,b)\right. \\
&\quad\left.+\frac{2}{l+2}\tilde{\mathrm{K}}_{l+1}(a,b)+\frac{1}{l+3}\tilde{\mathrm{K}}_{l+2}(a,b)\right],
\end{aligned} \tag{5.9.8}$$

where we recall the definition of the function $\tilde{\mathrm{K}}_l(a,b)$ defined in Eq. (5.4.9).

5.10. Appendix D: Properties of the integral kernels $\tilde{\mathrm{K}}_l(a,b)$

In this appendix we summarize some elementary properties of the integral

$$\tilde{\mathrm{K}}_l(a,b) := \frac{2}{\pi}\sqrt{1-b^2}\int_{1/a}^{1}\frac{d\lambda\lambda}{\sqrt{1-\lambda^2}}\frac{(a\lambda-1)^{l+1}}{1-b^2\lambda^2}, \qquad a>1, \quad 0<b<1, \tag{5.10.1}$$

which was defined in Eq. (5.4.9). First, observe that $\tilde{\mathrm{K}}_l(a,b)$ is continuous in (a,b) and that

$$\lim_{a\to 1}\tilde{\mathrm{K}}_l(a,b) = 0. \tag{5.10.2}$$

In order to analyze the behavior for large a and the limits $b \to 0$ and $b \to 1$ it is convenient to perform the variable substitution $\mu := \sqrt{1-\lambda^2}/\sqrt{1-b^2}$, which transforms the integral into

$$\tilde{\mathrm{K}}_l(a,b) := \frac{2}{\pi}\int_0^{\frac{1}{a}\sqrt{\frac{a^2-1}{1-b^2}}}\frac{d\mu}{1+b^2\mu^2}\left[a\sqrt{1-(1-b^2)\mu^2}-1\right]^{l+1}. \tag{5.10.3}$$

From this, we see that for all $a > 1$,

$$\lim_{b\to 1} \tilde{\mathrm{K}}_l(a,b) = \frac{2}{\pi}\int_0^\infty \frac{d\mu}{1+\mu^2}(a-1)^{l+1} = (a-1)^{l+1}. \tag{5.10.4}$$

Furthermore, using the fact that $\sqrt{a^2-1}/a \leq 1$, one obtains the estimate

$$0 \leq \tilde{\mathrm{K}}_l(a,b) \leq \frac{2}{\pi b}\arctan\left(\frac{b}{\sqrt{1-b^2}}\right)(a-1)^{l+1} \leq (a-1)^{l+1}, \quad a>1, \quad 0<b<1. \tag{5.10.5}$$

From Eq. (5.10.1) and the variable substitution $\lambda = (1-1/a)t + 1/a$ one also obtains the limit

$$\begin{aligned}\tilde{\mathrm{K}}_l(a,0) &:= \lim_{b\to 0} \tilde{\mathrm{K}}_l(a,b)\\ &= \frac{1}{\sqrt{\pi}}\frac{\Gamma(l+2)}{\Gamma\left(l+\frac{5}{2}\right)}\sqrt{1-\frac{1}{a^2}}(a-1)^{l+1}{}_2F_1\left(-\frac{1}{2}, l+1, l+\frac{5}{2}, -\frac{a-1}{a+1}\right)\end{aligned} \tag{5.10.6}$$

with ${}_2F_1(a,b;c;z)$ the Gauss hypergeometric function as defined, for instance, in Eq. (9.111) of [95].

Although we have not found an explicit expression for $\tilde{\mathrm{K}}_l(a,b)$ which is valid for *generic* values of l, the integral can be computed explicitly for the specific values of

$l = 0, 1, 2$:

$$
\begin{aligned}
\tilde{\mathrm{K}}_0(a,b) &= \frac{a}{b^2}\left[1-\sqrt{1-b^2}\left(1-\frac{2}{\pi}\arcsin\frac{1}{a}\right)\right] \\
&\quad +\frac{a-b}{\pi b^2}\arctan\frac{ab-1}{\sqrt{(a^2-1)(1-b^2)}} \\
&\quad -\frac{a+b}{\pi b^2}\arctan\frac{ab+1}{\sqrt{(a^2-1)(1-b^2)}}, \qquad (5.10.7)\\
\tilde{\mathrm{K}}_1(a,b) &= -\frac{2a}{b^2}\left[\frac{1}{\pi}\sqrt{(a^2-1)(1-b^2)}+1-\sqrt{1-b^2}\left(1-\frac{2}{\pi}\arcsin\frac{1}{a}\right)\right] \\
&\quad +\frac{(a-b)^2}{\pi b^3}\arctan\frac{ab-1}{\sqrt{(a^2-1)(1-b^2)}} \\
&\quad +\frac{(a+b)^2}{\pi b^3}\arctan\frac{ab+1}{\sqrt{(a^2-1)(1-b^2)}}, \qquad (5.10.8)\\
\tilde{\mathrm{K}}_2(a,b) &= \frac{a^3}{b^4}\left[1-\sqrt{1-b^2}\left(1+\frac{b^2}{2}\right)\left(1-\frac{2}{\pi}\arcsin\frac{1}{a}\right)\right] \\
&\quad +\frac{3a}{b^2}\left[\frac{5}{3\pi}\sqrt{(a^2-1)(1-b^2)}+1-\sqrt{1-b^2}\left(1-\frac{2}{\pi}\arcsin\frac{1}{a}\right)\right] \\
&\quad +\frac{(a-b)^3}{\pi b^4}\arctan\frac{ab-1}{\sqrt{(a^2-1)(1-b^2)}} \\
&\quad -\frac{(a+b)^3}{\pi b^4}\arctan\frac{ab+1}{\sqrt{(a^2-1)(1-b^2)}}. \qquad (5.10.9)
\end{aligned}
$$

We show corresponding plots of these functions in figure **5-18**.

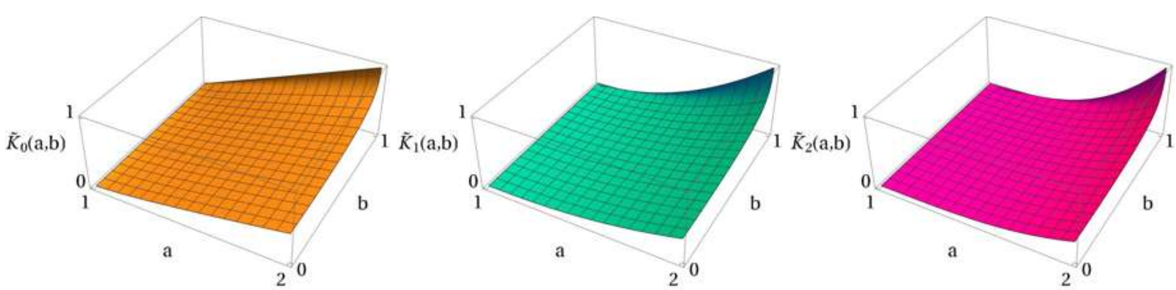

Figure 5-18: Behavior of the integrals $\tilde{\mathrm{K}}_l(a,b)$ for $l = 0, 1, 2$. Left $l = 0$, center $l = 1$, right $l = 2$.

5.11. Appendix E: Short review of polish doughnuts configurations

In this appendix we briefly review the “polish doughnutsçonfigurations describing stationary and axisymmetric hydrodynamic thick disks surrounding black holes (for more details see Refs. [56, 107–113]). To describe these configurations, we assume that the spacetime is stationary, axisymmetric and circular (the Kerr spacetime satisfies these properties; however for the moment we may assume a metric more general than Kerr). It can be shown (see for instance [59]) that such a spacetime admits local coordinates $(t, r, \vartheta, \varphi)$ in which the metric coefficients depend neither on the time coordinate t (stationarity) nor the azimuthal coordinate φ (axisymmetry), and such that $g_{tr} = g_{t\vartheta} = g_{\varphi r} = g_{\varphi\vartheta} = 0$ (circularity), that is,

$$g = g_{tt}dt^2 + 2g_{t\varphi}dtd\varphi + g_{rr}dr^2 + g_{\vartheta\vartheta}d\vartheta^2 + g_{\varphi\varphi}d\varphi^2. \tag{5.11.1}$$

The Killing vector fields associated with this spacetime are $k = \partial_t$ and $v = \partial_\varphi$.

Next, consider a perfect fluid flow in circular motion, which means that its four-velocity u is a linear combination of k and v, such that

$$u = A\,(k + \Omega v)\,, \tag{5.11.2}$$

for some normalization constant $A > 0$ and a function Ω describing the angular velocity of the flow. Denoting by $\rho = nm$, h and P the rest mass density, specific enthalpy and pressure, the relativistic Euler equations can be written as

$$a_\nu = -\frac{1}{\rho h}(\nabla_\nu P + u_\nu \nabla_u P), \tag{5.11.3}$$

with $a_\nu = (\nabla_u u)_\nu = u^\mu \nabla_\mu u_\nu$ the acceleration of the fluid elements.

For the following, we impose the Killing symmetries on the fluid quantities, such that ρ, h, p and u are invariant with respect to the flows generated by k and v. Assuming an adiabatic fluid in local thermodynamic equilibrium, such that $dh = dp/\rho$, one can show that the Bernoulli-type quantities

$$\mathcal{B} := -hu_\mu k^\mu = -hu_t, \qquad \mathcal{L} := hu_\mu v^\mu = hu_\varphi, \tag{5.11.4}$$

are constant along the flow lines. For the following, it is convenient to introduce the “fluid angular momentum”(the angular momentum per energy of a fluid element), defined as

$$\ell := \frac{\mathcal{L}}{\mathcal{B}} = -\frac{u_\varphi}{u_t}. \tag{5.11.5}$$

Combining this definition with the equation $\Omega = u^\varphi/u^t$ and the normalization condition $u_\mu u^\mu = -1$ yields

$$u_t u^t = -\frac{1}{1-\Omega\ell}, \tag{5.11.6}$$

which allows one to express the components u^t, $u^\varphi = \Omega u^t$, $u_\varphi = -\ell u_t$ in terms of u_t, Ω and ℓ. Computing the normalization constant $A = u^t$ and using Eq. (5.11.6) one also finds

$$u_t = -\frac{1}{1-\Omega\ell}\sqrt{-g_{tt} - 2\Omega g_{t\varphi} - \Omega^2 g_{\varphi\varphi}}. \tag{5.11.7}$$

Using Eq. (5.11.6), the formula $a_\nu = u^\mu(\partial_\mu u_\nu - \partial_\nu u_\mu)$, and taking into account the Killing symmetries, one obtains[4]

$$a_\nu = \partial_\nu \log|u_t| - \left(\frac{\Omega}{1-\Omega\ell}\right)\partial_\nu \ell. \tag{5.11.8}$$

Euler's equation (5.11.3) together with $\nabla_u P = 0$ and the first law lead to

$$-\,d\log[h] = d\log|u_t| - \left(\frac{\Omega}{1-\Omega\ell}\right) d\ell. \tag{5.11.9}$$

Taking the exterior derivative on both sides yields $d\Omega \wedge d\ell = 0$, implying that $d\Omega$ is proportional to $d\ell$. This in turn implies that the angular velocity Ω only depends on the specific angular momentum (or vice-versa) [114]. On the other hand, using $u_\mu = g_{\mu\nu}u^\nu$ one finds the following relation between ℓ and Ω:

$$g_{tt}\ell + g_{t\varphi}\left(1 + \Omega\ell\right) + g_{\varphi\varphi}\Omega = 0. \tag{5.11.10}$$

The surfaces of constant ℓ and Ω describe the "von Zeipel cylinders".

After these remarks, stationary, axisymmetric perfect fluid configuration in circular motion can be described as follows. One possibility is to specify a function $\Omega_0(\ell)$ of ℓ, such that Eq. (5.11.9) can be integrated to yield

$$\log(h) = -\log|u_t| + \int^{\ell} \frac{\Omega_0(\ell')d\ell'}{1-\Omega_0(\ell')\ell'}. \tag{5.11.11}$$

Here, u_t is given by Eq. (5.11.7) with Ω replaced by $\Omega_0(\ell)$ and ℓ is the function of (r,ϑ) which is determined from Eq. (5.11.10) by setting $\Omega = \Omega_0(\ell)$. The support of the fluid

[4] An elegant way of deriving Eq. (5.11.8) makes use of the calculus for differential forms. Denoting by $\underline{u} = u_\mu dx^\mu$ the one-form associated with the four-velocity, one obtains from Eq. (5.11.2)

$$a = i_u d\underline{u} = A(i_k d\underline{u} + \Omega i_v d\underline{u}) = -A(d i_k \underline{u} + \Omega d i_v \underline{u}) = -A\left[du_t - \Omega d(\ell u_t)\right]$$

where we have used the Cartan formula $\pounds_k \underline{u} = i_k d\underline{u} + d i_k \underline{u}$ in the third step. Taking into account that $A = u^t$ and using Eq. (5.11.6) yields the desired result.

configuration is determined by the region for which the right-hand side of Eq. (5.11.11) is positive, such that $h > 1$. Note that the location of the boundary surface $h = 1$ depends on a free integration constant. By construction, the quantity $h|u_t|$ is constant on the von Zeipel cylinders.

Alternatively, one can fix $\ell = \ell_0$ to be constant throughout the fluid configuration, such that

$$\log(h) = -\log|u_t| + const, \tag{5.11.12}$$

with u_t given again by Eq. (5.11.7) where now Ω is the function of (r, ϑ) determined by Eq. (5.11.10), which yields

$$\Omega(r,\vartheta) = -\frac{g_{t\varphi} + g_{tt}\ell_0}{g_{\varphi\varphi} + g_{t\varphi}\ell_0}. \tag{5.11.13}$$

Like in the previous case, the support of the fluid configuration corresponds to the region for which the right-hand side of Eq. (5.11.12) is positive. For a Schwarzschild black hole, these expressions simplify considerably and one obtains

$$\log h(r,\vartheta) = W_{\text{in}} - W_{\ell_0}(r,\vartheta) \tag{5.11.14}$$

with an integration constant W_{in} and the "effective potential"

$$\begin{aligned} W_{\ell_0}(r,\vartheta) \quad &:= \quad \log|u_t| = -\frac{1}{2}\log\left(\frac{r}{r-2M} - \frac{\ell_0^2}{r^2\sin^2\vartheta}\right), \\ & r > 2M, \quad \sin^2\vartheta > \ell_0^2\frac{r-2M}{r^3}. \end{aligned} \tag{5.11.15}$$

As can easily be verified, the critical points of $W_{\ell_0}(r,\vartheta)$ are located on the equatorial plane $\vartheta = \pi/2$ at radii determined by the equation

$$\ell_0^2(r-2M)^2 = Mr^3, \tag{5.11.16}$$

where $W_{\ell_0}(r,\pi/2) = -\log[\sqrt{r(r-3M)}/(r-2M)]$. There are no critical points when $\ell_0 < \ell_{\text{c}} = \sqrt{27/2}M \approx 3.67M$. For $\ell_0 > \ell_{\text{c}}$, there are two critical points with radii $2M < r_{\text{saddle}} < r_{\text{min}}$, the first one describing a saddle and the second one a minimum. As ℓ_0 increases from ℓ_{c} to $\sqrt{27}M$, r_{saddle} decreases monotonously from $6M$ to $3M$ and $W_{\ell_0}(r_{\text{saddle}},\pi/2)$ increases from $\log\sqrt{8/9}$ to ∞ while r_{min} increases monotonously from $6M$ to $6(2+\sqrt{3})M$ and $W_{\ell_0}(r_{\text{min}},\pi/2)$ from $\log\sqrt{8/9}$ to $-\log[3\sqrt{2\sqrt{3}-3}/2]$.

From these observations, we see that as long as $\ell_0 > \ell_{\text{c}}$, there are bound fluid configurations whose maximum specific enthalpy is located at r_{min} and is constant on the closed level sets surrounding r_{min} (see figure **5-19**). The surface of the configuration can be chosen as any of these closed level sets, setting W_{in} equal to the value of W at this level set, such that $h = 1$ at the surface and $h > 1$ inside it. The most extended surface that can be chosen is the one that approaches the separatrix through the saddle point.

The maximum of W_{ℓ_0} lies below its asymptotic value 0 if $\ell_c < \ell_0 < \ell_{mb} = 4M$. The upper limit $\ell_0 = \ell_{mb}$ corresponds to $r_{saddle} = 4M$ which is the radius of the marginally bound circular trajectory. For $\ell_0 > \ell_{mb}$ the saddle lies above 0 and hence bound fluid configurations cannot spill over the saddle and fall into the black hole. Therefore, the range $\ell_c < \ell_0 < \ell_{mb} = 4M$ is the one that is relevant for accretion disk models. Note also that at the minimum of W_{ℓ_0} the fluid elements follow circular geodesics due to the fact that the gradient of the pressure vanishes there. Recalling that ℓ represents the angular momentum per energy of the particles and making use of the formulae $L(r) = mM^{1/2}r^{3/2}/\sqrt{r(r-3M)}$ and $E(r) = m(r-2M)/\sqrt{r(r-3M)}$ for the angular momentum and energy of the circular timelike geodesics (see Eq. (5.7.4) with $e = 0$), one obtains $\ell_0 = L(r)/E(r) = M^{1/2}r^{3/2}/(r-2M)$ which satisfies equation (5.11.16).

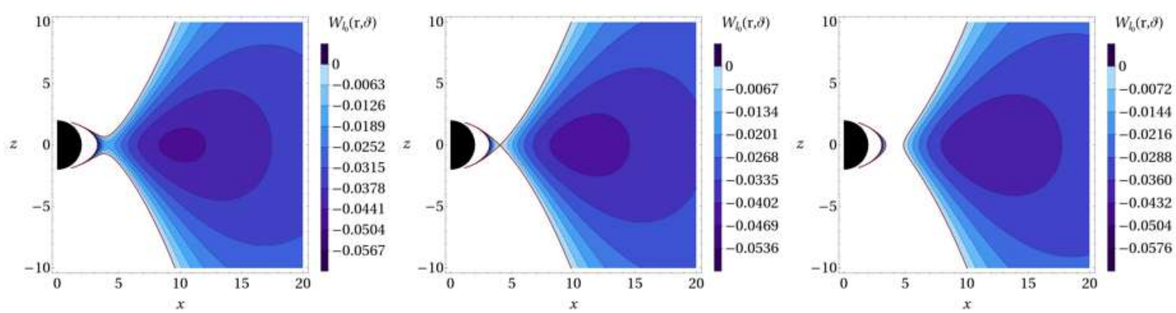

Figure 5-19: Contour plots for the effective potential defined in Eq. (5.11.15) in the xz-plane for the values for the fluid angular momentum given by $\ell_0 = \sqrt{31/2}M, \sqrt{32/2}M, \sqrt{33/2}M$ as shown in the left, center and right panels, respectively. In all plots the continuous red line represents the boundary surface where $W_{\ell_0} = 0$ and the black region represents the Schwarzschild black hole region.

6 Accretion of a Vlasov gas onto a black hole from a sphere of finite radius and the role of angular momentum

This chapter is a loyal reproduction (with some minor changes due to the format) of the free arXiv:2107.04830 version. However, the numbers of the equations and references could differ from the ones in the original version. The references are collected at the end of this thesis work. The content of this chapter has been published in Physical Review D [40].

6.1. Abstract

The accretion of a spherically symmetric, collisionless kinetic gas cloud onto a Schwarzschild black hole is analyzed. Whereas previous studies have treated this problem by specifying boundary conditions at infinity, here the properties of the gas are given at a sphere of finite radius. The corresponding steady-state solutions are computed using four different models with an increasing level of sophistication, starting with the purely radial infall of Newtonian particles and culminating with a fully general relativistic calculation in which individual particles have angular momentum. The resulting mass accretion rates are analyzed and compared with previous models, including the standard Bondi model for a hydrodynamic flow. We apply our models to the supermassive black holes Sgr A* and M87*, and we discuss how their low luminosity could be partially explained by a kinetic description involving angular momentum. Furthermore, we get results consistent with previous model-dependent bounds for the accretion rate imposed by rotation measures of the polarized light coming from Sgr A* and with estimations of the accretion rate of M87* from the Event Horizon Telescope collaboration. Our methods and results could serve as a first approximation for more realistic black hole accretion models in various astrophysical scenarios in which the accreted material is expected to be nearly collisionless.

6.2. Introduction

Accretion of matter is one of the most important processes in astrophysical systems due to its fundamental role in the formation and evolution of galaxies, stars and compact objects. The fact that different types of matter (e.g. kinetic gases, fluids or scalar fields) have distinctive features in their corresponding dynamics, makes essential to take into account the nature of the infalling matter for a physically correct description of the accretion process (the features of some of these types of matter can be seen e.g. in [115] where the dynamics of a collisionless kinetic gas in a dark matter halo is studied; in [116] for accretion studies based on fluid dynamics; or in [117] where the peculiar distribution of a scalar field surrounding a black hole (BH) is described).

The first studies on the phenomenon of accretion were developed in [118, 119] for a star moving at a steady speed through an infinite pressureless gas cloud. Later on, [120] studied the hydrodynamical steady spherical accretion of a gas at rest at infinity onto a Newtonian star. In these models, effects such as viscosity, turbulence, self-gravity or magnetic fields are neglected.

Further studies have been undertaken for different scenarios in which matter accretion was shown to be astrophysically relevant, for example in X-ray binaries (e.g. [121]), in gamma-ray bursts (e.g. [122]), in protoplanetary disks (e.g. [123]) or in active galactic nuclei (e.g. [124]). A great part of these scenarios involve BHs, because they naturally appear in the life cycle of massive stars ([125, 126]) and in the core of medium-to-large galaxies ([127, 128]). The radiation emanated from these powerful sources originates from a region close to the BH's event horizon, and therefore the corresponding accretion requires a fully general-relativistic modeling.

Substantial theoretical and numerical work has been done on the fluid or hydrodynamical approximation of the accreting flow onto BHs. In this context, the first general relativistic extension of the Bondi model was given by [129] who studied the steady spherical accretion flow of simple polytropic gases onto a Schwarzschild BH. Additional generalizations of these hydrodynamic solutions have been worked out over the years (see [130] and references therein for recent work providing a review of the Bondi and Michel solutions and their generalization to rotating BHs). In particular, recent numerical works make use of general relativistic magnetohydrodynamic (GRMHD) simulations to study different accretion models (see e.g. [131]). The fluid approximation in these models considers that the effective mean free path for the particles is sufficiently short with respect to the length over which macroscopic quantities, such as the particle number density, the bulk velocity or the temperature vary in a significant way, so that thermal equilibrium is attained locally. However, there are some cases in which the hydrodynamical approximation does not correspond to the nature of the infalling matter. This is the situation, e.g. for underluminous sources (with respect to the Eddington luminosity) such as Sgr A*, the supermassive black hole (SMBH) in the center of our galaxy [132–134], and M87*, the SMBH in the galactic center of Messier 87 [75, 135], whose accreting plasmas are in a low-density, high-temperature regime which makes them effectively collisionless [135–138].

A further important example is the accretion of dark matter (an exotic entity which is expected to be collisionless), which has been suggested to play a prominent role in the formation of SMBHs (see e.g. [139–141]). The low collisionality of these kind of flows makes necessary to take into account the kinetic approximation in order to correctly describe the dynamics of the accreting matter.

Analytically, the problem of accretion of kinetic gases onto BHs is studied using the formalism of the relativistic Boltzmann equation (see e.g. [4]. In particular, the collisionless approximation (also known as a *Vlasov gas*) in which the component particles do not interact directly with each other, has been studied both in the Newtonian (e.g. [142, 143] and in the general relativistic regimes (e.g. [36, 37, 144, 145]. Numerically, models of collisionless (or weakly collisional) plasmas which include some kinetic effects into the equations of GRMHD flows, have been developed ([146–148]). Nonetheless, modelling a fully 3D kinetic simulation has been a complex subject due to the high computational effort of calculating the evolution of the 6D distribution functions of ions and electrons in the accreting plasma (see e.g. [149] where a local shearing-box model of a collisionless accretion disk is used, and references therein).[1]

The analytical hydrodynamic and kinetic models with spherical symmetry mentioned so far, assume that the boundary conditions determining the properties of the gas (temperature and density) are specified at infinity. However, in practice such properties are measured at a finite distance from the black hole. Therefore, analytical modeling should take into account the finite nature of the accretion phenomenon in order to produce more realistic models. In the hydrodynamic case, such finite models have recently been proposed in the context of the ‘choked’ accretion mechanism (see [150–152] and references therein) in which the gas is injected from a sphere of finite radius, named the ‘injection sphere’, with a slight equatorial to polar density contrast, resulting in an inflow-outflow configuration.

In this article we present a series of illustrative and simplified analytic finite models which aim to solve the BH accretion problem from a kinetic and relativistic standpoint.

[1]For recent analytic work analyzing the dynamics of a collisionless gas in the equatorial plane of a (rotating) Kerr black hole and the phase space mixing phenomenon, see [77].

To this purpose, we analyze the steady, spherical accretion flow of a collisionless kinetic gas with negligible self-gravity from an injection sphere of finite radius R. We study the case of purely radial infall, in which none of the particles have angular momentum, as well as the case where individual particles have arbitrary angular momentum but the gas as a whole (averaged over the momentum space) moves in the pure radial direction. In the latter case, we obtain a general formula for the mass accretion rate which reduces to previous known results for $R \to \infty$ (see [36, 143]), while for fixed R one obtains new solutions.

Despite the simplicity of our models, we get reasonable results when applied to the flows onto Sgr A* and M87*. A smaller mass accretion rate for these BHs is predicted by our kinetic approach, which may contribute to the understanding of their low luminosity [138, 153] and the presence of polarized light at 230 GHz coming from regions near to the BH horizon [154–157]. The presence of this polarization would not be possible for an accretion rate similar to the predicted from the Bondi model, because larger mass accretion rates would depolarize the light through extreme Faraday rotation gradients (see e.g. [158, 159]). The conventional solutions to these problems involve radiatively inefficient accretion flow (RIAF) models [160–162]. In these models the low luminosity is explained by an inefficiency in the process of energy exchange between protons and electrons causing the advection of most of the viscously released energy into the BH's horizon. On the other hand, the presence of linearly polarized light at 230 GHz is explained by allowing a loss of mass in the inner regions of the flow through convection and/or outflows, reducing effectively the mass accretion rate via a dependence of the accretion rate with radius (see [163] for a comprehensive review of accretion flow models).

In this work, we derive the kinetic gas mass accretion formula analogous to the spherical Bondi fluid model. In the examples provided, we show that the accretion rate in a fluid model can be similar to the corresponding kinetic gas one, closing in this way the gap that existed in previous analysis of both models. This issue is discussed for instance in [143] where there is a huge difference between the fluid and kinetic accretion rates. We also derive the generalizations of the accretion rate predicted in [142] for a finite radius and show, in the examples presented, that the value of the accretion rate strongly depends on that radius and the environment. The expressions obtained in our manuscript should be ideally suited to be applied also in dark matter studies in which case the dynamic is expected to be described by a totally non-interacting matter. Furthermore, the obtained equations could be useful for studying the accretion of hot, low-density matter which is trapped inside the gravitational potential of a Schwarzschild BH. The developed formalism and our ideal solutions could serve as a starting point for more complex scenarios, such as the non-spherical accretion onto a Kerr BH, and/or the addition of magnetic fields.

This manuscript is organized as follows: in Section 6.3, we present an overview of the formalism of the general relativistic Vlasov equation and the definitions of the physical quantities relevant for the accretion flow; in Section 6.4, we treat the purely radial spherical infall of particles, both in the non-relativistic and relativistic limits, and we apply the resulting equations to particles obeying mono-energetic and Maxwell-Jüttner distribution functions; in Section 6.5, we analyze the spherical accretion in which the assumption of zero angular momentum for the individual particles is relaxed and we also apply the results to mono-energetic and Maxwell-Jüttner distribution functions; in Section 6.6, we summarize our results in a concise form suitable for its immediate application; in Section 6.7, we apply our results to the accretion flows onto Sgr A* and M87*; finally, in Section 6.8 we give final comments and suggestions for future research. An additional model which considers a distribution of particles with fixed angular momentum which is useful for the interpretation of some of our results is given in an appendix. Throughout this work, we use the signature convention $(-,+,+,+)$ for the space-time metric.

6.3. Review of the general relativistic Vlasov equation

The study of a collisionless kinetic gas interacting with a central object is based on the one-particle distribution function. In Newtonian theory, the distribution function f is a function of time and coordinates $(\mathbf{x},\mathbf{p})$ of the six-dimensional phase-space, such that $f(t,\mathbf{x},\mathbf{p})\,d^3x\,d^3p$ represents the expected number of particles in the phase-space volume element $d^3x\,d^3p$ at time t. In general relativity, the distribution function can be defined, *a priori*, on the eight-dimensional cotangent bundle $T^*\mathcal{M}$ associated with the curved space-time manifold $(\mathcal{M},g)$, that is, the set consisting of pairs (x,p) where $x\in\mathcal{M}$ is a space-time event and p is a momentum co-vector at x. Thus, locally the distribution function can be regarded as a function of the coordinates (x^μ,p_μ), $\mu=0,1,2,3$, parametrizing the cotangent bundle.[2]

For a relativistic, collisionless gas, the distribution function f is required to solve the *Vlasov* (or *collisionless Boltzmann*) *equation* which can be conveniently written as:

$$\{\mathcal{H},f\}\equiv\frac{\partial\mathcal{H}}{\partial p_\mu}\frac{\partial f}{\partial x^\mu}-\frac{\partial\mathcal{H}}{\partial x^\mu}\frac{\partial f}{\partial p_\mu}=0, \tag{6.3.1}$$

[2]Alternatively, one can work on the tangent bundle $T\mathcal{M}$ with local coordinates (x^μ,p^μ). Both formulations are equivalent since the space-time metric provides a natural way to identify $T\mathcal{M}$ with $T^*\mathcal{M}$.

where here $\mathcal{H}$ denotes the free particle Hamiltonian

$$\mathcal{H}(x,p) := \frac{1}{2} g^{\mu\nu}(x) p_\mu p_\nu, \tag{6.3.2}$$

with $g^{\mu\nu}(x)$ the components of the inverse metric at x. It follows immediately from Eq. (6.3.1), that any distribution function f which is only a function of integrals of motion satisfies the Vlasov equation.

Note that the Hamiltonian itself is an integral of motion; the corresponding conserved quantity is $-(mc)^2/2$ with m the rest mass of the particle. For the following, we consider a collisionless gas of identical particles of positive mass $m > 0$, such that f can be restricted on the future mass shell, the seven-dimensional submanifold of $T^*\mathcal{M}$ consisting of those points (x^μ, p_μ) for which

$$p^\mu p_\mu = -(mc)^2, \tag{6.3.3}$$

and p^μ is future-directed. The future mass shell can be parametrized in terms of the coordinates (x^μ, p_i), with $i = 1, 2, 3$, where the time component of the momentum does not appear as an independent coordinate since it can be reconstructed from the mass-shell constraint (6.3.3). For further details on the geometry of the relativistic phase we refer the reader to [12, 164, 165].

Among the space-time observables, the central quantity in our work describing the most relevant physical properties of the solution is the particle current density vector field, defined as (see for instance equation (12.35) in [4]):

$$J^\mu(x) := c \int\limits_{P_x^+(m)} p^\mu f(x,p)\, \mathrm{dvol}_x(p), \tag{6.3.4}$$

where $P_x^+(m)$ is the future mass hyperboloid consisting of those future-directed timelike vectors p^μ for which (6.3.3) is satisfied and $\mathrm{dvol}_x(p)$ is the Lorentz-invariant volume element on $P_x^+(m)$, defined as:

$$\mathrm{dvol}_x(p) := \frac{1}{\sqrt{-g}} \frac{d^3 p_*}{p^0}, \tag{6.3.5}$$

where $\sqrt{-g}$ is the square root of the metric's determinant and $p_* = (p_i)$ (with $i = 1, 2, 3$) refer to the covariant spatial components of the linear momentum [164].[3]

[3]The covariant and contravariant momentum volume elements can be related through $\frac{1}{\sqrt{-g}} \frac{d^3 p_*}{p^0} = \sqrt{-g} \frac{d^3 p}{|p_0|}$.

The corresponding invariant particle number density and mean four-velocity at x are given by:

$$n(x) := \frac{1}{c}\sqrt{-J^\mu(x)J_\mu(x)}, \tag{6.3.6}$$

$$u^\mu(x) := \frac{J^\mu(x)}{n(x)}. \tag{6.3.7}$$

For the following, we assume that the gravitational potential is dominated by the BH such that the self-gravity of the gas can be neglected. Omitting the rotation of the BH for simplicity, we thus consider a spherically symmetric static background described by the metric:

$$ds^2 = g_{ab}(r)\, dx^a dx^b + r^2 \left(d\vartheta^2 + \sin^2\vartheta d\varphi^2\right), \tag{6.3.8}$$

with $(x^a) = (ct, r)$, where c denotes the speed of light in vacuum, t is the time coordinate, r is the areal radius and (ϑ, φ) denote the usual angular coordinates on the two-sphere. The integrals of motion in this case consist of the rest mass $m = \sqrt{-2\mathcal{H}}$, the energy E and the angular momentum vector $\mathbf{L}$ associated with the spherical symmetry.

It can be shown (e.g. [4]) that for a distribution function f satisfying the Vlasov equation, J^μ automatically satisfies the continuity equation $\nabla_\mu J^\mu = 0$, which allows us to define the conserved (rest) mass accretion rate for the metric in Eq. (6.3.8):

$$\dot{M} := 4\pi r^2 m\, J^r(x). \tag{6.3.9}$$

Note that this definition is coordinate-independent, since it is defined in terms of the areal radius r and the contravariant r-component of the current density vector field, which can be written as $J^r = dr(J) = J^\mu \nabla_\mu r$.
Finally, it is straightforward to show that in the non-relativistic limit ($|u^i| \ll c$ and $p^0 = mc$), the well-known expressions for the particle number density, the mean radial velocity and the mass accretion rate are recovered:

$$n(x) = \int f(x,p)\, d^3p_*, \tag{6.3.10}$$

$$u^r(x) = \frac{1}{n(x)} \int \frac{p^r}{m} f(x,p)\, d^3p_*, \tag{6.3.11}$$

$$\dot{M} = 4\pi r^2 m\, n(x)\, u^r(x) = 4\pi r^2 \int p^r f(x,p)\, d^3p_*. \tag{6.3.12}$$

In the results presented in this article, the distribution function f is assumed to depend on (x, p) only through the integrals of motion, E and $\mathbf{L}$. Due to dispersion and mixing, it is in fact expected that any gas configuration relaxes in time to one described by such a distribution function [36, 73], provided the boundary conditions specified at the injection sphere are compatible with it. In addition, we focus on purely spherical accretion for which the distribution function depends only on the energy E and the total angular momentum $L = |\mathbf{L}|$ of each particle. We shall use F to denote the distribution function expressed in terms of E and L.

6.4. Purely radial infall from a finite radius

In this section, we focus on the spherically symmetric steady radial infall of a Vlasov gas into a central object, assuming that each individual particle has zero angular momentum. We assume that the particles are being accreted from an injection sphere at finite radius with specific density and energy or temperature which are the boundary conditions for the problem. The distribution function describing this scenario depends only on the radial coordinate r and its momentum p_r, and the corresponding observables only on r. We treat both the non-relativistic and relativistic limits. The definitions given in the previous section are specialized in order to describe adequately the radial accretion process.

6.4.1. Non-relativistic limit

In this limit, the particles are under the effect of a gravitational central potential $\Phi(r)$ generated by a mass M (e.g. $\Phi(r) = -GMm/r$), and the injection sphere of the particles is at radius R, where we specify the particle number density. We ignore interactions with the surface of the central object since we are interested in a scenario analogous to a Schwarzschild BH, where there is no physical surface. For spherical coordinates and under the assumption that the particles have zero angular momentum, the volume element (6.3.5) in momentum space can be replaced by [115]:[4]

$$\frac{d^3p_*}{\sqrt{-g}} \to \frac{1}{r^2}\, dp_r, \tag{6.4.1}$$

Thus, from Eqs. (6.3.10-6.3.12), we find that

$$\begin{aligned} n(r) &= \frac{1}{r^2}\int_{-\infty}^{p_{\rm m}(r,R)} f(r,p_r)\, dp_r, & (6.4.2)\\ u^r(r) &= \frac{1}{r^2\, m\, n(r)}\int_{-\infty}^{p_{\rm m}(r,R)} p_r\, f(r,p_r)\, dp_r, & (6.4.3)\\ \dot{M} &= 4\pi r^2\, m\, n(r)\, u^r(r) = 4\pi\int_{-\infty}^{p_{\rm m}(r,R)} p_r\, f(r,p_r)\, dp_r, & (6.4.4)\end{aligned}$$

where $p^r = p_r$. Here, the upper integration limit $p_{\rm m}(r,R) := -\sqrt{2\,m[\Phi(R)-\Phi(r)]}$ incorporates the physical requirement that all the particles in the system are falling

[4] There is a 2π difference with the result shown in [115] due to a change of variable in the momentum space done in that work.

radially from a radius R into the central mass, with $E = \Phi(R)$ being the minimum possible energy for the particles. Note that, if $R \to \infty$, then $n(r \to \infty) = 0$ (which is consistent with the fact that the distribution function vanishes at infinite radius), and thus we cannot apply the boundary condition $n(R) = n_R$.

A specific scenario, which is directly related with the analyzed case by [143], is the radial infall of mono-energetic particles with energy $E_0 \geq \Phi(R)$. The distribution function in this case is:

$$F(E) = f_0\, \delta(E - E_0) = f_0\, \delta\left(\frac{p_r^2}{2m} + \Phi(r) - E_0\right), \tag{6.4.5}$$

where f_0 is a constant with units of time^{-1} (because the radial distribution function, $f = f(r, p_r)$, has units of length $\times$ momentum^{-1}) and it is related with n_R. Next, we can use the properties of the Dirac delta distribution[5] to rewrite the distribution function as:

$$f(r, p_r) = f_0 \sqrt{\frac{m}{2}}\, \frac{\delta\left(p_r + \sqrt{2m[E_0 - \Phi(r)]}\right)}{\sqrt{E_0 - \Phi(r)}}, \tag{6.4.6}$$

where we have used the fact that all particles are falling and hence they can only have negative momentum. According to Eqs. (6.4.2-6.4.4) and the boundary condition n_R, the particle density, the average radial velocity and the accretion rate are, respectively:

$$n(r) = \frac{f_0}{r^2}\sqrt{\frac{m}{2[E_0 - \Phi(r)]}}, \tag{6.4.7}$$

$$u^r(r) = -\sqrt{\frac{2[E_0 - \Phi(r)]}{m}}, \tag{6.4.8}$$

$$|\dot{M}| = 4\pi r^2\, m\, n(r)|u^r(r)| = 4\pi m f_0, \tag{6.4.9}$$

where

$$f_0 = R^2 n_R \sqrt{\frac{2[E_0 - \Phi(R)]}{m}}, \tag{6.4.10}$$

which yields

$$\frac{|\dot{M}|}{m n_R} = 4\pi R^2 \sqrt{\frac{2\left[E_0 - \Phi(R)\right]}{m}}, \tag{6.4.11}$$

valid for $r \leq R$. If $E_0 = 0$ and the gravitational potential is due to a central mass such that $\Phi(r) \sim 1/r$, Eq. (6.4.8) is easily recognized as the free-fall velocity. Furthermore, we see from Eqs. (6.4.7) and (6.4.8) that the particle number density and velocity are proportional to $r^{-3/2}$ and $r^{-1/2}$, respectively, which is the expected behaviour for the fluid limit ([143]). If we set $E_0 = \Phi(R) + \frac{1}{2} m v_R^2$, where $v_R = u^r(R)$ is the speed of

[5]Namely, the composition of the Dirac delta distribution with a smooth function $g(x)$, is given by $\delta(g(x)) = \sum_i \frac{\delta(x - x_i)}{|g'(x_i)|}$, where the sum goes over all the different roots x_i of g.

the particles at the injection radius with respect to the central object, then Eq. (6.4.11) can be written as the well-known expression:

$$\frac{|\dot{M}|}{m n_R v_R} = 4\pi R^2. \tag{6.4.12}$$

Another scenario, similar to the Bondi case, consists of a stationary cloud of particles with mass m described by a Maxwell-Boltzmann distribution function (e.g. [35]), falling radially into a central object according to the gravitational potential $\Phi(r)$ generated by M. This has the form:

$$f(r, p_r) = A \exp\left[-\beta\left(\frac{p_r^2}{2\,m} + \Phi(r)\right)\right], \tag{6.4.13}$$

where as usual $\beta = 1/k_{\mathrm{B}}T$, with k_{B} the Boltzmann constant, $k_{\mathrm{B}} = 1.38 \times 10^{-23}$ m^2 kg K^{-1} s^{-2}, T the temperature of the cloud and A is a constant with units of [length $\times$ momentum]$^{-1}$. In this case, following Eqs. (6.4.2-6.4.4) and the boundary condition n_R, the particle number density, the average radial velocity and the accretion rate for $r \leq R$ are, respectively:

$$\begin{aligned}
n(r) &= \frac{A}{r^2}\sqrt{\frac{m\pi}{2\,\beta}}\, e^{-\beta\Phi(r)} \\
&\times \left[1 - \mathrm{Erf}\left(\sqrt{\beta[\Phi(R) - \Phi(r)]}\right)\right], && (6.4.14) \\
u^r(r) &= -\sqrt{\frac{2}{\beta m\pi}} e^{-\beta[\Phi(R) - \Phi(r)]} \\
&\times \left[1 - \mathrm{Erf}\left(\sqrt{\beta[\Phi(R) - \Phi(r)]}\right)\right]^{-1}, && (6.4.15) \\
|\dot{M}| &= 4\pi r^2\, m\, n(r)|u^r(r)| = 4\pi m \frac{A}{\beta} e^{-\beta\Phi(R)}, && (6.4.16)
\end{aligned}$$

where Erf(x) denotes the error function, and

$$A = n_R\, R^2 \sqrt{\frac{2\beta}{m\pi}} e^{\,\beta\Phi(R)}, \tag{6.4.17}$$

corresponding to the injection sphere at a radius R, which yields

$$\frac{|\dot{M}|}{m n_R} = 4\pi R^2 \sqrt{\frac{2}{\pi m \beta}} = 4\pi R^2 \sqrt{\frac{2}{\pi}\frac{k_{\mathrm{B}}T}{m}}\,. \tag{6.4.18}$$

6.4.2. Relativistic case

In the relativistic case one considers a Vlasov gas on a Schwarzschild background, with metric components $-g_{00} = 1/g_{rr} = \alpha(r)^2$ and $g_{0r} = 0$ in Eq. (6.3.8), where

$$\alpha(r)^2 := 1 - \frac{r_\mathrm{S}}{r}, \tag{6.4.19}$$

with r_S the Schwarzschild radius defined by $r_\mathrm{S} := 2GM/c^2$. The volume element in momentum space, Eq. (6.3.5), takes the form:

$$\mathrm{dvol}_x(p) = \frac{1}{r^2}\frac{dp_r}{p^0}, \tag{6.4.20}$$

with p^0 related to the relativistic energy E through

$$E = \alpha(r)^2 c\, p^0. \tag{6.4.21}$$

With Eqs. (6.3.4, 6.3.6) we find:

$$J^0(r) = \frac{c}{r^2}\int_{-\infty}^{p_\mathrm{m}(r,R)} f(r,p_r)\, dp_r\,, \tag{6.4.22}$$

$$J^r(r) = \frac{c}{r^2}\int_{-\infty}^{p_\mathrm{m}(r,R)} f(r,p_r)\,\frac{p^r}{p^0}\, dp_r, \tag{6.4.23}$$

$$n(r) = \frac{1}{c}\sqrt{[\alpha(r) J^0(r)]^2 - [J^r(r)/\alpha(r)]^2}, \tag{6.4.24}$$

where $p_\mathrm{m}(r,R) := -\frac{mc}{\alpha(r)^2}\sqrt{\alpha(R)^2 - \alpha(r)^2}$ (whose definition reduces to the one used in Eqs. (6.4.2-6.4.4) in the non-relativistic limit) originates from the requirement that all the particles are infalling and have minimum possible energy equal to $E = \alpha(r)mc^2$ [see Eq. (6.4.26)]. The boundary conditions are given by the particle number density at the injection sphere n_R, and the energy or temperature as before.

As an example, we reconsider the Vlasov gas of mono-energetic particles of mass m, now with relativistic energy $E_0 \geq \alpha(R)mc^2$. The expected distribution function is:

$$F(E) = f_0\,\delta(E - E_0), \tag{6.4.25}$$

where, again, f_0 is a constant with units of [time]$^{-1}$ related to n_R. From the general relation (6.3.3), we obtain:

$$E = \sqrt{[\alpha(r)^2\, p_r\, c]^2 + \alpha(r)^2\, m^2 c^4}, \tag{6.4.26}$$

so that the distribution function is written as:

$$\begin{aligned} f(r,p_r) &= f_0\,\delta\left(\sqrt{[\alpha(r)^2\, p_r\, c]^2 + \alpha(r)^2\, m^2 c^4} - E_0\right) \\ &= \frac{f_0\,\delta\left(p_r + \frac{mc}{\alpha(r)^2}\sqrt{\left(\frac{E_0}{mc^2}\right)^2 - \alpha(r)^2}\right)}{c\,\alpha(r)^2\sqrt{1 - \alpha(r)^2\left(\frac{mc^2}{E_0}\right)^2}}, \end{aligned} \tag{6.4.27}$$

where we have used the fact that all the particles have negative radial momentum. The invariant particle number density, the average radial velocity and the mass accretion rate computed from Eqs. (6.3.9, 6.4.22-6.4.24) and the boundary condition n_R, yield

$$n(r) = \frac{f_0}{r^2 c}\left[\left(\frac{E_0}{mc^2}\right)^2 - \alpha(r)^2\right]^{-1/2}, \tag{6.4.28}$$

$$u^r(r) = -c\left[\left(\frac{E_0}{mc^2}\right)^2 - \alpha(r)^2\right]^{1/2}, \tag{6.4.29}$$

$$|\dot{M}| = 4\pi m f_0, \tag{6.4.30}$$

valid for $r \leq R$, and with f_0 given by:

$$f_0 = n_R\, cR^2\sqrt{\left(\frac{E_0}{mc^2}\right)^2 - \alpha(R)^2}, \tag{6.4.31}$$

which yields

$$\frac{|\dot{M}|}{mcn_R} = 4\pi R^2\sqrt{\left(\frac{E_0}{mc^2}\right)^2 - \alpha(R)^2}. \tag{6.4.32}$$

Using Eq. (6.4.29), we get the familiar result

$$\frac{|\dot{M}|}{mn_R u^r(R)} = 4\pi R^2, \tag{6.4.33}$$

as follows directly from integrating the continuity equation for radially infalling dust in which case $\rho = mn$. Nevertheless, for our purposes it is convenient to express the accretion rate in terms of the 3-velocity v_R of the gas particles calculated by a static observer at the shell $r = R$, because the injection sphere is static with respect to the black hole. The relation between v_R and $u^r(R)$ is given by (see e.g. [166])

$$u^r(R) = \alpha(R)\, v_R\, \gamma, \tag{6.4.34}$$

where $\gamma := (1 - v_R^2/c^2)^{-1/2}$ is the Lorentz factor associated with v_R, which implies that

$$\frac{|\dot{M}|}{mn_R v_R} = 4\pi R^2\alpha(R)\gamma. \tag{6.4.35}$$

In the non-relativistic limit, with $v_R \ll c$ and $r_S \ll R$, the previous equations reduce to Eqs. (6.4.7-6.4.12), as expected.

We now consider a distribution function of the Maxwell-Jüttner-type [13],

$$F(E) = A\, e^{-\beta E}, \tag{6.4.36}$$

where $\beta = 1/k_{\mathrm{B}}T$, A is a constant with units of [length $\times$ momentum]$^{-1}$, the energy is given by Eq. (6.4.26), and T is the temperature of the gas at the injection sphere.[6] The resulting expressions from Eqs. (6.4.22-6.4.24) have no analytical closed form. Nevertheless, we can make a change of integration variable from p_r to the relativistic energy E through Eq. (6.4.26). In this way, for the Schwarzschild metric we get:

$$J^0(r) = \frac{1}{\alpha(r)^2 r^2}\int_{\alpha(R)mc^2}^{\infty} F(E)\,\frac{E}{\sqrt{E^2-\alpha(r)^2m^2c^4}}\,dE, \tag{6.4.37}$$

$$J^r(r) = \frac{1}{r^2}\int_{\alpha(R)mc^2}^{\infty} F(E)\,dE. \tag{6.4.38}$$

This set of equations can also be applied to the distribution function in Eq. (6.4.25) and the resulting expressions are again Eqs. (6.4.28-6.4.32). For the distribution function in Eq. (6.4.36), we obtain:

$$n_R = \frac{Amc}{R^2}\,\frac{\sqrt{\mathbf{K}_1(z)^2e^{2z}-z^{-2}}}{e^z}, \tag{6.4.39}$$

$$u^r(R) = -\frac{1}{\beta mc}\,\frac{1}{\sqrt{\mathbf{K}_1(z)^2e^{2z}-z^{-2}}}, \tag{6.4.40}$$

$$|\dot{M}| = 4\pi m\frac{A}{\beta}e^{-z}, \tag{6.4.41}$$

where $z := mc^2\alpha(R)\beta$ and $\mathbf{K}_1(z)$ is the modified Bessel function of the second kind and first order (see e.g. [92]). Note that the previous expressions are evaluated at $r = R$; this was necessary to get an analytical closed form. Eliminating A, we get an expression for the accretion rate:

$$\frac{|\dot{M}|}{mcn_R} = \frac{4\pi R^2\alpha(R)}{\sqrt{\left[\mathbf{K}_1(z)ze^z\right]^2-1}}. \tag{6.4.42}$$

Finally, considering the non-relativistic limit $mc^2 \gg k_{\mathrm{B}}T$, so that $z \gg 1$, we obtain:

$$\frac{|\dot{M}|}{mcn_R} \approx 4\pi R^2\alpha(R)\sqrt{\frac{2}{\pi z}} = 4\pi R^2\sqrt{\frac{2\alpha(R)}{\pi}\frac{k_{\mathrm{B}}T}{mc^2}}, \tag{6.4.43}$$

which reduces to the expression in Eq. (6.4.18) when $R \gg r_{\mathrm{S}}$.

6.5. Spherical accretion with angular momentum from a finite radius

In this section, we generalise the calculations of the previous section to the case in which individual gas particles are allowed to have angular momentum; however, we

[6] Strictly speaking, the distribution function described by (6.4.36) does not describe a configuration in thermodynamical equilibrium since in this section we restrict all the particles to have zero angular momentum.

assume that the averaged quantities describing the gas (i.e. the space-time observables) are still spherical. For simplicity, we shall assume a uniform distribution in the total angular momentum L, and take the same mono-energetic or Maxwell-Jüttner-like distribution in the energy as considered in the previous section. The analysis in this section is performed directly in the relativistic case with the Schwarzschild BH with mass M as an accretor.

We assume that the injection sphere is located at a radius $R > r_{\text{ISCO}} = 6GM/c^2$ larger than the radius of the innermost stable circular orbit (ISCO) (it will become clear in a moment why the restriction $R > r_{\text{ISCO}}$ is required). As in the previous section, we impose the particle number density n_R on the injection sphere, and we compute the solution satisfying this boundary condition and the corresponding accretion rate.

For the following, it is convenient to express the momentum in terms of orthonormal components (p^0, p^1, p^2, p^3) such that

$$p^\mu \frac{\partial}{\partial x^\mu} = p^0 \frac{1}{\alpha(r)} \frac{\partial}{\partial(ct)} + p^1 \alpha(r) \frac{\partial}{\partial r} + p^2 \frac{1}{r} \frac{\partial}{\partial \vartheta} + p^3 \frac{1}{r \sin\vartheta} \frac{\partial}{\partial \varphi} \tag{6.5.1}$$

where as before, $\alpha(r)^2 = 1 - \frac{r_S}{r}$. In terms of these orthonormal components the volume element (6.3.5) reads

$$\text{dvol}_x(p) = \frac{dp^1 dp^2 dp^3}{\sqrt{m^2c^2 + (p^1)^2 + (p^2)^2 + (p^3)^2}}. \tag{6.5.2}$$

Expressed in terms of the integrals of motion (E, L) and the angle χ defined by $L_z/L = \sin\vartheta \sin\chi$, one obtains

$$(p^\sigma_\pm) = \left(\frac{E}{c\,\alpha(r)}, \pm \frac{\sqrt{E^2 - V_L(r)}}{c\,\alpha(r)}, \frac{L\cos\chi}{r}, \frac{L\sin\chi}{r} \right), \tag{6.5.3}$$

$$\text{dvol}_x(p) = \frac{dE\ LdL\ d\chi}{r^2\sqrt{E^2 - V_L(r)}}, \tag{6.5.4}$$

where the $\pm$ sign in p^1 determines whether the particle is infalling or outgoing and $V_L(r)$ is the effective potential describing the radial motion, defined as

$$V_L(r) := c^2\alpha(r)^2 \left(m^2c^2 + \frac{L^2}{r^2} \right). \tag{6.5.5}$$

The behavior of the effective potential V_L is well-known but critical for what follows, so we briefly review its main features (see e.g. Appendix A in [36] for more details). For $L \leq L_{\text{ISCO}} := \sqrt{12}GMm/c$ the function V_L is monotonously increasing, which means that any infalling particle released from $r = R$ whose total angular momentum lies in this range inevitably falls into the black hole within a finite amount of its proper time. For $L > L_{\text{ISCO}}$ the function V_L has a local maximum inside the interval $(3GM/c^2, 6GM/c^2)$, which is due to the presence of the centrifugal term and which gives rise to a potential well with corresponding minimum lying in the interval $(6GM/c^2, \infty)$. Whether or not an infalling particle released from $r = R$ with $L > L_{\text{ISCO}}$ falls into the black hole depends on its energy (see Fig. **6-1**). If E^2 is larger than the maximum of the potential, the particle is absorbed by the black hole; otherwise it bounces off the centrifugal barrier and is reflected towards $r = R$.

Therefore, given $L \geq 0$, the relevant energy range for describing the aforementioned accretion scenario is $\sqrt{V_L(R)} \leq E < \infty$, with particles being absorbed or reflected depending on whether or not E^2 is larger than the centrifugal barrier of V_L. (We do not consider particles with energies lower than $\sqrt{V_L(R)}$ since they correspond to either bound trajectories whose turning points r_i satisfy $r_{\text{S}} < r_1 < r_2 < R$, and hence do not affect the value of n_R nor the accretion rate, or to particles emanating at a radius $r < R$ which are absorbed by the black hole in finite proper time.

When computing the current density (6.3.4) with the volume form expressed in terms of E, L and χ as in Eq. (6.5.3), the appropriate limits of integration for each variable have to be taken into account. The range for χ is obviously $(0, 2\pi)$, while $0 \leq L < \infty$ and $\sqrt{V_L(R)} \leq E < \infty$, as we have just described, where values of E^2 exceeding the local maximum of V_L give rise only to incoming particles with momentum p_-^σ and values of E^2 less than this maximum giving rise to both incoming and outgoing particles with momenta $p_\pm^\sigma$.

Since the distribution functions considered in this work depend only on E, one can perform the integrals over L explicitly, as shown below. For this, it is necessary to fix the energy level first and determine the correct limits for L as a function of E. Thus, the energy range is now $\sqrt{V_{L=0}(R)} = mc^2\alpha(R) \leq E < \infty$, while the value of the total angular momentum L is limited by the requirement that $V_L(R) \leq E^2$, which translates into an upper bound $L \leq L_{\text{max}}(E, R)$ for L. Furthermore, there is a critical value $L = L_{\text{c}}(E)$, corresponding to the value of L for which the effective potential has a local maximum equal to E^2, such that particles with $L < L_{\text{c}}(E)$ are absorbed and particles with $L > L_{\text{c}}(E)$ are reflected.

By analyzing the behavior of the two limits $L_{\text{max}}(E, R)$ and $L_{\text{c}}(E)$ as functions of E, one finds that there is a critical energy $E = E_{\text{c}}(R)$ for which they are equal, $L_{\text{max}}(E_{\text{c}}(R), R) = L_{\text{c}}(E_{\text{c}})$. Furthermore, we have $L_{\text{max}}(E, R) < L_{\text{c}}(E)$ for $mc^2\alpha(R) \leq E < E_{\text{c}}(R)$, and $L_{\text{max}}(E, R) > L_{\text{c}}(E)$ when $E > E_{\text{c}}(R)$. This leads to the following characterizations in the parameter space (E, L):

1. *Absorbed particles*

$$\begin{cases} mc^2\alpha(R) \leq E < E_{\text{c}}(R) \quad \text{and} \quad 0 \leq L \leq L_{\text{max}}(E, R), \\ E_{\text{c}}(R) < E < \infty \quad \text{and} \quad 0 \leq L < L_{\text{c}}(E). \end{cases}$$

2. *Scattered particles*

$$E_c(R) \leq E < \infty \quad \text{and} \quad L_c(E) < L < L_{\text{max}}(E, R). \tag{6.5.6}$$

The explicit expressions for E_c, L_{max} and L_c are derived in Gabarrete and Sarbach (paper in preparation) and [36] and they are:

$$E_c(R) = mc^2 \frac{R + r_S}{\sqrt{R(R + 3r_S)}}, \tag{6.5.7}$$

$$L_{\text{max}}(E, R) = mcR\sqrt{\frac{E^2}{m^2c^4\alpha(R)^2} - 1}, \tag{6.5.8}$$

$$L_c(E) = \frac{4\sqrt{2}GMm^3c^3}{\sqrt{36m^2c^4E^2 - 8m^4c^8 - 27E^4 + E(9E^2 - 8m^2c^4)^{3/2}}}, \tag{6.5.9}$$

where Eq. (6.5.9) is defined for $E \geq E_{\text{ISCO}} = 2\sqrt{2}mc^2/3$, which is the energy corresponding to the ISCO.[7] After these comments, it is straightforward to compute the mass accretion rate $\dot{M}$ and the particle number density n_R at the injection sphere. Using Eqs. (6.3.4, 6.5.3), we obtain

$$\begin{aligned} J^\sigma_{\text{abs}}|_{r=R} &= c\int\limits_{mc^2\alpha(R)}^{E_c(R)} \int\limits_0^{L_{\text{max}}(E,R)} \int\limits_0^{2\pi} \frac{p^\sigma_- F(E) dE L dL d\chi}{R^2\sqrt{E^2 - V_L(R)}} \\ &\quad + c\int\limits_{E_c(R)}^{+\infty} \int\limits_0^{L_c(E)} \int\limits_0^{2\pi} \frac{p^\sigma_- F(E) dE L dL d\chi}{R^2\sqrt{E^2 - V_L(R)}}, \end{aligned} \tag{6.5.10}$$

$$J^\sigma_{\text{sca}}|_{r=R} = c\sum_\pm \int\limits_{E_c(R)}^{+\infty} \int\limits_{L_c(E)}^{L_{\text{max}}(E,R)} \int\limits_0^{2\pi} \frac{p^\sigma_\pm F(E) dE L dL d\chi}{R^2\sqrt{E^2 - V_L(R)}}, \tag{6.5.11}$$

with $p^\sigma_\pm$ given by Eq. (6.5.3). We note from these expressions, that only the absorbed trajectories contribute to the mass accretion rate $\dot{M}$, since the terms p^1_+ and p^1_- in Eq. (6.5.11) cancel each other out. In contrast to this, all the trajectories (absorbed and scattered) contribute to the particle number density n_R. The non-vanishing orthonormal components yield:

$$\begin{aligned} J^0_{\text{abs}}\Big|_{r=R} &= \left\{ \int\limits_{mc^2\alpha(R)}^{+\infty} E\sqrt{E^2 - m^2c^4\alpha(R)^2} F(E) dE \right. \\ &\quad \left. - \int\limits_{E_c(R)}^{+\infty} E\sqrt{E^2 - V_c(E, R)} F(E) dE \right\} \frac{2\pi}{\alpha(R)^3c^2}, \end{aligned} \tag{6.5.12}$$

[7] As E increases from E_{ISCO} to ∞, $L_c(E)$ increases from L_{ISCO} to ∞, with $L_c(E) = 4GMm/c$ for $E = mc^2$.

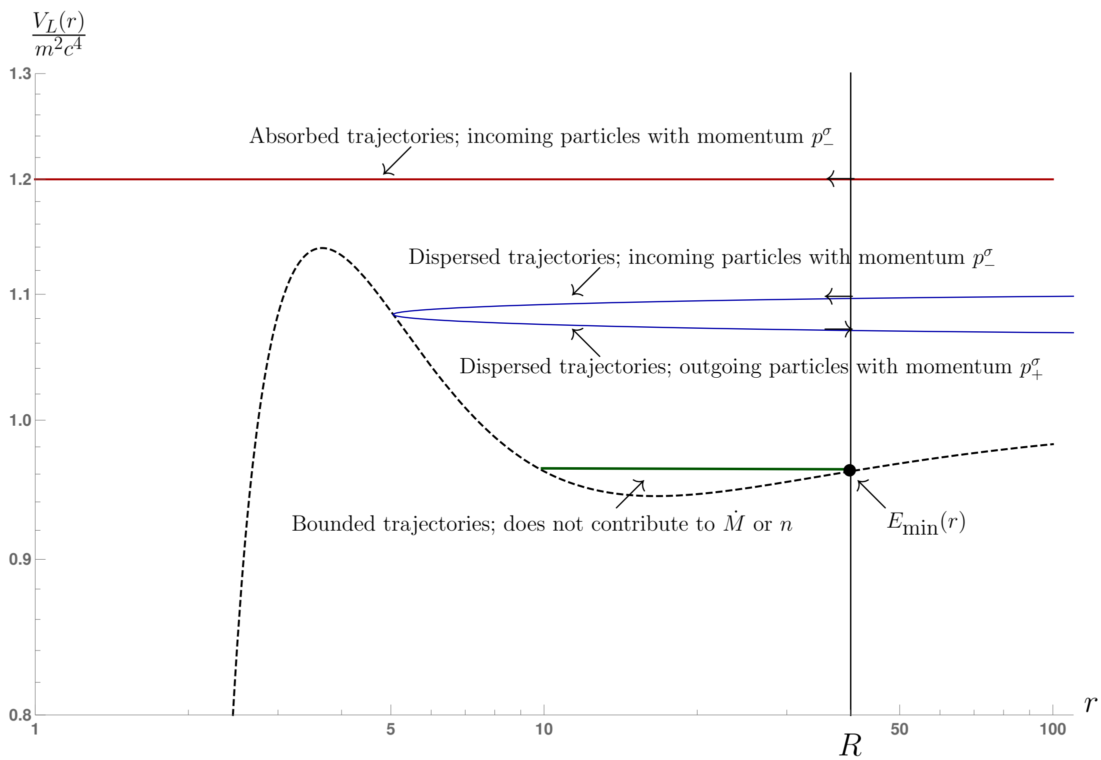

Figure 6-1: Plot of the Schwarzschild effective potential $V_L(r)$ vs r (with r in units of $r_{\rm S}$) and $L = 4.5GMm/c$. We have identified for the absorbed trajectories the incoming moments by p^σ_-, while for the scattered trajectories the incoming moments are p^σ_- and the outgoing moments are p^σ_+. Here, the $\pm$ sign in $p^\sigma_\pm$ refers to the same sign appearing in the p^1 component of Eq. (6.5.3). For more details on the effective potential see [52, 56] and Appendix A of [36].

$$J^1_{\text{abs}}\Big|_{r=R} = -\left\{ \int\limits_{mc^2\alpha(R)}^{E_c(R)} L_{\max}(E,R)^2 F(E)dE + \int\limits_{E_c(R)}^{+\infty} L_c(E)^2 F(E)dE \right\} \frac{\pi}{R^2\alpha(R)}, \tag{6.5.13}$$

$$J^0_{\text{sca}}\Big|_{r=R} = \frac{4\pi}{\alpha(R)^3c^2} \int\limits_{E_c(R)}^{+\infty} E\sqrt{E^2 - V_c(E,R)}F(E)dE, \tag{6.5.14}$$

where we have introduced the shorthand notation $V_c(E,R) := V_{L_c(E)}(R)$. Note that by definition, $E_c(R)^2 \geq V_c(E,R)$ for all $R \geq r_{\text{ISCO}}$ and $V_{L_c(E)}(R) \to m^2c^4$ for $R \to \infty$; hence only the scattered particles yield a non-vanishing contribution to $J^\alpha|_{r=R}$ when $R \to \infty$. Using Eqs. (6.3.9, 6.5.12, 6.5.13, 6.5.14), and $J^r = \alpha J^1_{\text{abs}}$, one obtains the mass accretion rate

$$\dot{M} := 4\pi m R^2 \, J^r|_{r=R} = -4\pi^2 m \left\{ \int\limits_{E_c(R)}^{+\infty} L_c(E)^2 F(E)dE + \int\limits_{mc^2\alpha(R)}^{E_c(R)} L_{\max}(E,R)^2 F(E)dE \right\}, \tag{6.5.15}$$

and the particle number density at $r = R$,

$$n_R = \frac{1}{c}\sqrt{\left[J^0_{\text{abs}}(R) + J^0_{\text{sca}}(R)\right]^2 - \left[J^1_{\text{abs}}(R)\right]^2}. \tag{6.5.16}$$

In the following, we further analyze these results for the mono-energetic and Maxwell-Jüttner-type distributions in the energy.

6.5.1. Mono-energetic model

For the mono-energetic model $F(E) = f_0\,\delta(E - E_0)$, one obtains

$$\frac{|\dot{M}|}{mcn_R} = 4\pi R^2\alpha(R)\sqrt{\frac{\gamma^2-1}{3\gamma^2+1}}, \quad \text{for} \quad 1 < \gamma < \gamma_c(R), \tag{6.5.17}$$

$$\frac{|\dot{M}|}{mcn_R} = \frac{4\pi R^2\alpha(R)h(R,\gamma)}{\left[4\gamma^2\left(\sqrt{\gamma^2-1} + \sqrt{\gamma^2-1-h(R,\gamma)}\right)^2 - h(R,\gamma)^2\right]^{1/2}}, \quad \text{for} \quad \gamma > \gamma_c(R), \tag{6.5.18}$$

where we recall that $\gamma = (1 - v_R^2/c^2)^{-1/2}$ is the Lorentz factor associated with the 3-velocity of the gas particles measured by a static observer at the injection sphere (see

Section 6.4.2), such that the energy E_0 is given by[8]

$$E_0 = mc^2\alpha(R)\gamma. \tag{6.5.19}$$

Further, $\gamma_{\mathrm{c}}(R) := E_{\mathrm{c}}(R)/(mc^2\alpha(R))$ and h denotes the function

$$\begin{aligned} h(R,\gamma) &:= \left[\frac{L_{\mathrm{c}}(E_0)}{mcR}\right]^2 \\ &= \frac{8r_{\mathrm{S}}^2}{R^2}\frac{1}{36\,\alpha^2\gamma^2 - 8 - 27\alpha^4\gamma^4 + \alpha\gamma[9\alpha^2\gamma^2 - 8]^{3/2}}. \end{aligned} \tag{6.5.20}$$

The formulae (6.5.17, 6.5.18) generalize the Bondi-type formula that can be found, for instance in [143, Chapter 14, Section 2], to the accretion of a mono-energetic gas of arbitrary energy $E_0 > mc^2\alpha(R)$ accreting from a sphere of finite radius $R > r_{\mathrm{ISCO}}$. Using the fact that for $E = E_{\mathrm{c}}(R)$ one has $L_{\mathrm{c}}(E) = L_{\mathrm{max}}(E, R)$, it is simple to verify that $|\dot{M}|$ is continuous at the transition point $\gamma = \gamma_{\mathrm{c}}(R)$, where it has the value

$$\frac{|\dot{M}|}{mcn_R} = \frac{4\pi r_{\mathrm{S}} R\alpha(R)}{\sqrt{1 + \frac{2r_{\mathrm{S}}}{R}}}. \tag{6.5.21}$$

In fact, for fixed R, $|\dot{M}|$ is a monotonically increasing function of γ in the interval $1 < \gamma < \gamma_{\mathrm{c}}(R)$, while it decreases monotonically for $\gamma > \gamma_{\mathrm{c}}(R)$. Thus, Eq. (6.5.21) is the maximum accretion rate for the mono-energetic model with angular momentum. In the limit $R \to \infty$ it follows that $E_{\mathrm{c}}(R) \to mc^2$ [see Eq. (6.5.7)] such that $\gamma_{\mathrm{c}}(R) \to 1$ and Eq. (6.5.18) reduces to

$$\begin{aligned} \frac{|\dot{M}|}{mcn_\infty} &= \frac{\pi L_{\mathrm{c}}^2(mc^2\gamma_\infty)}{m^2c^2\gamma_\infty\sqrt{\gamma_\infty^2 - 1}} \\ &= \frac{16\pi G^2M^2}{c^3 v_\infty}\left[1 + \frac{v_\infty^2}{c^2} - \frac{v_\infty^4}{c^4} + \mathcal{O}\left(\frac{v_\infty^6}{c^6}\right)\right], \end{aligned} \tag{6.5.22}$$

where $n_\infty := \lim\limits_{R\to\infty} n_R$, $v_\infty := \lim\limits_{R\to\infty} v_R$, and $\gamma_\infty := \lim\limits_{R\to\infty} \gamma_R$. The leading-order term in v_∞/c agrees with Eq. (14.2.20) in [143].

Comparing Eq. (6.5.17) with the corresponding expression for the mass accretion rate in the absence of angular momentum [see Eq. (6.4.32)], the difference relies in the factor $(3\gamma^2+1)^{-1/2} \leq 1$ which implies that for $\gamma < \gamma_{\mathrm{c}}(R)$ the accretion rate is smaller when the angular momentum is considered. This is expected since the tangential movement of particles with angular momentum reduces the net infall of particles. Note that in the non-relativistic limit $\gamma \to 1$ and fixed R one obtains half the value given in

[8] The relation between the energy E_0 and the speed v_R in Eq. (6.5.19) can be computed using the formula $\frac{|\vec{v}_R|^2}{c^2} = \frac{|\vec{p}|^2}{(p^0)^2}$, with $|\vec{p}|^2 \equiv (p^1)^2 + (p^2)^2 + (p^3)^2$, where p^i are the orthonormal components defined in Eq. (6.5.3).

Eq. (6.4.35) computed for the purely radial infall. As further analyzed in Appendix 6.9, this is due to the fact that when angular momentum is present, the three-velocity contains non-trivial angular components.

A simplified form of Eqs. (6.5.17, 6.5.18) can be obtained in the limit when the injection sphere is far from the horizon: $R \gg r_\mathrm{S}$ and for non-relativistic energies, such that $v_R \ll c$. For this, one notices that

$$\gamma_\mathrm{c}(R) - 1 = 2\left(\frac{r_\mathrm{S}}{R}\right)^2 + \mathcal{O}\left(\frac{r_\mathrm{S}}{R}\right)^3, \tag{6.5.23}$$

and that the denominator of the second factor on the right-hand side of (6.5.20) converges to 2 when $\alpha(R) \to 1$ and $\gamma \to 1$. Using this, one finds to leading order,

$$\frac{|\dot{M}|}{mcn_R} = 4\pi R^2 \times \begin{cases} \dfrac{v_R}{2c}, & \dfrac{v_R}{2c} < \dfrac{r_\mathrm{S}}{R}, \\[2ex] \dfrac{2c}{v_R}\left(\dfrac{r_\mathrm{S}}{R}\right)^2 \dfrac{1}{1+\sqrt{1-\left(\frac{2c}{v_R}\frac{r_\mathrm{S}}{R}\right)^2}}, & \dfrac{v_R}{2c} > \dfrac{r_\mathrm{S}}{R}, \end{cases} \tag{6.5.24}$$

which is valid for $R \gg r_\mathrm{S}$ and $v_R \ll c$.

In Fig. **6-2** we show the behaviour of the dimensionless quantity $\Gamma = \dfrac{|\dot{M}|}{4\pi R^2 \alpha(R) mcn_R}$ as a function of γ for different values of R. As can be observed from this figure, $|\dot{M}|$ increases with γ for small velocities v_R, the quantity Γ being independent of R, as follows from Eq. (6.5.17). Hence, in this regime the qualitative behaviour of the accretion rate as a function of v_R is similar to the case of purely radial infall (the only difference consisting of the factor $(3\gamma^2+1)^{-1/2}$, as explained above). However, as soon as γ reaches the critical value $\gamma_\mathrm{c}(R)$, $|\dot{M}|$ starts decreasing, converging to a finite (R-dependent value) in the limit $\gamma \to \infty$. This can be understood as follows: when $\gamma < \gamma_\mathrm{c}(R)$, all the particles have their energy below the critical value $E_\mathrm{c}(R)$ and thus all of them are absorbed by the black hole. This leads to an accretion rate which increases with v_R. However, when $\gamma > \gamma_\mathrm{c}(R)$, the particles have their energy lying above $E_\mathrm{c}(R)$ and hence a fraction of them (namely, those with angular momentum larger than $L_\mathrm{c}(E)$) are scattered off the effective potential, leading to a smaller accretion rate. As v_R increases this fraction becomes larger which leads to a smaller mass accretion rate (see [37] for a more extended discussion regarding this effect for a similar model with $R \to \infty$).

6.5.2. Maxwell-Jüttner-type distribution function

Next, we analyze the Maxwell-Jüttner-type distribution (6.4.36) which was also considered in [36,37].[9] To understand this limit, it is convenient to perform the variable subs-

[9] Again, one should be careful with associating T with temperature. Although in this section the gas particles are not restricted to zero angular momentum, the gas is still not in strict thermodynamic

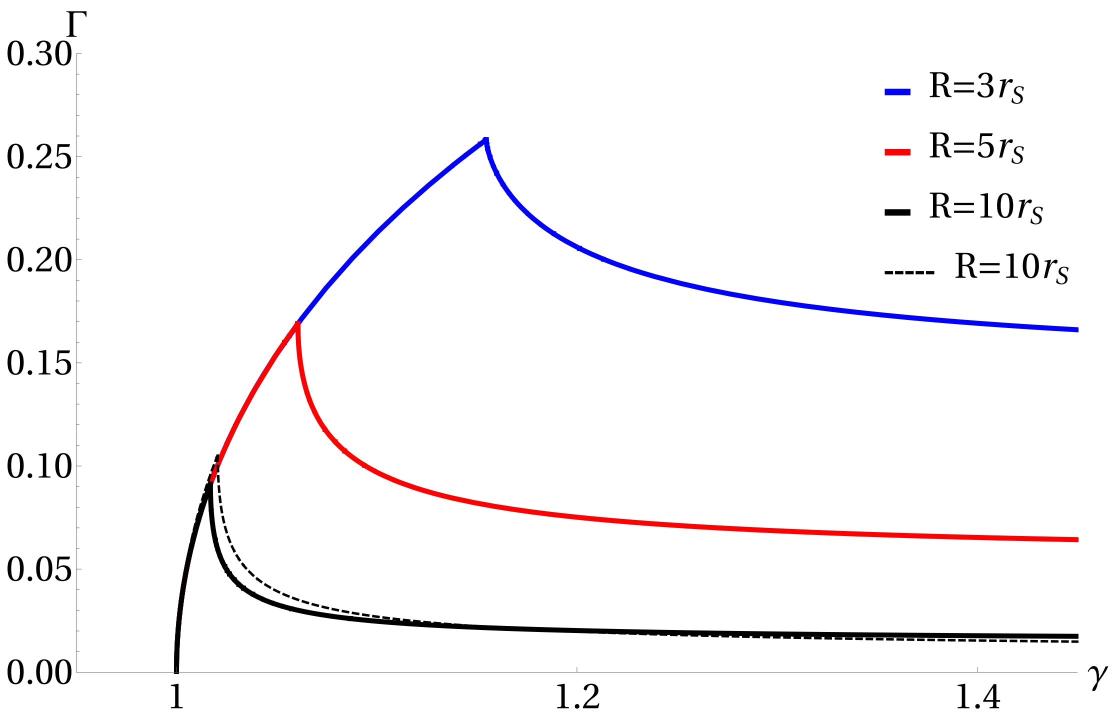

Figure 6-2: The dimensionless quantity $\Gamma = |\dot{M}|/(4\pi R^2 \alpha(R) mcn_R)$ vs the Lorentz factor $\gamma = (1 - v_R^2/c^2)^{-1/2}$ for some fixed values of the injection sphere's radius R. The solid lines are computed from Eqs. (6.5.17,6.5.18) for different values of R. The black dashed line shows the same quantity Γ for the case $R = 10r_\text{S}$, using the approximation from Eqs. (6.5.24, 6.5.24) which is valid for $R \gg r_\text{S}$ and non-relativistic velocities $v_R \ll c$.

titutions $E = mc^2\alpha(R)(1+x/z)$ and $E = E_{\rm c}(R)(1+y/z)$ in the integrals Eqs. (6.5.12, 6.5.13, 6.5.14), where we set $z(R,T) := z = mc^2\beta\alpha(R)$. This yields

$$J^0 \quad := \left(J^0_{\rm abs} + J^0_{\rm sca}\right)\Big|_{r=R} = \frac{2\pi A m^3 c^4}{z^{3/2}} e^{-z} I_1(R,z), \tag{6.5.25}$$

$$J^1 \quad := J^1_{\rm abs}\Big|_{r=R} = -\frac{\pi A m^3 c^4}{z^2} e^{-z} I_2(R,z), \tag{6.5.26}$$

with the integrals $I_1(R,z)$ and $I_2(R,z)$ given by

$$\begin{aligned} I_1(R,z) \;=\; & \int\limits_0^\infty \left(1+\frac{x}{z}\right)\sqrt{2x+\frac{x^2}{z}}e^{-x}dx \\ & + \gamma_{\rm c}(R)^3 e^{-\Lambda(R,z)} \int\limits_0^\infty \left(1+\frac{y}{z}\right) e^{-\gamma_{\rm c}(R)y} \\ & \times \sqrt{z\left[1-\frac{V_{\rm c}\left[E_{\rm c}(R)\left(1+\frac{y}{z}\right),R\right]}{E_{\rm c}(R)^2}\right]+2y+\frac{y^2}{z}}dy, \end{aligned} \tag{6.5.27}$$

$$\begin{aligned} I_2(R,z) \;=\; & \int\limits_0^{\Lambda(R,z)} \left(2x+\frac{x^2}{z}\right)e^{-x}dx + \frac{\gamma_{\rm c}(R)}{R^2} z e^{-\Lambda(R,z)} \\ & \times \int\limits_0^\infty \frac{L_{\rm c}\left[E_{\rm c}(R)\left(1+\frac{y}{z}\right)\right]^2}{m^2c^2} e^{-\gamma_{\rm c}(R)y} dy, \end{aligned} \tag{6.5.28}$$

where we recall the shorthand notation $\gamma_{\rm c}(R) := E_{\rm c}(R)/(mc^2\alpha(R))$ and where we have set $\Lambda(R,z) := (\gamma_{\rm c}(R)-1)z$. From Eqs. (6.5.25, 6.5.26), one obtains the following expression for the mass accretion rate:

$$\frac{|\dot{M}|}{mcn_R} = \frac{4\pi R^2\alpha(R)}{\sqrt{4z\left[\frac{I_1(R,z)}{I_2(R,z)}\right]^2-1}}. \tag{6.5.29}$$

Eq. (6.5.29), together with the integrals defined in Eqs. (6.5.27, 6.5.28), provides an exact expression for the mass accretion rate as a function of the injection radius R and the temperature T. Unfortunately, the integrals involved are rather complicated, and for this reason it is advantageous to obtain simplified expressions for certain limits. One such expression can be obtained assuming that the gas temperature is low, such that $k_{\rm B}T \ll mc^2$, and that $R \gg r_{\rm S}$ is much larger than the Schwarzschild radius of the accreting black hole. In order to discuss this limit, we first note that

$$1-\frac{V_{\rm c}\left[E_{\rm c}(R)\left(1+\frac{y}{z}\right),R\right]}{E_{\rm c}^2(R)} = -\frac{16r_{\rm S}^2}{R^2-r_{\rm S}^2}\frac{y}{z}+\mathcal{O}\left(\frac{y^2}{z^2}\right), \tag{6.5.30}$$

equilibrium at finite R because we are not considering hypothetical incoming particles emanating from the white hole. See the discussion in Section 4 of [37].

and hence for $z \gg 1$ one obtains

$$\begin{aligned} I_1(R,z) &\approx \int_0^\infty \sqrt{2x}e^{-x}dx \\ &+ \gamma_c(R)^3 e^{-\Lambda(R,z)} \int_0^\infty \sqrt{2y\frac{1-(3r_S/R)^2}{1-(r_S/R)^2}}e^{-\gamma_c(R)y}dy. \end{aligned} \tag{6.5.31}$$

Now the integrals can be evaluated explicitly which yields, for $z \gg 1$,

$$I_1(R,z) \approx \sqrt{\frac{\pi}{2}}\left[1+\gamma_c(R)^{3/2}e^{-\Lambda(R,z)}\sqrt{\frac{1-(3r_S/R)^2}{1-(r_S/R)^2}}\right]. \tag{6.5.32}$$

Similarly,

$$\begin{aligned} I_2(R,z) &\approx 2-2[1+\Lambda(R,z)]e^{-\Lambda(R,z)} \\ &+ \frac{4r_S^2}{R^2[\gamma_c(R)-1]}\frac{\Lambda(R,z)e^{-\Lambda(R,z)}}{\alpha(R)^2\,(1+3r_S/R)}, \end{aligned} \tag{6.5.33}$$

for $z \gg 1$, where we have used that $L_c\,[E_c(R)]^2\,/(mc)^2 = 4r_S^2/[\alpha(R)^2\,(1+3r_S/R)]$. The expressions (6.5.32, 6.5.33) are valid when z is much larger than one, independent of the value of R. When $R \gg r_S$ one can use the expansion (6.5.23) to show that $\Lambda(R,z) \approx 2(r_S/R)^2 z$. Therefore, $\Lambda(R,z)$ depends on the ratio between the two large quantities z and R^2, implying that it varies over the whole range $(0,\infty)$. Assuming that $R \gg r_S$ in Eqs. (6.5.32, 6.5.33) leads to a further simplification,

$$I_1(R,z) \approx \sqrt{\frac{\pi}{2}}\left[1+e^{-\Lambda(R,z)}\right], \tag{6.5.34}$$

$$I_2(R,z) \approx 2\left[1-e^{-\Lambda(R,z)}\right], \tag{6.5.35}$$

and introduced into Eq. (6.5.29) one obtains the simple expression

$$\frac{|\dot{M}|}{mcn_R} \approx R^2\alpha(R)\tanh\left(\frac{r_S^2}{R^2}z\right)\sqrt{\frac{32\pi}{z}}, \tag{6.5.36}$$

which is valid for arbitrary values of $R \gg r_S$ and $z = mc^2/(k_B T) \gg 1$. In the limit $R \to \infty$ one obtains, setting $z_\infty := \lim\limits_{R\to\infty} z$,

$$\frac{|\dot{M}|}{mcn_\infty} \approx \sqrt{32\pi z_\infty}r_S^2, \tag{6.5.37}$$

which agrees with Eq. (87) in [36].

In Fig. **6-3** we show the dimensionless quantity $\Gamma = |\dot{M}|/(4\pi R^2\alpha(R)mcn_R)$ as a function of the temperature T for different values of R. The behaviour is very similar to the one of the mono-energetic model, except that the function is smooth at the maximum value of the accretion rate, which is due to the non-trivial velocity dispersion in the distribution function.

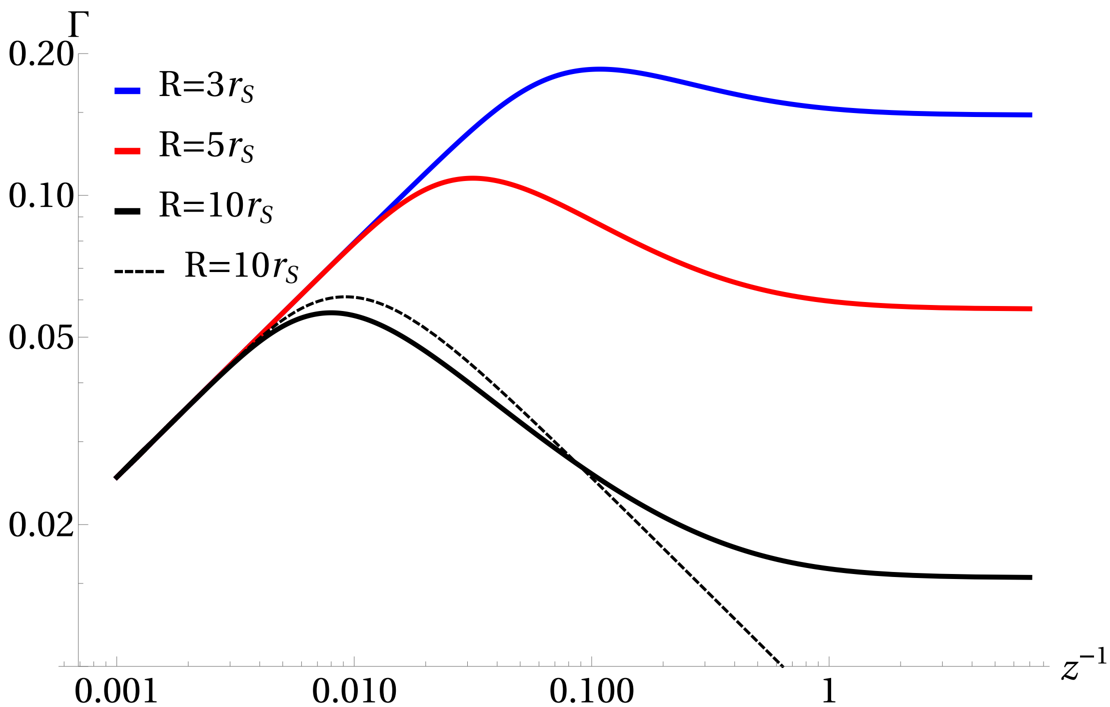

Figure 6-3: The dimensionless quantity $\Gamma = |\dot{M}|/(4\pi R^2\alpha(R)mcn_R)$ vs $z^{-1} = k_BT/(mc^2\alpha(R))$ for some fixed values of the radius R of the injection sphere. The solid lines are computed from Eq. (6.5.29) for different values of R. The black dashed line shows the same quantity Γ for the case $R = 10r_{\rm S}$, using the approximation from Eq. (6.5.36) which is valid for $R \gg r_{\rm S}$ and non-relativistic temperatures $z^{-1} \ll 1$.

6.6. Summary of analytic models

In this section we provide a summary of the expressions we have obtained for the mass accretion rate in the different models presented in Sections 6.4 and 6.5. We restrict ourselves to the relativistic models which describe the spherical accretion of a collisionless kinetic gas onto a Schwarzschild BH. In all these models, the mass accretion rate can be written in the following general form:

$$|\dot{M}| = 4\pi R^2 \alpha(R) m c n_R \Gamma, \tag{6.6.1}$$

where R is the areal radius of the injection sphere, $\alpha(R) = \sqrt{1 - r_{\mathrm{S}}/R}$, with $r_{\mathrm{S}} = 2GM/c^2$ the Schwarzschild radius of the black hole, m the mass of the particles and n_R the particle density at the injection sphere. Here, Γ is a model-dependent dimensionless factor which is defined as follows.

1. Purely radial mono-energetic model:

$$\Gamma = \frac{v_R}{c} \frac{1}{\sqrt{1 - \frac{v_R^2}{c^2}}}, \tag{6.6.2}$$

   where v_R is the magnitude of the three-velocity measured by static observers at the injection sphere.

2. Purely radial Maxwell-Jüttner model:

$$\Gamma = \frac{1}{\sqrt{\left[\mathbf{K}_1(z) z e^z\right]^2 - 1}}, \tag{6.6.3}$$

   where $z = mc^2\alpha(R)/k_{\mathrm{B}}T$ with T the gas temperature at the injection sphere and where $\mathbf{K}_1(z)$ is the modified Bessel function of the second kind of first order. In the low-temperature limit $z \gg 1$ this factor reduces to $\Gamma \approx \sqrt{2/(\pi z)}$.

3. Mono-energetic model with angular momentum: In this case, Γ can be read off from Eqs. (6.5.17, 6.5.18). However, in the limit $R \gg r_{\mathrm{S}}$ and $v_R \ll c$ this simplifies to

$$\Gamma \approx \begin{cases} \dfrac{v_R}{2c}, & \frac{v_R}{2c} < \frac{r_{\mathrm{S}}}{R}, \\ \dfrac{\frac{2c}{v_R}\left(\frac{r_{\mathrm{S}}}{R}\right)^2}{1 + \sqrt{1 - \left(\frac{2c}{v_R}\frac{r_{\mathrm{S}}}{R}\right)^2}}, & \frac{v_R}{2c} > \frac{r_{\mathrm{S}}}{R}. \end{cases} \tag{6.6.4}$$

4. Maxwell-Jüttner model with angular momentum:

$$\Gamma = \frac{1}{\sqrt{4z\left[\frac{I_1(R,z)}{I_2(R,z)}\right]^2 - 1}}, \tag{6.6.5}$$

where the integrals I_1 and I_2 are defined in Eqs. (6.5.27, 6.5.28). In the limit $R \gg r_S$ and $z \gg 1$ this simplifies to

$$\Gamma \approx \sqrt{\frac{2}{\pi z}} \tanh\left(\frac{r_S^2}{R^2} z\right). \tag{6.6.6}$$

Note that in the limit $z \gg R^2/r_S^2$ one obtains precisely the same result as the low-temperature limit of the purely radial Maxwell-Jüttner model. This shows that at very low temperatures the angular momentum is unimportant which is expected, since at low temperature most of the particles have low energy and hence must have low angular momentum as well.[10]

6.7. Applications

In this section, we discuss a couple of astrophysical scenarios which allow us to point out some important quantitative differences between the mass accretion rates predicted by our and previous models.

6.7.1. Accretion onto Sgr A* from matter located near the Bondi radius

In most scenarios, the Bondi accretion can be considered as a reliable first approximation.[11] For a polytropic transonic accretion flow, the Bondi mass accretion rate $\dot{M}_B$ is defined through the following expression ([120, 167]):

$$\frac{|\dot{M}_B|}{c_\infty \rho_\infty} = 4\pi\lambda r_B^2, \tag{6.7.1}$$

where c_∞ is the sound speed of the fluid at infinity, ρ_∞ is the fluid density at infinity, and λ is a function of the adiabatic index of the fluid γ_a (e.g. [120]). For a monoatomic adiabatic process, one has $\gamma_a = 5/3$ and $\lambda = 1/4$. Note that we have written Eq. (6.7.1)

[10] See Eq. (6.5.8): L_{max} is small if E is close to its minimum value $\alpha(R)mc^2$.

[11] Strictly speaking, the mass accretion rate for the case the central object is a black hole should be computed by means of a general relativistic calculation. However, when $\gamma_a \leq 5/3$ and for low temperatures (such that $k_B T_\infty/(m_p c^2) \ll 1$), the Newtonian calculation yields a very good approximation to the general relativistic case even if the central black hole is rotating [130].

as a ratio in order to keep the same format that we followed in the previous sections. The Bondi radius r_{B} in Eq. (6.7.1) is defined as

$$r_{\mathrm{B}} = \frac{GM}{c_{\infty}^{2}}. \tag{6.7.2}$$

Note that the adiabatic speed of sound of the fluid is defined as

$$c_s = \left(\frac{\partial P}{\partial \rho}\right)^{1/2} = \left(\gamma_{\mathrm{a}}\frac{P}{\rho}\right)^{1/2} = \left(\frac{\gamma_{\mathrm{a}} k_{\mathrm{B}} T}{\mu m_{\mathrm{p}}}\right)^{1/2}, \tag{6.7.3}$$

where the ideal gas equation of state is assumed, $P = \frac{\rho k_{\mathrm{B}} T}{\mu m_{\mathrm{p}}}$, and $\mu = \langle m\rangle / m_{\mathrm{p}}$ is the mean molecular weight which depends on the ionisation state of the gas. The relation between the particle number density n and mass density is $\rho = n\langle m\rangle$, and the former has a contribution from the electrons and ions. Therefore it is common to consider the mean molecular weight separately. In the case of electrons, the mean molecular weight per electron is $\mu_{\mathrm{e}} \approx 2/(1+X)$, where X is the hydrogen mass fraction. For example, a fully ionised purely hydrogen gas has $\mu = 0.5$ and $\mu_{\mathrm{e}} = 1$.

In practice, one substitutes the values of the particle number density and temperature obtained from X-ray observations at a finite radius from the SMBH in the Bondi accretion rate model given by Eq. (6.7.1). In this way, considering the characteristic parameters for Sgr A*: a mass of $\sim 4.3 \times 10^{6}\,\mathrm{M}_{\odot}$ ([132, 133]), a flow with temperature of 2.2×10^{7} K (1.9 keV), a sound speed of 550 km s^{-1} and an electron number density of 160 cm^{-3} measured at $R \sim 0.06$ pc (e.g. [138, 168]), the Bondi accretion rate yields

$$\begin{aligned} |\dot{M}_{\mathrm{B}}| \;&\sim\; 10^{-4}\,\mathrm{M}_{\odot}\mathrm{yr}^{-1}\left(\frac{\mathrm{M}}{4.3\times 10^{6}\mathrm{M}_{\odot}}\right)^{2}\left(\frac{n_{\mathrm{e}}}{160\,\mathrm{cm}^{-3}}\right) \\ &\times\; \left(\frac{k_{\mathrm{B}}T}{1.9\,\mathrm{keV}}\right)^{-\frac{3}{2}}, \end{aligned} \tag{6.7.4}$$

where an adiabatic index $\gamma_{\mathrm{a}} = 5/3$, $\rho = \mu_{\mathrm{e}} m_{\mathrm{p}} n_{\mathrm{e}}$ and $\mu = 1$ and $\mu_{\mathrm{e}} = 1$ was assumed as in [134]. In this case, it is implicit that one assumes the selected finite radius to be a good approximation for the values n_{∞} and T_{∞}. Nevertheless, this assumption can lead to an overestimate of the actual mass accretion rate (see e.g. [167]. In the past years, accretion models based on numerical hydrodynamical simulations have estimated a mass accretion rate of order $\sim 10^{-6} M_{\odot}\,\mathrm{yr}^{-1}$ at the Bondi radius scales (e.g. [169–171]).

Another plausible way to estimate the mass accretion rate in these systems is through rotation measures (RM) derived from the observed polarized emission as has been previously done with Sgr A*. The RM is proportional to the integrated electron density and the parallel component of the magnetic field to the line of sight.[12] Therefore, the

[12] RM = $0.81 \int n_{\mathrm{e}} B_{\|}\, dl$ rad m^{-2}, with n_{e} in units of cm^{-3}, B in μG and dl in pc.

interpretation of the RM relies on a radial model for both the density and the magnetic field. On the other hand, the radial dependency changes according to the assumed accretion model (e.g. Bondi or the various RIAF models). These model-dependent radial profiles are used in combination with certain assumptions on the magnetic field, such as equipartition between the magnetic and gravitational energy, in order to get upper and lower limits on the mass accretion rate in the vicinity of the BH horizon ([172–174]).

In these polarimetry observations, a low mass accretion rate near Sgr A*'s horizon is inferred from the RM of a few $\times 10^5\,\mathrm{rad\,m^{-2}}$ at 230 GHz ([173, 175]). The inferred mass accretion rate lies in the range of 10^{-9}–$10^{-7}\,\mathrm{M_\odot yr^{-1}}$, or even lower depending on the assumed inner and outer radii enclosing the polarized emission (see fig. 4 in [173], and [174]). The polarized emission is variable in time and as a consequence, there is variability on the RM. This RM variability can then be translated into a specific radius from which one takes the RM to originate, i.e. the observed RM comes from a wide range of radii. At very large radii, the RM inferred and extrapolated mass accretion rate is at least one order of magnitude smaller than the $\sim 10^{-5}$–$10^{-4}\,\mathrm{M_\odot yr^{-1}}$ rate estimated from X-ray measurements at a few $\times 10^5\, r_\mathrm{S}$ (see [172]). At such radii and assuming a magnetic field strength of $\sim\ 1$ mG, the RM should be of the order of $\sim\ 10^3$ rad m^{-2}, which is two orders of magnitude smaller than what is obtained in observations. In principle this suggests that the observed RM is produced at distances much smaller than $10^5\, r_\mathrm{S}$. Nevertheless, [175] more recently carried out a careful study on the RM variability of Sgr A* where they found that the variability remains consistent with the average long-term RM value. Based on this long-term variability result, the authors suggest that the magnetic configuration at large radii could be stable and therefore, they support the interpretation of the observed Faraday Rotation to arise mainly from $\sim\ 10^3$–$10^5\, r_\mathrm{S}$ (see more details in [175]). This means that overall, RM observations favor models predicting low mass accretion rates in the vicinities of Sgr A*'s horizon.

In the following, we estimate the mass accretion rate of Sgr A* for our different models. One variable needed for our estimates is the velocity of the particles at the injection radius, v_R. Although this velocity is not known a priori, it is reasonable to suppose that it is of the order of the fluid sound speed or to assume that its value is of the order of the wind velocity from known massive stars (O-type stars and/or Wolfâ€“Rayet (WR) stars) that are embedded within the dilute accretion flow towards Sgr A*. These wind velocities are of the order of $\sim\ 450$–$3000\,\mathrm{km\,s^{-1}}$ depending if they are O-type stars (e.g. [176–178]), or WR stars ([179, 180]). The accretion flow of Sgr A* from stellar winds has been extensively studied using hydrodynamical numerical simulations. For example, results from simulations of wind-fed accretion from WR stars have been shown to be consistent with observational constraints such as X-ray luminosities and RM ([169, 170, 181–183]). Knowing that these stellar winds could be the main contributors of the accretion towards Sgr A*, we will assume an infall velocity that lies within the aforementioned velocity range.

In our models, we use the same temperature for the cases described by a Maxwell-Boltzmann or Maxwell-Jüttner distribution, whereas in the mono-energetic cases we convert this temperature to a velocity by choosing v_R such that $m_\mathrm{p} v_R^2$ matches $2k_\mathrm{B}T$ in a first approximation. This yields $v_R = 600\,\mathrm{km\,s^{-1}}$, which lies within the velocity range of stellar winds. Furthermore, we also use this v_R to compute the mass accretion rate for the Shapiro-Teukolsky model for mono-energetic particles (Eq. (14.2.20) in [143]) and the same temperature for the Rioseco-Sarbach model (Eq. (87) in [36]). We show the comparisons in Table **6-1**. The mass accretion rates are obtained at the fixed finite radius $R = 0.06\,\mathrm{pc}$ for the different models studied in this work. Note that in this case we have considered the observational approach and assumed that the values of n_∞ or n_R correspond to the measured electron number density n_e at $R = 0.06\,\mathrm{pc}$ as is regularly done when applying the Bondi model.

We see from Table **6-1** that our models predict significantly different mass accretion rates depending on whether or not the infalling particles have angular momentum. The results from the purely radial infall in the kinetic description, both in the relativistic and non-relativistic cases, agree in order of magnitude with those of the hydrodynamical Bondi model. In contrast to this, the models with angular momentum predict a significantly lower mass accretion rate (by about $\sim$ 4–5 orders of magnitude) than the Bondi formula, and have rates similar to the ones from the Zeldovich-Novikov model ([142,143]), where the infall is assumed to start from infinity, clearly indicating that the angular momentum is a decisive parameter in determining the magnitude of the mass accretion rate.

To shed some light on these results, we first note that in the scenario considered in Table **6-1**, the parameter $z \approx mc^2/k_\mathrm{B}T \approx 0.5 \times 10^6$ is still smaller than the ratio $\left(\frac{R}{r_\mathrm{S}}\right)^2 \approx 2.1 \times 10^{10}$, and thus the results for Maxwell-Jüttner model with or without angular momentum differ significantly.[13] Next, we note that the ratio between the Bondi radius and the radius of the injection sphere is about $r_\mathrm{B}/R \approx 1.02$. Furthermore, we observe that the models describing a pure radial infall can be written in the form (taking into account the aforementioned relation $2k_\mathrm{B}T = mv_R^2$ which yields $v_R/c \approx \sqrt{2/z}$):

$$\frac{|\dot{M}|}{mn_R v_R} = 4\pi\lambda_{L=0} R^2, \tag{6.7.5}$$

with the factor $\lambda_{L=0} = \alpha(R)\Gamma c/v_\mathrm{R}$ being of order unity. This has the same form as the Bondi formula (6.7.1) with the Bondi radius r_B replaced with R and the sound speed c_∞ replaced with v_R. Since in our example $R \approx r_\mathrm{B}$ and v_R is comparable with c_∞, it follows that the mass accretion rates yield similar results. In contrast, the models with

[13] The only way the role of the angular momentum could be neglected is to have $z \gg \left(\frac{R}{r_\mathrm{S}}\right)^2$. This means that only at very low temperatures (of the order of the Cosmic Microwave background, $T \sim 2.73\,\mathrm{K}$ or lower), the models with and without angular momentum yield comparable mass accretion rates for the ratio between R and r_S considered in our example.

Table 6-1: Mass accretion rate inferred for Sgr A* at $R = 0.06\,\mathrm{pc}$ for the models studied in this work and results from the literature. We assume $m = m_\mathrm{p} = 1.67 \times 10^{-27}\,\mathrm{kg}$, the characteristic values of $M = 4.3 \times 10^6\ \mathrm{M}_\odot$, $T = 2.2 \times 10^7\,\mathrm{K}$ and $n_R = 160\,\mathrm{cm}^{-3}$ as mentioned in the text. We consider an infall velocity of $v_R = 600\,\mathrm{km\,s}^{-1}$ at the radius R for the mono-energetic models. The Bondi model result is taken from Eq. (6.7.4). In the mono-energetic models we have used $E_0 = \frac{1}{2} m_\mathrm{p} v_R^2 - GMm_\mathrm{p}/R$ for the non-relativistic case and $E_0 = mc^2\alpha(R)\gamma$ for the relativistic case. Note that in the latter case with angular momentum it turns out that $\gamma > \gamma_\mathrm{c}(R)$, and since both conditions $R \gg r_\mathrm{S}$ and $v_\mathrm{R} \ll c$ are met, one can use the corresponding approximation (6.5.24). Non-rel and rel stand for the non-relativistic and relativistic cases, respectively.

Accretion model	Approximation	Distribution function	$\lvert\dot{M}\rvert$ [$\mathrm{M}_\odot\ \mathrm{yr}^{-1}$]	Reference
Bondi	non-rel	(Perfect fluid)	$\sim 10^{-4}$	[134]
Zeldovich-Novikov	non-rel	Mono-energetic	$\sim 1.29 \times 10^{-9}$	[142]
Rioseco-Sarbach	rel	Maxwell-Jüttner	$\sim 1.48 \times 10^{-9}$	[36]
Radial infall	non-rel	Mono-energetic	$\sim 1.09 \times 10^{-4}$	This work, Eq. (6.4.12)
Radial infall	non-rel	Maxwell-Boltzmann	$\sim 6.22 \times 10^{-5}$	This work, Eq. (6.4.18)
Radial infall	rel	Mono-energetic	$\sim 1.09 \times 10^{-4}$	This work, Eq. (6.4.32)
Radial infall	rel	Maxwell-Jüttner	$\sim 6.22 \times 10^{-5}$	This work, Eq. (6.4.43)
Infall with angular momentum	rel	Mono-energetic	$\sim 1.23 \times 10^{-9}$	This work, Eq. (6.5.24)
Infall with angular momentum	rel	Maxwell-Jüttner	$\sim 1.38 \times 10^{-9}$	This work, Eq. (6.5.36)

angular momentum in the limit $z \ll (R/r_\mathrm{S})^2$ relevant for our example have

$$\frac{|\dot{M}|}{mn_R v_R} = 4\pi\lambda_{L>0} r_\mathrm{S}^2 z, \tag{6.7.6}$$

with $\lambda_{L>0} = R^2\alpha(R)\Gamma c/(v_R r_S^2 z)$ a numerical factor of order one. Accordingly, the mass accretion rate is suppressed by a factor of $(r_\mathrm{S}/r_\mathrm{B})^2 z \sim 2.4 \times 10^{-5}$ compared to the Bondi rate. As mentioned in the introduction, a long standing problem is that the measured luminosity of Sgr A* (and other underluminous sources such as M87*) is way lower than that expected from the Eddington luminosity. Since the luminosity of the accreting flow of BHs is proportional to the mass accretion rate, there have been mainly two proposed solutions to explain the observed low luminosity: 1) a Bondi accretion rate with a very low radiative efficiency or 2) a much lower mass accretion rate than the Bondi rate. In the literature, various RIAF models have been proposed to solve this problem by taking into account one or both of these solutions.

Comparing the results from Table **6-1**, we conclude that part of the solution to the low luminosity problem of Sgr A* could be that the mass accretion rate should be inferred from the accretion of a kinetic gas at a finite radius, taking into account the angular momentum of the individual particles. In this case, our mass accretion rate estimates for the models with angular momentum are of the order of the mass accretion rates bounds inferred from RM. Note, however, that these bounds are supposed to be for the vicinity of the BH horizon. Therefore, there is a significant difference in the results of the hydrodynamical and kinetic approaches for the wind accretion at $R \sim 0.06\,\mathrm{pc}$, at least for our simplified models with angular momentum. A more complete theoretical kinetic treatment and future kinetic simulations of this accretion scenario could explain this difference, by confirming the important disparity between the accretion rates, or by endowing the kinetic flow with an accretion rate-reduction mechanism as a consequence of the more complex modelling of the problem. We note that our explanation of the low luminosity problem relies solely in the assumption that the luminosity is proportional to the accretion rate, not in the mechanism of radiation of a collisionless kinetic gas, which we do not study here.

6.7.2. Accretion in the vicinity of Sgr A* and M87*

As a second example, we also cautiously apply our models to the vicinity of Sgr A*'s event horizon. The values of temperatures and densities near the BH are estimated from the results of GRMHD simulations for a two-temperature plasma of electrons and ions (e.g. [184, 185]). The accretion in these simulations proceeds through a geometrically thick, optically thin hydrodynamical flow, coming initially from a weakly magnetized torus in hydrodynamic equilibrium, orbiting a Kerr BH. Despite the significant physical differences with the more realistic case studied in the GRMHD simulations, we apply our models of the Maxwell-Jüttner distribution function as an illustrative first approximation for the kinetic scenario.[14] In particular, we take the values of density and temperature of a two-temperature radial inflow-outflow hydrodynamical model near Sgr A* with self-consistent feeding and conduction presented in [186]; we assume a fully ionized plasma so that there is an equality between electron and proton densities, $n_\mathrm{e} = n_\mathrm{p}$, and we take $R = 5\,r_\mathrm{S}$, $n_R = n_\mathrm{e} = 2 \times 10^6\,\mathrm{cm}^{-3}$ and $T = T_\mathrm{p} = 30\,T_\mathrm{e} = 1.2 \times 10^{12}\,\mathrm{K}$. Furthermore, since the proton mass is much greater than the electron mass, we assume $m = m_\mathrm{p}$. The accretion rates calculated are shown in Table **6-2**. We found consistency with the values of the RM constraints for the vicinity of Sgr A*. Moreover, the radial infall in our models produces a greater mass accretion rate by a factor of ~ 3. Thus, the role of angular momentum is not significant close to the BH horizon. This is consistent with the well-known fact that particles fall almost radially as they approach to the ISCO (see e.g. [187, 188]). It is important to note that we took values of temperature and densities from hydrodynamical models as a first approximation, due to the lack of model-independent estimations of the conditions near the SMBHs.
Finally, another interesting scenario to study with our models (with the same caveats as in the Sgr A* case), is the vicinity of the galactic centre of M87*. Recently, the Event Horizon Telescope Collaboration (EHTC) has provided results for the mass accretion

[14] In this case, we do not consider the mono-energetic models due to their more idealized nature.

Table 6-2: Mass accretion rate inferred for Sgr A* at $R = 5\,r_{\rm S}$, for the Maxwell-Jüttner models. We have used $m = m_{\rm p}$, $M = 4.3 \times 10^6\,{\rm M}_\odot$, $T = 1.2 \times 10^{12}$ K and $n_R = 2 \times 10^6\,{\rm cm}^{-3}$ (see [186]).

Accretion model	Distribution function	$\lvert\dot{M}\rvert$ $\left[{\rm M}_\odot\,{\rm yr}^{-1}\right]$	Reference
Radial infall	Maxwell-Jüttner	$\sim 1.92 \times 10^{-7}$	This work, Eq. (6.4.42)
Infall with angular momentum	Maxwell-Jüttner	$\sim 5.77 \times 10^{-8}$	This work, Eq. (6.5.29)

Table 6-3: Mass accretion rate inferred for M87* at $R = 5\,r_{\rm S}$, for the Maxwell-Jüttner models. We have used $m = m_{\rm p}$, $M = 6.5 \times 10^9\,{\rm M}_\odot$, $T = 6.25 \times 10^{10}$ K and $n_R = 2.9 \times 10^4\,{\rm cm}^{-3}$ (see [157, 189]).

Accretion model	Distribution function	$\lvert\dot{M}\rvert$ $\left[{\rm M}_\odot\,{\rm yr}^{-1}\right]$	Reference
Radial infall	Maxwell-Jüttner	$\sim 1.526 \times 10^{-3}$	This work, Eq. (6.4.42)
Infall with angular momentum	Maxwell-Jüttner	$\sim 1.521 \times 10^{-3}$	This work, Eq. (6.5.29)

rate due to the plasma around this SMBH. They report an estimated average number density of $n_{\rm e} \sim 2.9 \times 10^{4--7}\,{\rm cm}^{-3}$, an electron temperature $T_{\rm e} \sim$ (1–12) $\times 10^{10}$ K, and an inferred mass accretion rate for M87* of (3 – 20) $\times 10^{-4}\,{\rm M}_\odot\,{\rm yr}^{-1}$ from a simple one-zone emission model ([135, 156, 157]). For the specific isothermal sphere model, they estimate the plasma number density $n_{\rm e} \simeq 2.9 \times 10^4$ cm^{-3} and the electron temperature $T_{\rm e} \simeq 6.25 \times 10^{10}$ K, for an emission radius assumed to be $r \simeq 5r_{\rm S}/2$. In Table **6-3** we present the mass accretion rates obtained from these values, assuming a fully ionized hydrogen plasma ($n_{\rm ions} = n_{\rm e}$) and assuming thermal equilibrium between the ions and electrons ($T_{\rm ions} = T_{\rm e}$) as a first approximation. Furthermore, we impose these values at radius $R \sim 5r_{\rm S}$, as in the example of Sgr A*.[15] In this case, we got similar mass accretion rates for the models with and without angular momentum. Therefore, angular momentum does not play an important role, just like the case of the vicinity of Sgr A*'s event horizon. Despite our crude approximation for the accretion flow of M87*, the inferred mass accretion rates are consistent with the reported bounds by the [157].

6.8. Summary and conclusions

Low collisionality is a general property expected in underluminous flows near BHs due to the conditions of high temperatures and low densities. Thus, a kinetic approach is needed in order to explain correctly the accretion process onto these BHs. Additionally, most previous analytic studies treat the problem of spherical mass accretion specifying boundary conditions at infinity, both in the fluid and the kinetic approxima-

[15] The reason for not choosing $R = 5r_{\rm S}/2$ is that this value is smaller than the ISCO radius of a Schwarzschild BH assumed in our model.

tions, whereas in many situations of interest the gas is accreted from a region of finite radius.

In this work, we presented several analytic models and their corresponding steady-state solutions for the mass accretion of a spherically symmetric, collisionless kinetic gas cloud onto a Schwarzschild BH. The novelty of this article consists in specifying the properties of the kinetic gas (its particle density n_R and mean velocity or temperature) at an injection sphere of finite radius R. The models we have discussed include the simple case of purely radial infall, in which all the particles have zero angular momentum (both in the Newtonian and relativistic regimes) and the case of a kinetic gas with a uniform distribution in the angular momentum, such that individual gas particles may rotate about the BH, yet the gas configuration as a whole is spherically symmetric. Regarding the energy distribution, we considered the mono-energetic case in which all particles have the same energy E (or associated three-velocity v_R at the injection sphere) as well as the Maxwell-Boltzmann (non-relativistic case) and Maxwell-Jüttner distribution with corresponding temperature T, assuming that the gas is accreted from a reservoir of particles in thermodynamic equilibrium. In each model, the mass accretion rate depends linearly on n_R which is a direct consequence of our test field approximation (we have neglected the self gravity of the kinetic gas) while its dependency on R and v_R or T is more intricate and is summarized in Section 6.6.

We have checked that for fixed positive values of n_R, v_R and T, our models with angular momentum have the property that their mass accretion rates converge to the corresponding expressions of previously known results ([36, 142, 143]) in the limit $R \to \infty$, while the models with purely radial infall have associated to them a mass accretion rate which diverges as $R \to \infty$. This means the latter do not possess well-defined Bondi-type formulae which relate the mass accretion rate to the properties of the gas at infinity. This is analogous to the case of accretion of pure dust in spherical symmetry, in which the only steady-state solution has vanishing mass density at infinity ([190]). In fact, our mono-energetic model with purely radial infall does correspond precisely to this simple dust model, since its velocity dispersion is exactly zero.

However, for the more realistic case of an injection sphere of finite radius R it turns out that the purely radial infall models may lead to similar accretion rates than those predicted from the well-known Bondi model for a hydrodynamic flow. In particular, we have shown that for boundary conditions corresponding to non-relativistic velocities or temperatures, the mass accretion rates in both models yield comparable results, provided R is of the same order as the Bondi radius. Regarding our models with angular momentum, their mass accretion rate behaves qualitatively similarly to the purely radial infall models, and it increases with increasing values of v_R or T as long as they lie below a critical value. However, above this critical value the mass accretion rate reverses its behaviour and decreases with increasing v_R or T until it reaches a finite value. As we have explained, this reversal is due to the fact that as the particle's energy increases above a certain threshold, not all the particles are absorbed by the BH, and the fraction of absorbed particles becomes smaller as the energy increases, leading to a diminishing mass accretion rate.

Finally, we calculated the mass accretion rate onto the SMBHs Sgr A* and M87* with our models, estimating the condition of the gas at different radii based on recent observations. Our results, which are summarized in Tables **6-1**, **6-2** and **6-3**, are of the order of the model-dependent RM bounds for the mass accretion rate of Sgr A* and the bounds estimated for M87* by the Event Horizon Telescope collaboration. We found that our kinetic models can overall predict lower mass accretion rates than the Bondi fluid model. The above suggests that a complete kinetic treatment to the accretion problem could explain some of the current questions associated with underluminous sources such as Sgr A* or M87*.

There are several ingredients which, for simplicity, we did not take into account in our models. In particular, we restricted ourselves to spherical steady accretion onto a Schwarzschild BH, instead of the more realistic non-spherical and unsteady accretion onto a (rotating) Kerr BH. Furthermore, we did not included the effects of radiative processes, magnetic fields, the consequences of outflows, convection currents or jets nor the effects due to net angular momentum of the gas. We intend to generalize our models to include some of these effects in future work.

Despite its simplicity, the presented models could serve as reference for more generic kinetic models, and they could be useful as a starting point to describe other physical scenarios where the assumptions of very low collisionality or quasi-spherical symmetry are approximately satisfied. This is the case, for example, in the BH accretion of dark matter, which is expected to be very weakly interactive, or in the accretion of low-luminosity active galactic nuclei whose corresponding flows are in a hot and low-density state. Thus, future generalizations of the presented formalism could be a key step in understanding accretion processes.

6.9. Appendix: Fixed-L-models

To shed some light on the factor 2 difference between Eq. (6.4.35) and Eq. (6.5.17) in the non-relativistic limit $\gamma \to 1$ we consider the following model:

$$F(E, L) = f(E)\frac{\delta(L - L_0)}{L_0} \tag{6.9.1}$$

with a constant $L_0 > 0$ and a function $f(E)$ which we specify later. Assuming that L_0 is small enough such that $L_0 < L_c(E)$ for all $E > mc^2\alpha(R)$ (which is guaranteed to be the case if $L_0 < L_{\text{ISCO}}$), one obtains from Eqs. (6.5.10, 6.5.11) the expressions

$$J^\sigma_{\text{abs}}|_{r=R} = c \int\limits_{\sqrt{V_{L_0}(R)}}^{\infty} \int\limits_0^{2\pi} \frac{p^\sigma_- f(E) dE d\chi}{R^2 \sqrt{E^2 - V_{L_0}(R)}}, \tag{6.9.2}$$

$$J^\sigma_{\text{sca}}|_{r=R} = 0, \tag{6.9.3}$$

from which one immediately obtains

$$J^0_{\text{abs}}\Big|_{r=R} = \frac{2\pi}{\alpha(R)R^2} \int\limits_{\sqrt{V_{L_0}(R)}}^{\infty} \frac{f(E)EdE}{\sqrt{E^2 - V_{L_0}(R)}}, \tag{6.9.4}$$

$$J^1_{\text{abs}}\Big|_{r=R} = -\frac{2\pi}{\alpha(R)R^2} \int\limits_{\sqrt{V_{L_0}(R)}}^{\infty} f(E)dE, \tag{6.9.5}$$

and $J^2_{\text{abs}}|_{r=R} = J^3_{\text{abs}}|_{r=R} = 0$, where we have introduced the shorthand notation $V_{L_0}(r) := V_L(r)|_{L\to L_0}$. For the mono-energetic model with $f(E) = f_0\delta(E - E_0)$ and $E_0 = mc^2\alpha\gamma$ this yields (assuming $V_{L_0}(R) < E_0^2$ or, equivalently, $L_0 < L_{\text{max}}(E_0, R)$)

$$\frac{|\dot{M}|}{mcn_R} = 4\pi R^2 \alpha(R) \sqrt{\frac{\gamma^2}{1+\kappa^2} - 1}, \tag{6.9.6}$$

where we have defined $\kappa := L_0/(Rmc)$. In the limit $L_0 \to 0$ one recovers the result from Eq. (6.4.35) which has been derived directly with the assumption that all the gas particles have vanishing angular momentum. If instead of $L_0 \to 0$ one sets $L_0 = R|v_\perp|$ with $v_\perp$ the angular components of the velocity, one obtains in the limit $|v_R| \ll c$,

$$\frac{|\dot{M}|}{mcn_R} \approx 4\pi R^2 \alpha(R) \frac{v_{\text{rad}}}{c}, \tag{6.9.7}$$

where $v_{\text{rad}} = \sqrt{v_R^2 - |v_\perp|^2}$ denotes the radial component of the three-velocity of the particles. For purely radial infall $v_{\text{rad}} = v_R$ and this result agrees precisely with Eq. (6.4.12). However, when angular momentum is present, the accretion rate is suppressed by a factor of v_{rad}/v_R.

It is also a simple task to reproduce the results for the purely radial infall and the Maxwell-Jüttner-type distribution function by inserting $f(E) = Ae^{-\beta E}$ into Eqs. (6.9.4, 6.9.5) and taking the limit $L_0 \to 0$. This yields the following non-vanish components of the current density

$$J^0_{\text{abs}}\Big|_{r=R} = \frac{2\pi Amc^2}{R^2} \mathbf{K}_1(z), \tag{6.9.8}$$

$$J^1_{\text{abs}}\Big|_{r=R} = \frac{2\pi A}{\alpha(R)R^2\beta} e^{-z} \tag{6.9.9}$$

with $z \coloneqq mc^2\alpha(R)\beta$. This in turn leads to the mass accretion rate

$$\frac{|\dot{M}|}{mcn_R} = \frac{4\pi\alpha(R)R^2}{\sqrt{\left[\mathbf{K}_1(z)ze^z\right]^2 - 1}}, \tag{6.9.10}$$

in concordance with Eq. (6.4.42).

7 Conclusions and future work

We have started this thesis work by providing a review of the relativistic kinetic gas theory on a curved spacetime manifold (M, g), based on the cotangent bundle formulation which is naturally adapted to the Hamiltonian framework. In chapter one, we have reviewed the most important geometric structures of the theory, including the four-dimensional spacetime manifold (M, g) and the associated cotangent bundle $T^*\mathcal{M}$. Our geometric point of view has the advantage of naturally incorporating the covariance of the theory by formulating the laws of physics in a coordinate-independent way. Regarding $(\mathcal{M}, g)$, we surveyed the concepts of tangent vectors, tensor fields, affine connections, geodesics, metric tensor and its associated Levi-Civita connection, parallel transport, covariant derivative, the Riemann curvature tensor, and the most relevant field equations in general relativity, the Einstein equations. The geometric structures on the cotangent bundle that have been reviewed are: the Poincaré one-form, the symplectic form, the Liouville vector field, the future mass shell, the future mass hyperboloid, and the volume form. We also provided the principal properties regarding the geodesic motion of a massive gas particle propagating in the exterior Schwarzschild spacetime. We focused our attention on the properties of the radial effective potential and the conserved quantities. The qualitative behavior of the trajectories with this potential depends on the parameter space (E, L), where E and L are the energy and the total angular momentum of the particles, respectively. We have classified the phase space in regions corresponding to bound, scattered, and absorbed orbits.

Next, in chapter two we have summarized the principal concepts of relativistic kinetic theory. We highlighted the role of the one-particle distribution function as one of the key concepts of the theory, discussed its covariant interpretation through a flux integral, and provided a bridge with the familiar non-relativistic interpretation. We also derived the collisionless Boltzmann equation which describes the dynamics of a relativistic collisionless kinetic gas. As we showed, the physical spacetime observables constructed from the one-particle distribution function are obtained by suitable fibre integrals over the momenta. Further, the invariant particle, energy and entropy densities, principal pressures, and the mean particle, mean energy, and mean entropy velocities have been introduced. We defined these quantities solely in terms of the particle current vector field, energy-momentum-stress tensor, and entropy flux vector field, without introducing any fiducial observer.

Next, in chapter three we provided a brief overview of the relativistic integro-differential Boltzmann equation in which the individual gas particles are subject to elastic binary collisions. We also derived the relativistic version of the H-theorem. The conditions giving rise to global and local thermodynamical equilibrium were reviewed for a system with zero entropy production. As we explained, such states are characterized by a single four-velocity vector field, the macroscopic quantities behaving like a perfect fluid. Further, we showed that the kinetic temperature of these states satisfies the Gibbs relation, such that they can be considered to describe thermal states. As we have seen, the existence of global thermodynamical equilibrium is very restrictive, requiring spacetime to be globally stationary. For the situation in which spacetime is not globally stationary, the solutions of the Boltzmann equation can be analyzed through two typical length scales associated to them. This study provided two limits: one in which the Boltzmann equation is dominated by the collision term and the other one in which it is dominated by the transport term. For the case in which collisions between the gas particles can be completely neglected one obtains the collisionless Boltzmann equation, and we have briefly summarized a method for solving it under the assumption that the underlying geodesic flow is integrable.

Based on relativistic kinetic theory, we described in chapters four and five collisionless gas configurations trapped by the potential of a central object. In this scenario the gas particles follow spatially bound future-directed timelike geodesics trajectories in the vicinity of the central object. We discussed the properties of an axisymmetric, stationary gas cloud surrounding a massive central object in which several models for the one-particle distribution function were considered, both in the relativistic and non-relativistic regimes. The resulting configurations and the properties of the relevant macroscopical observables were analyzed in detail. We also specified configurations with finite total mass, energy and (zero or non-zero) angular momentum. In particular, for the relativistic case in chapter five, we have derived explicit expressions for the spacetime observables in terms of a single integral over a function depending solely on the energy. This has been achieved by rewriting the fibre integrals over the particles' momenta as integrals over the constants of motion E, L and L_z. A challenging problem in this change of variables is the determination of the correct range of integration over which E, L and L_z vary, as this range depends on the observer's radius r. Finally, each configurations (relativistic and non-relativistic) were compared to their hydrodynamic analogs.

In chapter six, we investigated steady-state solutions for the mass accretion of a spherically symmetric, collisionless kinetic gas cloud onto a Schwarzschild black hole. In this scenario the accreted gas particles were examined using different ansätze. One of the novel features was the specification of boundary conditions of the kinetic gas (such as the particle density and mean velocity or temperature) at an injection sphere of finite radius R. We calculated the mass accretion rate onto the supermassive black holes Sgr A* and M87* with our models, estimating the condition of the gas at different radii based on recent observations. The resulting mass accretion rates were analyzed and compared to the ones predicted by previous models. We discussed how the low luminosities of Sgr A* and M87* could be partially explained by a kinetic description of the accreted gas involving angular momentum.

Potential future work derived from this research project includes the following interesting scenarios. First, a generalization of the models discussed here to include the effects of binary collisions between the gas particles should be interesting, since in this case a particle following a bound trajectory can be deflected to an unbound trajectory after the collision, and hence could be accreted by the black hole. In this scenario, the Vlasov limit described in section 3.3.1 should be helpful to understand this behavior, as long as collisions are sufficiently rare. Second, we intend to generalize our models to include radiative processes and electromagnetic effects for a gas consisting of charged particles. In particular, this scenario is of special interest for the recent breakthrough observations by the Event Horizon Telescope Collaboration [74] showing the first image of the shadows of the supermassive black holes M87* and Sgr A*, and it could provide an understanding of the behavior of a hot plasma in the vicinity of a strong gravitational field beyond the hydrodynamic approximation. Third, the addition of the self-gravity of the gas needs to be modeled by the Einstein-Vlasov system of equations. Recent progress in this direction has been achieved by Jabiri [102, 103] who proves that the effects from the self-gravity can be included for stationary, axially symmetric configurations similar to the ones we have constructed, provided the amplitude of the distribution function is sufficiently small. Finally, is should also be interesting to generalize the models studied here to a Kerr black hole, analyzing the effects of the rotation of the black hole.

References

[1] D. Tong. *Kinetic Theory*. University of Cambridge Graduate Course, Cambridge, CB3 OBA, UK, 2012.

[2] K. Huang. *Statistical Mechanics*. John Wiley & Sons, New York, USA, 1987.

[3] C. Cercignani. *Ludwig Boltzmann, The Man Who Trusted Atoms*. Oxford University Press, Oxford, 2010.

[4] C. Cercignani and G.M. Kremer. *The Relativistic Boltzmann Equation: Theory and Applications*. Birkhäuser, Basel, 2002.

[5] G.V. Vereshchagin and A.G. Aksenov. *Relativistic Kinetic Theory with Applications in Astrophysics and Cosmology*. Cambridge University Press, University Printing House, Cambridge CB2 8BS, United Kingdom, 2017.

[6] S.R. de Groot, W.A. van Leeuwen, and Ch. G. van Weert. *Relativistic Kinetic Theory*. North-Holland Publishing Company, Amsterdam, New York, Oxford, 1980.

[7] R.L. Liboff. *Kinetic Theory: Classical, Quantum, and Relativistic Descriptions*. Springer, New York, USA, 2003.

[8] H. Andréasson. The Einstein-Vlasov system/kinetic theory. *Living Reviews in Relativity*, 14(4), 2011.

[9] O. Sarbach and T. Zannias. Relativistic kinetic theory: An introduction. *AIP Conf. Proc.*, 1548:134–155, 2013.

[10] O. Sarbach and T. Zannias. Tangent bundle formulation of a charged gas. *AIP Conf. Proc.*, 1577:192–207, 2014.

[11] O. Sarbach and T. Zannias. The geometry of the tangent bundle and the relativistic kinetic theory of gases. *Class. Quantum Grav.*, 31:085013, 2014.

[12] R. Acuña-Cárdenas, C. Gabarrete, and O. Sarbach. An introduction to the relativistic kinetic theory on curved spacetimes. *General Relativity and Gravitation*, 54(23), February 2022.

[13] F. Jüttner. Maxwell's law of speed distribution in the theory of relativity. *Annal. Phys.*, 34:856–882, 1911.

[14] F. Jüttner. The dynamics of an inert gas in the theory of relativity. *Annal. Phys.*, 35:145–161, 1911.

[15] J.L. Synge. The energy tensor of a continuous medium. *Trans. Royal Soc. Canada*, 28:127–171, 1934.

[16] W. Israel. Relativistic kinetic theory of a simple gas. *J. Math. Phys.*, 4:1163–1181, 1963.

[17] W. Israel. The relativistic boltzmann equation. In L. O'Raifeartaigh, editor, *General Relativity*, pages 201–241, 1972.

[18] R.W. Lindquist. Relativistic transport theory. *Ann. Phys. (N.Y.)*, 37:487–518, 1966.

[19] J. Ehlers. General relativity and kinetic theory. In R.K. Sachs, editor, *General Relativity and Cosmology*, pages 1–70, New York, 1971. Academic Press.

[20] N. Noutchegueme and E. Takou. Global existence of solutions for the Einstein-Boltzmann system with cosmological constant in the Robertson-Walker space-time. *Comm. Math. Sci.*, 4:291–314, 2006.

[21] P. Attard. *Thermodynamics and Statistical Mechanics: Equilibrium by Entropy Maximisation*. Academic Press, San Diego, California, USA, 2002.

[22] J. Batt, W. Faltenbacher, and E. Horst. Stationary spherically symmetric models in stellar dynamics. *E. Arch. Rational Mech. Anal.*, 93:159–183, 1986.

[23] G. Rein. Static solutions of the spherically symmetric Vlasov-Einstein system. *Math. Proc. Cambridge Phil. Soc.*, 115:559–570, 1994.

[24] G. Rein and A.D. Rendall. Global existence of solutions of the spherically symmetric Vlasov–Einstein system with small initial data. *Comm. Math. Phys.*, 150:561–583, 1992.

[25] J. Schaeffer. A class of counterexamples to Jeans' theorem for the Vlasov-Einstein system. *J. Comm. Math. Phys.*, 204:313–327, 1999.

[26] A. Rendall. The Einstein-Vlasov system. In P.T. Chrusciel and H. Friedrich, editors, *The Einstein equations and the large scale behavior of gravitational fields*, pages 231–250, Basel, 2004. Birkhäuser.

[27] H. Andréasson and G. Rein. On the steady states of the spherically symmetric Einstein-Vlasov system. *Class. Quantum Grav.*, 24:1809–1832, 2007.

[28] A. Rendall and J. Velazquez. A class of dust-like self-similar solutions of the massless Einstein-Vlasov system. *Annales Henri Poincaré*, 12:919–964, 2011.

[29] H. Andréasson, M. Kunze, and G. Rein. Existence of axially symmetric static solutions of the Einstein-Vlasov system. *Commun. Math. Phys.*, 308:23–47, 2011.

[30] H. Andréasson, D. Fajman, and M. Thaller. Static solutions to the Einstein-Vlasov system with non-vanishing cosmological constant. *SIAM J. Math. Anal.*, 47:2657–2688, 2015.

[31] H. Andréasson, M. Eklund, and G. Rein. A numerical investigation of the steady states of the spherically symmetric Einstein-Vlasov-Maxwell system. *Class. Quantum Grav.*, 26:145003, 2009.

[32] P. Noundjeu, N. Noutchegueme, and A.D. Rendall. Existence of initial data satisfying the constraints for the spherically symmetric Einstein-Vlasov-Maxwell system. *J. Math. Phys.*, 45:668–676, 2004.

[33] P. Noundjeu. The Einstein-Vlasov-Maxwell (evm) system with spherical symmetry. *Class. Quantum Grav.*, 22:5365–5384, 2005.

[34] C. Mouhot and C. Villani. On Landau damping. *Acta Math.*, 207:29–201, 2011.

[35] J. Binney and S. Tremaine. *Galactic Dynamics (Second Edition)*. Princeton University Press, Princeton, New Jersey, 2008.

[36] P. Rioseco and O. Sarbach. Accretion of a relativistic, collisionless kinetic gas into a Schwarzschild black hole. *Class. Quantum Grav.*, 34(9):095007, 2017.

[37] P. Rioseco and O. Sarbach. Spherical steady-state accretion of a relativistic collisionless gas into a Schwarzschild black hole. *J. Phys. Conf. Ser.*, 831(1):012009, 2017.

[38] A. Cieślik and P. Mach. Accretion of the Vlasov gas on Reissner-Nordström black holes. *Phys. Rev. D*, 102:024032, Jul 2020.

[39] P. Mach and A. Odrzywołek. Accretion of the relativistic Vlasov gas onto a moving Schwarzschild black hole: Exact solutions. *Phys. Rev. D*, 103:024044, Jan 2021.

[40] A. Gamboa, C. Gabarrete, P. Domínguez-Fernández, D. Núñez, and O. Sarbach. Accretion of a Vlasov gas onto a black hole from a sphere of finite radius and the role of angular momentum. *Phys. Rev. D*, 104:083001, Oct 2021.

[41] P. Mach and A. Odrzywołek. Accretion of the relativistic Vlasov gas onto a moving Schwarzschild black hole: low-temperature limit and numerical aspects. *Acta Phys. Pol. B Proc. Suppl.*, 15(1-A7), January 2022. Presented at the 7th conference of the Polish Society on Relativity, Łódź, Poland, 20-23 september 2021.

[42] P. Domínguez, E. Jiménez, M. Alcubierre, E. Montoya, and D. Núñez. Description of the evolution of inhomogeneities on a dark matter halo with the Vlasov equation. *Gen.Rel.Grav.*, 49:123, 2017.

[43] P. Mach and A. Odrzywołek. Accretion of dark matter onto a moving Schwarzschild black hole: An exact solution. *Phys. Rev. Lett.*, 126:101104, Mar 2021.

[44] F. Astorga, O. Sarbach, and T. Zannias. The evolution of a spatially homogeneous and isotropic universe filled with a collisionless gas. *J. Phys. Conf. Ser.*, 545(1):012001, 2014.

[45] D. Bazow, G. Denicol, U. Heinz, M. Martinez, and J. Noronha. Analytic solution of the Boltzmann equation in an expanding system. *Phys. Rev. Lett.*, 116:022301, 2016.

[46] D. Bazow, G. Denicol, U. Heinz, M. Martinez, and J. Noronha. Nonlinear dynamics from the relativistic Boltzmann equation in the Friedmann-Lemaître-Robertson-Walker spacetime. *Phys. Rev. D*, 94:125006, 2016.

[47] C. Gabarrete and O. Sarbach. Axisymmetric, stationary collisionless gas clouds trapped in a Newtonian potential, *arXiv:2209.053525*. 2022.

[48] C. Gabarrete and O. Sarbach. Kinetic gas disks surrounding Schwarzschild black holes. *Acta Phys. Pol. B Proc. Suppl.*, 15(1-A10), January 2022. Presented at the 7th conference of the Polish Society on Relativity, Łódź, Poland, 20-23 september 2021.

[49] C. Gabarrete and O. Sarbach. Axisymmetric, stationary collisionless gas configurations surrounding black holes, *arXiv:2209.053527*. 2022.

[50] K. Yano and S. Ishihara. *Tangent and cotangent bundles; differential geometry*. New York, Dekker, New York, 1973.

[51] R.M. Wald. *General Relativity*. The University of Chicago Press, Chicago, London, 1984.

[52] C.W. Misner, K.S. Thorne, and J.A. Wheeler. *Gravitation*. W. H. Freeman, 1973.

[53] S. Carroll. *Spacetime and Geometry: An introduction to General Relativity*. Addison Wesley, San Francisco, USA, 2004.

[54] S. Chandrasekhar. *The Mathematical Theory of Black Holes*. Oxford University Press, Great Clarendon Street, Oxford 0X2 6DP, 1992.

[55] S.W. Hawking and G.F.R. Ellis. *The Large Scale Structure of Space Time*. Cambridge University Press, Cambridge, 1973.

[56] N. Straumann. *General Relativity*. Springer-Verlag, Berlin, 2013.

[57] R.K. Sachs and H. Wu. *General Relativity for Mathematicians*. Springer-Verlag, New York-Heidelberg-Berlin, 1977.

[58] V.I. Arnold. *Mathematical Methods of Classical Mechanics*. Springer-Verlag, New York, 1989.

[59] M. Heusler. *Black Hole Uniqueness Theorems*. Cambridge University Press, Cambridge, England, 1996.

[60] P.T. Chruściel, J. Lopes Costa, and M. Heusler. Stationary black holes: Uniqueness and beyond. *Liv. Rev. Relativ.*, 15(7), 2012.

[61] A. Cieślik and P. Mach. Revisiting timelike geodesics in the Schwarzschild spacetime: general expressions in terms of Weierstrass elliptic functions. *arXiv e-prints*, page arXiv:2203.12401, March 2022.

[62] S. Sasaki. On the differential geometry of tangent bundles of Riemannian manifolds. *Tohoku Math. J.*, 10:338–354, 1958.

[63] S. Sasaki. On the differential geometry of tangent bundles of Riemannian manifolds, II. *Tohoku Math. J.*, 14:135–232, 1962.

[64] J.L. Synge. *Relativity: The Special Theory*. Elsevier Science, Amsterdam, 1956.

[65] R. Strain. Coordinates in the relativistic Boltzmann theory. *Kinetic and Related Models*, 4:345–359, 2011.

[66] C. Cercignani and G.M. Kremer. On relativistic collisional invariants. *Journal of Statistical Physics*, 96:439–445, Jul 1999.

[67] R.C. Tolman. On the weight of heat and thermal equilibrium in general relativity. *Phys. Rev.*, 35:904–924, Apr 1930.

[68] R. Tolman and P. Ehrenfest. Temperature equilibrium in a static gravitational field. *Phys. Rev.*, 36:1791–1798, Dec 1930.

[69] F. Olver, D. Lozier, R. Boisvert, and Ch. Clark. *NIST Handbook of Mathematical Functions*. 01 2010.

[70] M. Knudsen. Die Gesetze der Molekularströmung und der inneren Reibungsströmung der Gase durch Röhren. *Annals of Physics*, pages 75–130, 1909.

[71] W. Steckelmacher. Knudsen flow 75 years on: the current state of the art for flow of rarefied gases in tubes and systems. *Rep. Prog. Phys*, 49:1083–1107, 1986.

[72] C. Villani. A review of mathematical topics in collisional kinetic theory. *Handbook of Mathematical Fluid Dynamics*, 1:211, 2002.

[73] P. Rioseco and O. Sarbach. Phase space mixing in an external gravitational central potential. *Class. Quantum Grav.*, 37(19):195027, 2020.

[74] Event Horizon Telescope Collaboration. `http://www.eventhorizontelescope.org`.

[75] K. Akiyama and et al. First M87 Event Horizon Telescope Results. I. The Shadow of the Supermassive Black Hole. *Astrophys. J. Letters*, 875:17, 2019.

[76] The EHT Collaboration et al. First Sagittarius A* Event Horizon Telescope Results. I. The Shadow of the Supermassive Black Hole in the Center of the Milky Way. *Astrophys. J. Letters*, 930:21, 2022.

[77] P. Rioseco and O. Sarbach. Phase space mixing in the equatorial plane of a Kerr black hole. *Phys. Rev. D*, 98(12):124024, 2018.

[78] S.L. Shapiro and S.A. Teukolsky. Equilibrium stellar systems with spindle singularities. *The Astrophysical Journal*, 388, 05 1992.

[79] S.L. Shapiro and S.A. Teukolsky. Relativistic Stellar Systems with Spindle Singularities. *Astrophysical Journal*, 419:622, December 1993.

[80] S.L. Shapiro and S.A. Teukolsky. Relativistic Stellar Systems with Rotation. *Astrophysical Journal*, 419:636, December 1993.

[81] H. Andréasson and G. Rein. On the rotation curves for axially symmetric disc solutions of the Vlasov-Poisson system. *Monthly Notices of the Royal Astronomical Society*, 446(4):3932–3942, 12 2015.

[82] G. Rein and Y. Guo. Stable models of elliptical galaxies. *Monthly Notices of the Royal Astronomical Society*, 344(4):1296–1306, 10 2003.

[83] E. Ames, H. Andréasson, and A. Logg. On axisymmetric and stationary solutions of the self-gravitating Vlasov system. *Class. Quantum Grav.*, 32:155008, 2016.

[84] E. Ames, H. Andréasson, and A. Logg. Cosmic string and black hole limits of toroidal Vlasov bodies in general relativity. *Phys. Rev. D*, 99(2):024012, 2019.

[85] H. Andréasson, M. Kunze, and G. Rein. Rotating, stationary, axially symmetric spacetimes with collisionless matter. *Commun. Math. Phys.*, 329:787–808, 2014.

[86] M. Thaller. Rotating clouds of charged Vlasov matter in general relativity. *Classical and Quantum Gravity*, 37, 12 2019.

[87] C. Cremaschini and Z. Stuchlík. Magnetic loop generation by collisionless gravitationally bound plasmas in axisymmetric tori. *Phys. Rev. E*, 87:043113, 2013.

[88] C. Cremaschini and et al. Kinetic theory of equilibrium axisymmetric collisionless plasmas in off-equatorial tori around compact objects. *The Astrophysical Journal Supplement Series*, 209, 09 2013.

[89] Y.B. Zel'dovich and I.D. Novikov. *Stars and Relativity*. Dover Publications, Inc., Mineola, New York, 1971.

[90] S.L. Shapiro and S.A. Teukolsky. *Black Holes, White Dwarfs, and Neutron Stars*. John Wiley & Sons, New York, 1983.

[91] J. Binney. Henon's isochrone model. 2014. arXiv:1411.4937v1 [astro-ph.GA].

[92] Digital library of mathematical functions. `http://dlmf.nist.gov/`.

[93] S. Chandrasekhar. *An Introduction to the Study of Stellar Structure*. Dover Publications Inc., New York, 1958.

[94] A. Toomre. Some flattened isothermal models of galaxies. *Astrophysical Journal*, 259:535–543, August 1982.

[95] I. Gradshteyn and I. Ryzhik. *Table of Integrals, Series, and Products*. Academic Press, INC., San Diego, CA, 2007.

[96] L. Chemin. A mass-velocity anisotropy relation in galactic stellar disks. *Astronomy & Astrophysics*, 618(A121):19, 2018.

[97] O. Zanotti and D. Pugliese. Von Zeipel's theorem for a magnetized circular flow around a compact object. *Gen. Rel. Grav.*, 47(4):44, 2015.

[98] H. von Zeipel. The radiative equilibrium of a rotating system of gaseous masses. *Monthly Notices of the Royal Astronomical Society*, 84:665–683, 1924.

[99] M. Kunz, J. Stone, and E. Quataert. Magnetorotational turbulence and dynamo in a collisionless plasma. *Phys. Rev. Lett.*, 117:235101, Dec 2016.

[100] S.L. Shapiro and S.A. Teukolsky. Relativistic stellar dynamics on the computer. I - Motivation and numerical method. *Astrophys. J.*, 298:34–79, 1985.

[101] S.L. Shapiro and S.A. Teukolsky. Relativistic stellar dynamics on the computer. II - Physical Applications. *Astrophys. J.*, 298:58–79, 1985.

[102] F.E. Jabiri. Stationary axisymmetric Einstein-Vlasov bifurcations of the Kerr spacetime. 2 2022. arXiv:2202.10245 [math.AP].

[103] F.E. Jabiri. Static spherically symmetric Einstein-Vlasov bifurcations of the Schwarzschild spacetime. *Annales Henri Poincaré*, 22(7):2355–2406, 2021.

[104] A. Cieślik, P. Mach, and A. Odrzywolek. Accretion of the relativistic Vlasov gas in the equatorial plane of the Kerr black hole. *arXiv e-prints*, page arXiv:2203.12401, 2022.

[105] W. Schmidt. Celestial mechanics in Kerr space-time. *Class. Quantum Grav.*, 19:2743–2764, 2002.

[106] J. Brink, M. Geyer, and T. Hinderer. Astrophysics of resonant orbits in the Kerr metric. *Phys. Rev. D*, 91(8):083001, 2015.

[107] L.G. Fishbone and V. Moncrief. Relativistic fluid disks in orbit around Kerr black holes. *The Astrophysical Journal*, 207:962–976, 1976.

[108] M. Abramowicz, M. Jaroszyński, and M. Sikora. Relativistic, accreting disks. *Astronomy and Astrophysics*, 63:221–224, 1978.

[109] M. Kozlowski, M. Jaroszynski, and M. A. Abramowicz. The analytic theory of fluid disks orbiting the Kerr black hole. *Astronomy and Astrophysics*, 63(1-2):209–220, February 1978.

[110] J. Font and F. Daigne. The runaway instability of thick discs around black holes-I. The constant angular momentum case. *Monthly Notices of the Royal Astronomical Society*, 334:383–400, 2002.

[111] J. Font and F. Daigne. The runaway instability of thick disks around black holes-II. Non-constant angular momentum discs. *Monthly Notices of the Royal Astronomical Society*, 349(3):841–868, 2004.

[112] O. Straub et. al. Modelling the black hole silhouette in Sgr A* with ion tori. *Astron. Astrophys.*, 543:A83, 2012.

[113] L. Rezzolla and O. Zanotti. *Relativistic Hydrodynamics*. Oxford University Press, Great Clarendon Street, Oxford, OX2 6DP, United Kingdom, 2013.

[114] M. A. Abramowicz. The Relativistic von Zeipel's Theorem. *Acta Astronomica*, 21(1):81–85, 1971.

[115] P. Domínguez-Fernández, E. Jiménez-Vázquez, M. Alcubierre, E. Montoya, and D. Núñez. Description of the evolution of inhomogeneities on a dark matter halo with the Vlasov equation. *General Relativity and Gravitation*, 49(9):123, Sep. 2017.

[116] J. Frank, A. King, and D. Raine. *Accretion Power in Astrophysics: Third Edition*. 2002.

[117] J. Barranco et al. Are black holes a serious threat to scalar field dark matter models? *Phys. Rev.*, D84:083008, 2011.

[118] F. Hoyle and R. A. Lyttleton. The effect of interstellar matter on climatic variation. *Proceedings of the Cambridge Philosophical Society*, 35(3):405, January 1939.

[119] H. Bondi and F. Hoyle. On the Mechanism of Accretion by Stars. *Monthly Notices of the Royal Astronomical Society*, 104(5):273–282, 10 1944.

[120] H. Bondi. On spherically symmetrical accretion. *Monthly Notices of the Royal Astronomical Society*, 112:195, January 1952.

[121] W. Lewin, J. van Paradijs, and E. van den Heuvel. X-ray binaries. *Cambridge Astrophysics Series*, 26, January 1997.

[122] R. Popham, S. Woosley, and Ch. Fryer. Hyperaccreting Black Holes and Gamma-Ray Bursts. *Astrophysical Journal*, 518(1):356–374, June 1999.

[123] J. Williams and L. Cieza. Protoplanetary Disks and Their Evolution. *ARAA*, 49(1):67–117, September 2011.

[124] J. Krolik. *Active galactic nuclei : from the central black hole to the galactic environment*. 1999.

[125] R. Penrose. Gravitational Collapse and Space-Time Singularities. *Phys. Rev. Lett.*, 14(3):57–59, January 1965.

[126] A. Celotti, J. Miller, and D. Sciama. Astrophysical evidence for the existence of black holes. *Classical and Quantum Gravity*, 16(12A):A3–A21, December 1999.

[127] J. Kormendy and D. Richstone. Inward Bound—The Search For Supermassive Black Holes In Galactic Nuclei. *ARAA*, 33:581, January 1995.

[128] J. Kormendy and L. C. Ho. Coevolution (Or Not) of Supermassive Black Holes and Host Galaxies. *Ann. Rev. Astron. Astrophys.*, 51:511–653, 2013.

[129] F. Curtis Michel. Accretion of Matter by Condensed Objects. *APSS*, 15(1):153–160, January 1972.

[130] A. Aguayo-Ortiz, E. Tejeda, O. Sarbach, and D. López-Cámara. Spherical accretion: Bondi, Michel, and rotating black holes. *MNRAS*, April 2021.

[131] O. Porth, H. Olivares, Y. Mizuno, Z. Younsi, L. Rezzolla, M. Moscibrodzka, H. Falcke, and M. Kramer. The black hole accretion code. *Computational Astrophysics and Cosmology*, 4(1), May 2017.

[132] A. M. Ghez et al. The First Measurement of Spectral Lines in a Short-Period Star Bound to the Galaxy's Central Black Hole: A Paradox of Youth. *Astrophysical Journal*, 586(2):L127–L131, April 2003.

[133] S. Gillessen, F. Eisenhauer, S. Trippe, T. Alexander, R. Genzel, F. Martins, and T. Ott. Monitoring Stellar Orbits Around the Massive Black Hole in the Galactic Center. *Astrophysical Journal*, 692(2):1075–1109, February 2009.

[134] H. Falcke and S. Markoff. Toward the event horizon?the supermassive black hole in the galactic center. *Classical and Quantum Gravity*, 30(24):244003, Nov 2013.

[135] K. Akiyama and et al. First M87 Event Horizon Telescope Results. V. Physical Origin of the Asymmetric Ring. *Astrophys. J. Letters*, 875:31, 2019.

[136] R. Mahadevan and E. Quataert. Are particles in advection-dominated accretion flows thermal? *The Astrophysical Journal*, 490(2):605–618, dec 1997.

[137] W. Harris, G. Harris, and D. McLaughlin. M87, Globular Clusters, and Galactic Winds: Issues in Giant Galaxy Formation. *AJ*, 115(5):1801–1822, May 1998.

[138] F. K. Baganoff et al. Chandra X-Ray Spectroscopic Imaging of Sagittarius A* and the Central Parsec of the Galaxy. *Astrophysical Journal Letters*, 591(2):891–915, July 2003.

[139] J. Read and G. Gilmore. Can supermassive black holes alter cold dark matter cusps through accretion? *Mon. Not. Roy. Astron. Soc.*, 339:949, 2003.

[140] J. Choquette, J. Cline, and J. Cornell. Early formation of supermassive black holes via dark matter self-interactions. *JCAP*, 2019(7):036, July 2019.

[141] C. Argüelles, M. Díaz, A. Krut, and R. Yunis. On the formation and stability of fermionic dark matter haloes in a cosmological framework. *Mon. Not. Roy. Astron. Soc.*, 502(3):4227–4246, April 2021.

[142] Ya. B. Zeldovich and Igor D. Novikov. *Relativistic astrophysics. Vol.1: Stars and relativity*. 1971.

[143] S. Shapiro and S. Teukolsky. *Black holes, white dwarfs, and neutron stars : the physics of compact objects*. 1983.

[144] P. Mach and A. Odrzywołek. Accretion of the relativistic Vlasov gas onto a moving Schwarzschild black hole: Exact solutions. *Phys. Rev. D*, 103(2):024044, 2021.

[145] P. Mach and A. Odrzywołek. Accretion of dark matter onto a moving Schwarzschild black hole: An exact solution. *Phys. Rev. Lett.*, 126(10):101104, 2021.

[146] P. Sharma, G. Hammett, E. Quataert, and J. Stone. Shearing box simulations of the mri in a collisionless plasma. *Astrophys. J.*, 637:952–967, 2006.

[147] M. Chandra, C. Gammie, F. Foucart, and E. Quataert. An Extended Magnetohydrodynamics Model for Relativistic Weakly Collisional Plasmas. *Astrophys. J.*, 810(2):162, 2015.

[148] F. Foucart, M. Chandra, C. Gammie, E. Quataert, and A. Tchekhovskoy. How important is non-ideal physics in simulations of sub-Eddington accretion on to spinning black holes? *Mon. Not. Roy. Astron. Soc.*, 470(2):2240–2252, 2017.

[149] M. Kunz, J. Stone, and E. Quataert. Magnetorotational turbulence and dynamo in a collisionless plasma. *Physical Review Letters*, 117(23), Dec 2016.

[150] A. Aguayo-Ortiz, E. Tejeda, and X. Hernandez. Choked accretion: from radial infall to bipolar outflows by breaking spherical symmetry. *Mon. Not. Roy. Astron. Soc.*, 490(4):5078–5087, 2019.

[151] E. Tejeda, A. Aguayo-Ortiz, and X. Hernandez. Choked accretion onto a Schwarzschild black hole: A hydrodynamical jet-launching mechanism. *Astrophys. J.*, 893:81, 2020.

[152] A. Aguayo-Ortiz, O. Sarbach, and E. Tejeda. Choked accretion onto a Kerr black hole. *Phys. Rev. D*, 103(2):023003, 2021.

[153] T. Di Matteo, S. Allen, A. Fabian, A. Wilson, and A. Young. Accretion onto the Supermassive Black Hole in M87. *Astrophysical Journal*, 582(1):133–140, January 2003.

[154] D. K. Aitken, J. Greaves, Antonio Chrysostomou, T. Jenness, W. Holland, J. H. Hough, D. Pierce-Price, and J. Richer. Detection of Polarized Millimeter and Submillimeter Emission from Sagittarius A*. *Astrophysical Journal Letters*, 534(2):L173–L176, May 2000.

[155] C. Kuo et al. Measuring Mass Accretion Rate onto the Supermassive Black Hole in M87 Using Faraday Rotation Measure with the Submillimeter Array. *Astrophysical Journal Letters*, 783(2):L33, March 2014.

[156] Event Horizon Telescope Collaboration. First M87 Event Horizon Telescope Results. VII. Polarization of the Ring. *Astrophysical Journal Letters*, 910(1):L12, March 2021.

[157] K. Akiyama and et al. First M87 Event Horizon Telescope Results. VIII. Magnetic Field Structure near The Event Horizon. *Astrophys. J. Letters*, 910:43, 2021.

[158] E. Quataert and A. Gruzinov. Constraining the Accretion Rate onto Sagittarius A* Using Linear Polarization. *Astrophysical Journal*, 545(2):842–846, December 2000.

[159] A. Jiménez-Rosales and J. Dexter. The impact of Faraday effects on polarized black hole images of Sagittarius A*. *MNRAS*, 478(2):1875–1883, August 2018.

[160] R. Narayan and I. Yi. Advection-dominated Accretion: Underfed Black Holes and Neutron Stars. *Astrophysical Journal*, 452:710, October 1995.

[161] E. Quataert and R. Narayan. On the Energetics of Advection-dominated Accretion Flows. *Astrophysical Journal*, 516(1):399–410, May 1999.

[162] F. Yuan, E. Quataert, and R. Narayan. Nonthermal Electrons in Radiatively Inefficient Accretion Flow Models of Sagittarius A*. *Astrophysical Journal*, 598(1):301–312, November 2003.

[163] F. Yuan and R. Narayan. Hot Accretion Flows Around Black Holes. *ARAA*, 52:529–588, August 2014.

[164] F. Debbasch and W. van Leeuwen. General relativistic Boltzmann equation, I: Covariant treatment. *Physica A Statistical Mechanics and its Applications*, 388(7):1079–1104, April 2009.

[165] O. Sarbach and T. Zannias. The geometry of the tangent bundle and the relativistic kinetic theory of gases. *Class. Quant. Grav.*, 31:085013, 2014.

[166] P. Crawford and I. Tereno. Generalized Observers and Velocity Measurements in General Relativity. *General Relativity and Gravitation*, 34(12):2075–2088, December 2002.

[167] V. Korol, L. Ciotti, and S. Pellegrini. Bondi accretion in early-type galaxies. *Monthly Notices of the Royal Astronomical Society*, 460(2):1188?1200, May 2016.

[168] R. P. Eatough et al. A strong magnetic field around the supermassive black hole at the centre of the Galaxy. *NAT*, 501(7467):391–394, September 2013.

[169] J. Cuadra and S. Nayakshin. Variable accretion of stellar winds onto Sgr A*. In *Journal of Physics Conference Series*, volume 54 of *Journal of Physics Conference Series*, pages 436–442, December 2006.

[170] J. Cuadra, S. Nayakshin, and F. Martins. Variable accretion and emission from the stellar winds in the Galactic Centre. *Mon. Not. Roy. Astron. Soc.*, 383(2):458–466, January 2008.

[171] J. Cuadra, S. Nayakshin, and Q. Wang. The role of feedback in accretion on low-luminosity AGN: Sgr A* case study. *Monthly Notices of the Royal Astronomical Society*, 450(1):277–287, 04 2015.

[172] G. Bower, M. Wright, H. Falcke, and D. Backer. Interferometric Detection of Linear Polarization from Sagittarius A* at 230 GHz. *Astrophysical Journal*, 588(1):331–337, May 2003.

[173] D. Marrone, J. Moran, J. Zhao, and R. Rao. Interferometric Measurements of Variable 340 GHz Linear Polarization in Sagittarius A*. *Astrophysical Journal*, 640(1):308–318, March 2006.

[174] D. Marrone, J. Moran, J. Zhao, and R. Rao. An Unambiguous Detection of Faraday Rotation in Sagittarius A*. *Astrophysical Journal Letters*, 654(1):L57–L60, January 2007.

[175] G. Bower et al. ALMA Polarimetry of Sgr A*: Probing the Accretion Flow from the Event Horizon to the Bondi Radius. *Astrophysical Journal*, 868(2):101, December 2018.

[176] D. Allen, A. Hyland, and D. Hillier. The source of luminosity at the Galactic Centre. *Mon. Not. Roy. Astron. Soc.*, 244:706, June 1990.

[177] J. Puls et al. O-star mass-loss and wind momentum rates in the Galaxy and the Magellanic Clouds Observations and theoretical predictions. *AAP*, 305:171, January 1996.

[178] T. Repolust, J. Puls, and A. Herrero. Stellar and wind parameters of Galactic O-stars. The influence of line-blocking/blanketing. *AAP*, 415:349–376, February 2004.

[179] T. Paumard et al. The Two Young Star Disks in the Central Parsec of the Galaxy: Properties, Dynamics, and Formation. *Astrophysical Journal*, 643(2):1011–1035, June 2006.

[180] F. Martins, R. Genzel, D. J. Hillier, F. Eisenhauer, T. Paumard, S. Gillessen, T. Ott, and S. Trippe. Stellar and wind properties of massive stars in the central parsec of the Galaxy. *AAP*, 468(1):233–254, June 2007.

[181] S. Ressler, E. Quataert, and J. Stone. Hydrodynamic simulations of the inner accretion flow of Sagittarius A* fuelled by stellar winds. *Mon. Not. Roy. Astron. Soc.*, 478(3):3544–3563, August 2018.

[182] S. Ressler, C. White, E. Quataert, and J. Stone. Ab Initio Horizon-scale Simulations of Magnetically Arrested Accretion in Sagittarius A* Fed by Stellar Winds. *Astrophysical Journal Letters*, 896(1):L6, June 2020.

[183] D. Calderón, J. Cuadra, M. Schartmann, A. Burkert, and C. Russell. Stellar Winds Pump the Heart of the Milky Way. *Astrophysical Journal Letters*, 888(1):L2, January 2020.

[184] M. Mościbrodzka, C. Gammi, J. Dolence, H. Shiokawa, and P. Leung. Radiative Models of Sgr A* from GRMHD Simulations. *Astrophysical Journal*, 706(1):497–507, November 2009.

[185] M. Mościbrodzka and H. Falcke. Coupled jet-disk model for Sagittarius A*: explaining the flat-spectrum radio core with GRMHD simulations of jets. *AAP*, 559:L3, November 2013.

[186] R. Shcherbakov and F. Baganoff. Inflow-Outflow Model with Conduction and Self-consistent Feeding for Sgr A*. *Astrophysical Journal*, 716(1):504–509, June 2010.

[187] S. Chandrasekhar. *The Mathematical Theory of Black Holes*. Oxford University Press, Oxford, England, 1983.

[188] D. Núñez and J. Degollado. *Relatividad General*. online, Facultad de Ciencias, UNAM, Mexico City, Mexico, 2005.

[189] K. Akiyama and et al. First M87 Event Horizon Telescope Results. VI. The Shadow and Mass of the Central Black Hole. *Astrophys. J. Letters*, 875:44, 2019.

[190] E. Chaverra and O. Sarbach. Radial accretion flows on static, spherically symmetric black holes. *Class. Quantum Grav.*, 32:155006, 2015.